UNIVERSITY OF LIVERPOOL

School of Engineering

PhD Thesis

Optimised Ultrafast Laser Modulation with Spatial Light Modulators for Material Micro-Structuring

Thesis submitted in accordance with the requirements of The University of Liverpool for the degree of Doctor in Philosophy

By

Yue Tang

February 2020

Laser Group
Department of Engineering
The University of Liverpool
Brownlow Street
Liverpool
L69 3GH
UK

Declaration

I hereby declare that all of the work contained within this dissertation has not been submitted for any other qualification.

Signed:

Date:

Abstract

In this thesis, advanced laser modulation techniques with reflective phase only liquid crystal spatial light modulators (SLMs) addressed with optimised computer generated holograms (CGHs) have been presented. By integrating a picosecond pulsed laser system with a SLM and a motion control stage, dynamic beam shaping and polarization control has been achieved during ultrafast laser material surface micro processing.

A novel method of dynamic control of polarization states and beam shapes of an ultrafast laser using a SLM with an additional polarization converter, S-waveplate is achieved. Applying binary CGHs on the SLM, shaped beam outlines were generated at the imaging plane of an optical processing system. Consequently, several beam shapes were dynamically switched while synchronized with a motion control system. Shaped beam with cylindrical vector (CV) polarization states, such as radial and azimuthal were obtained by using an S-waveplate. Imprinting laser induced periodic surface structures (LIPSS) was employed to investigate the detailed vector fields at the image plane. The ablation footprint and micro-structure was found to match the selected beam shape and polarization states accurately. In addition, by applying grey level CGHs on two SLMs, the multiple parallel beam processing with shaped beam outlines and uniform intensity distributions have been obtained.

Combining binary Dammann grating CGHs with an S-waveplate, diffractive 1x5, 2x2 and 5x5 CV polarized multiple-spot arrays have been generated with high polarization purity. The vector quality factor (concurrence C and entanglement entropy E) of multiple CV beam arrays has been measured for the first time. The average vector quality factor (VQF) was measured to be $\langle C_{1x5} \rangle = 0.95 \pm 0.01$, $\langle E_{1x5} \rangle = 0.94 \pm 0.01$ while for the 2x2 array, $\langle C_{2x2} \rangle = 0.86 \pm 0.02$ and $\langle E_{2x2} \rangle = 0.82 \pm 0.02$ respectively, and hence geometry dependent. As these vector beams are non-separable (entangled) in spatial and polarization modes, the degree of entanglement allows a test of Bell's Theorem on a single photon. The measured violation of a Bell-like inequality $|S| \leq 2$ of each diffractive order in the 1x5 spot array yielded $|S_{1x5}| = 2.35 \pm 0.02$, which violates the Clauser-Horne-Shimony-Holt (CHSH) inequality by more than 17 standard deviations.

The CV beams were used to ablate polished metal samples (Ti-6Al-4V) with Laser Induced Periodic Surface Structure (LIPSS) which confirm the polarization states unambiguously.The measured ablation threshold on Titanium alloy of the ring mode radial and azimuthal polarisations as well as high order vortex beams is close to that of a Gaussian mode taking into account the expected absolute intensity distribution of ring beams generated from a Gaussian. The comparison of each machined spot has been analysed with a machine learning method - cosine similarity.

The cylindrical vector polarization state has been dynamically controlled at 12.5Hz from radial to azimuthal with a spatial Light modulator (SLM) and an S-waveplate, to generate single complex cylindrical vector beams for material surface modification while synchronized to the motion control system. The real time micro machining technique has been used for metal colour marking using complex LIPSS on Titanium while the addition of LIPSS to a micro structured Ti surface transformed this to surperhydrophobic. The laser polarization states enable to be real-time controlled for various colour marking and material wettability modification by producing the LIPSS on polished Ti6Al4V samples with a picosecond pulsed laser.

Finally, I demonstrated the use of Dammann grating (only 0 and π phase) for extending the power range of a liquid cooled SLM, beyond the previous limit of 120W to $P \geq 160$W.

Acknowledgement

I would like to express my gratitude to everyone who has supported and encouraged me during my PhD. In particular I would like to thank the following people.

First of all, thanks must go to my supervisors, Dr. Stuart Edwardson and Prof. Geoff Dearden for their unwavering support, guidance and encourage during my studies and researches. I would like to thank Dr.Walter Perrie for his invaluable advice, constant help and endless support. Without their dedication, this work would not have been possible. I am grateful everyone from the Laser group of University of Liverpool who was involved in my research, in particular Mr Andy Snaylam and Mrs Jones Andrea.

I also appreciate the friendship, help and advice from all my fellow labmates: Qianliang Li, David Rico Sierra and Tong Zhou.

Additionally, I would like to thank all my friends for your support, in particular Yu Dong, Wenjia Wang, Gaopeng Dong and Zijun Huang.

Special thanks to my girlfriend, Yuhui Gan, for her support and understanding.

Last but not least, I would like to thank my family members, especially my parents who always offering me unconditionally support and constant encouragement whenever I met difficulties.

I love you all.

List of publications to date by author

Published Papers

[1]. **Tang, Y***., J. Li, T. Zhou, J. Schille, U. Loeschner, W. Perrie, G. Dearden, and S. P. Edwardson. "Dynamic Beam Shaping with Polarization Control at the Image Plane for Material Processing." Procedia CIRP 74 (2018): 581-84.

[2]. Zhu, G., D. Whitehead, W. Perrie, O. J. Allegre, V. Olle, Q. Li, **Y. Tang**, et al. "Investigation of the Thermal and Optical Performance of a Spatial Light Modulator with High Average Power Picosecond Laser Exposure for Materials Processing Applications." Journal of Physics D: Applied Physics 51, no. 9 (2018).

[3]. Li, Jiangning, **Yue Tang***, Zheng Kuang, Joerg Schille, Udo Loeschner, Walter Perrie, Dun Liu, Geoff Dearden, and Stuart Edwardson. "Multi Imaging-Based Beam Shaping for Ultrafast Laser-Material Processing Using Spatial Light Modulators." Optics and Lasers in Engineering 112 (2019): 59-67.

[4]. Li, Qianliang; Perrie, Walter; Potter, R; Allegre, Olivier; Li, Zhaoqing; **Tang, Yue**; Zhu, Guangyu; Liu, Dun; Chalker, Paul; Edwardson, Stuart; Dearden, Geoff, "Femtosecond laser micro-structuring of amorphous Polyether(ether)ketone (PEEK) at 775 nm and 387 nm" Journal of Physics D: Applied Physics 53, no. 36 (2020).

[5]. **Yue Tang**, Walter Perrie, Joerg Schille, Udo Loeschner, Qianliang Li, Dun Liu, Stuart. P. Edwardson, Andrew Forbes and Geoff Dearden "High-quality vector vortex arrays by holographic and geometric phase control" Journal of Physics D: Applied Physics **-Accepted.**

[6]. **Yue Tang**, Walter Perrie, Guangyu Zhu , David Rico Sierra , Qianliang Li , Dun Liu, Stuart. P. Edwardson and Geoff Dearden "The generation of ultrafast cylindrical vector laser beam arrays for material processing" - **The paper has been fully completed and will be submitted in April, 2020**.

Conference contributions

[1]. **Tang, Y**., Lopez Espiricueta, D., Sheikholeslami, G., Dearden, G., & Edwardson, S. (2017). FE modelling of laser sintering of copper nano-particulate paste using a laser line source. In Proceedings of 39th MATADOR Conference Vol. Session LMN-2, Laser Micro/Nano Fabrication 2 (pp. Paper #092). University of Manchester, Manchester, UK.

[2]. Zhu, G., Whitehead, D., Perrie, W., Allegre, O. J., Olle, V., Li, Q., **Tang,Y**., K. Dawson, Y.Jin, Dearden, G. (2018). Thermal and optical performance characteristics of a spatial light modulator with high average power picosecond laser exposure applied to materials processing applications. In Procedia CIRP Vol. 74 (pp. 594-597). Elsevier BV. doi:10.1016/j.procir.2018.08.080.

[3]. Zhu, G., Whitehead, D., Perrie, W., Allegre, O. J., Olle, V., Li, Q.,**Tang,Y**., . . . Dearden, G. (2018, June 25). Femtosecond Inscription inside Poly-Methyl Pentene with Numerical Aperture, Wavelength and with Polarised Helical Beams carrying Orbital and Spin Angular Momentum. In Proceedings of LPM2018 Vol. Session: Functional surfaces (pp. Thu-5-OR2). Edinburgh, Scotland, UK.

[4]. Li, Q., Perrie, W., **Tang, Y**., Allegre, O., Ho, J., Chalker, P., . . . Dearden, G. (2020). Ablation of amorphous Polyethy(ethyl)letone (PEEK) by a femtosecond Ti:sapphire laser. In Laser-based Micro- and Nanoprocessing XIV. SPIE. doi:10.1117/12.2543735.

Table of contents

Declaration....................i
Abstract....................ii
Acknowledgement....................iv
List of publications to date by author....................vi
Table of contents....................vi
List of figures....................xi
List of tables....................xxiii
List of abbreviations....................xxvi

Chapter 1 Introduction....................1

1.1 Background and motivation....................2
1.2 Aim and Objectives....................4

Chapter 2 Literature Review....................6

2.1 Introduction....................7
2.2 Laser systems and ultrafast laser material interaction....................7
2.2.1 Introduction of laser systems....................7
2.2.2 Short and ultrashort pulsed laser generation techniques....................8
2.2.2.1 Q-switching....................8
2.2.2.2 Mode locking....................9
2.2.2.3 Chirped pulse amplification (CPA)....................11
2.2.3 Ultrafast laser material interaction....................13
2.2.3.1 Absorption and Optical penetration....................14
2.2.3.2 Heat diffusion....................15
2.2.3.3 Long pulse and ultrashort pulse....................15
2.3 Laser Induced Periodic Surface Structure (LIPSS)....................18
2.3.1 Classification of LIPSS and formation theory....................19
2.3.1.1 Low spatial frequency LIPSS (LSFL)....................19
2.3.1.2 High spatial frequency LIPSS (HSFL)....................20
2.3.2 LIPSS modification....................20
2.3.3 Applications of LIPSS....................22
2.3.3.1 Colour marking....................22
2.3.3.2 Material wettability modification....................24
2.4 Introduction to phase and polarization....................25
2.4.1 Definition of phase and polarization....................25
2.4.2 Cylindrical vector polarizations....................28
2.4.2.1 Generation methods....................29
2.4.2.2 S-waveplate....................31

2.4.3 Polarization effects on laser material interaction 31
2.4.3.1 Linear interaction 32
2.4.3.2 Non-linear interaction 32
2.5.1 Intensity and polarization control with SLM 33
2.5.2 Theory of light modulation with spatial light modulator 33
2.5.3 Intensity and polarization control with optics 34
2.6 Introduction to laser beam shaping 38
2.6.1 Typical intensity distribution for laser beam shaping 38
2.6.2 Beam shaping using refractive geometrical optics 38
2.6.3 Beam shaping using diffractive elements 40
2.6.4 Optimization of laser beam shaping 41
2.6.4.1 Modulation of phase and intensity 41
2.6.4.2 Optical vector and polarization modification 43
2.7 Laser parallel processing with a Spatial Light modulator (SLM) 44
2.7.1 Working principle of a phase only SLM 44
2.7.2 Generation of multiple beams with SLM 46
2.7.2.1 Parallel micro-processing using periodic structures 46
2.7.2.2 Parallel micro-processing using arbitary structures 47
2.7.3 Algorithms for calculating computer generated holograms (CGHs) 49
2.7.3.1 Iterative Gerchberg-Saxton(GS) algorithm 49
2.7.3.2 Non-Iterative algorithm 51
2.8 State of the Art 52
Chapter 3 Experimental Equipment and Techniques 53
3.1 Introduction 54
3.2 Laser systems 54
3.2.1 High-Q 10ps laser system 54
3.2.2 Edgewave 10ps laser 57
3.2.3 SPI fibre laser system 58
3.3 Spatial light modulators and diffractive optical element 59
3.3.1 Output test of X10468-03 SLM 61
3.3.2 Output test of X13138-5785 SLM 62
3.3.3 Output test of X13138-03 SLM 64
3.3.4 S-waveplate 67
3.4 Scanning equipment and multi-axis motion control system 69
3.4.1.1 High-Q laser system scan head 69
3.4.1.2 Edgewave laser system scan head 70
3.4. 2 Motion control system and control software 70
3.5 Sychronization of ultrafast laser system 71

3.6 Measurement and analysis equipment 72
3.6.1 Beam profiler 72
3.6.2 Nikon Eclipse LV150NL optical microscope 74
3.6.3 WYKO NT1100 white light interferometer microscope 74
3.6.4 FLIR SC660 thermal camera 75
3.6.5 Scanning Electron Microscope (SEM) 75
3.6.6 Drop shape analysis system 76
3.7 Modelling and simulation software 76
3.7.1 ZEMAX 76
3.7.2 MATLAB 77
3.8 Summary 77
Chapter 4 Diffractive Dynamic Beam Shaping with Polarization Control at the Image Plane 79
4.1 Introduction 80
4.2 Methodology of beam shaping at the image plane 80
4.3 Experimental and methodology 83
4.3.1 Experimental setup 83
4.3.2 Beam shaping using a SLM 84
4.3.3 Polarization control using an S-waveplate 84
4.3.4 Polarization confirmation with ZEMAX modelling 84
4.3.5 Shaping reconstruction at the imaging plane 85
4.4 Result and discussion 86
4.4.1 Polarized beam observed by a CCD camera 86
4.4.2 Dynamic beam shaping machining results 88
4.4.3 Beam shaping efficiency-with Binary masks 91
4.5 Beam shaping with grey level masks 92
4.6 Multiple parallel beam shaping with two SLMs 93
4.6.1 Beam shaping efficiency -with grey level masks 95
4.7 Summary 96
Chapter 5 Generation of cylindrical vector beam arrays using binary CGHs 98
5.1 Introduction 99
5.2 Experimental 100
5.2.1 Experimental setup 100
5.2.2 Polarization control using an S-waveplate 101
5.3 Results and discussion 102
5.3.1 Cylindrical vector (CV) beams generation 102
5.3.2 Ablation test on Ti-6Al-4V and Cr thin film with Gaussian and CV beam 103
5.3.2.1 Intensity comparison of Gaussian and CV beams 103

5.3.2.2 Single beam Surface Ablation with Gaussian and Ring modes 105
5.4 Multiple cylindrical vector (CV) beam generation 109
5.5 Reducing intensity of zero order 111
5.6 Measuring cylindrical vector beams 112
5.6.1 Measuring of single CV beam 112
5.6.2 Measuring of Multiple CV beams 115
5.6.3 Measurement with Stokes projections 119
5.7 Parallel processing on a Ti-6Al-4V surface using uniform multiple cylindrical vector beam arrays 120
5.8 Similarity of each spot - Cosine Similarity 123
5.9 High Power processing with cooled SLM / Dammann gratings 125
5.10 Laser surface patterning and texturing 126
5.10.1 Dynamic laser surface patterning with multiple CV beams 126
5.10.2 Arrays of laser spots with different polarization states 127
5.10.3 Continuous scanning with different polarization states 127
5.11 Summary 128
Chapter 6 Dynamically controlled cylindrical vector beams and applications in surface processing 131
6.1 Introduction 132
6.2. Experimental 133
6.2.1 Experimental setup 133
6.2.2 Polarization control using an S-waveplate 134
6. 3 Cylindrical vector polarization states confirmed with ZEMAX 135
6.4 Results and discussion 136
6.4.1 Dynamic controlled linear polarization 136
6.4.2 Dynamic controlled cylindrical vector polarization 137
6.4.2.1 Synchronized CV polarized beams generation 137
6.4.2.2 Scanned lines using synchronized CV beams 138
6.4.2.3 Overlaid CV polarization states 140
6.4.2.4 Fabrication of large surface area structures using a single synchronized CV beam 141
6.5 Wettability properties 143
6.6 Summary 150
Chapter 7 Conclusions and future work 152
7.1 Conclusions 153
7.2 Recommendations for future work 157
References 160
Appendix 1 i
Appendix 2 iv
Appendix 3 v

Appendix 4 vi

List of figures

Figure 2. 1 The diagram scheme of a three-level laser energy [48] 8
Figure 2. 2 (a) laser effect once the optical cavity is suddenly opened (b) Depletion of the optical cavity once all the atoms have returned to the ground state [54]. 9
Figure 2. 3 Mechanism of laser pulse modelocking [57]. 10
Figure 2. 4 Diagrammatic scheme of chirped pulse [66]..12
Figure 2. 5 Diagrammatic scheme of different pulse frequency will be dispersed into different directions and with different travelling path[67]. 12
Figure 2. 6 (a) The factors that affect stretching ability of CPA (b) factors that affect compressing ability of CPA [67]..13
Figure 2. 7 The mechanism of laser-material interaction under long laser pulse [82]. 16
Figure 2. 8 The mechanism of laser-material interaction under ultrashort laser pulse duration [83]........17
Figure 2. 9 Laser precision machining on glass with nanosecond laser (left) and femtosecond laser (right) [85]..17
Figure 2. 10 LIPSS was fabricated with different polarization states.(a) Linear polarization (b) circular polarization and corresponding Fast Fourier Transform (FFT) (c) CV polarization [95],[102], [103]...18
Figure 2. 11 Scanning electron micrograph of two different types of LIPSS formed on titanium alloy (Ti6Al4V) surfaces after irradiation with fs-laser pulses (30fs,800nm,1kHz). (a) LSFL [∅_0=0.11J/,N~56]; (b) HSFL [∅_0=0.08J/,N~560] [106]..19
Figure 2. 12 Uniformity of LIPSS generation based on different scanning direction [110]. 21
Figure 2. 13 Different overlaps empolyed for different UV LIPSS morphologies generation. The red arrows indicate the polarization orientation. The yellow arrows indicate the edge of the groove. (fluence=0.11J/cm2 ,pps=overlap per spots) [113]. 21
Figure 2. 14 SEM image for uniform LIPSS that on a polished metal surface. Arrow shows alignment of the incident E-field [117]..22
Figure 2. 15 Schematic illustration of white light diffraction on LIPSS covered metal surface, end up with different colour dependent on viewing angle 22
Figure 2. 16 Selective colour appearance on LIPSS covered areas with two orthogonal LIPSS direction. The red arrows indicate the illumination source direction. (a) Selective colour appearance of one LIPSS covered area with the LIPSS's direction perpendicular to the illumination source direction. (b) Colour appearance on both areas covered with orthogonal LIPSS direction and illuminated with orthogonal light sources [8]..23

Figure 2. 17 The multicoloured area of the treated surface was taken by a camera with the illumination of a white light. Irradiated fluencies : left column, 1.38J/cm^2 (top), 1.26J/cm^2 (middle), and 1.13J/cm^2 (bottom); middle column, 1.00 J/cm^2 (top), 0.88 J/cm^2 (middle), and 0.75 J/cm^2 (bottom) and right column, 0.63J/cm^2 (top), 0.50 J/cm^2 (middle), and 0.38 J/cm^2 (bottom) [7]. 23

Figure 2. 18 Stainless steel (SS) wettablity comparison with a fixed pitch distance of LIPSS treated surface and no LIPSS treated surface. (a-c) The wettability of SS without LIPSS covered surface (d-f) the wettability of SS with LIPSS covered surface [95]. 24

Figure 2. 19 Triangular-LIPSS produced by circular polarization. (a) Triangular-LIPSS pattern and corresponding Fast Fourier Transform (FFT). Bottom (b) Produced triangular-LIPSS for wettability properties modification (c) Produced linear-LIPSS for properties modification. [102]. 25

Figure 2. 20 Illustration of phase shift. The horizontal axis represents an phase angle (ϴ) that is shifted [121]. 26

Figure 2. 21 Illustration the different polarization states [123]. 26

Figure 2. 22 Formation of radial and azimuthal polarizations using linear superposition of orthogonally polarized HG modes [127] 29

Figure 2. 23 Plasmonic structures of complex polarization states generated by rotating S-waveplate (a) -67.5° , (b)-45°, (c)-22.5°, (d) 0°(radial), (e)+22.5°, (f)+45°, (g) +67.5°, (h)+90°(azimuthal) [131]. 30

Figure 2. 24 CV beams generation using an SLM [88]. 30

Figure 2. 25 S-waveplate (Altechna) used to convert incident linear polarization to radial and azimuthal polarizations [133]. 31

Figure 2. 26 A schematic of 3D beam shaping using Dammann Zone Plate (DZP). DG is Dammann grating [115]. 34

Figure 2. 27 A schematic of perfect vortex beam generation by using optics [158]. 35

Figure 2. 28 (a)experimental setup. PH is a pinhole (~100μm), P is a polarizer, D is a diaphragm, S is an S-waveplate, DOE is an amplitude diffractive optical element forming a superposition of eight vortex beams with orders of ±1,±2,±3,±4, L is a lens with f=150mm, A is an analyser, and CMOS is a CMOS-video camera. (b) simulated diffraction pattern in far-field region when passing the laser beam through the amplitude diffractive optical element (c) experimentally obtained interference patterns of the generated vortex beams [162]. 35

Figure 2. 29 (a) Experimental setup and (b) orientation of the E-field vector E relative to the scanning velocity v [46]. 36

Figure 2. 30 Printed LIPSS with dynamic controlled polarization sates on stainless steel surface utilising an E-field vector rotating by an angle $\Delta\boldsymbol{\alpha}$ of (a) 2.9°, (b) 8.6°, (c) 14.4° and (d) 28.8°in comparison to the utilisation of (e) circular polarisation; left: SEM micrographs and right: optical micrographs imaged with

side-illumination at grazing incidence (arrows indicate the direction of illumination, v=0.5mms/, f=250Hz, f=1J/cm^2) [46]. 37

Figure 2. 31 Dynamic controlled polarization states and a formed diffractive pattern. (a) Dynamic controlled linear, radial and azimuthal polarizations (b) a diffractive pattern formed based on dynamic controlled polarization states [163]..37

Figure 2. 32 To evaluation of efficiency of using the laser energy [13]..39

Figure 2. 33 The basic structure of a LCOS-SLM and a typical diffractive optical element [20, 21........41

Figure 2. 34 Phase and amplitude modification with two SLMs. SLM1 for phase modification and SLM2 for OAM beams generation. (a) Intensity profiles of the generated spot. System A is one-lens imaging system and system B is a 4f system. (b) Phase pattern employed on SLM1 for phase modulation and SLM 2 for OAM beams generation [164]...42

Figure 2. 35 The far-field from the conjugate gradient optimization showing normalized intensity and phase in the region of interest [181]. 43

Figure 2. 36 Combined phase modulation with vortex beams by a SLM. 22.5° and 45° represent the fast axis angle of the S-waveplate [131]..43

Figure 2. 37 36 segments produced on polished brass sample with dynamic polarization control. 0° stands for horizontal linear polarization and the polarization rotates clockwise with an incremental change of 5°, which gives a different LIPSS orientation in each segment of the pattern [163]. 44

Figure 2. 38 Schematic of a typical reflective type SLM structure [10]. 45

Figure 2. 39 Schematic of the laser with an SLM. Modulated results will be produced at focal plane of the focal length (a) modulated intensity results [188] (b) modulated phase/polarization results (c) modulated laser multiple patterns. 45

Figure 2. 40 The results of arbitrary multi-beam pattern generated by a DOE. (a) The designed pattern, (b) The generated beam profile observed on a CCD camera, (c) observed machined pattern on focal plane. (d) laser glass processing using the arbitrary multi-beam. Observed by optical microscopy, left: top view, right: side view [189]. 47

Figure 2. 41 Example images for individual intensity control. (a)Computer generated hologram (b)Producing intensity pattern which is measured with a beam profiler (c) machined pattern with period of 32µm on silicon wafer [183]. 48

Figure 2. 42 The mechanism of GS algorism for CGHs generation [25]. 49

Figure 2.43 Diffractive schematic for (a) Dammann grating DOE [196]. D indicates the structure period (b) Dammann grating Computer generated hologram (CGH). Red rectangular represents the Grating Unit Cell, G1 is the area with phase equals to 0 and G2 is the area with phase equals to π.............................51

Figure 3. 1 Three mainly parts of the High-Q laser system: (top) laser head, (bottom left) laser controller with power unit and (bottom right) water-air cooling system……………………………………………54
Figure 3. 2 (a) Schematic of optical setup inside of the High-Q laser head and (b) the corresponding image of laser head internals. 55
Figure 3. 3 A particular optical setup for laser polarization control. Blue arrows indicate the laser propagation direction. 56
Figure 3. 4 Original beam profile measured using a CCD beam profiler of the High-Q laser system......56
Figure 3. 5 Interface of High-Q laser system control software 57
Figure 3. 6 The setup for an Innoslab laser [198]..57
Figure 3. 7 Experimental device (a) A Edgewave laser indicated with a red rectangle (b) SCANLAB intelliSCAN 14 scan head with a F-theta lens, loaned from the University of Liverpool (c) SLM chiller (d) Hamamatsu X13138-03 SLM. 58
Figure 3. 8 Experimental setup for a SPI fibre laser system..59
Figure 3. 9 Corresponding phase modulation with input grey level for X10468/X13138 series Hamamatsu SLMs [199]. 61
Figure 3. 10 Experimental setup for X10468 SLM output test. A beam expander was used to enlarge beam size. 61
Figure 3. 11 Correspond measured power with input grey level applied on the SLM. 62
Figure 3. 12 Experimental setup for X13138-5785 SLM output test. A beam expander was used to enlarge beam size..63
Figure 3. 13 Calculations for theoretical intensity output with an SLM. All elements are expressed with corresponded Jones matrices and laser passes from right to left [186] 63
Figure 3. 14 Output intensity vs grey level with rotating half wave plate fast axis angle @ 0.2W,10kHz,10ps. 64
Figure 3. 15 Experimental setup for X13138-03 SLM output test. A beam expander was used to enlarge beam size..65
Figure 3. 16 The calculated phase response with incident average power at M2. (a) Experimental data at low average power, P=26.2W compared with a pure $cos2\theta$ function, (b) Experimental data at high average power, P=160W compared with a pure $cos2\theta$ function. [32]..65
Figure 3. 17 Phase response of cooled X13138-03 SLM at M1(P1) and M2(P2). (a) P=2.6W, (b) P=26.2W, (c) P=60.9W, (d) P=109W, (e) P=160W, (f) P=190W. The phase response of the SLM only reaching over a π instead of 2π when applied power P$\geq$ 160W [32]...66

Figure 3. 18 Measured temperature rise with reflected laser power. Laser repetition f=1MHz. Temperature response with a gradient m=0.026° C W-1. Errors represent 1σ and fit is least squares with high confidence, R=0.99, emissivity=0.73 [32]....67

Figure 3. 19 Experimental setup for S-waveplate output loss test. A beam expander was used to enlarge beam size. Various grey level CGHs were applied on the SLM. 67

Figure 3. 20 Corresponding measured power with input grey level applied on the SLM @ 1W, 10ps, 10kHz....68

Figure 3. 21 Polarization purity measurement of CV beams by rotating a half wave plate from 0° to 360°. 68

Figure 3. 22 (a) a scanning galvanometer system Nutfield XLR-8-10; (b)Structures of a scanning galvanometer system....69

Figure 3. 24 a schematic of synchronization system for a laser and a computer....71

Figure 3. 25 Labview software interface for the dynamic control system 72

Figure 3. 26 Thorlabs BC106 camera. This camera consists of filter wheel (with four filters), computer-camera connector, sensor and an extension [4]. 73

Figure 3. 27 BC106 beam profiler software interface [4]....73

Figure 3. 28 (a) Spiricon SP620U beam profiler with wedge beam splitter and (b) its software (BeamGage) interface 74

Figure 3. 29 WYKO white light interferometer with a control PC 75

Figure 3. 30 (a) A Krüss EasyDrop standard drop shape analysis system. (b) A saved image which was observed by a camera....76

Figure 3. 31 The interface of ZEMAX optical studio 15....77

Figure 3. 32 The interface of MATLAB R2014a 77

Figure 4. 1 Schematic of processing at the imaging plane....81

Figure 4. 2 Experimental setup 83

Figure 4. 1 Representation of the electric field of radial and azimuthal axially symmetric beams with polar angle Ø [131]….85

Figure 4. 5 Complex polarization states confirmation of the S-waveplate in ZEMAX. By defining different polar angle (Ø), different output polarization can be achieved with the same input polarization direction (a) Ø=0° (Radial) (b) Ø=90° (Azimuthal), (c) Ø=45° (d) Ø= -45°, (logarithmic spirals of opposite handedness)....85

Figure 4. 6 Beam shaping with an S-waveplate. A shaped square beam can be achieved by an incident beam plus a binary mask at A1. An S-waveplate has been added to achieve a polarized beam at A2. The central hole at A2 indicates that the beam is aligned with the centre of the S-waveplate. 87

Figure 4. 7 Beam shaping with an S-waveplate. A shaped star beam can be achieved by an incident beam plus a binary mask at A1. An S-waveplate has been added to achieve a polarized beam at A2. The central hole at A2 indicates that the beam is aligned with the centre of the S-waveplate. 87

Figure 4. 8 Beam shaping with an S-waveplate. A shaped triangular beam can be achieved by an incident beam plus a binary mask at A1. An S-waveplate has been added to achieve a polarized beam at A2. The central hole at A2 indicates that the beam is aligned with the centre of the S-waveplate. 87

Figure 4. 9 Dynamic control of machined beam shapes with radial polarization. Row (a) shows three different shapes with radial polarization. Row (b) shows a high magnification of each beam footprint. Row (c) shows the radial polarization states for each beam confirmed by LIPSS orientation. 88

Figure 4. 8 Dynamic control of machined beam shapes with azimuthal polarization. Row (a) shows three different shapes with azimuthal polarization. Row (b) shows a high magnification of each beam footprint. Row (c) shows the azimuthal polarization states for each beam confirmed by LIPSS orientation. 89

Figure 4. 10 Dynamic control of machined beam shapes with (a) radial polarization (10kHz, 2μJ/pulse, 50pulses) (b) A single magnified star shaped beam with radial polarization (10kHz, 2μJ/pulse, 50pulses). The red arrows indicate the direction of polarization states. 89

Figure 4. 11 SEM results. (a) The star shape with azimuthal polarization. (b) The star shape with radial polarization. Both shapes were machined by Gaussian type laser beam. The red arrows indicate the direction of polarization states. (10kHz, 2μJ/pulse, 50pulses). 90

Figure 4. 12 Optical and WYKO images for star shapes with azimuthal and radial polarization states.(a) azimuthally polarized star shape. (b) radially polarized star shape. Both results were fabricated at the image plane with the same laser energy and processing time. (10kHz, 2μJ/pulse, 50pulses). 90

Figure 4. 13 Calculated and measured shaping efficiency with different sizes of binary masks. 91

Figure 4. 14 The binary mask with continuous grey level (grey level =90) and its observed result on the CCD beam profiler..92

Figure 4. 15 Plotted measured and theoretical transmission efficiency of the SLM based on the equation 4-20. 93

Figure 4. 16 The grey level mask with a grey level gradient (grey level: 0-255) and its observed result on the CCD beam profiler. 93

Figure 4. 17 Experimental setup for multipule shaped beam generation. 94

Figure 4. 18 Target multiple beam pattern and its CGH generating by Hamamatsu LcosControl (a) Target pattern (b) Generated CGH. 94

Figure 4. 19 Multiple squared beams produced at image plane with (a) binary mask (b) grey level mask. 95

Figure 4. 20 Calculated and measured shaping efficiency of different size of grey level masks. 95

Figure 4. 21 WYKO image of machined footprints with binary and grey level masks at the image plane. (a) machined results with binary mask. (b) machined results with grey level mask. (10kHz, 10μJ, 1s, 0.19J/cm2)....................96

Figure 5. 1 Experimental setup with an S-waveplate 100

Figure 5. 2 Azimuthally polarized single beam observed on a Spiricon CCD beam analyzer. (a) The beam profiler image. The small image on the right top is the electric field direction. (b) SEM image to confirm the polarization state (Ti-6Al-4V,10kHz, 4μJ/pulse, 50pulses). (c)-(f) The beam profile images with a polarizer analyser. The white arrows represent the direction of the fast axis of the polarizer analyser. The double lobe intensity distribution rotates as expected with the polariser fast axis but also highlights some non-uniformity in the ring intensity mode due likely to residual wavefront aberration of the incident Gaussian beam. 102

Figure 5. 3 Radially polarized single beam observed on a Spiricon CCD beam analyzer. (a) The beam profiler image, radial polarization. The small image on the right top is the electric field directions. (b) SEM image to confirm the polarization state (10kHz, 4μJ/pulse, 50pulses). (c)-(f)The beam profile images with a polarizer analyser. The white arrows represent the direction of the fast axis of the polariser. Again, the double lobe intensity distribution rotates as expected with the polariser fast axis but highlights some non-uniformity in the ring mode possibly due to the non-perfect Gaussian beam. 103

Figure 5.4 The simulated intensity distribution in MATLAB: (a) a Gaussian distribution, m = 0. (b) a CV beam distribution, m=1 with the same total pulse energy. (c) Cross section view of a Gaussian distribution and a CV beam distribution. The two lines show the $1/e^2$ intensity levels, red line for the Gaussian distribution beam and blue line for the CV beam distribution. 104

Figure 5. 5 Measured beam intensity using Spiricon SP602U. (a) the intensity of a Gaussian beam. (b) the intensity of a CV beam with S-waveplate. A focus lens with focal length of 500mm was used to ensure more pixels were activated for measurement. Intensities are measured with the same input power. Both images are with the same scale when measuring....................105

Figure 5. 6 (a) optical image of ablated Cr thin film with CV single pulse. (b) SEM image of ablated Cr thin film with CV single pulse. (22μJ/pulse,10kHz,400mm/s), showing the ring structure. 106

Figure 5. 7 Single pulse ablation with (a) vortex beam (m=1) and (b) CV beam (Radial) on Cr coated thin film. By overlapping two images, the beam size for m=1 and CV beam are similar (30μJ,10kHz, 500mm/s). 106

Figure 5. 8 (a) Plot of squared diameter D^2 versus ln(E) for Gaussian beam ablation threshold fluence calculation of Ti-6Al-4V with single pulse (b) Plot of $D^2 - D_0^2$ versus ln(E) for radially polarised CV beam ablation threshold energy calculation of Ti-6Al-4V with single pulse (c) Plot of squared diameter D^2 versus ln(E) for Gaussian beam ablation threshold fluence calculation of Cr coated thin film with single

pulse (d) Plot of $D^2 - {D_0}^2$ versus ln(E) for CV beam ablation threshold fluence calculation of Ti-6Al-4V with single pulse. 107
Figure 5. 9 (a) Plot of squared diameter $D^2 - {D_0}^2$ versus ln(E) for vortex beam (m=1) ablation threshold fluence calculation of Ti-6Al-4V with single pulse (b) Plot of $D^2 - {D_0}^2$ versus ln(E) for vortex beam (m=2) ablation threshold energy calculation of Ti-6Al-4V with single pulse...108
Figure 5. 10 Laser ablated polished Ti-6Al-4V with (a) Gaussian beam, 15mW (b) m=1 vortex beam, 42mW (c) m=3 vortex beam, 70mW. All beams have the same peak intensities (fluence)...................109
Figure 5. 11 1x5(left) and 2x2 (middle) Dammann gratings and a Dammann grating with transition points, a-e (left)...110
Figure 5. 12 Uniformity η of the ablated spot diameters on Ti-6Al-4V with variation of grey level of the binary Dammann grating. (10kHz, 20μJ/pulse, 100pulses). 110
Figure 5. 13 Multiple vector beam generation, by combing binary Dammann gratings with an S-waveplate. The red squares indicate the 0-th order...111
Figure 5. 14 (a)Schematic showing the method of 0-th order removal with a Fresnel zone lens (FZL). (b) The upper is the hologram of a positive FZL and the lower image is the hologram of a negative FZL. 111
Figure 5. 15 (a) Experimental setup for a single CV beam measurement (b) Summarization of polarization selection of an S-waveplate. 112
Figure 5. 16 Normalized experimental measured intensities with a combination of a quarter wave plate and half wave plate. The entanglement entropy of the vector beam was calculated by the measurements in outlined red dash lines. 114
Figure 5. 17 Bell curve for a single CV with four different orientations of the half wave plate (θ_1) and associated hologram angle (θ_2). Curves are fitted with pure $\cos^2\theta$ function. 115
Figure 5. 18 Measured concurrence of a single beam from scalar mode (C=0.14) to vector mode (C=0.95). Fitted with a pure $cos^2\theta$ function...115
Figure 5. 19 Experimental setup. Two spatial light modulators were applied (SLM1 and SLM2). Two 4f systems (highlight with blue rectangle dash box) were applied to re-constructer the image plane of SLM 1 to SLM 2. The re-constructured image (1x5 Damann grating) plane of each 4f system were highlight with green rectangle dash box. The reconstructured images were captured by using a CCD camera (Thorlabs, BC106-VIS). 116
Figure 5. 20 Bell curve for each diffractive spot in a 1x5 spot array with four different orientations of the half wave plate (θ_1) and associated hologram angle (θ_2). (a-d) Bell curves for four diffractive orders with pure $\cos^2\theta$ function fit. (e) Bell curve for the 0th order with pure $\cos^2\theta$ function fit...........................117
Figure 5. 21 Typical graphical depiction of intensity measurement of a vector vortex mode in multiple spot arrays (a) measured intensity of a beam in 1x5 spots array with six OAM states; (b) measured intensity

of a beam in 1x5 spots array with six polarization states;(c) measured intensity of a beam in 2x2 spots array with six OAM states;(d) measured intensity of a beam in 1x5 spots array with six polarization states . Either the measuements with OAM states or polarization states can be chosen as the basis state forward to calculate concurrence and entanglement entropy. 118

Figure 5. 22 A typical graphical depiction of intensity measurement of a scalar vortex mode (with fix fast axis angle of the QWP=45°). Calculated concurrence C=0.14. 119

Figure 5. 23 Polarization states after the QWP used in measurement with Stokes parameter. 119

Figure 5. 24 5x5 CV beam arrays on CCD beam profiler (a) 5x5Radially polarized beam arrays (b). 5x5 Radially polarized beam arrays with a analyse polarizer. The white arrow represents the direction of the fast axis (c) 5x5 Azimuthally polarized beam arrays. (d) 5x5 Azimuthally polarized beam arrays with a analyse polarizer. The white arrow represents the direction of the fast axis. 121

Figure 5. 25 Azimuthally polarized uniform 1x5 vector beam array. (a) Beam profiler image. (b) Beam profiler image with a polarizer analyser. The white arrow represents the direction of the fast axis of the polarizer analyser. (c) Machined uniform 1x5 vector beam arrays on a Ti-6Al-4V sample. The diameter of each spot is approximately 40μm. (d)-(e) The SEM images. (10kHz, 40μJ/Pulse, 45 pulses).......... 121

Figure 5. 26 Radially polarized uniform 1x5 vector beam array. (a) Beam profiler image. (b) Beam profiler image with a polarizer analyser. The white arrow represents the direction of the fast axis of the polarizer analyser. (c) Machined uniform 1x5 vector beam arrays on a Ti-6Al-4V sample. The diameter of each spot is approximately 40μm. (d)-(e) SEM images. (10kHz, 40μJ/Pulse, 45 pulses) with azimuthal LIPSS confirming the radial polarization state. 122

Figure 5. 27 Azimuthally polarized uniform 2x2 vector beam array. (a) Beam profiler image. (b) Beam profiler image with a polarizer analyser. The white arrow represents the direction of the fast axis of the polarizer analyser. (c) Machined uniform 2x2 vector beam arrays on a Ti-6Al-4V sample. The diameter of each spot is approximately 40μm. (d) SEM images. (10kHz, 40μJ/Pulse, 45 pulses) with radial LIPSS confirming azimuthal polarization state. 122

Figure 5. 28 Radially polarized uniform 2x2 vector beam array. (a) Beam profiler image. (b) Beam profiler image with a polarizer analyser. The white arrow represents the direction of the fast axis of the polarizer analyser. (c) Machined uniform 2x2 vector beam arrays on a Ti-6Al-4V sample. The diameter of each spot is approximately 40μm. (d) SEM images. (10kHz, 40μJ/Pulse, 45 pulses). 123

Figure 5. 29 Examples of grey scale histograms that can be extracted from the SEM images for azimuthal polarization (a) Measured area (inside of the red dash line) (c) The grey scale histogram extracted from (a). (d) The grey scale histogram extracted from (b). 124

Figure 5. 30 (a) Line graph of cosine similarity for 1x5 cylindrical vector beams. (b) Line graph of cosine similarity for 2x2 cylindrical vector beams. 124

Figure 5. 31 Optical images of machined "M" pattern on a polished brass plate with increasing laser powers (a) 30W (b) 120W (c) 160W and (d) 250W. Diffraction efficiency drops while applying P≥ 120W [32]. 125

Figure 5. 32 Generated 5x5 beam arrays using Edge wave picosecond laser. (a) 5x5 beam arrays at Fourier and (b) machined 5x5 arrays on stainless steel foil (2kHz, 0.64W). The ghost diffraction can be observed in (a). The diffractive zero order is in centre of the beam array. 126

Figure 5. 33 Machined 5x5 beam arrays on stainless steel foil with (a) 404kHz, 96.4W (b) 404kHz, 130W (c) 1MHz, 160W. Diffraction efficiency remains at higher level as expected. 126

Figure 5. 34 Dynamic control of multiple parallel spots with azimuthal polarization. “UOL” shaped pattern has been demonstrated with multiple 5 spot groups synchronised with galvo movement (10kHz, 40µJ/pulse, 100pulses)....127

Figure 5. 35 Optical micrograph showing the produced T-shape array of laser spots. (a) Machined T-shapes pattern on a Ti-6Al-4V sample at 10kHz, 40µJ/Pulse, 45 pulses. (b) SEM results with different polarizations states for each spot. 127

Figure 5. 36 Continuous scanning results with different polarization states. (a)The SEM result of azimuthal polarization (10kHz, 40µJ/pulse, 10mm/s,). (b) Optical micrograph of line patterns with side illumination (c) SEM result of radial polarization (10kHz, 40µJ/pulse,10mm/s). The red arrows represent the laser scanning direction. The green arrows represent the E field. (d-e) Images at higher magnifications of areas inside the blue and red squares, showing shark skin-like morphologies. 128

Figure 6. 1 Modified experimental setup....133

Figure 6. 2 Operations of a S-waveplate with different fast axis angle and various input polarization states. 135

Figure 6. 3 By keeping the fast axis of the S-waveplate equal to 0° in ZEMAX, the output CV polarization will be related to the input linear polarization orientations: (a) radial polarization achieved with horizontal linear polarization, (b) anti-clockwise spiral polarization achieved with -45° linear polarization, (c) Azimuthal polarization achieved with vertical linear polarization and (d) Clockwise spiral polarization achieved with +45° linear polarization. 135

Figure 6. 4 Optical images of linear LIPSS orientations with dynamic grey level CGHs on polished Ti-6Al-4V. LIPSS orientations are switched with the grey levels of the CGHs. Red arrows indicate the direction of the incident linear polarization angle ($\boldsymbol{\theta}$) (10kHz, 100mm/s, 8µJ). LIPSS orientation is perpendicular to polarization state. 136

Figure 6. 5 SEM images of laser processing with generated corresponded linear polarization. (a) LIPSS orientation angle horizontal (b) LIPSS orientation angle -45° (c) LIPSS orientation angle vertical (d) LIPSS orientation angle 45° (d). 10kHz, 25mm/s, 5.5µJ. LIPSS spatial period ~1µm....137

Figure 6. 6 Top line: Optical images of cylindrical vector polarizations created from desired input linear polarization orientations. (a) Azimuthal polarization (b) Spiral (anti-clockwise) polarization (c) radial polarization (d) Spiral (clockwise). (a'-d') SEM images of cylindrical vector polarization states. LIPSS spatial period ~1µm. The scale bar in a SEM image is 10µm. (10kHz, 5µJ, 50pulses). 138

Figure 6. 7 SEM images of scanned lines using generated CV beams with a range of scanning speeds from 7mm/s to 15mm/s. The used polarization direction from top line to bottom line is azimuthal, spiral (anti-clockwise), radial and spiral (clockwise). (Column a) Schematic of beam overlap process at 7mm/s with four CV beams (Column b) Schematic of beam overlap process at 10mm/s with four CV beams (Column c) Schematic of beam overlap process at 15mm/s with four CV beams. All of the scans used peak fluence=0.6J/cm^2. 139

Figure 6. 8 Schematic and SEM images with overlaid polarization states. Top line: LIPSS of overlaid radial and azimuthal polarizations (a) at the centre of the scanned line (b) at the edge of the scanned line. Middle line: (c) Overlaid azimuthal and clockwise spiral (SP1) polarizations. (d) Overlaid radial and clockwise spiral polarizations. (e) Overlaid azimuthal and counter clockwise spiral (SP2) polarizations. Bottom line: (f) Overlapped radial and counter clockwise spiral polarizations. (g) Overlaid clockwise spiral and counter clockwise spiral polarizations. The Image (c-g) are measured at the scanned line centre. (0.2J/cm^2, 10mm/s). 140

Figure 6. 9 Optical and SEM images of "University of Liverpool" (top) and "UoL" (bottom). Patterns were fabricated by azimuthally polarized CV beams with different hatch distance (100µm for the top pattern and 50µm for the bottom UOL pattern). The top pattern is not as clear due to the large hatch distance. Practising speed v=15mm/s and fluence=0.6J/cm^2. Processing time for "UOL" pattern ≈37s. 141

Figure 6. 10 Optical and SEM images of 18 segments pie chart with various CV beams. Structural coloration exhibited on an 18 segments pie chart, fabricated by 18 linearly-corresponding polarized CV beams with fluence = 0.6J/cm^2 at velocity =15mm/s, hatch distance=27µm. Total processing time s≈93s, includes 200ms delay for each grey level map switching. 142

Figure 6. 11 Treated material surface with SPI nanosecond fibre laser. Spikes on the surface are presented. (a) Top view. (b) Tilt view. The applied Gaussian beam size was approximately 50µm, 15% overlap rate for processing, 5.09J/cm^2. 143

Figure 6. 12 SEM images of combining polarization dependent nanostructures and microstructures. (column A) microstructures with radial polarization; (column B) microstructures with spiral polarizations (clockwise LIPSS orientation); (column C) microstructures with azimuthal polarization; (column D) microstructures with spiral polarizations (counter clockwise). (E) Tilt view of column A. (F) Tilt view of

column B. Red arrows represent the electric field E. The scale bar is 20μm for top line and 10μm for middle line. 144

Figure 6. 13 SEM images of combining polarization dependent nanostructures and microstructures. (column A) microstructures with radial polarization plus azimuthal polarization; (column B) microstructures with azimuthal polarization and counter-clockwise spiral LIPSS orientation; (column C) microstructures with clockwise and counter-clockwise LIPSS orientation; (column D) microstructures with radial, azimuthal clockwise and counter-clockwise polarizations. (E) Tilt view of column A. (F) Tilt view of column B. The scale bar is 20μm for top line and 10μm for middle line. 145

Figure 6. 14 contact angle measurements for (a-c) LIPSS covered microstructures or only microstructures surfaces (no LIPSS), (d-e) only LIPSS covered surfaces. Black dash line indicates 150° (superhydrophobic point). Red dotted line indicates 57° (the CA for an untreated sample). LIPSS produced with various polarization states. RP: radial polarization, SP1: clockwise spiral polarization, AP: azimuthal polarization, SP2: counter-clockwise spiral polarization. The laser parameters was set to 33kHz, 5.09J/cm^2 for microstructures formation and 10kHz, 0.6J/cm^2 for LIPSS formation..147

Figure 6. 15 Contact angles for different laser induced structures on Ti64 at day 31. (a) Untreated Ti64 surface. (b-e) Microstructure plus one-state polarization LIPSS. (f-i) Microstructure plus dual-state polarization LIPSS. (j) Microstructure plus four-state polarization LIPSS...147

Figure 6. 16 Water contact angle changes with different surface roughness after the thermal treatment. 148

Figure 6. 17 The rolling off angle of samples covered with microstructures plus (a-b) one-state CV polarization LIPSS, (c-e) dual-state CV polarization LIPSS...149

Figure 6. 18 Contact angle hysteresis and rolling off angle for one-state and dual-state CV LIPSS covered samples..149

Figure 6. 19 (a) Image of a lotus leaf (b) the SEM image of the lotus leaf showing the hierarchical structures with papillose cells; (c) SEM image a two level structures which was formed by combining a nanosecond pulsed laser and a picosecond pulsed laser. Image (a) and (b) are taken from [257]. 150

List of tables

Table 2. 1 Jones Matrices for some linear optical elements 28
Table 3. 1 Output power (Watts) of Edgewave laser with internal/external trigger................................ 58
Table 3. 2 Structures and optical characters of the SLMs used in this current research 60
Table 3. 3 parameters for the SEM6610 75
Table 5. 1 Measured results using the Spiricon camera.. 105
Table 5. 2 Peak intensity with different topological charge m and corresponded maximum r where ω_0, I_0 is beam waist and peak intensity of a Gaussian mode. 108
Table 5. 3 shows the projective measured intensity and its respective basis state for a vector vortex mode. 113
Table 5. 4 Measured Bell parameter S for each diffraction spots in 1x5 spots array 117
Table 5. 5 Measured Concurrence and Entanglement entropy of a 1x5 spot array 118
Table 5. 6 Measured Concurrence and Entanglement entropy of a 2x2 spot array 118
Table 5. 7 Measured concurrence of a 1x5 scalar vortex beams 119
Table 5. 8 Measured concurrence of a single beam, 1x5 and 2x2 multiple beams with Stokes Projections. 120
Table 6. 1 Jones matrixes of polarization control using an S-waveplate.. 134

List of symbols

Symbol	Unit	Description
A	n/a	Amplitude of electric field
D	$W/(m^2 \cdot K)$	Heat diffusion coefficient
E	N/C	Electric field
H	n/a	Transfer function in frequency spectrum
I	W/cm^2	Laser power intensity
J	n/a	Jones matrix
M	n/a	Magnification factor
P	n/a	Pupil function of a lens
R	n/a	reflectivity
T	n/a	Complex amplitude function
FT	n/a	Fourier transform
GL	n/a	Grey level
f	mm	Focal length
k	m^{-1}	Wave vector
n	n/a	Refractive index
t	n/a	Transmittance function of a CGH
u	mm	Objective distance
v	mm	Imaging distance
D	mm	Beam diameter at focal plane
θ	degree	Phase angle of a laser beam
Δv	Hz	Spectrum bandwidth
η	n/a	Shaping efficiency
τ_p	s	Pulse duration/pulse timescale/pulse regime
N	n/a	Pulse numbers

T_e	K	Electron temperature
T_i	K	Lattice temperature
C	$J/(m^2 \cdot K^2)$	Heat capacity
K_e	$W/(m \cdot K)$	Electron thermal conductivity
Q	W	Absorbed laser power
α	cm^{-1}	Absorption coefficient
Z	nm	Penetration depth
g	n/a	Electron-phonon coupling constant
h	$W/(m \cdot K)$	Thermal diffusivity
Ω	J/m	Heat evaporation
λ	nm	Wavelength
F	Hz	Frequency
∧	nm	Ripple period
v	mm/s	Velocity/speed
M^2	n/a	Laser beam quality
ω	Hz	Angular frequency
c	m/s	Light speed
ϕ	n/a	Phase function
U	n/a	Amplitude of Optical field
ω_0	µm	Gaussian beam waist
m	n/a	Topological charge
P	W	Laser power
R_{out}	µm	Outer ring mode beam diameter
r	µm	Inner ring mode beam diameter
ρ	g/m^3	Density
K_B	J/K	Boltzmann constant

List of abbreviations

AOM	Acousto-Optic Modulator
AP	Azimuthal polarization
CGH	Computer generated hologram
CPA	Chirped pulse Amplification
DVI	Digital Visual Interface
GS	Gerchberg-Saxton
GSW	Weighted Gerchberg-Saxton
LC	Liquid Crystal
LCoS	Liquid-Crystal on Silicon
LIPSS	Laser Induced Periodic Surface Structures
PRF	Pulse Repetition Frequency
FZL	Fresnel Zone lens
ND	Neutral density
OAM	Orbital angular momentum
RP	Radial polarization
SESAM	Semiconductor Saturable Absorber Mirror
SWP	S-waveplate
CV	Cylindrical vector
HAZ	Heat affect zone
MPI	Multi-photon ionization
CW	Continue waved
SLM	Spatial Light Modulator
DOE	Diffractive optical element
PMMA	Polymer poly(methyl)methacrylate
KLM	Kerr lens modelocking

GVD	Group Velocity Dispersion
MOPA	Master Oscillator Power Amplifier
MPA	Multiphoton absorption
SERS	Surface Enhanced Raman Scattering
LSFL	Low spatial frequency LIPSS
HSFL	High spatial frequency LIPSS
CA	Contact angle
HG	Hermite-Gauss
NA	Numerical aperture
DZP	Dammann Zone Plate
LG	Laguerre-Gaussian
CMOS	Complementary metal-oxide semiconductor
CCD	Charge-coupled device
IFTA	Iterative Fourier Transform Algorithm
DG	Dammann Grating
PAL-SLM	Parallel aligned nematic Spatial Light Modulator
HWP	Half wave Plate
QWP	Quarter wave Plate
PBS	Polarization beam splitter
TFP	Thin film polarizer
PA	Polarization analyser
RTC	Real Time Control
SEM	Scanning Electron Microscope

Chapter 1

Introduction

1.1 Background and motivation

This work is concerned with precision manufacturing using ultrashort pulsed lasers. Ultrashort pulsed lasers have the unique property of pulses length less than a few tens of picoseconds, making them widely used in micro-nano precision manufacturing [1-4], and laser based surgery [5]. Figure 1 shows the images of high quality machining by ultrashort pulsed lasers. To satisfy the requirements of high processing efficiency, ultra-short pulsed laser systems with their applications have been widely investigated. In the past few decades, the pulse duration of a laser has been compressed shorter and shorter to achieve extremely high peak powers (~Petawatt) and extremely short pulse timescales (τ_p~femtosecond) for both linear and non-linear laser material interactions [1, 6]. With the benefits of high beam quality and short pulse duration capability, the ultrashort pulse laser has been empolyed for precision micromaching. For example, micro drilling and cutting materials with minimised heat affect zone (HAZ) [3], functional surface production [7-9] and microwelding of similar and dissimilar materials [10]. Due to the high intensity (I>$10^{12} W/cm^2$) of a focused ultrafast laser beam, non-linear light interaction, such as self-focusing[11], filamentation [12-14], and multi-photon ionization (MPI) in atoms [15, 16] and molecules [17] have been investigated. Continue waved (CW) lasers, such as the fibre laser, also have a number of key industrial applications, such as laser cutting [18], selective laser melting [19] and laser forming [20] with precisely controlled power .

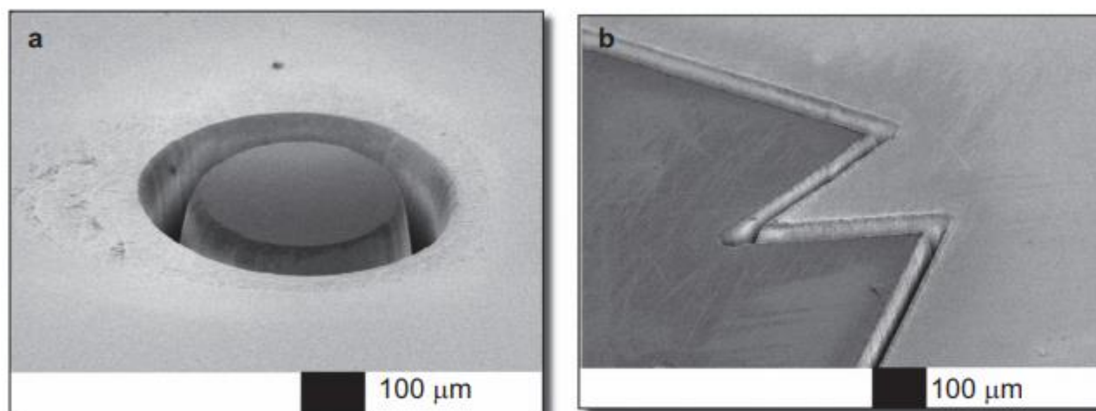

Figure 1.1 SEM images of (a) a micromachined glass surface and (b) a glass material cut by femtosecond laser ablation [3].

In the field of laser industrial applications, laser processing efficiency is of significant interest, including the use of high average power laser system and other process improvements. One of the methods to improve laser processing efficiency and throughput can be laser beam shaping. Typically a laser will have a Gaussian mode distribution which is very useful for laser welding, laser drilling and laser cutting where a high central peak intensity is beneficial. In order to optimize the manufacturing efficiency and product quality of other manufacturing applications, such as material modification by laser-induced periodic surface structures (LIPSS) and thin film processing, other laser beam shapes and distributions are needed. Beam shaping is the process of redistributing the irradiance and phase of a beam of optical radiation [21].

The beam shape is defined by the irradiance distribution. The beam profile properties are affected by laser phase and intensity. In the past few years, laser beam shaping techniques have been employed in many fields including scientific research and industrial applications. Various laser shapes and irradiance distributions have been demonstrated by many researchers with different methods such as refractive beam shaping [22, 23] and diffractive beam shaping [24, 25]. The early theoretical research about beam shaping was investigated by Frieden [26] and Kreuzer [27] during the 1960s. A laser with a uniform irradiance is still of most interest, no matter what kind of shape due to the uniform intensity distribution over an illuminated area. Although numerous geometrical optics have been designed to satisfy many beam shaping requirements for industrial applications, such as the Powell lens to generate a line source for laser material processing [22], their flexibility is not sufficient for some complex requirements, since one optic is normally designed for one application. In this thesis, the focus is in the use of more flexible optical device, a Spatial Light Modulator (SLM), for complex ultrafast laser beam shaping to improve processing efficiency.

Not only the processing efficiency and throughput can be improved by different laser shapes and irradiance distributions but also the improvements can also be made by increasing the repetition rate of an ultrashort pulse laser. However, a typical laser system is always optimized for a specific repetition rate which is not easily re-configured for other higher frequencies. Thus, generating multiple beams can be the other method to increase the efficiency and throughput of ultrashort pulse laser processing. In this case the input laser energy is spatially split into many lower energy laser pulses required for high quality non-thermal micro-machining. Many previous studies have demonstrated many approaches to create multiple beams to improve ultrashort pulse laser micro-fabrication [28-30]. In order to generate arbitrary multiple beam patterns, the used methods range from diffractive optical elements (DOEs) to the spatial light modulator (SLM) to attempt parallel processing flexibly.

With the development of Liquid Crystal on Silicon (LCoS) SLMs that can operate at higher average power, a potential way to improve laser processing efficiency further is possible. More recently, researchers have tested the thermal effect on LCOS SLMs while applying high average power for high speed laser processing [31, 32]. In this thesis, beam shaping results for high average power, high speed laser processing are presented.

Polarization of a laser beam can affect absorption and material processing efficiency. The ability to control and manipulate the polarization state of an incident laser beam is desirable and beneficial for laser processing improvement. For example, surface nano-structuring of metals, semi-conductors and dielectrics using structured optical field [33-35], high aspect ratio micro-drilling of metal sheet using cylindrical vector beams [36, 37], and polarization dependent surface ablation of polymer

poly(methyl)methacrylate (PMMA) [14]. Static methods for modulation include for example the generation of spatially structured polarization fields such as radial or azimuthal with a birefringent plate [38, 39] or a Spatial Light Modulator (SLM) [40-44]. Dynamic methods include continuously rotating wave plates [45, 46] or using low bandwidth orthogonal linear polarization state switching liquid crystal polarization rotator [44, 47]. Novel simultaneous modulation of combining beam shaping and polarization state to generate single or multiple cylindrical vector shaped beams is reported in this thesis.

All three techniques, laser beam shaping, laser parallel processing and dynamic laser polarization control, enhance laser processing efficiency and throughput. Hence, by combining laser beam shaping and complex polarization control with single/multiple beam spots leads to a new approach for higher laser processing efficiency or may even open up a new research area for ultrashort pulsed laser material interactions.

1.2 Aim and Objectives

The aim of this research is to investigate the use of diffractive techniques to optimise laser beam intensity distribution and polarization states for laser based manufacturing processes including laser micromachining under high average power and laser surface modification. The objectives of this work are:

- To develop and demonstrate a dynamic diffractive polarized beam shaping method with spatial light modulators and geometrical optics for laser material processing.
- Develop and test grey level computer generated holograms (CGHs) for laser parallel processing with desired shaped laser beams for laser material processing
- Develop and test binary computer generated holograms (CGHs) for laser parallel processing under high average power and low average power.
- Develop and test combined laser parallel processing and cylindrical vector polarization for laser material processing.
- To develop and demonstrate a dynamic complex polarization control method using a spatial light modulator for laser surface modification.

1.3 Overview of the thesis

This thesis consists of 7 chapters and 4 appendixes.

Chapter 1 provides an introduction of this thesis. The background and motivation, aim and objectives and overview of this thesis are included in this chapter.

Chapter 2 provides an overview of relevant background information ranging from a brief introduction of ultrafast laser micro-processing, polarization and wavefront control of laser beams. Also included is a

literature review on laser beam shaping and multiple ultrafast laser beam generation for surface processing and their applications.

Chapter 3 provides a description of the experimental equipment, setup and methodology used to implement and analyze the experiments described in this thesis.

Chapter 4 provides the difference of beam shaping at focal plane and imaging plane. This chapter includes a diffractive original ultrafast laser beam shaping technique combined with polarization control for material processing using a spatial light modulator and a diffractive optical element (S-waveplate). Two different masks, binary and grey level masks will be applied on a SLM to shape the input laser beam in both outline profile and intensity distribution. In addition, laser parallel processing with an imaging based beam shaping method with two SLMs is provided. The second SLM will be applied with a grey level (phase changes from 0 to 2π) computer generated holograms (CGHs) to split the beam to desired laser spot arrays. Complex and time-consuming diffraction far-field phase hologram based on Fourier transformation are avoided, while simple and direct geometric masks are used to shape the incident beam at diffraction near-field.

Chapter 5 provides a method of uniform cylindrical vector (CV) laser parallel processing with binary (phase changes from 0 and π) computer generated holograms (CGHs). A novel method of comparing the ablation threshold of a ring mode beam and a Gaussian beam is introduced. The vector quality factor of multiple CV beam arrays has been measured for the first time. This chapter also includes some results of high average power test of a cooled SLM. The generated binary CGHs can be applied for extending the power range of a liquid cooled SLM up to P=160W.

Chapter 6 provides a method of dynamic altering cylindrical vector (CV) polarized ultrafast laser for material surface modification. A novel method to change cylindrical vector polarization dynamically has been used for material surface modification by combining the SLM and an S-waveplate. The cylindrical vector polarization can be altered from radial to azimuthal from corresponded various linear polarization.

Chapter 7 Provides conclusions from the results achieved in this research project and maps out potential future industrial applications and provides suggestions for future work.

Chapter 2

Literature Review

2.1 Introduction

In this chapter, the background literature of current research will be reviewed. First of all, ultrafast laser systems and ultrafast laser material interaction mechanism will be reviewed. Then, an introduction to Laser Induced Periodic Surface Structures (LIPSS), followed by the introduction to phase and polarization, methods of polarization control using diffractive elements. After that, a section on beam shaping techniques will be introduced in this chapter. Finally, multiple beam processing with Spatial Light Modulator (SLM) will be demonstrated.

2.2 Laser systems and ultrafast laser material interaction

2.2.1 Introduction of laser systems

Since the stimulated emission phenomenon was predicted by Einstein in 1916, laser technology has developed very quickly. The stimulated emission phenomenon is a process of light amplification. However, under the condition of thermal equilibrium, the light amplification is not dominant. The number of atoms at each level following Boltzmann distribution [48]. The number of atoms at E3 (Upper level) will transit to E2 (lower level) and the number of atoms at E2 also will transit to E1 (ground state) due to the spontaneous radiation. Thus, the number of atoms at each energy level follows $N3<N2<N1$, as shown in Figure 2.1 a). This is very difficult to generate a laser as the energy level at thermal equilibrium. Thus, in order to generate a laser, the thermal equilibrium should be changed. If the atoms at E1 can be pumped to E3, more atoms at E3 will be transited to E2 and more atoms at E2 will be transited to E1, as shown in Figure 2.1 b). At the process of transition, a lot of light or heat will be emitted. This process is called the population inversion. With the repetition of the population inversion, the energy of E1, E2, E3 cannot be at thermal equilibrium, the huge difference of atoms between each energy will be presented. Thus, amount of light and heat will be emitted to generate a laser. For a laser generation, at least a three-level laser energy system is required, but a four-level laser energy system is used with higher pumping transition efficiency [49]. A typical laser includes three basic components: active medium (to get simulated emission), pumping source (to inverse atoms numbers) and optical resonator (to repeat the process of particle inversion).

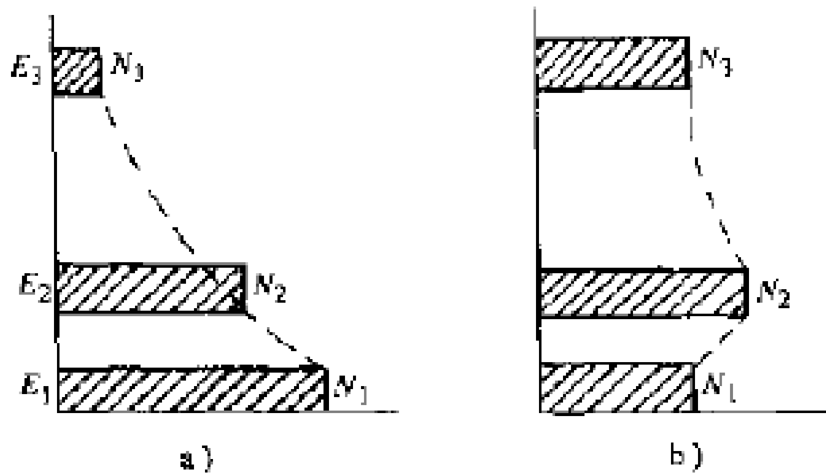

Figure 2. 1 The diagram scheme of a three-level laser energy [48]

With the repetition of the inversion of particle number to the highest energy level E3, a series of energy peak will be produced. Each energy peak is called laser pulse and the time step between each step called pulse duration. Ultrafast laser refers to a laser that generates light pulses with temporal duration shorter than a few tens of picoseconds (1 ps $=10^{-12}$s) [3]. This is very useful for laser precision processing as lower thermal effects will be presented.

In order to achieve shorter and higher intensive pulses for laser micro-processing, special technologies such as Q-switching [50], modelocking and chirped pulse amplification (CPA) [51] are beneficial.

2.2.2 Short and ultrashort pulsed laser generation techniques

2.2.2.1 Q-switching

Q-switching is a technique for obtaining energetic short pulses from a laser by modulating the intracavity losses and thus the Q factor of the laser resonator. At the beginning of pumping, the Q factor should be modulated to a low level, so the laser cannot be generated even the atoms have pumped to the upper level. The number of particles at lower energy level will keep accumulating. Then, the Q factor should be changed to a higher level, so the huge amounts of particles will be transit to the lowest energy level with emitted energy for a laser formation, as presented in Figure 2.2. There are many methods to modulate the Q factor including electro-optic Q-switching [52], acousto-optic Q-switching [53]. This technique is mainly used to generate a laser with high laser peak power (typically > MW) and short pulse duration (ns<pulse duration<ms), which is insufficient for laser precised processing and many other applications. Thus, a laser with higher peak power and shorter pulse duration (τp<ns) is required.

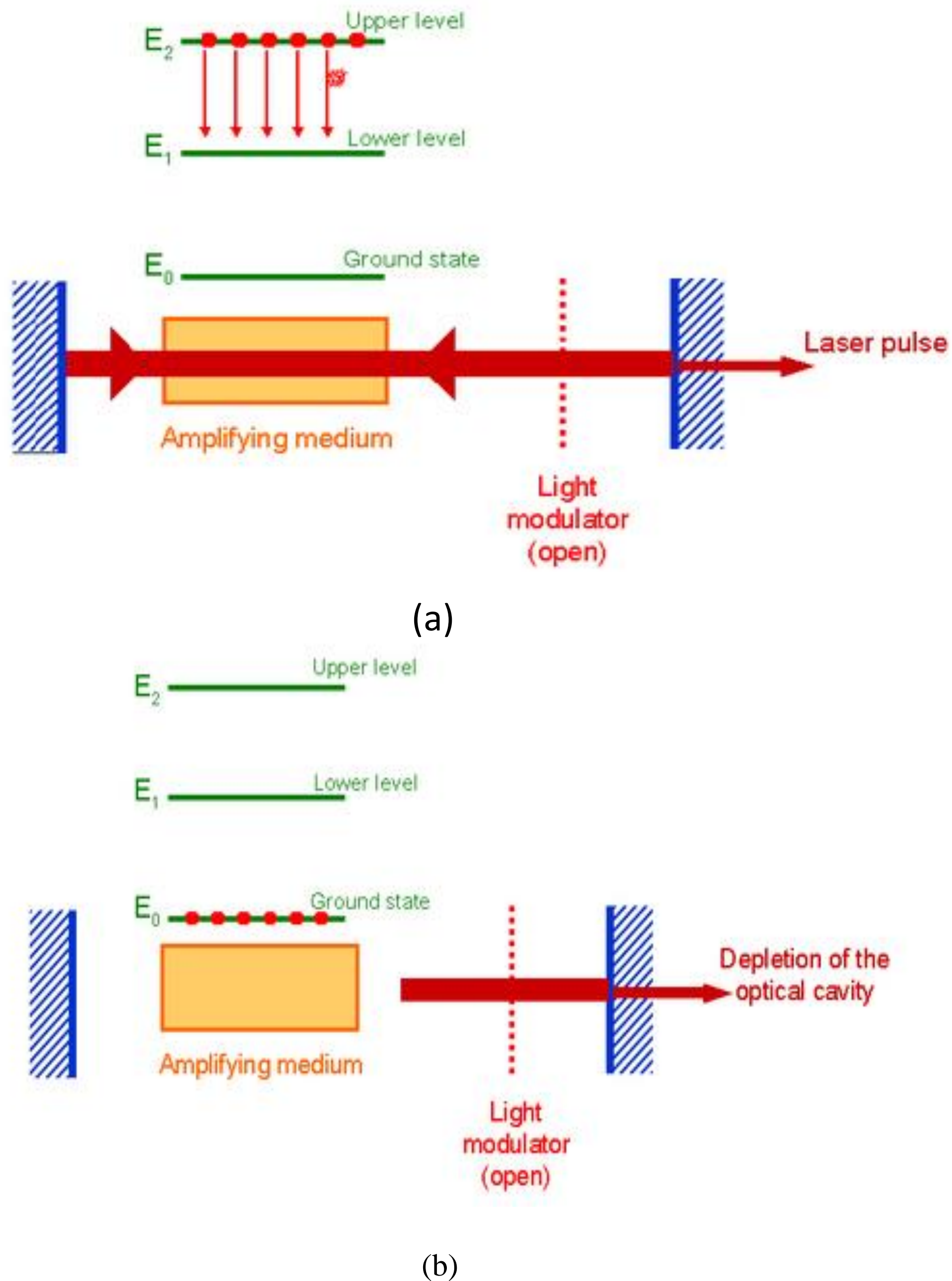

(b)

Figure 2. 2 (a) laser effect once the optical cavity is suddenly opened (b) Depletion of the optical cavity once all the atoms have returned to the ground state [54].

2.2.2.2 Mode locking

Mode locking is a widely used technique in optics to obtain ultrashort laser pulses on the order of picoseconds (10^{-12}s) or femtoseconds (10^{-15}s). For laser beams in the laser's resonant cavity, a wide spectrum bandwidth of each beam will causing the longitudinal models oscillate randomly. Modelocking is a technique used for generating ultrashort laser pulses by inducing a fix phase relationship between the longitudinal modes. The aim of modelocking is going to establish coherent interference that making the longitudinal modes output with desired orderliness in the same laser mode. The relationship between the

spectrum bandwidth $\Delta\nu$ and the generated output pulse of duration τ_p can be expressed as: $\Delta\nu \cdot \tau_p = constant$ [55, 56]. By modelocking broadband laser modes in the laser cavity, ultrashort pulses can be created by constructive and destructive interference, as shown in Figure 2.3.

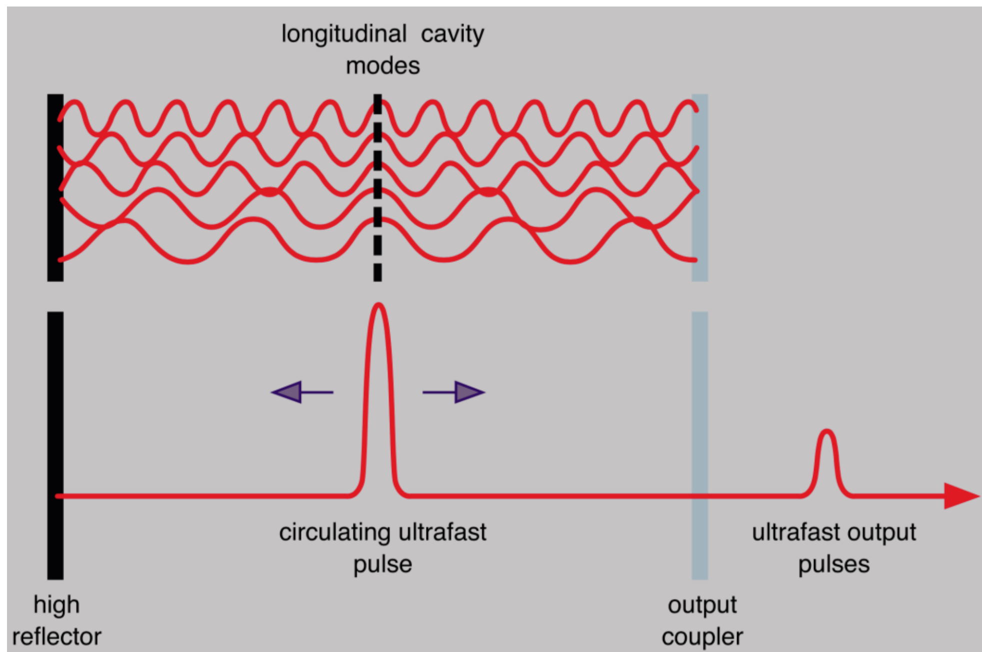

Figure 2. 3 Mechanism of laser pulse modelocking [57].

Modelocking methods are classified as active and passive modelocking [58]. Active modelocking uses an intracavity dynamic optical modulator, such as an acousto-optic modulator or an electro-optic modulator, which are periodic modulated of the resonator losses or of the round-trip phase change. Active modelocking is usually for picosecond pulse duration generation

Passive modelocking allows the generation of much shorter (femtosecond) pulses by using nonlinear materials, such as a saturable absorber or artificial saturable absorber (Kerr lens) inside the cavity. The saturable resonator is mainly used for modulation of the losses of the cavity itself, so an external signal is not needed anymore. A saturable absorber used in passive modelocking is a nonlinear material that selectively transmits high intensity light while absorbing low intensity light. Saturable absorbers can be organic dyes, solid state, and semi-conductors [59-61]. For the picosecond pulses generation, the most commonly used satuable absorber is a semiconductor saturable absorber mirror (SESAM) which has advantages of lower reflectivity of low intensity and higher reflectivity for ultrashort high intensity pulses [60]. Thanks to these unique properties of SESAM, most diode-pumped picosecond lasers adopt this method. In order to generate a shorter pulse duration, like femtosecond, the used passive modelocking method is Kerr lens modelocking (KLM) [62, 63]. For example, pulse duration less than 6 femtosecond has been generated with a large bandwidth gain medium when compensating Group Velocity Dispersion (GVD) [63]. The most popular way of laser output power scaling is the Master Oscillator Power Amplifier

(MOPA) system. The MOPA system is consisting of a seed laser and an optical amplifier to boost the output power with required wavelength range, beam quality and even pulse duration. However, due to the nonlinear effects occurred when boosting the laser to extra high output power, another laser amplifier technique is widely used, which is called Chirped pulse amplification (CPA).

2.2.2.3 Chirped pulse amplification (CPA)

As there is a limit to the amplification by the active medium, the laser peak power also has limitations that making the laser peak power at the level of MW (10^6W). Even with modelocking techniques, ultrashort pulses are generated with high repetition rate (typically >30 MHz) and low pulse energy typically in the nanojoule (nJ) level. However, this is insufficient for laser precised micromachining and many other applications, which requires much lower thermal effects.

Donna Strickland et al [64] dispersed the initial short pulse into a thousand by using a pair of gratings before amplification, then used another pair of gratings to reverse the dispersion of the first pair and recompresses the pulse after amplification to get higher laser peak power and ultrashort pulsed laser (fs) This technique is called Chirped pulse amplification (CPA), which is used to amplify an ultrafast laser pulse to high intensities while avoiding excessive nonlinear pulse durations or optical damage [65]. In order to avoid the damage to amplifying medium and optical surfaces that caused by the nonlinear effects of the ultrahigh peak intensities, CPA is ideal for amplification. A diagrammatic scheme of CPA has presented in Figure.2.4

As shown in Figure 2.4, in CPA, the broad-bandwidth pulses from the oscillator are temporally stretched in a dispersive delay line, e.g. using a pair of gratings, which is introduced as a positive GVD. An ultrashort pulse carries broad frequency spectural bandwith, Δv, the pulse will be stretched while travelling between the optical grating. Different frequency components in the pulse are dispersed into different directions each time reflected on the gratings, for example the red end of the spectrum travels a shorter path than the blue end as they have different frequency (or wavelength). This is shown in Figure.2.5.

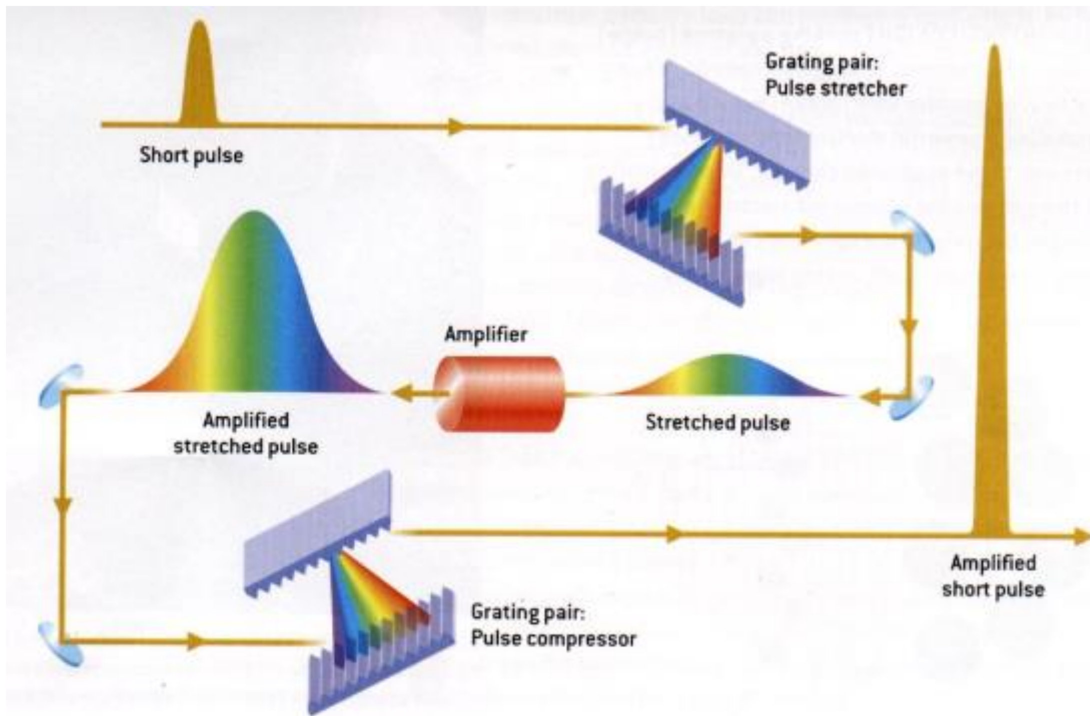

Figure 2. 4 Diagrammatic scheme of chirped pulse [66].

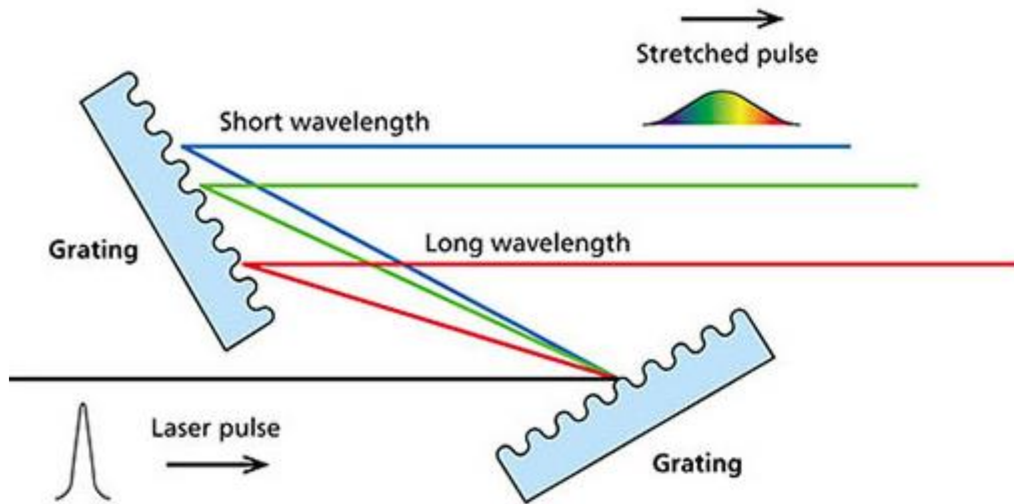

Figure 2. 5 Diagrammatic scheme of different pulse frequency will be dispersed into different directions and with different travelling path[67].

Thus, the ability of stretching will be determined by the distance $L_s = 4f - L_g^s$, where L_g^s is the separation of the gratings (seen in Figure.2.6 (a)). Before compressed the pulses, the dispersed pulses are selected and injected into a regenerative amplifier with gain G~10^6 to bring pulse energy back to the mJ level. As demonstrated in Figure.2.6 (b), for the laser compressing, by using a grating pair with opposite, negative GVD, the stretched pulse is compressed to the original pulse duration. The ability of compression is also determined by the separation of the grating, $L_c = L_g^s$. In order to obtain the shortest compressed pulse while the ideal grating separations for stretching and compressing should be $4f - L_g^s = L_g^c$, namely $L_s =$

L_c. Therefore, the pulse duration can be achieved by varying the grating separation of the stretching to the compressing.

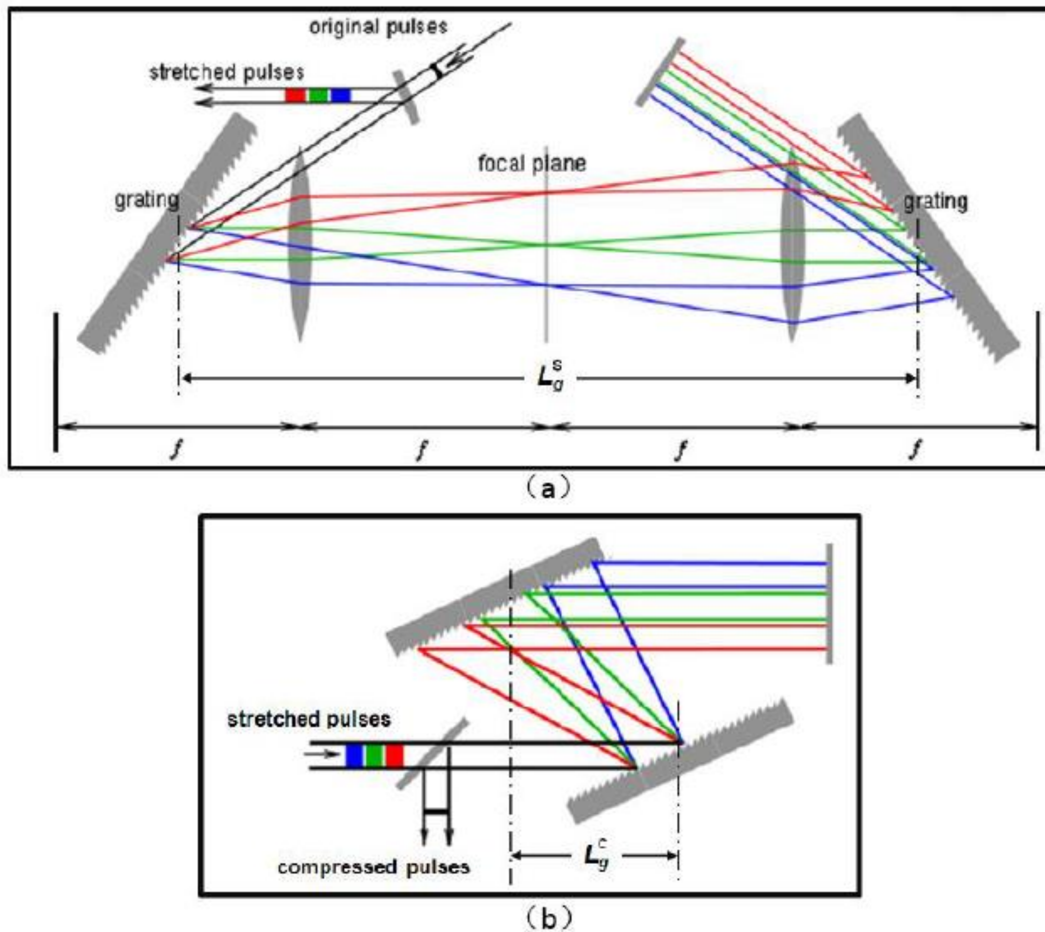

Figure 2. 6 (a) The factors that affect stretching ability of CPA (b) factors that affect compressing ability of CPA [67].

With the development of the laser over the past few decades, some pulsed lasers with extra high average power to 200W have been produced [68]. The power of a laser is limited by overheating issues during laser pumping, thus, an advanced laser with a disk based active medium has been produced [69]. The disk is attached to a heat sink for heat dissipation, the disk thickness is smaller than the laser beam diameter. The disk laser allows very high average and peak power due to large area of the disk can be leaded to moderate power densities on an active medium. Based on the CPA technique, femtosecond laser with pulse energy of 1.8nJ, 1Ghz pulse repetition rate is possible [70].

2.2.3 Ultrafast laser material interaction

This section gives a brief review of laser material interaction mechanisms of ultrashort pulse regime (τ_p at ps/fs level). As a comparison, mechanisms of material processing with long pulse duration (τ_p at ns level) will also be introduced here.

Depending on the reflectivity of the surface material, a portion of light penetrates a very thin layer of the substrate. When material under laser irradiation, the laser energy will be absorbed by the material to heat the material electrons to high temperature. Due to the electron-phonon coupling, the electron will transfer to the ion lattice with in a picosecond time. This is causing laser irradiated material transformed to a liquid or a vapour. However, in the real laser processing, especially laser drilling, the melted liquid is expelled from the interaction due to the recoil action. For most materials. Pulses that is longer than picosecond induce more energy transfer to the ion lattice, resulting in heating, melting and vaporization of the material. In addition, heat conduction, radiation, and plasma expansion are also associated with the laser-material interaction.

2.2.3.1 Absorption and Optical penetration

The target material will absorb laser energy while laser irradiating. Three stages, light absorption, electron heat diffusion and electron-lattice, can be used to describe the procedure of absorbed energy to the target material [71, 72]. This is also can be described in the frame of the one-dimensional two temperature model [73]:

$$C_e(T_e)\frac{\partial T_e}{\partial t} = \frac{\partial}{\partial x}\left(K_e\frac{\partial T_e}{\partial x}\right) - g(T_e - T_l) + Q \tag{2-1}$$

$$C_l(T_l)\frac{\partial T_l}{\partial t} = g(T_e - T_l) \tag{2-2}$$

Where T_e and T_l are the temperatures of electron and lattice respectively, C_e and C_l are the corresponding temperature dependent specific heat capacities, K_e is the electron thermal conductivity, g is the electron-phonon coupling constant describing the energy exchange rate between electron and phonon subsystems, Q is the absorbed laser power.

In laser material processing, no matter the thickness of the material, the absorbed energy will be diffused around the irradiated area. The intensity of transmitted light into a material decreases exponentially with distance when the light absorption is linear, described using Beer-Lamberts' law [74]:

$$I(z) = I_0 \exp(-\alpha z) \tag{2-3}$$

where I_0 ($W \cdot cm^{-2}$) and I_z ($W \cdot cm^{-2}$) are the incident intensity on the material surface and transmitted intensity reaching depth z from the surface respectively. α (cm^{-1}) is the absorption coefficient of the target material which determines how far a particular wavelength can penetrate the material before it is absorbed. The optical penetration depth or optical skin depth is a useful term that describes how much energy is absorbed by the material within a depth of:

$$l_s = 1/\alpha \tag{2-4}$$

Therefore, considering with the penetration depth Z and material reflectivity R, the Gaussian mode related laser absorbed power Q can be described as [75]:

$$Q = (1 - R)\frac{F}{\tau_p}\alpha \cdot \exp\left(-2\frac{r^2}{r_0^2}\right) \cdot \exp\left(4ln2\left(\frac{(t-\tau_p)^2}{(\tau_p)^2}\right)\right) \cdot \exp(-\alpha z) \quad (2\text{-}5)$$

where R is reflectivity of material, F is laser fluence, τ_p is laser pulse duration, α is absorption coefficient of material, r_0 is Gaussian laser beam waist, z is penetration direction.

The non-equilibrium temperature difference between the electrons and lattice will cause the energy absorption, and then, the absorbed energy will be applied to process material. The time for electron-phonon coupling is from 1 to 100 picoseconds for most metallic materials. Therefore, for long laser pulses (τ_p>1ps, like nanosecond level), thermalization between the electron subsystem and the lattice will happen.

2.2.3.2 Heat diffusion

Based on the equations of the two-temperature model (TTM), laser energy will be absorbed by the material electrons and then the absorbed energy will be transferred to lattice by electron-phonon interaction. The depth of heat penetration in the material during the pulse is defined as the heat diffusion depth, which is given by:

$$l_h = 2\sqrt{h\tau_p} \quad (2\text{-}6)$$

where h is the thermal diffusivity ($cm^2 \cdot s^{-1}$) and τ_p is the pulse duration. From equation 2-6, the electron-phono transfer time is laser pulse duration dependent. If the electron-phonon transfer time larger than the pulse duration, the heat diffusion will be lower comparing with the electron-phonon transfer time longer than the pulse duration. It is obvious that shorter pulse duration τ_p limits heat diffusion to a small volume in the material, increasing absorbed energy density. With a particular target material, the heat diffusion depth is determined by the laser pulse duration. If $l_s > l_h$, which is means the ultrashort laser has used for processing, and then the optical penetration depth will play a key role of heating the material with volumes and vice versa with a long pulse [76]. The heat material with volumes will affect the ablation threshold.

2.2.3.3 Long pulse and ultrashort pulse

A multiphoton absorption (MPA) initiated process is generally considered to the interaction of ultrafast pulses and materials [77]. A laser with long pulse duration will increase the threshold fluence and decrease the effective energy penetration depth as the electron-phonon time is longer than the pulse duration [78]. The target material surface will be melted and vaporized when a long pulse illuminating due to a mount of energy absorbed with long processing time. The electron and lattice temperatures are equal (T_e=T_i=T)

[79]. In the case of nanosecond laser-material interaction, as the laser pulse duration is long in comparison with the electron-phonon energy-transfer time ($\tau_p \gg \tau_{transfer}$), the electrons and lattice temperature will remain at the same thermal equilibrium point [80]. Thus, under the material processing with a nanosecond laser, the target surface will be heated to melting point rapidly and then to vaporisation temperature. As the input energy will be absorbed and lost as the heat conduction into the target material, the heat penetration depth should be quite larger than the optical penetration depth [73]. As the long laser pulse duration leads sufficient time for thermal waves propagating, and the absorbed energy will be stored in a layer with a thickness of target material, more energy are needed to vaporise than to melt. The evaporation will occur while the energy is higher than the material heat of evaporation Ω. Evaporation occurrence makes challenge to precise laser processing with nanosecond laser pulses [81]. Due to the heat conduction and absorbed energy stored in the material, even a low intensity nanosecond laser can ablate the target material in both the vapour and liquid phase [79]. Figure 2.7 demonstrated the mechanism of laser-material interaction under long laser pulse duration.

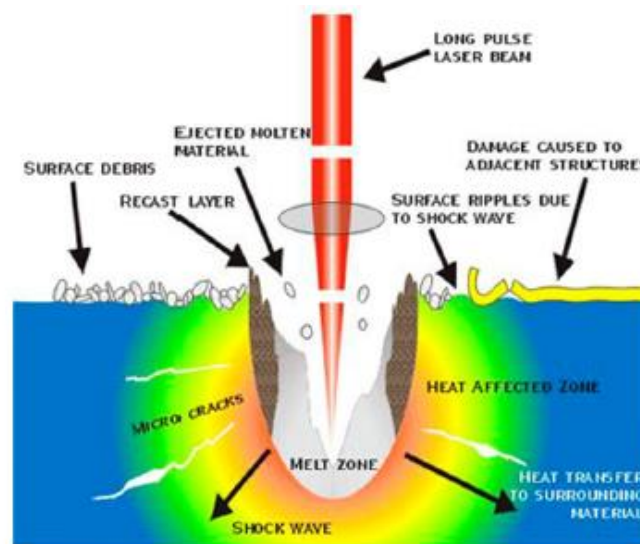

Figure 2. 7 The mechanism of laser-material interaction under long laser pulse [82].

In the case of laser processing under a picosecond or a femotosecond regime, the heat conduction of the target material can be neglected due to the pulse duration is shorter than the electron-phonon energy transfer time ($\tau_p \ll \tau_{transfer}$). For the picosecond pulse duration is longer than the electron cooling time $\tau_{ps} \gg \tau_e$, the lattice temperature remains lower than the electron temperature in which the lattice temperature can be neglected. In the case of laser processing with femosecond laser pulse, the pulse duration is shorter than the electron cooling time $\tau_{fs} \ll \tau_e$, so the electron-lattice coupling can be neglected. Figure.2.8 demonstrated the mechanism of laser-material interaction under ultrashort laser pulse duration.

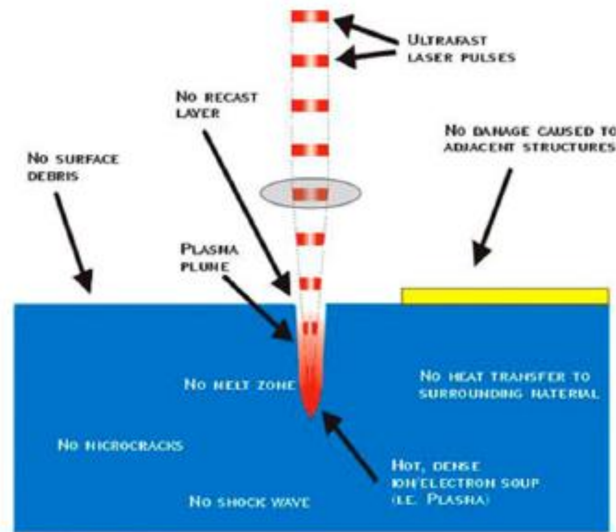

Figure 2. 8 The mechanism of laser-material interaction under ultrashort laser pulse duration [83].

Laser processing by using an ultrashort pulse has less ejected material and heat affect area, therefore, the precision laser processing with a ultrashort pulsed laser is possible. Thanks to the advanced properties of ultrashort laser ablation, highly and pure laser material processing are achievable, as has been experimentally demonstrated by many researchers for various applications [84-86]. Figure 2.9 compared the results of laser processing with nanosecond pulsed laser and femtosecond pulsed laser.

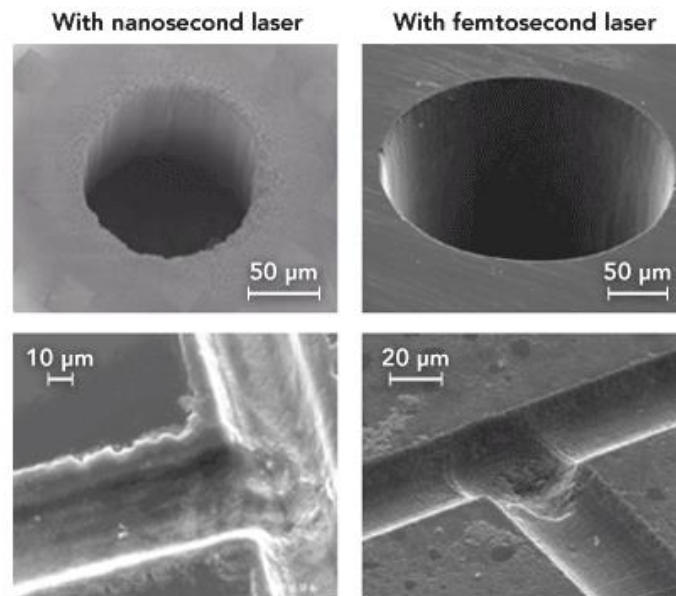

Figure 2. 9 Laser precision machining on glass with nanosecond laser (left) and femtosecond laser (right) [85].

The laser ablation threshold will be a key factor for precise laser material processing. The laser ablation threshold measurement with different laser parameters (i.e. beam shapes, intensities) will play a significant role in laser-material interactions. However, an issue with ring mode beams is being able to define the beam size and peak intensity in the same terms as a Gaussian beam. Recently, Oosterbeek et al [87] have demonstrated a method of ablation threshold measurement with vortex and bessel beams. Ashkenasi et al

demonstrated the equivalence of ablation thresholds independent of Gaussian beam diameter [88]. In the Chapter 5, a novel method of the ablation threshold measurement with a ring mode picosecond pulsed beam will be demonstrated.

2.3 Laser Induced Periodic Surface Structure (LIPSS)

Laser induced periodic surface structure (LIPSS), which is usually regarded as surface periodic lines (or ripples) that can be used to indicate the polarization state of laser radiation. It is essential a micro/nano surface structure that was first observed on silicon in 1965 [89] by Birnbaum. A number of LIPSS structures have been produced on metals [90, 91], dielectrics [92] and semiconductor surfaces [93] for various applications. For example, surface wettability modification on LIPSS covered metal [94, 95], selected colour marking on metallic surfaces [91, 96], anti-microbial [97] and some analytical applications based on Surface Enhanced Raman Scattering (SERS)[98, 99]. Two commonly observed LIPSS types, Low Spatial Frequency LIPSS (LSFL, LSFL periods $\wedge_{LSFL} \leq \lambda_{laser}$) and High Spatial Frequency LIPSS (HSFL, HSFL periods $\wedge_{HSFL} \ll \lambda_{laser}$) , can be created only when the laser fluence approaches the ablation threshold of the material [8] with CW laser or pulsed laser [94, 97, 100]. However, the mechanism of HSFL formation is the still under debate. Details of LIPSS formation are discussed in next section. Most of the reported LIPSS have been produced on the material surface directly by polarized lasers with desired laser fluence. Some literature also reported that the LIPSS structures can be transferred to polymers from LIPSS covered metals [101]. Commonly, LIPSS are formed with linearly polarized beams and cylindrical vector (CV) polarized beams and have demonstrated different morphologies. LIPSSs are typically ripple formed, some researchers however have shown LIPSSs with a specific pattern , such as triangular [102] or a shark skin pattern [103] by overlaying polarized beams, as presented in Figure 2.10.

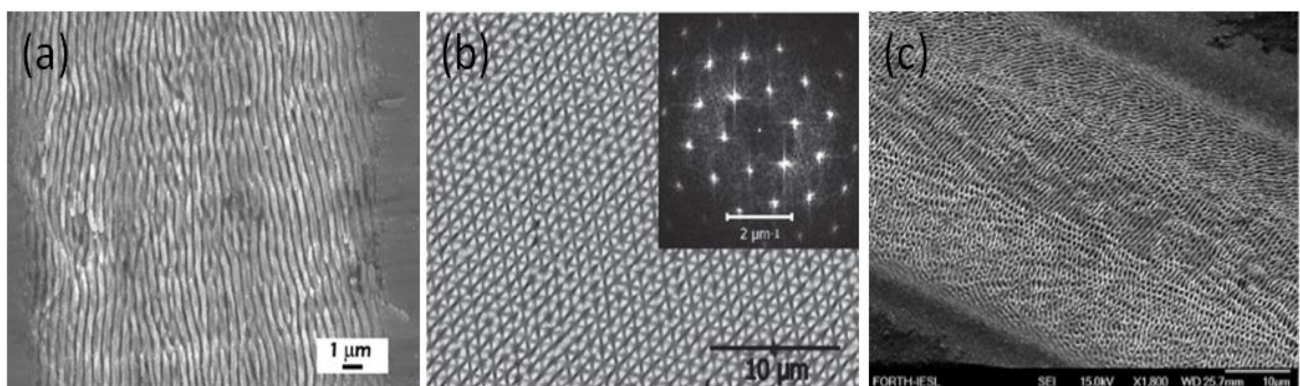

Figure 2. 10 LIPSS was fabricated with different polarization states.(a) Linear polarization (b) circular polarization and corresponding Fast Fourier Transform (FFT) (c) CV polarization [95],[102], [103].

2.3.1 Classification of LIPSS and formation theory

2.3.1.1 Low spatial frequency LIPSS (LSFL)

The periods of LSFL are close to the irradiation wavelength ($\wedge_{LSFL} \leq \lambda$) and also commonly oriented perpendicular to the laser beam polarization, as shown in Figure 2.11 (a).

The first explanation of LSFL has been proposed by D.C. Emmony et al in 1973 that LSFLs were a consequence of the interference between the incident laser beam and surface-scattered waves which were created by laser imping on dust or scratches on the sample surface [104]. An equation was given in the paper to predict the period of the LIPSS with laser beam incident at θ:

$$\Lambda = \frac{\lambda}{1 \pm \sin\theta} \tag{2-7}$$

Where Λ is the ripples period, λ is the irradiation wavelength, θ is the light incident angle. The symbol "±" corresponds to the cases where the scattered radiation has a component of velocity towards or away from the incident laser beam.

Besides, the periodicity of LSFL according to the classical theory can be demonstrated below by considering polarization states [104]:

for refraction of p-polarized beam, $\wedge_p = \frac{\lambda}{1 \pm \sin\theta}$ (2-8)

for refraction of s-polarized beam, $\wedge_s = \frac{\lambda}{\cos\theta}$ (2-9)

For the transparent material, the width of the ripples will not only be increased with the laser incident angle θ but also will be affected by the modified refractive index n due to the light will be refracted inside of the material, thus the equation which shows above will be corrected to a new equation [105]:

$$\Lambda = \frac{\lambda}{n - \sin\theta} \tag{2-10}$$

Where Λ is the period of the ripples, λ is the irradiation wavelength, n is the refractive index of the modified material and θ is the light incident angle.

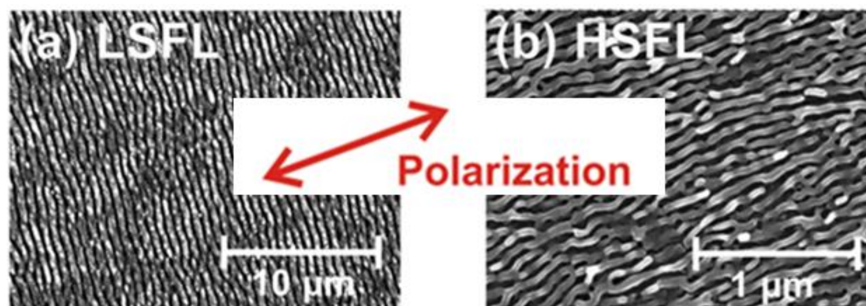

Figure 2. 11 Scanning electron micrograph of two different types of LIPSS formed on titanium alloy (Ti6Al4V) surfaces after irradiation with fs-laser pulses (30fs,800nm,1kHz). (a) LSFL [∅_0=0.11J/,N~56]; (b) HSFL [∅_0=0.08J/,N~560] [106].

2.3.1.2 High spatial frequency LIPSS (HSFL)

Different from the LSFL, the HSFL are only observed with an ultrafast laser, such as picosecond and femtosecond pulsed lasers. The fundamental mechanism of HSFL formation is not yet fully understood and apart for debate. Several theories have been proposed to explain HSFL, including self-organization [107], second-harmonic generation [93], excitation of surface plasmon polaritons [108], and coulomb explosion [109].

2.3.2 LIPSS modification

The formation of LIPSS is very sensitive to the laser parameters, such as input fluence and laser exposure time. Both LSFL and HSFL can be produced by careful choosing the laser fluence and exposure [102, 103]. It has been shown that the laser fluence for LIPSS formation should be close to the material ablation threshold. With CW and long pulse laser, only LSFL can be produced, whereas ultrafast laser can generate both LSFL and HSFL. Thus, LSFL and HSFL can co-exist on material produced with ultrashort pulse Gaussian laser irradiation. LSFL can be observed in the centre of the spot, where the fluence is higher than the wings of the Gaussian beam, whereas HSFL can be formed around the edge of the spot where laser fluence is relative low [110]. Expected the Gaussian beam, LSFL and HSFL also can be produced with uniform distribution, such as a flattop beam [111], by careful choosing the input laser fluence and exposure. Based on the equation 2-7, the period of the LIPSS are affected by the wavelength (λ), incident angle (θ). The LIPSS period can be tailored by changing those parameters. According to the different direction of linear polarization of the incident beam, orientations of LSFL are always observed perpendicular to the incident linear polarization direction on strong absorbing material surface [110]. However, orientations of HSFL can be either parallel or perpendicular to the incident linear polarization [106]. Thus, LSFL directions are commonly used to recognise incident laser polarization direction. A laser system always optimized for typical wavelength, so period of LIPSS is closer to the incident laser wavelength with normal incident angle. Whereas, when producing laser LIPSS covered surface, the laser scan direction is an important factor affects the LIPSS quality. The highly uniformed LIPSS can be generated when the laser scan direction is parallel to the LIPSS direction [110]. While the worse LIPSS uniformity will be presented if the scan direction is perpendicular to the LIPSS direction, as shown in Figure 2.12.

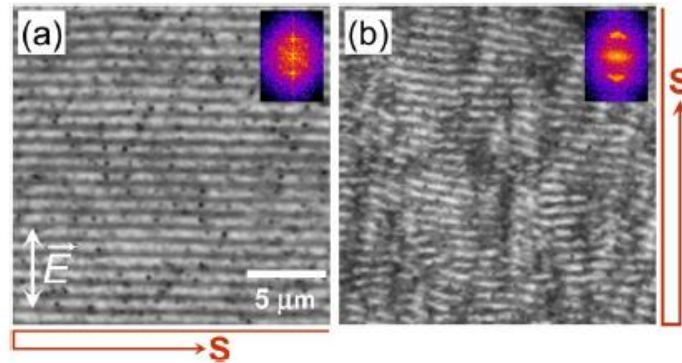

Figure 2. 12 Uniformity of LIPSS generation based on different scanning direction [110].

Various parameters will affect LIPSS uniformity, not only the relative angle between the LIPSS orientation and the beam scanning direction [112] but also beam intensity distribution. For LIPSS formation with a Gaussian distribution which has a higher intensity at the middle of the beam than the other areas of the beam. This will cause the LIPSS to degrade in the centre because of the over-exposure. There is another LIPSS structure that can be observed on stainless steel under over-exposure [113], which is called grooves, as in Figure 2.13. The period of the grooves is larger than the laser wavelength ($\wedge_{groove} > \lambda_{laser}$). Thus, the pulse overlap could be another factor to the LIPSS uniformity and period.

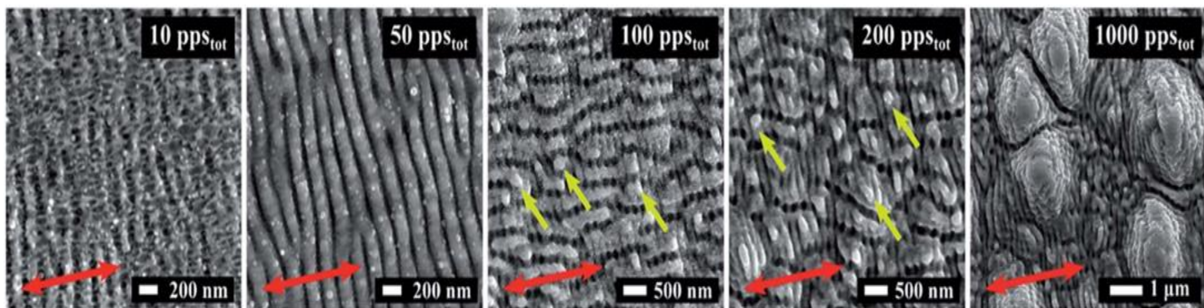

Figure 2. 13 Different overlaps empolyed for different UV LIPSS morphologies generation. The red arrows indicate the polarization orientation. The yellow arrows indicate the edge of the groove. (fluence=0.11J/cm2 ,pps=overlap per spots) [113].

Whereas, the LIPSSs produced with a top-hat intensity profile significantly reduced this effects [114]. As the fluence of laser for LIPSS formation should be closed to the material ablation threshold, thus, the laser fluence could be the other factor that can be affected the LIPSS quality. LIPSSs produced with high fluence have a worse uniformity than those produced with proper chosen laser fluence. If the fluence is further reduced, the LIPSSs become discontinuous [95]. Results indicated that the LIPSSs are not connected and uniform if there is a lack of pulse overlapped on the material surface. They become discontinuous and start to disappear when the pulse overlap is too high [113]. Therefore, the increase of pulse overlap can improve the LIPSS quality. It was also reported that the period of the LIPSS reduces with the increase of the pulse overlap [115, 116]. Carefully selected laser parameters for LIPSS generation are essential. It was reported that the surface roughness and polishing direction will affect the LIPSS uniformity [115]. If the surface roughness is higher, which means more light will be scattered and the laser fluence for LIPSS

generation should be increased. Whereas, if the surface has been polished for roughness reduction, the LIPSS will be uniform when the scan direction is perpendicular to the polishing direction [117].

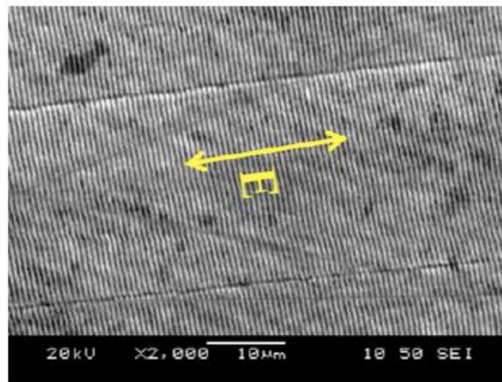

Figure 2. 14 SEM image for uniform LIPSS that on a polished metal surface. Arrow shows alignment of the incident E-field [117].

The LIPSS formation is co-determined with polarization states and laser processing parameters. For the metal material, the laser E field is always perpendicular to the LIPSS orientation. However, for the polymer, the laser E field has been found mainly parallel to the LIPSS orientation [118].

2.3.3 Applications of LIPSS

2.3.3.1 Colour marking

The LIPSS can act as diffractive gratings as some ripples will be machined on the material surface. Figure 2.15 shows the mechanism of colour marking. Z.Ou et al [7] reported the colour will not only change with the inspecting angle but also related with the period of the LIPSS. When a white light illuminate the LIPSS, different colour will be diffracted according on the different period of the LIPSS for different viewing angles and the different incident angle of the incident light.

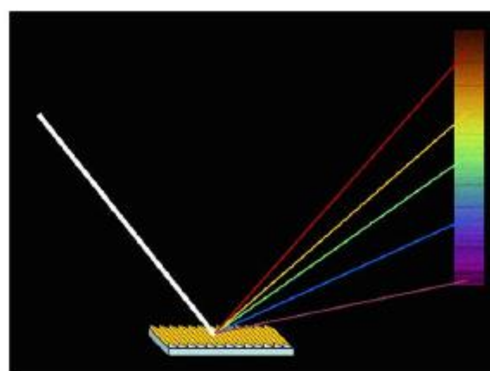

Figure 2. 15 Schematic illustration of white light diffraction on LIPSS covered metal surface, end up with different colour dependent on viewing angle

Commonly, the LIPSS covered area on target surface will appear coloured while the LIPSS with their direction perpendicular to the illumination source direction, and the target surface will remain dark while the LIPSS with their direction parallel to the illumination source direction, as shown in Figure 2.16 (a) [8].

Therefore, the area covered with horizontal and vertical LIPSS will appear coloured with two illumination sources, as shown in figure 2.16 (b).

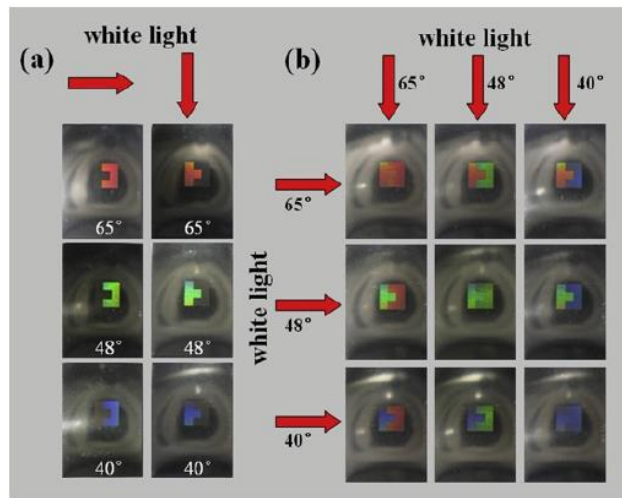

Figure 2. 16 Selective colour appearance on LIPSS covered areas with two orthogonal LIPSS direction. The red arrows indicate the illumination source direction. (a) Selective colour appearance of one LIPSS covered area with the LIPSS's direction perpendicular to the illumination source direction. (b) Colour appearance on both areas covered with orthogonal LIPSS direction and illuminated with orthogonal light sources [8].

By careful changing the laser fluence and exposure time on the target surface, LIPSS will be formed with different qualities. Therefore, the separation between the ripples will be different and the machined samples will present different diffracted colours even with the same incident light angle, as shown in Figure 2.17.

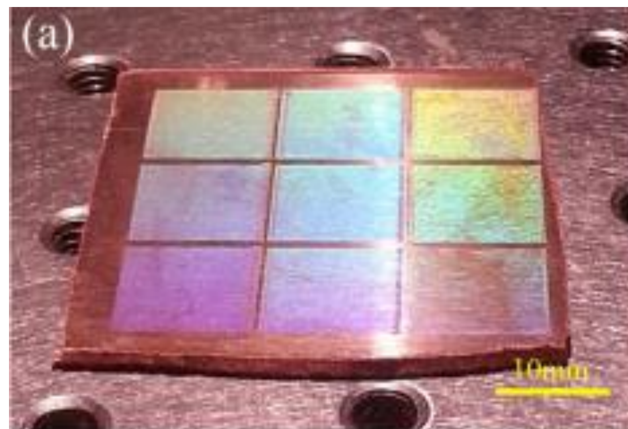

Figure 2. 17 The multicoloured area of the treated surface was taken by a camera with the illumination of a white light. Irradiated fluencies : left column, 1.38J/cm^2 (top), 1.26J/cm^2 (middle), and 1.13J/cm^2 (bottom); middle column, 1.00 J/cm^2 (top), 0.88 J/cm^2 (middle), and 0.75 J/cm^2 (bottom) and right column, 0.63J/cm^2 (top), 0.50 J/cm^2 (middle), and 0.38 J/cm^2 (bottom) [7].

2.3.3.2 Material wettability modification

The period of the LIPPS can modify the surface tension on of a material surface. A number of researchers have used different laser types to print LIPSS on different materials surface for hydrophobicity or hydrophilicity applications. For instance, superhydrophobic surfaces were reported upon fs laser irradiation of stainless steel with M. Martinez-Calderon et al [95]. The contact angle (CA) could be increased from 120° for the processed surface up to 156°, if the suitable power energy for the LIPSS generation has been chosen. Due to the increased surface roughness of the LIPSS covered samples, air remains trapped underneath the liquid and thus the surface becomes superhydrophobic. Compared with the surface treated with LIPSS and without LIPSS, different contract angle will be presented even with the same machined picture distance (Figure2.18). Kietzig et al. established the fact that metallic surfaces (steel, pure metals and alloys) with initial CAs between 60° and 85° change their CA with time from superhydrophilic (CA < 30°) shortly after laser processing to superhydrophobic (CA = 120°—160°), which can be done with the different period of LIPSSs [119].

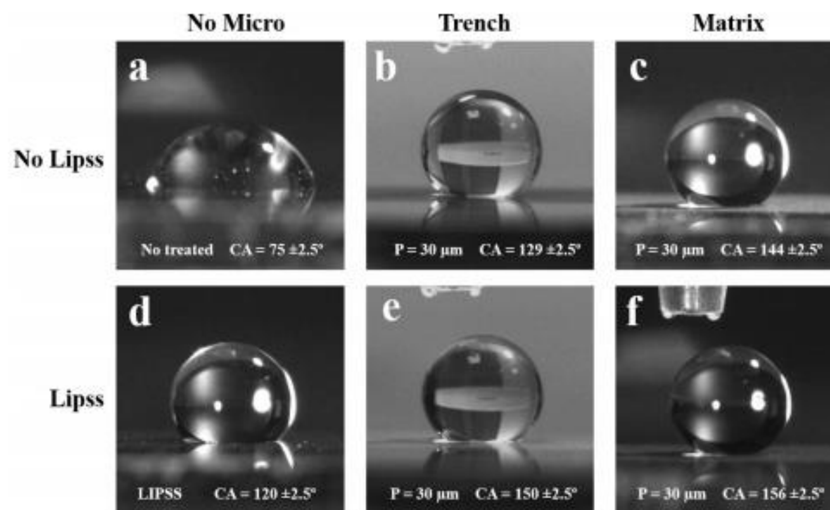

Figure 2. 18 Stainless steel (SS) wettablity comparison with a fixed pitch distance of LIPSS treated surface and no LIPSS treated surface. (a-c) The wettability of SS without LIPSS covered surface (d-f) the wettability of SS with LIPSS covered surface [95].

Comparing with the linearly polarized beam, the circularly polarized beam is seldom used to produce LIPSS as the circularly polarized beam produces spherical nano-dots which are difficult to identify [120]. Recently, J.M. Romano et al [102] presented the results of triangular-shaped LSFL formation by overlapping (overlap rate ≈ 92%) a circularly polarized beam on stainless steel. The triangular-shaped LSFL on the surface exhibited light scattering and superhydrophobic properties with contact angle (CA) of 157°, as shown in Figure 2.19.

Figure 2. 19 Triangular-LIPSS produced by circular polarization. (a) Triangular-LIPSS pattern and corresponding Fast Fourier Transform (FFT). Bottom (b) Produced triangular-LIPSS for wettability properties modification (c) Produced linear-LIPSS for properties modification. [102].

2.4 Introduction to phase and polarization

2.4.1 Definition of phase and polarization

- Phase

The beam emitted from a laser cavity is a form of self-propagating coherent transverse oscillating electromagnetic wave. In the electromagnetic wave, the phase can be defined as the position of a point in time on the wave, or the position of a point on the wave where it has a specified amplitude value. Phase can be shifted to different position that occurs in the phase of one quantity, or in the phase different between two or more quantities, which can be seen in Figure 2.20. If the shift along vertical direction, both of the amplitude and phase angle will be changed. And if the shift along the horizontal direction, only phase angle will be changed.

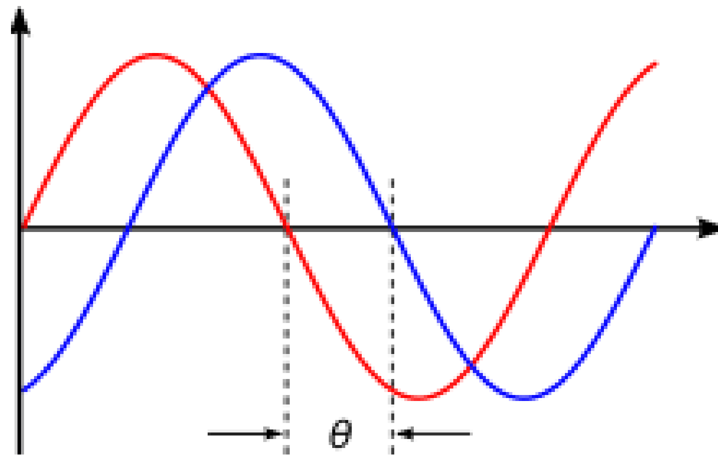

Figure 2. 20 Illustration of phase shift. The horizontal axis represents an phase angle (Θ) that is shifted **[**121**].**

- Polarization

Light has wave-particle duality. The interference and diffraction phenomena reveal the wave nature of light. Polarization is a term that refers to the asymmetry of the oscillating direction of the wave with respect to the direction of the electric field of the electromagnetic wave [122]. While the electric field of the electromagnetic wave is oscillating in a plane perpendicular to the direction of propagation, the polarization within in this case is so called a linear polarization or plane polarization. In the case where the amplitude and the direction of the electric field of a wave are both varying during the propagation, and the tip of the electric field vector at a given time in space describes an ellipse as time progresses, this is called an elliptical polarization. Similar to elliptical polarization, when the electric field amplitude is constant but the electric field direction is changing during propagation, this is called circular polarization. A schematic of polarization state propagation is shown in Figure 2.21.

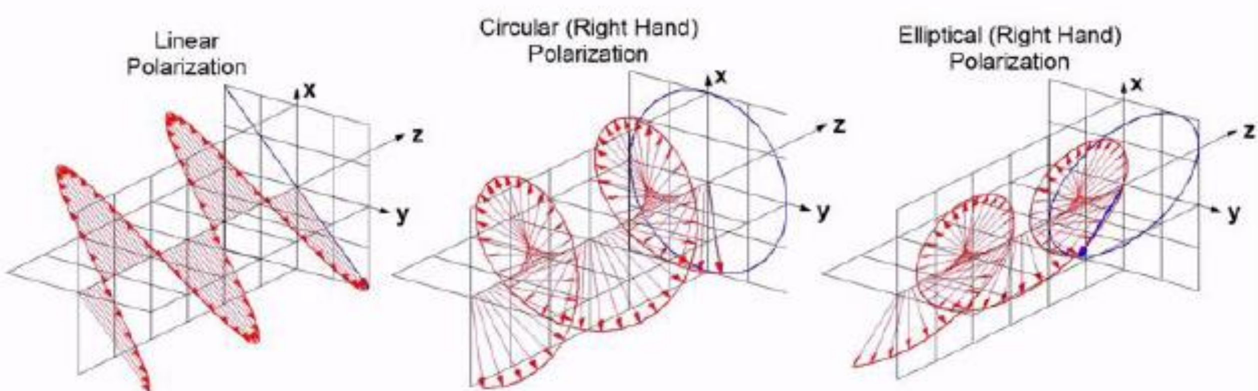

Figure 2. 21 Illustration the different polarization states [123].

- Jones vector and Jones matrix

As the electric field of a light can be resolved into two orthogonal components (Ex and Ey) for different propagation of light. An easy way to describe light polarization and phase was devised by R.C Jones with matrixes in 1941 [124]. This is called Jones matrix, which is widely used for describing polarizations for light propagation.

- Linear polarization

By the definition of linear polarization, the phase difference between two electric field orthogonal components (E_x, E_y) and axis (x,y) is zero. In other words, the angle of linear polarization is only depends on the ratio of $|E_x| / |E_y|$. By resolving in a coordinate system with degrees to the x axis, the E_x and E_y can be expressed with $|Ex| = |E| cos\theta$ and $|Ey| = |E| sin\theta$ (where θ is the angle between the linearly polarized wave and x axis), respectively. Thus, by considering the light phase, E_x and E_y can also be indicated below:

$$\begin{bmatrix} E_x \\ E_y \end{bmatrix} = \begin{bmatrix} |E| \, cos\theta exp(i\varphi_x) \\ |E| \, sin\theta exp(i\varphi_y) \end{bmatrix} = |E| \exp(i\varphi) \begin{bmatrix} cos\theta \\ sin\theta \end{bmatrix} \quad (2\text{-}11)$$

In addition, a Jones vector can also be used to represent a linearly polarized wave with a matrix of $\begin{bmatrix} cos\theta \\ sin\theta \end{bmatrix}$ where θ is the angle between the linearly polarized wave and x axis. For example, at the situation of the wave is linear polarized in the x axis and θ =0°, the Jones vector is $\begin{bmatrix} 1 \\ 0 \end{bmatrix}$. Similarly, if θ =90° or θ =45°, then the normalized Jones vector for the corresponding wave is $\begin{bmatrix} 0 \\ 1 \end{bmatrix}$ or $\frac{1}{\sqrt{2}} \begin{bmatrix} 1 \\ 1 \end{bmatrix}$. Normalized vectors have

$$|E_x|^2 + |E_y|^2 = 1 \quad (2\text{-}12)$$

- Circular polarization

Circular polarization, which is the phase delay between the orthogonal components (delay value $\delta = \pm \frac{\pi}{2}$), and the amplitude of the two components is equal $|E_x| = |E_y| = |E|$. As with linear polarization, resolving the relationship of the orthogonal components within a coordinate system, the orthogonal components can be expressed as below:

$$\begin{bmatrix} E_x \\ E_y \end{bmatrix} = \begin{bmatrix} |E| \, exp(i\varphi_x) \\ |E| \, exp(i\varphi_x \pm \frac{\pi}{2}) \end{bmatrix} = |E| \exp(i\varphi_x) \begin{bmatrix} 1 \\ \exp\left(\pm \frac{i\pi}{2}\right) \end{bmatrix} = |E| \exp(i\varphi_x) \begin{bmatrix} 1 \\ \pm i \end{bmatrix} \quad (2\text{-}13)$$

The last part of the equation can be used to represent the polarization of the wave $\begin{bmatrix} 1 \\ \pm i \end{bmatrix}$. $\begin{bmatrix} 1 \\ i \end{bmatrix}$ represents left hand circular polarization, and $\begin{bmatrix} 1 \\ -i \end{bmatrix}$ represents right hand circular polarization.

- Jones matrix represents linear optical components

The polarization states can be affected by a number of optical elements with desired phase delay. Commonly, two optical elements are usually used to indicate the polarization states of the light source: polarisers and phase retarders. The polarization states on a light wave can be represented by the Jones matrix. For a specific optical element, such as polarizer or phase retarder, by varying the fast axis angle (θ) of the optical element, the output polarization states will be changing and this is related to the fast axis angle, θ. Hence, the corresponding Jones matrix can be found while the incident polarized light propagation to the optical components. The Jones matrix for several optical elements are represented in Table 2.1.

Table 2. 1 Jones Matrices for some linear optical elements

Optical element	$\theta = 0$	$\theta = \pm\frac{\pi}{4}$	$\theta = \frac{\pi}{2}$
Linear polarizer at angle θ	$\begin{bmatrix} 1 & 0 \\ 0 & 0 \end{bmatrix}$	$\frac{1}{2}\begin{bmatrix} 1 & \pm1 \\ \pm1 & 1 \end{bmatrix}$	$\begin{bmatrix} 0 & 0 \\ 0 & 1 \end{bmatrix}$
Quarter-wave plate with fast axis at angle θ	$\begin{bmatrix} 1 & 0 \\ 0 & -i \end{bmatrix}$	$\frac{e^{i\pi/4}}{\sqrt{2}}\begin{bmatrix} 1 & -i \\ -i & 1 \end{bmatrix}$	$\begin{bmatrix} -i & 0 \\ 0 & 1 \end{bmatrix}$
Half-wave plate with fast axis at angle θ	$\begin{bmatrix} 1 & 0 \\ 0 & -1 \end{bmatrix}$	$\begin{bmatrix} 0 & 1 \\ 1 & 0 \end{bmatrix}$	$\begin{bmatrix} -1 & 0 \\ 0 & 1 \end{bmatrix}$
Linear retarder with retardation σ and with fast axis at angle θ	$\begin{bmatrix} 1 & 0 \\ 0 & e^{-i\sigma} \end{bmatrix}$	$\frac{e^{-i\sigma}}{\sqrt{2}}\begin{bmatrix} 1 & \pm1 \\ \pm1 & 1 \end{bmatrix}$	$\begin{bmatrix} e^{-i\sigma} & 0 \\ 0 & 1 \end{bmatrix}$

In this thesis, some of the above optical elements are employed to change the polarization of a laser beam.

2.4.2 Cylindrical vector polarizations

Cylindrical vector (CV) polarization is an inhomogenous state of polarization that is different from the homogeneous polarization states, such as linear, circular and elliptical polarization states. The laser beams with cylindrical vector polarization are the vector-beam solutions of Maxwell's equations that obey axial symmetry in both amplitude and phase [125]. Since 1972, many methods of generating CV beams have been reported. Depending on whether the generation methods involve amplifying media, these methods that used to produce CV polarizations can be categorized as active or passive. The passive method that used to produce CV beams used widely. In general, the passive methods are mainly to convert spatially homogeneous polarizations to spatially inhomogeneous CV polarizations by using optical plates or devices. Details of the generation methods of the CV beams will be discussed later.

The typical cylindrical vector polarization includes radial and azimuthal polarization. By considering the solutions of the scalar Helmholtz equation and the full vector wave equation, the CV beams can be expressed as the superposition of orthogonally polarized Hermite-Gauss HG_{01} and HG_{10} modes [126]:

$$\overrightarrow{E_r} = HG_{10}\overrightarrow{e_x} + HG_{01}\overrightarrow{e_y} \tag{2-14}$$

$$\overrightarrow{E_\emptyset} = HG_{01}\overrightarrow{e_x} + HG_{10}\overrightarrow{e_y} \tag{2-15}$$

where E_r and $E_\emptyset$ denote radial and azimuthal polarization respectively, as seen in Figure 2.22.

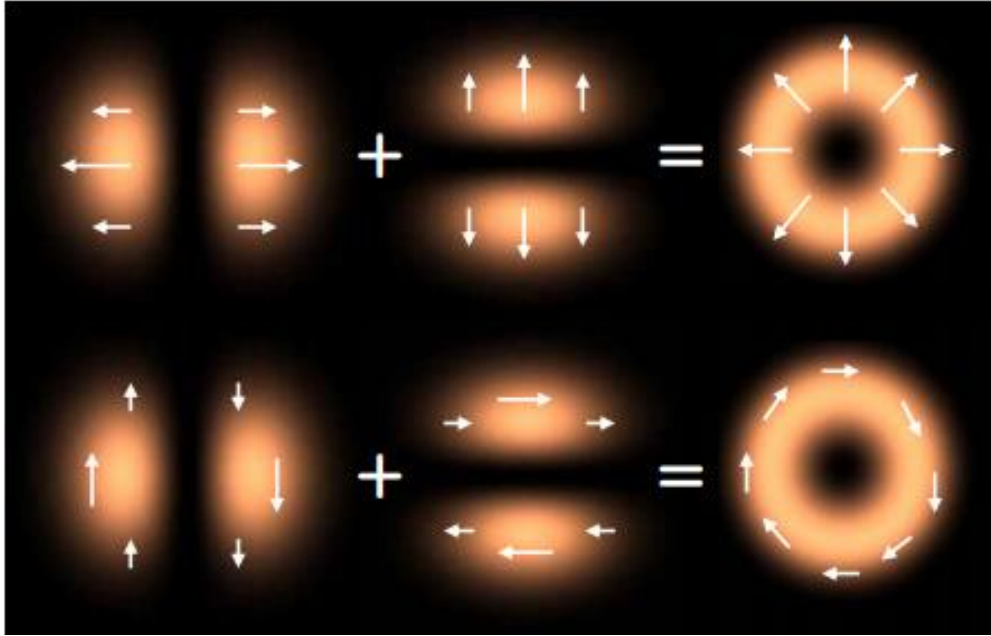

Figure 2. 22 Formation of radial and azimuthal polarizations using linear superposition of orthogonally polarized HG modes [127].

The CV Cylindrical vector polarization has many applications from optical trapping [128, 129] to laser machining [37, 130]. The laser cutting efficient for a radially polarized beam is shown to be 1.5-2 times higher than circularly polarized beams [37] due to the different absorption rate for radially polarization.

2.4.2.1 Generation methods

The CV beams can be generated with a diffractive optical element (DoE) and spatial light modulators (SLM). The method of CV beams generation with optics or a SLM can be regarded as a passive CV beam generation method. The most common used DoE to generate CV beams so called S-waveplate, which is a nano-structured diffractive optical element. Ouyang, J [131] et al reported the tailored optical vector/ vortex fields generation using an S-waveplate with picosecond laser. Spiral plasmons have been generated by altering S-waveplate with horizontal linear polarization. They also showed how the orbital angular

momentum (OAM) associated with a helical wavefront induces rotation of vector field along the optic axis of a focusing lens, as shown in Figure 2.23.

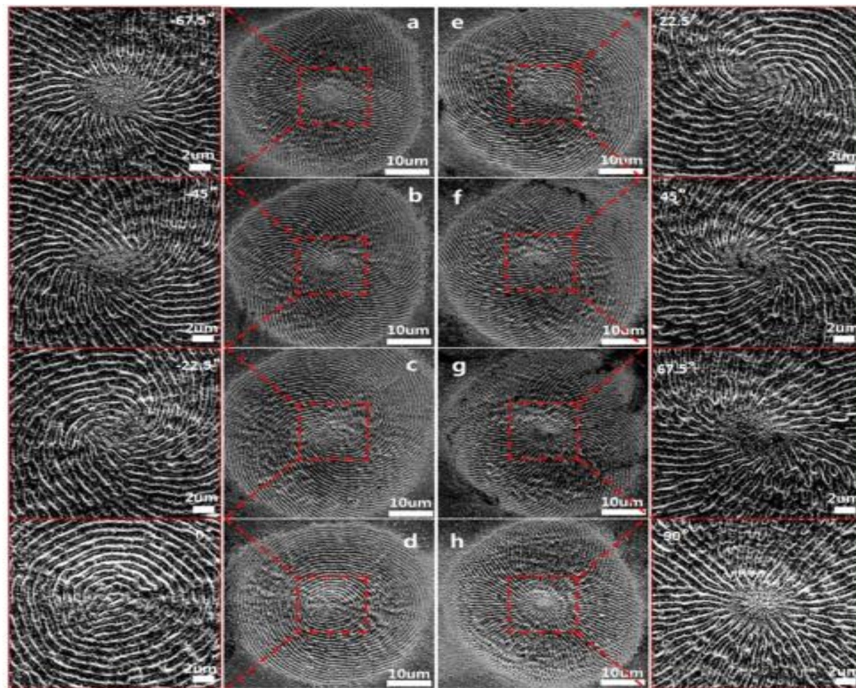

Figure 2. 23 Plasmonic structures of complex polarization states generated by rotating S-waveplate (a) -67.5° , (b)-45°, (c)-22.5°, (d) 0°(radial), (e)+22.5°, (f)+45°, (g) +67.5°, (h)+90°(azimuthal) [131].

In addition to CV beams generation with an DOE, the use of a spatial light modulator (SLM) to generate CV beams has been shown to be easier and more flexible. O J Allegre et al [132] provided a new method to produce multiple first -order CV beams with a SLM for real-time processes. Therefore, as shown in Figure 2.24, the processing with arbitary multiple CV beams is possible. As the wide applications of CV beams, multiple CV beams seem more efficiency for industrial applications and research fields.

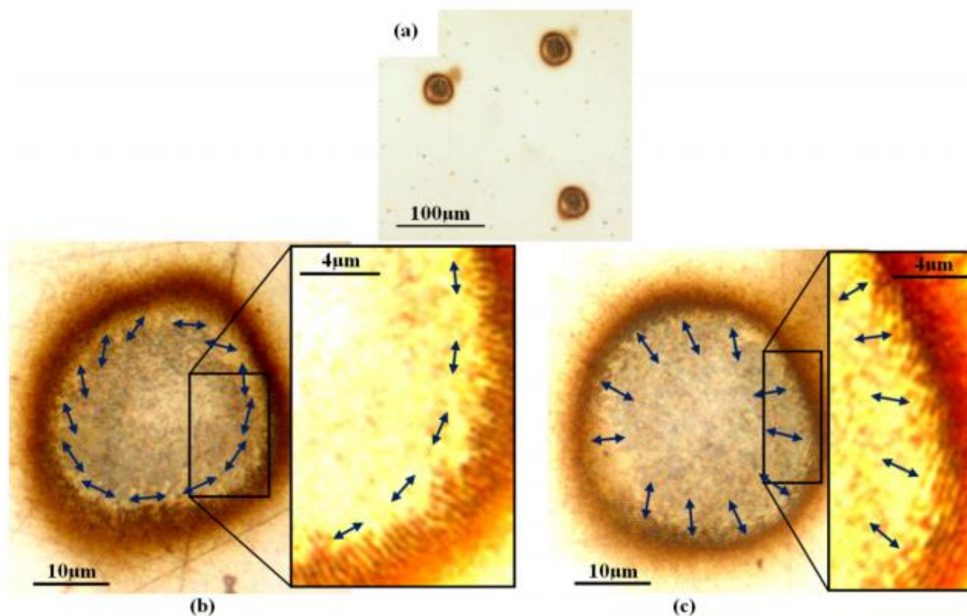

Figure 2. 24 CV beams generation using an SLM [88].

As well as passive methods of CV beam generation, active CV beam generation methods includ the use of laser intracavity devices that force the laser to oscillate in CV modes [127]. However, the active CV beam generation methods are complex and practical implementation has not been taken up.

2.4.2.2 S-waveplate

An S-waveplate is a polarization converter based on the nano-structing imprint inside of a fused silica substrate. For optical configuration, the incident laser beam needs to be aligned to the centre of the S-waveplate, then rotate the alignment mark on the substrate is rotated parallel to the incident linear polarization orientation. If the linear polarization state of incident beam is parallel to the alignment mark, the output will be radially polarized and azimuthally polarized for the incident linear polarization is perpendicular to the alignment mark.

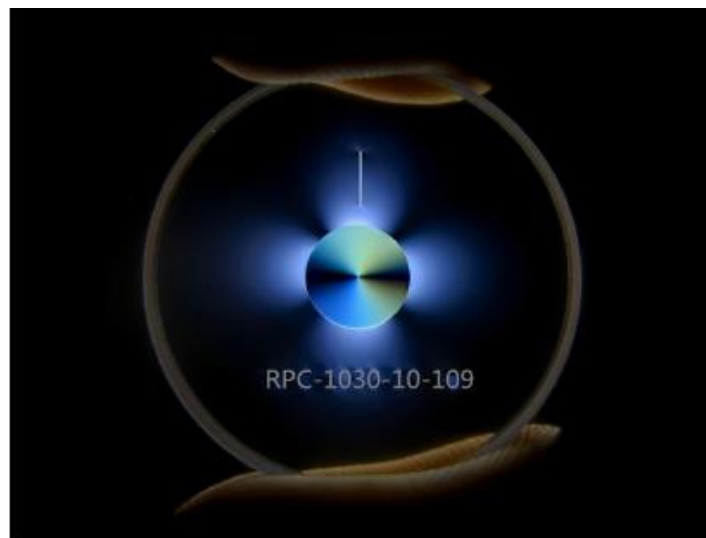

Figure 2. 25 S-waveplate (Altechna) used to convert incident linear polarization to radial and azimuthal polarizations [133].

For the incident linearly polarized beam, the S-waveplate rotates the incident linear polarization by the angle necessary to produce a radial distribution of the electric field. The Jones matrix can be used to describe the polarization transformations appropriately. The Jones matrix for the S-wavelate as shown in below [134]:

$$Ms=\begin{pmatrix} cos\emptyset & -sin\emptyset \\ sin\emptyset & cos\emptyset \end{pmatrix} \quad (2\text{-}16)$$

Where $\emptyset$ is the polar angle, the polarization states after the S-waveplate is position dependent.

2.4.3 Polarization effects on laser material interaction

Linear and non-linear laser material interaction are highly dependent on the laser polarization state. For example, simple Fresnel reflection from a dielectric interface near Brewster's angle [135], ultrafast laser

surface texturing with a number of polarizations [131, 132, 136]. High intensity non-linear phenomena, such as self-focusing [137], filamentation [14, 138], and multi-photon ionization [139-141]

2.4.3.1 Linear interaction

A polarized light incident on an object can be presented as two orthogonal linear polarization components of the incident light field, parallel (s-polarization) and perpendicular (p-polarization). The reflectivity of a non-transparent material, such as metals can be expressed below with s- and p- orthogonal components [142]:

$$R_p(\theta) = \frac{(n^2+k^2)\cos^2\theta - 2n\cos\theta + 1}{(n^2+k^2)\cos^2\theta + 2n\cos\theta + 1} \tag{2-17}$$

$$R_s(\theta) = \frac{(n^2+k^2)\cos^2\theta - 2n\cos\theta + \cos^2\theta}{(n^2+k^2)\cos^2\theta + 2n\cos\theta + \cos^2\theta} \tag{2-18}$$

Where n is refractive index, k is wavevector and θ is laser incident angle. Then, according to the Beer-Lambert Law, the intensity that is absorbed by the material has been demonstrated below:

$$I = (1 - R)I_0 e^{-\alpha z} \tag{2-19}$$

Where R is the reflectivity of the material, α is the linear absorption coefficient and z is the optical penetration depth. Thus, if an angle between polarization direction and incident direction >0°, different absorption rate will be different with various polarization direction. Polarization effects on laser cutting and drilling can be briefly explained by the polarization dependent selective energy absorption on the sidewall of the hole drilled by the first few laser pulses [37, 132]. In addition, Darke R. Austin [143] observed high and low spatial frequency linear LIPSS at oblique (45°) incident laser with multiple 3μm femtosecond laser pulses. Skoulas E et al [103] observed that the angle between the radial/azimuthal polarization states and the laser scanning direction could be a factor of different period LIPSS generation.

2.4.3.2 Non-linear interaction

Due to the ultra-high intensity (I>$10^{12} W/cm^2$) generated by the ultrashort pulse laser, non-linear laser-material effects may occur, such as filamentation and multi-photon ionization (MPI). Both are also relative to the polarization states. Linear and circular polarization dependent filamentation has been demonstrated in deoped phosphate glass with a factor of 1.5 [144]. In addition, radial and azimuthal polarization carries orbital angular momentum (OAM) and have been used for filamentation in PMMA with a femosecond laser [145]. Polarization also has effects on multi-photon ionization, which is indicates that multiphoton ionization in atoms [15], molecules [141], and solids [140] are all polarization sensitive. At low nonlinear order ≤4, circular polarization has higher multi-photon ionization than the linear polarization [15, 139]. However, for higher nonlinear order > 4, circular polarization has lower multi-photon ionization than

linear polarization [141]. In addition, the polarization state also affects the refractive index in transparent materials [146]. In this thesis, linear interaction is the main focus, so further details of the non-linear effect will not be discussed here.

2.5 Intensity and polarization control with diffractive elements

2.5.1 Intensity and polarization control with SLM

Intensity modification and polarization control with SLMs have been investigated separately in recent years. However, modification of both intensity and polarization in an optical configuration has been seldom investigated. Flattop beams with associated uniform intensity distribution are widely used in the applications where a uniform intensity distribution is needed, for example thin film processing [147], optical trapping [148] and laser drilling [149]. A recent study has shown that a 2D flattop beam shaping with spatially variant polarization under lower NA focusing is possible [150]. This is also suitable for flattop beam shaping with different input beam sizes. More recently a study has shown that various shaped beams with intensity variation can be achieved on the image plane using an SLM [151]. For the applications requiring radial/azimutal polarization states but with other beam shapes, both beam shapes and polarization need to be modified in the same optical configuration. In addition, multiple diffracted beams with polarization distribution control was reported to reduce the intensity of the original diffracted spots after focus [152]. This is very useful for precision intensity control by employing polarization states and no necessary to re-configure the laser parameters. Furthermore, distortion of the diffractive beams arises due to the mutual interference when the beams get too close [152]. By applying orthogonal linear polarization states on the adjacent diffractive spots, the interval can be reduced to half compared to diffractive beams with no polarization control [152].

2.5.2 Theory of light modulation with spatial light modulator

The optical setup for tailoring the phase or the polarization of an incident laser beam are different using an SLM. Due to the parallel-aligned nematic liquid crystal in an SLM, the liquid crystal molecules in the SLM are aligned horizontally or vertically, in which the phase will delayed when applying horizontally or vertically polarized components. As the liquid crystal molecules in the Hamamatsu SLM are aligned horizontally, the phase delay caused by the liquid crystals only applies to laser light horizontally polarized components whereas the vertical polarized components suffers no phase delay. Hence, the SLM has a birefringent property and the fast axis (extraordinary axis) of the Hamamatsu SLM is horizontal. Details of the Hamamatsu SLM principles and structures will be discussed in section 2.7.

For only phase modulation using the Hamamatsu SLM, the incident linear polarization of a laser should be parallel to the fast axis of the SLM. A desired tailored laser wavefront will be achieved, i.e. vortex

beam [153] and multiple diffractive beams [30, 154] while applying appropriate CGH. However, the polarization states of the laser beam is thus unaffected by the SLM in this situation. To control the polarization of the incident laser beam on a SLM, the incident polarization needs to be either circular polarization [155], or linear polarization at 45 degrees to the fast axis of the SLM [152]. A quarter-wave plate needs to be placed after the SLM for both cases to keep the polarization after the quarter-wave plate is always linear. For the SLMs, the phase delay can operate with various grey level CGHs (grey level ranges from 0 to 255, the ability of phase modulation with grey levels is discussed in Chapter 3). The relative phase delay between the horizontal component of the light and the vertical component of the light leads to a change of polarization, from $+45\ °$ linear polarization to elliptical polarization. For special cases, i.e. zero phase delay or $\pi/2$ phase delay to the horizontal component light, the output polarization states are $+45\ °$ linear polarization or circular polarization, respectively. The quarter wave plate placed after the SLM with its fast axis set at ±45°, changing the elliptical polarization after the SLM to linear polarization. In other word, with $+45\ °$ linearly polarized beam incident, a SLM and a quarter-wave plate with its fast axis at +45° forms a polarization converter. In this thesis, all polarization control using the SLM are with incident linear polarization at 45° to the fast axis of the SLM.

2.5.3 Intensity and polarization control with optics

Phase and polarization control based on optics is related to the microstructures which can be etched in optical materials, such as glass and polymers. Polarization control with diffractive optical elements (DOEs) have the advantages of convenience, high average power capability and high efficiency. However, DoEs are customised and fixed for specific applications. A typical application of a diffractive optic is to produce numerous diffractive orders with symmetric intensities. An example is a Dammann grating, which is fabricated with phase changes 0 and π in order to produce equal intensities in a given number of orders in 2D. Recently, C. Zhou et al [156] have demonstrated a new optic for laser 3D patterning called a Dammann Zone Plate (DZP). By using the DZP, J. Yu [157] have introduced a 3D symmetric pattern by combing a conventional Dammann grating and a Dammann Zone Plate (DZP), as shown in Figure 2.26.

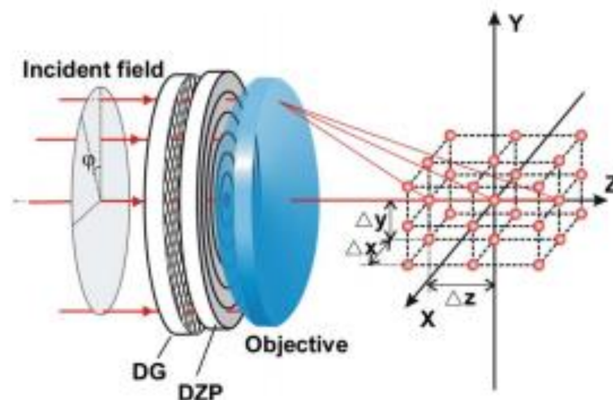

Figure 2. 26 A schematic of 3D beam shaping using Dammann Zone Plate (DZP). DG is Dammann grating [115].

Furthermore, diffractive optics can also be used to control the phase of a laser beam, for example vortex beam generation [158, 159] and airy beam generation [160]. The best-known vortex beam is the doughnut-shaped Laguerre-Gaussian (LG) mode LG_0^1. Yachao Liu et al [158] have produced a perfect vortex beam by combining a vortex plate, an axicon lens and a convex lens, as shown in Figure 2.27.

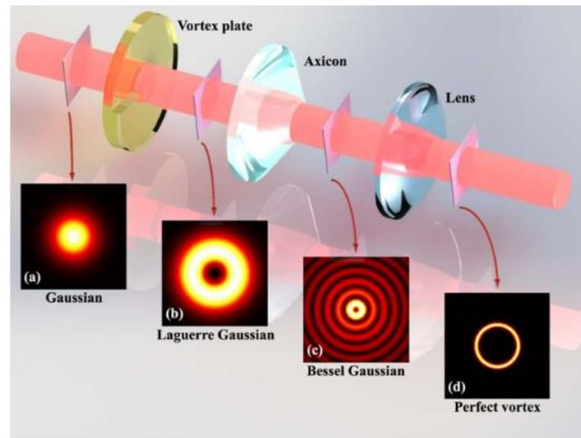

Figure 2. 27 A schematic of perfect vortex beam generation by using optics [158].

DOEs allow not only complex transformation of the amplitude-phase distribution of laser radiation, but also to perform a redistribution of energy between the vector components of the electromagnetic field, consequently, the change in the polarization state under condition of sharp focusing and non-paraxial propagation [161].

Methods of polarization control with diffractive optics have been widely investigated by researchers for a number of applications. A. P. Porfirev et al [162] combined polarization states of a focused cylindrical polarized vortex beams with a multi-order diffractive optical element, as shown in Figure.2.28.

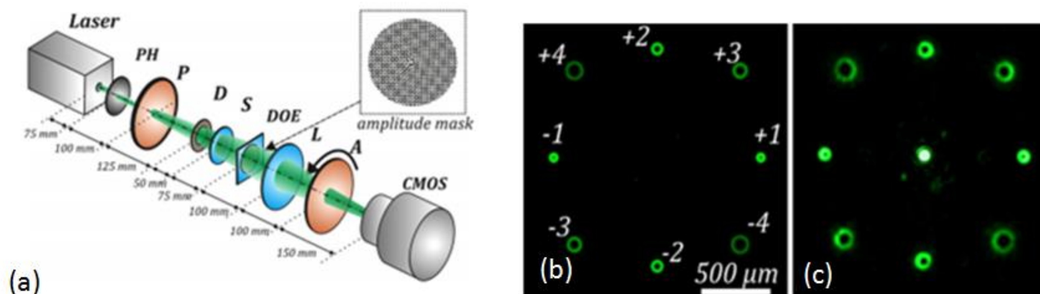

Figure 2. 28 (a)experimental setup. PH is a pinhole (~100μm), P is a polarizer, D is a diaphragm, S is an S-waveplate, DOE is an amplitude diffractive optical element forming a superposition of eight vortex beams with orders of ±1,±2,±3,±4, L is a lens with f=150mm, A is an analyser, and CMOS is a CMOS-video camera. (b) simulated diffraction pattern in far-field region when passing the laser beam through the amplitude diffractive optical element (c) experimentally obtained interference patterns of the generated vortex beams [162].

2.5.4 Dynamic control of phase and polarization for laser material processing

Tailoring the optical field and the wave front dynamically has the potential to maximise the throughput and optimise the quality of ultrafast laser processing. Stephan Graf et al [46] proposed a method for dynamic linear polarization controlling by a motor-driven rotated polarizer for fs laser surface modification, the schematic of experimental setup as shown in Figure.2.29.

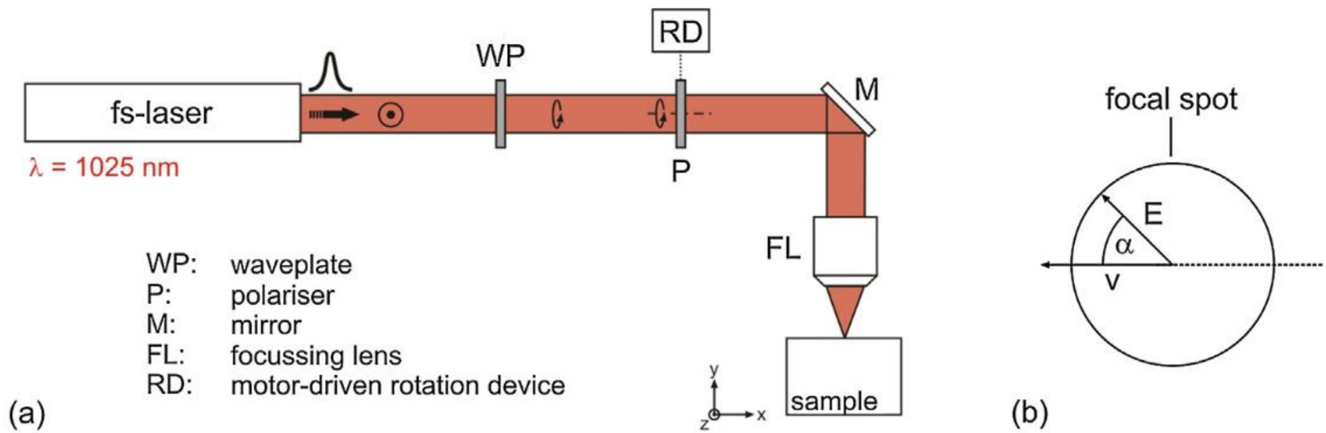

Figure 2. 29 (a) Experimental setup and (b) orientation of the E-field vector E relative to the scanning velocity v [46].

In the setup of [121], a femtosecond laser with wavelength λ=1025nm was emitted and passed through a quarter-wave plate, which was used to alter the input linear polarization to output circular polarization, then it was passed through a motor-driven linear film polarizer, which was used to achieve different output polarization states (which means the direction of the E-field is different). By coupling with the application of laser surface texturing with this dynamic polarization control method, the continuous complex linear polarizations have been printed on stainless steel surface, as shown in Figure 2.30. This technique can also be widely used for large area security colour marking and antimicrobial purpose.

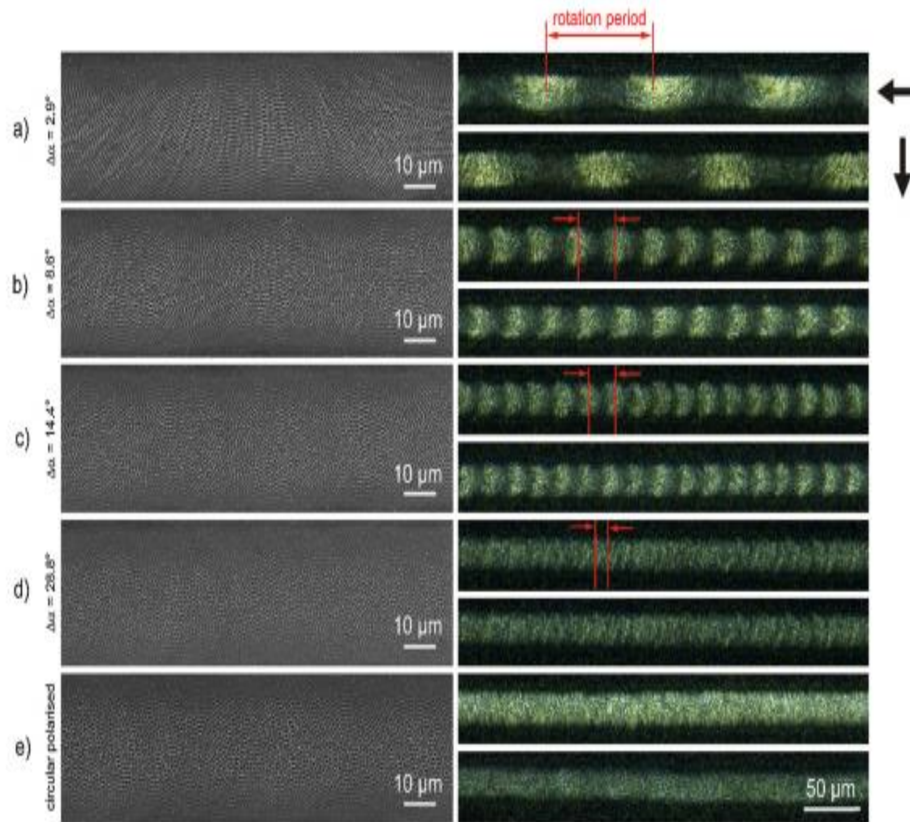

Figure 2. 30 Printed LIPSS with dynamic controlled polarization sates on stainless steel surface utilising an E-field vector rotating by an angle $\Delta\alpha$ of (a) 2.9°, (b) 8.6°, (c) 14.4° and (d) 28.8°in comparison to the utilisation of (e) circular polarisation; left: SEM micrographs and right: optical micrographs imaged with side-illumination at grazing incidence (arrows indicate the direction of illumination, v=0.5mms/, f=250Hz, f=1J/cm^2) [46].

There is increasing interest in inhomogeneous polarization modification, like radial and azimuthal polarization states. Yang Jin et al [163] proposed a method for dynamic vortex radial and azimuthal polarization control by combining two SLMs for ps-laser processing, results as shown in figure.2.31. The first SLM was used to generate a linear polarized vortex which carries orbital angular momentum (OAM) and then the second SLM was used to alter the input linearly polarized vortex beam to a radially or azimuthally polarized vortex beam. The results have been demonstrated in figure 2.31 (a) and (b).

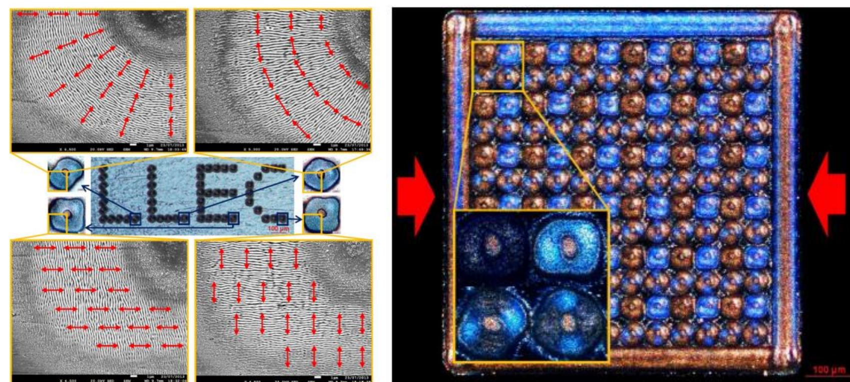

Figure 2. 31 Dynamic controlled polarization states and a formed diffractive pattern. (a) Dynamic controlled linear, radial and azimuthal polarizations (b) a diffractive pattern formed based on dynamic controlled polarization states [163].

In this thesis, a novel method of dynamic beam shaping with polarization control with several SLMs and another method of dynamic polarization control using one SLM will be introduced in chapter 4 and chapter 6 respectively.

2.6 Introduction to laser beam shaping

2.6.1 Typical intensity distribution for laser beam shaping

Beam shaping is the process of redistributing the irradiance and phase of a beam of optical radiation. The beam shape is defined by the irradiance distribution. The phase of the shaped beam is a major factor in determining the propagation properties of the beam profile. Most of the laser beam shaping techniques, including laser phase and wavefront control [164], top-hat beam generation [165-167] are used for many industrial applications.

Typically, a top-hat (flat top) beam is widely used for many applications, such as laser printing [167], thin film processing [147, 168] , material annealing [169], material deposition [83] and laser welding [170] with improved intensity distribution requirements and repeatability. This due to the fact that the same interaction is accomplished over the same illuminated area when applying a flat-top beam. More recently, Xi Ye et al [165] generated a high frequency (THz) flattop beam based on two phase plates. Due to the properties of high frequency, this method has huge potential applications in laser precision 3D-printing. A top-hat beam can be obtained by expanding the beam to obtain a pattern with the desired degree of uniformity by using refractive or diffractive methods. However, no matter the method of refractive or diffractive beam shaping, they are introducing very large losses in energy throughput [21] due to the laser beam quality (M^2) reduction ($M_{Ga}^2 < M_{FT}^2$).

Furthermore, there are several non-conventional intensity distributions which give advantages over Gaussian or Top-hat in some specific applications. For example, Bessel beam, which is described by a zeroth-order Bessel function of the kind (J_0), has widespread applications in laser drilling [171], particle manipulation (optical tweezers) [172] and corneal surgery [173]. Bessel beam can be easily generated by an axicon lens. The Bessel beam also can be used to convert to the annual beam while the Bessel beam is in the far field. This is due the beam intensity in the central axis decreasing with the separation between the wave vectors increasing. There is another modulated beam with annualr shape, which is vortex beam. Vortex beam is defined as a beam whose carried with optical phase singularity in the middle of the beam. This kind of beams carrying optical angular momentum.

2.6.2 Beam shaping using refractive geometrical optics

Lasers are used in industry and have a huge variety of applications. These applications can be divided between those that involve the processing of materials and all other applications. The main function of

refractive laser beam shaping using geometrical optics is to transform Gaussian beam into a uniform distributed beam (Top-hat beam). Typically the Gaussian distributed beam has been commonly used in manufacturing fields, this follows a Gaussian distribution of the delivered energy. The Gaussian distribution is shown in Figure 2.32. Commonly, the Gaussian function can be express as:

$$I(r) = I_0 \exp(-2 \cdot r^2/\omega^2) \tag{2-20}$$

Where r designates a variable beam radius in polar coordinates, ω designates a waist radius of the Gaussian laser beam, I_0 is constant.

As shown in Figure 2.1, the Gaussian distribution can be derived to three variable parts (E1,E2,E3) [174]:

E1 top of the Gaussian distribution which has most of the energy. This usually causes overheating while laser processing.

E2 edges of Gaussian distribution, almost always this is a loss of energy or a source of undesired effects such as heat affected zone (HAZ).

E3 "effective cylinder" of energy. This area is defined as a shaped area with uniformity power distribution (flattop beam).

All E1, E2 and E3 can be expressed as below [174]:

$$\begin{Bmatrix} E_1 = 1 - h + \ln h \cdot h \\ E_2 = h \\ E_3 = -\ln h \cdot h \\ E_1 + E_2 = 1 + \ln h \cdot h \end{Bmatrix} \tag{2-21}$$

Where $h = I_h/I_{max}$.

Thus, the aim of refractive laser beam shaping using geometrical optics for uniform distribution is to eliminate or minimize the undesired part E1 and E2.

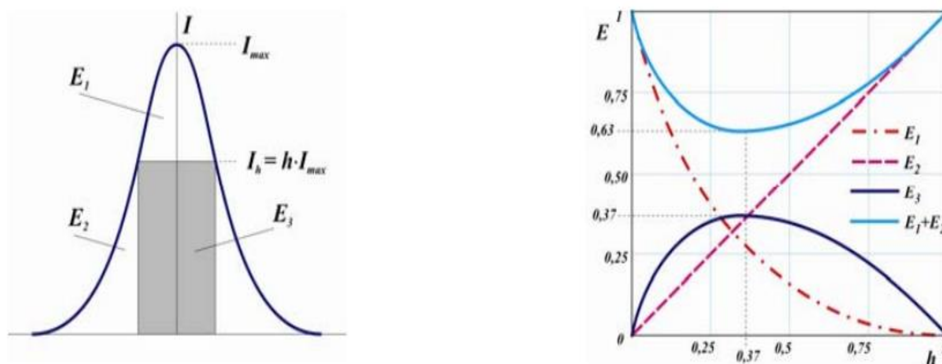

Figure 2. 32 To evaluation of efficiency of using the laser energy [13].

In order to eliminate or minimize the undesired part of E1 and E2, geometrical optics are required with a specific shape. Further, optical design software, such as ZEMAX, can be used to help to design the desired optics geometry [175].

The quality of any beam shaping techniques have beam identified by Bokor and David [15], which is as follows: (1) it forms the desired beam shape with high accuracy and has minimal losses of the total power; (2) the output beam shape is not sensitive to small changes of the input beam irradiance profile or phase distribution; (3) the beam brightness with minimal reduction. Because of the beam shaping lens is a small energy absorbed element, refractive beam shaping is a lossless beam shaping method.

2.6.3 Beam shaping using diffractive elements

The basic theory for diffractive laser beam shaping is Fourier transformation. Notably, the Fourier transform of a Gaussian beam remains a Gaussian and thus preserves its shape as it passes through an optical system consisting of simple lenses [21]. Because the Gaussian beam has the lowest divergence, which allows for a small focused spot on the work piece, this makes them ideal for laser micro processing with lower thermal effects. Based on Fourier transformation, an input single Gaussian beam can be transformed to desired laser beam pattern and intensity distribution, such as multiple parallel Gaussian beams [30], cylindrical vector polarized beams [131, 163] and uniform distributed beam(top-hat beam) [167]. The shaping problem is independent of laser wavelength and shaped irradiance pattern and can be obtained at distance z as expressed below [21]:

$$z = \frac{f\lambda'}{\lambda} \tag{2-22}$$

Where f is the focal length, λ' is the beam shaping design wavelength, λ is the applied wavelength.

Diffractive beam shaping is different from refractive beam shaping methods. There are two diffractive beam shaping aspects: one is using a spatial light modulator (SLM) which is a computer-controlled device and the other method is using fixed diffractive optical elements (DOEs) [83]. The input images to an SLM for laser modulation are called Computer Generated Holograms (CGH). The details of CGHs will be introduced in section 2.7.3. Thus, the SLM can be used to produce laser beams based on different CGHs by modulating phase and polarizations. Figure 2.33 shows the beam shaping elements of a SLM and a DOE.

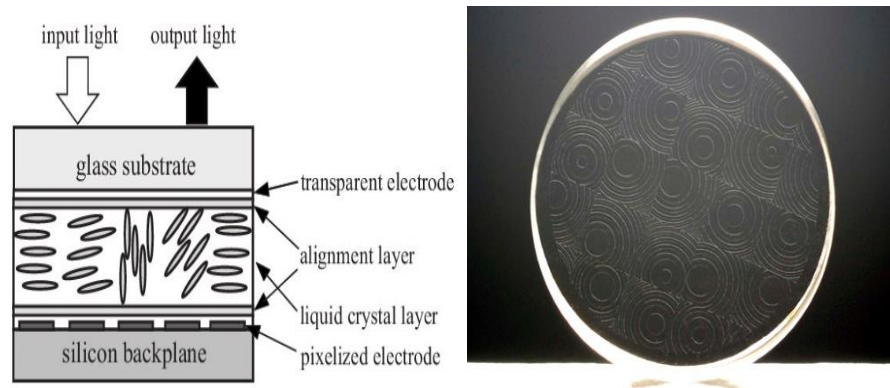

Figure 2. 33 The basic structure of a LCOS-SLM and a typical diffractive optical element [20, 21

Beam shaping with an SLM has been used more widely than refractive beam shaping methods, as it can be used to generate any complex beam shapes with less ray-tracing calculations only by applying complex CGHs. A lot of researchers have generated many complex laser shapes for various applications by using SLMs. For example, Yue Tang et al [176] demonstrated a dynamic method to of a various polarized shaped laser beam by SLM. Dun Liu et al [177] used a SLM to produce any laser shapes with hybrid holograms. Using DOEs, Račiukatis et al have generated different laser beam shapes and intensties, including top-hat square beam [168]. The common drawback of beam shaping with SLMs is energy loss due to reflection and material absorption on the SLM [30, 176]. For DOEs, the fabrication of DOEs are complex and money-consuming. In this thesis, one of the task is to generate different laser beam shapes with uniform intensity distribution or complex polarization states by applying CGHs.

2.6.4 Optimization of laser beam shaping

Laser beam shaping techniques can be used to shape a beam in both phase and polarization, in addition it can be applied to produce multiple laser beams for laser parallel processing. All of these methods are regarded as a way to optimize the laser.

2.6.4.1 Modulation of phase and intensity

For further laser-based processing efficiency increases, precise control of the light phase and intensity distribution can allow significant efficiency improvement in micro processing [178] and optical trapping [179, 180]. Methods of arbitrary control over phase and distribution have been developed and demonstrated in many [164, 178-180]. For instance, complex collinear OAM beams have generated with two phase-only spatial light modulator(SLM) in one-lens imaging system and 4f system [164] , as shown in Figure 2.34.

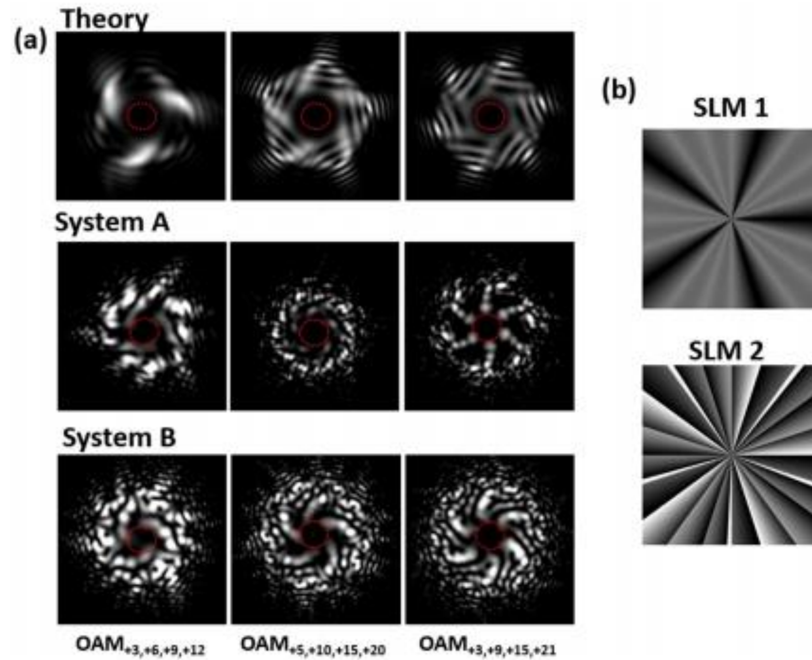

Figure 2. 34 Phase and amplitude modification with two SLMs. SLM1 for phase modification and SLM2 for OAM beams generation. (a) Intensity profiles of the generated spot. System A is one-lens imaging system and system B is a 4f system. (b) Phase pattern employed on SLM1 for phase modulation and SLM 2 for OAM beams generation [164].

The most significant role of phase and amplitude modulation for laser beams is to produce beams with spatial structures. Spatial light has more degree of freedom compared to the nature light in a given plane.

An SLM is typically used for a specific propose, such as multiple beam generation, phase modification and intensity modulation. However, due to the limitations of the SLM, such as optical path difference caused by the curvature of the SLM screen window, the diffraction efficiency will vary significantly. This issue can be solved by conjugating a specific hologram called a "correction file" on the desired hologram. Based on this idea, holograms calculated using conjugate gradient minimization techniques have also been applied for controlling both phase and amplitude [181] for shaping optimization. Conjugate gradient minimization is a numerical method to optimize high dimensional function [30]. By tailoring the output-plane amplitude of phase-only holograms, new holograms are generated and applied on SLMs (see Figure 2.35). In this thesis, a method of conjugating intensity and phase CGHs for processing efficiency improvement has been investigated.

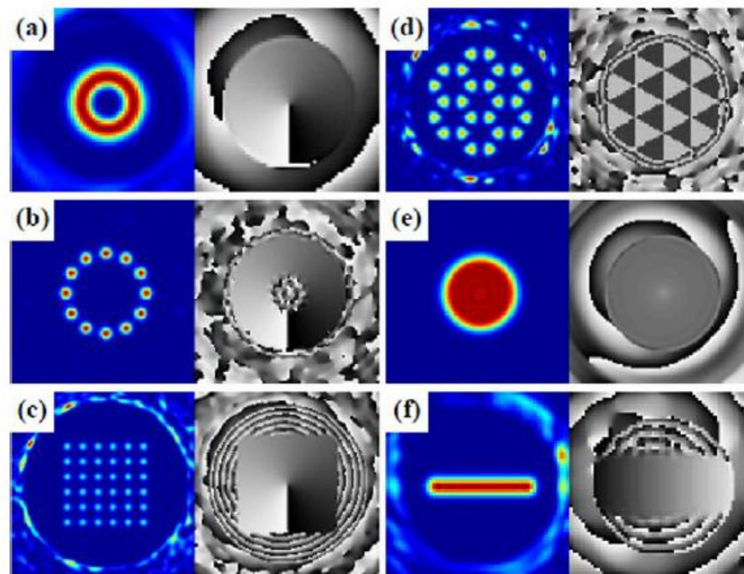

Figure 2. 35 The far-field from the conjugate gradient optimization showing normalized intensity and phase in the region of interest [181].

2.6.4.2 Optical vector and polarization modification

The complex polarization of light has been shown to improve processing efficiency in laser micro-processing. Thus, polarization modulation by using an SLM is another significant way of optimizing the laser beam for processing efficiency improvement. More recently, Ouyang et al [131] had showed a technique for tailoring the optical vector beams using a SLM and a micro-structured S-waveplate. The influence of the Orbital Angular Momentum (OAM) on vector fields have been confirmed by the observed surface micro-structures. A laser beam was illumined onto a SLM with a spiral phase hologram to control the OAM and then passed through an S-waveplate to obtain radial and azimuthal states. The polarization will be tailored along the light propagation direction. Figure 2.36 shows a clear distortion between the vector beams with the OAM. All the beam with orbital angular momentum (OAM) had a twisted profile indicating the influence of the OAM on the vector fields.

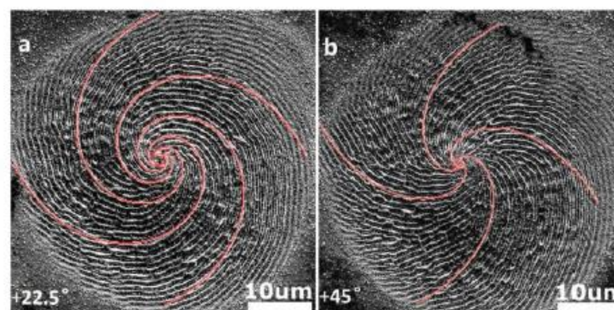

Figure 2. 36 Combined phase modulation with vortex beams by a SLM. 22.5° and 45° represent the fast axis angle of the S-waveplate [131].

Nevertheless, dynamic polarization modulation based on a fixed physical devices, such as a motor-driven half-wave plate [46] and time-synchronized shutter [163] have presented huge potential for laser

processing improvement. Recently, Yang Jin et al [163] have used a time-synchronized shutter for dynamic linear polarization direction altering for laser security colour marking, can be seen in Figure2.37. With the benefit of dynamic polarization control, impressive colour marking was possible with reduced manufacturing time.

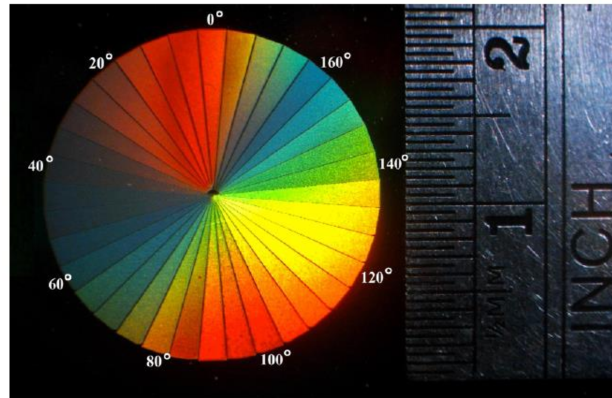

Figure 2. 37 36 segments produced on polished brass sample with dynamic polarization control. 0° stands for horizontal linear polarization and the polarization rotates clockwise with an incremental change of 5°, which gives a different LIPSS orientation in each segment of the pattern [163].

2.7 Laser parallel processing with a Spatial Light modulator (SLM)

2.7.1 Working principle of a phase only SLM

Most laser beam modulation is based on a spatial light modulator (SLM). A spatial light modulator (SLM) is a real time optical wavefront modulation electronic device that is widely used in laser processing. Figure 2.38 shows the detail of an SLM. The SLMs are reported in laser beam parallel processing [182-184], beam shaping [185, 186], phase and wavefront modulation [41]. With the thermal limitations of the components of an SLM, the SLM is usually used for low laser intensity applications. However, with the development of laser micro processing in industry, more and more researchers are interested in high power affordable SLM investigation. Klerks and Eifel [187] has demonstrated a laser processing based on SLM up to 60w average power. Zhu et al [145] has tested the SLM up to 220W average power and they reported the phase modulation of the SLM with grey level holograms cannot be reached at 2π when the average power ≥ 120W.

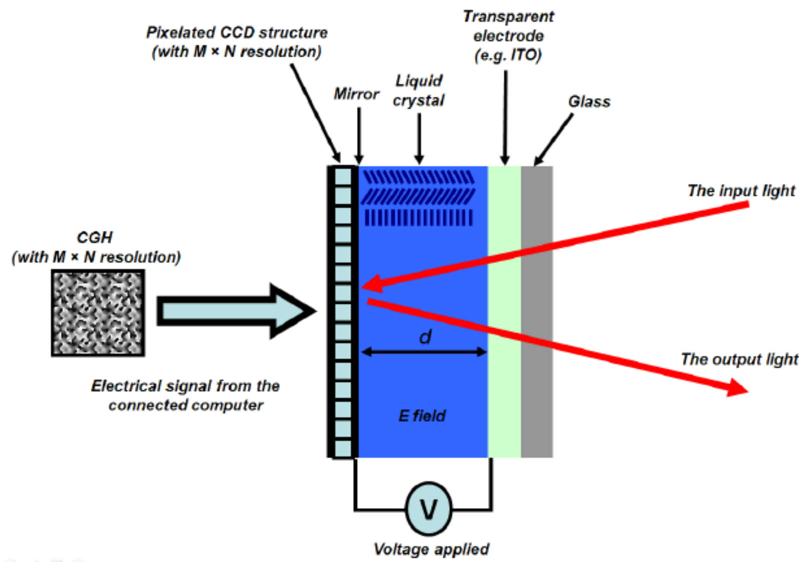

Figure 2. 38 Schematic of a typical reflective type SLM structure [10].

Figure 2.38 shows typical structures of an SLM. With an SLM, phase holograms can be applied on the SLM via an PC to generate modulated beams for different applications, which are includes from multi-trapping of micro-particles in optical tweezers to ultrashort pulse laser material micro-processing. In addition, the holograms also have significant applications, such as in laser beam shaping where the hologram works as an intensity mask to modulate the intensity distribution of the input laser beam [186].

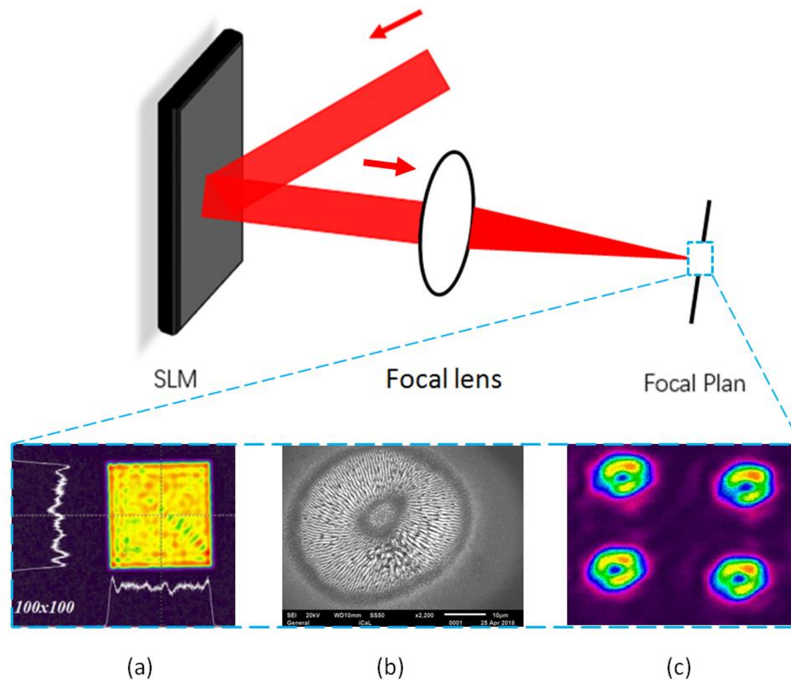

Figure 2. 39 Schematic of the laser with an SLM. Modulated results will be produced at focal plane of the focal length (a) modulated intensity results [188] (b) modulated phase/polarization results (c) modulated laser multiple patterns.

Figure 2.39 demonstrates a typical optical path used to modulate beam intensity/phase and polarization/multiple laser generation with a SLM and a Fourier lens (focal lens). The hologram that is used for beam modulation will be applied on the SLM first, laser will illuminate the SLM and will be

passed through a Fourier lens (focal lens). After the Fourier transformation, modulated beam will be focused at the focal plane of the Fourier lens (focal lens). The quality of the modulated beam depends on the calculated phase/ amplitude on the hologram.

2.7.2 Generation of multiple beams with SLM

2.7.2.1 Parallel micro-processing using periodic structures

Diffraction gratings can be used to split a laser beam into many diffracted beams depending on the period of the gratings [156]. The calculation of the period structure of the diffraction gratings is based on Iterative Fourier Transform Algorithm (IFTA), therefore the diffraction grating also can be called a Fourier optic. If λ is the wavelength of the light and d is the period of the grating, the direction cosines of the diffracted beams will be integer multiples of λ/d near the axis. However, many publications only introduce the theory of how to split the beam, few of the books have introduced the theory of how to make the split beam with equal intensity.

Assuming the beam splitting gratings are thin and losses are small, so that the amplitude of a light wave will remain constant when the light wave passes through the grating. The phase will be changed by $\varphi = \omega\tau_{\delta}$, where ω is the angular frequency of the light and τ_{δ} is the time that it takes to pass through the grating [21]. As the beam splitting gratings are assumed to be thin and losses are small, τ_{δ} can be regarded as unchanged for a specific grating. Thus, the angular frequency of the light will be the significant factor to affect the phase change. Based on the equation of $\omega=2\pi f= 2\pi(c/\lambda)$, where ω is the angular frequency, c the light speed in free space and λ is the light wavelength, thus the angular frequency is related to the light wavelength. In order words, for beam splitting gratings illuminated by different light wavelengths, different phases and different amplitudes will be produced. Thus, the beam splitting grating is always designed for a specific working wavelength. On the other hand, a function of the distance x in a direction tangent to the surface of the grating can be used to describe the phase shift of a one-dimensional grating. A phase function ϕ(x) describing the phase shift as light waves passes through the thin and lossless one-dimensional grating.

For example, if the grating is made out of a material of constant refractive index n and has a variable thickness h(x), the additional time (over the time if the grating were not there) that it takes to pass through the grating at x will be [67]:

$$\delta\tau(x) = \frac{h(x)(n-1)}{c} \quad (2\text{-}23)$$

And the phase shift will be given by

$$\phi(x) = \frac{h(x)\omega(n-1)}{c} = \frac{2\pi h(x)(n-1)}{\lambda} \quad (2\text{-}24)$$

where λ is the wavelength of the light in free space.

The theory of Fourier optics [15] shows that the amplitude of the kth diffracted beam will be proportional to the kth Fourier coefficient α_k of the transmission function $t(x)=e^{i\phi(x)}$ [5, 16,17]:

$$\alpha_k=\frac{1}{d}\int_{-d/2}^{d/2} t(x)e^{-ik(\frac{2\pi}{d})x}dx \qquad k=0, \pm1, \pm2, \ldots \tag{2-25}$$

where, for a lossless grating, the transmission function t(x) is given by

$$t(x)=e^{i\phi(x)} \tag{2-26}$$

in particular, the intensity I_k of the kth order is given by

$$I_k=|\alpha_k|^2 \tag{2-27}$$

The upper bound on k is related to the ratio d/λ, where d is the spacing of the grating and λ is the wavelength of the incoming light. The equation for the amplitude of different orders assumes that the illumination is uniform [21]. In addition, the periodic structures also can be generated by using a spatial light modulator when addressing desired computer generated holograms.

2.7.2.2 Parallel micro-processing using arbitary structures

Compared with periodic structures, arbitary structures are more flexible when they are employed in laser micro-processing as the position of the parallel spot can be customized as required. As with the periodic structures, the arbitary structures also can be generated by an SLM and Diffractive Optical Elements (DOEs). Laser surface ablation and internal structuring using an arbitary multi-beam pattern has been demonstrated by Y. Kuroiwa on a SiO_2 glass sample, as shown in Figure 2.40 [189]. In this technique, a SiO_2 glass with 6.35mm thickness and effective area of 8mmx8mm has been made for a 4 phase level DOE.

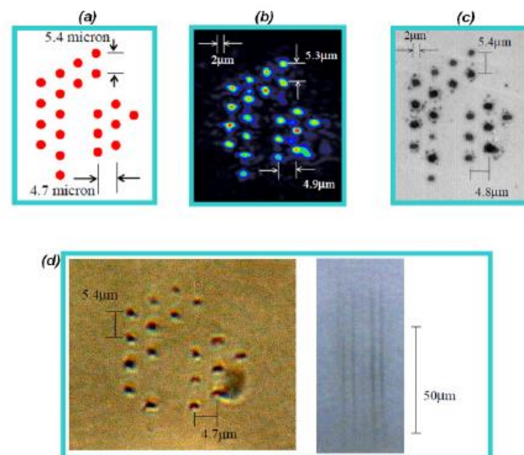

Figure 2. 40 The results of arbitrary multi-beam pattern generated by a DOE. (a) The designed pattern, (b) The generated beam profile observed on a CCD camera, (c) observed machined pattern on focal plane. (d) laser glass processing using the arbitrary multi-beam. Observed by optical microscopy, left: top view, right: side view [189].

In addition, with femtosecond laser pulses (τp ≈ 120fs, λ = 790nm), M. Silvennoinen et al [183] successfully demonstrated surface material ablation on a silicon sample using a phase-only SLM generated arbitrary multi-beam pattern with different intensity, as shown in Figure 2.41. This technique enables each beam intensity to be controlled individually.

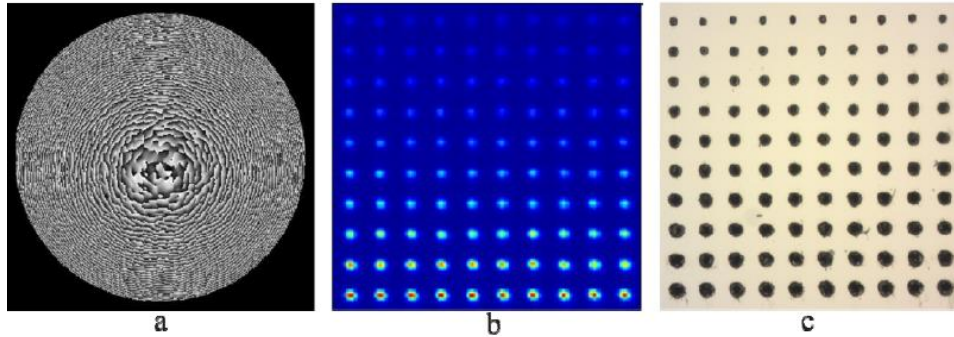

Figure 2. 41 Example images for individual intensity control. (a)Computer generated hologram (b)Producing intensity pattern which is measured with a beam profiler (c) machined pattern with period of 32μm on silicon wafer [183].

Both beam shaping elements Spatial Light Modulator (SLM) and diffractive optical elements have been widely employed to modulate picosecond and femtosesond laser pulses and demonstrated material processing capable of parallel, arbitrary, and variable patterning [190]. However, the diffraction theory [191, 192] shows that the generated original beam patterns always has a zero-order diffractive spot, which has higher intensity than other diffractive orders. For the requirement of laser processing with parallel spots, the diffractive 0th order is better to eliminate. There are some commonly used methods to eliminate diffractive 0th order [22]:

- Zero-order reduction by special diffractive design
  Diffractive optics and computer generated holograms (CGHs) can be designed using Iterative Fourier Transform Algorithm to shift the diffractive zero-order.
- Lateral shifting of zero-order – adding a diffractive prism or diffractive prism related CGHs
  This method is also going to shift the zero-order from the diffractive pattern by adding a diffractive prism or diffractive prism liked CGHs.
- Focal shifting of zero-order – adding a diffractive (Fresnel) lens.
  The Fresnel lens can be used to generate laser spot at different focal position according to its different lens size, so the focal point can be defocused. However, the parameters of an optical lens are fixed when it is fabricated, so the Fresnel lens holograms are widely used in spatial light modulator (SLM), because the parameters of Fresnel lens holograms are easy to change.
- Mechanical mask to block the zero-order at an intermediate image plane
  An aperture is required in a virtual intermediate focal plane that physically blocks the diffractive zero-order.

2.7.3 Algorithms for calculating computer generated holograms (CGHs)

The aim of a CGH is to modulate the input beam spatially in amplitude and phase.

The modulated phase and intensity for a complex optical field U can be expressed below:

$$U = Aexp[(i(\varphi + \varphi_0)] \quad (2\text{-}28)$$

Where A is the amplitude of the modulated optical field, φ is the phase of initial optical field, φ_0 is the phase of a CGH.

In order to get a modulated laser beam, the initial laser beam should pass through a hologram and be focused by a Fourier optic. Thus, the modulated laser beam with complex phase on focal plane can be related with the phase of the hologram by:

$$U_m = FT(U_h) \quad (2\text{-}29)$$

where FT represent Fourier transformation, U_h is the optical field of a hologram which contains phase function, U_h=exp(iφ_0). In other words, even if a Gaussian laser beam passes through a Fourier optic, without the hologram, the modulated laser beam is still a Gaussian mode. Because of the Fourier transformation of a Gaussian mode is still a Gaussian. Methods of hologram phase and amplitude redistribution can be achieved by many algorithms, like Iterative Gerchberg-Saxton (GS)algorithm [193], lens and grating[194].

2.7.3.1 Iterative Gerchberg-Saxton(GS) algorithm

The GS algorithm is widely used to generate CGHs for laser micro machining as it has good accuracy and fast calculation speed. The mechanism of GS algorithm can be seen in Figure 2.42 below:

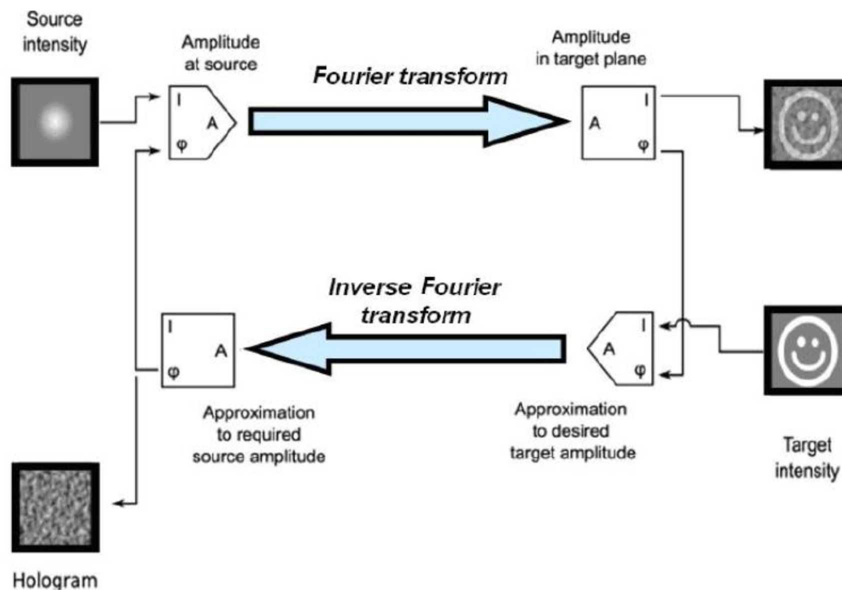

Figure 2. 42 The mechanism of GS algorism for CGHs generation [25].

As the GS algorithm has been set a target to iterate towards, each generated phase and amplitude will be compared with the target phase and amplitude for next CGH calculation, until the desired target has been achieved. The target optical field can be expressed:

$$U_t = U_m = FT(U_h) \tag{2-30}$$

Its intensity can be expressed as $I_t = [FT(U_h)]^2$. The aim of GS algorithm is to find the CGH phase distribution $\varphi_h(x_0, y_0)$ satisfied with $[FT(\exp(\varphi_h))]^2 = I_t$. At the beginning of the GS algorithm, a random phase φ_r will be employed to the first iteration. Thus, the initial phase can be expressed as $\varphi_1 = \exp(i\varphi_r)$. For following subsequent iteration, for k-th iteration, optical field can be expressed as:

$$U_s = FT(U_k) \tag{2-31}$$

Then, the light field in the image space is modified by keeping the phase but replacing the intensity with the target intensity I_t:

$$\varphi_k = \arg(U_s) \tag{2-32}$$

$$U_s' = \sqrt{I_t}\exp(i\varphi_k) \tag{2-33}$$

The resulting light field is then propagated back to the hologram plane by taking its inverse Fourier transform:

$$\varphi_{s,k+1} = FT^{-1}(U_s') \tag{2-34}$$

The iteration is finally completed by again keeping the phase but replacing the intensity with uniform constant intensity:

$$\varphi_{k+1} = \arg(U_{s,k+1}) \tag{2-35}$$

$$U_{s,k+1}' = \exp(i\varphi_{k+1}) \tag{2-36}$$

The GS algorithm has also been applied for two-dimensional intensity distributions and modulating intensity distribution in several planes simultaneously. The holograms generated with this method are grey level phase holograms, which means the hologram is going to modulate the input laser phase with a range from 0 to 2π. The iterative algorithms are widely used for complex CGHs generation. On the other hand, much simpler algorithms are used for CGHs generation with specific requirements.

More recently, Dmitrity Mikhaylov et al [195] demonstrated a method of high accuracy laser beam splitting with machine learning algorithms. High uniformity and accuracy of the generated multiple spots has been presented. The control of laser spots with high uniformity in a beam array has potential applications in multi-layer thin film processing and security pattern marking.

2.7.3.2 Non-Iterative algorithm

As an alternative to the iterative GS algorithm, there are many simpler algorithms that can be used to generate a hologram for multiple beam generation. Typically, for the Dammann grating (DG) hologram generation. Dammann grating which has the phase ranges 0 and π. As shown in Figure 2.43. When light illuminates a Dammann grating with normal incident, diffractive orders (1st order, -1st order, 2nd order, -2nd order) will be generated with different angles (seen in Figure 2.43(a)), based on the equation below:

$$\sin\theta = m\lambda/\wedge \tag{2-37}$$

where $\wedge$ is the pitch of the grating. Based on this theory, the structures of a Dammann grating can be presented on SLM with a binary Dammann grating hologram, which is shown in Figure 2.43 (b). However, as the SLM is a digital device, its cannot to engroove lines. Then, the height of the pillars on the Dammann grating DOE can be expressed as white and black columns on a Dammann grating CGH. The white and black columns are consisted of a "grating unit cell". The hologram can be achieved by repeating the periodic structures with MATLAB codes, in which the complex Fourier transformation for CGH generation can be avoided.

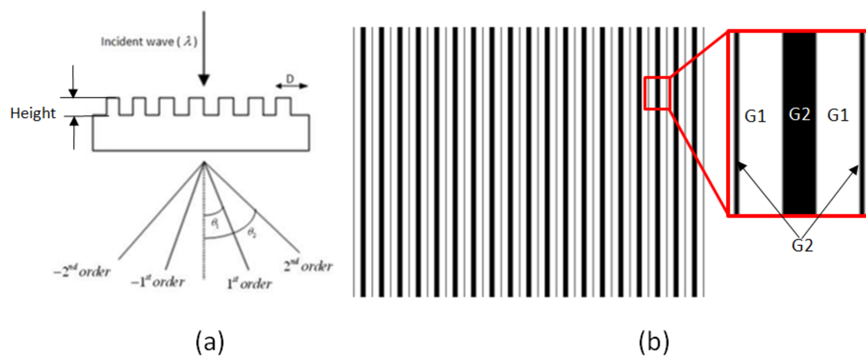

Figure 2.43 Diffractive schematic for (a) Dammann grating DOE [196]. D indicates the structure period (b) Dammann grating Computer generated hologram (CGH). Red rectangular represents the Grating Unit Cell, G1 is the area with phase equals to 0 and G2 is the area with phase equals to π.

The phase at the Dammann grating hologram required to produce a laterial shift $(\Delta x, \Delta y)$ with the position of the diffractive spots to form a spot array:

$$\varphi_{Dam}(x_d, y_d) = \alpha_1(\Delta x_1 x_d + \Delta y_1 y_d) + \alpha_2(\Delta x_2 x_d + \Delta y_2 y_d) + \cdots + \alpha_n(\Delta x_n x_d + \Delta y_n y_d) \tag{2-41}$$

Science Dammann et al put forward the binary-phase Dammann grating for multiple beam generation, more and more researchers also have developed the DG hologram for 3D multiple generation with non-iterative algorithm[197]. The diffraction efficiency of the CGH generated pattern with different algorithms also have been demonstrated for different diffraction efficiency requirement. In this thesis, a method of Dammann grating CGH generation using a self-programmed MATLAB code for complex applications has been demonstrated.

2.8 State of the Art

By reviewing the polarization control and beam shaping methods for high throughput ultrafast processing, there is still a gap in understanding of laser processing combined with beam shaping and polarization control. Laser material processing with different polarization states commonly use circular shaped, Gaussian distributed single beams. Thus, a combination of beam shaping with polarization control to generate various shaped polarized beams and multiple complex polarized beams could be useful for laser material processing efficiency improvements. In addition, the applied CGH for laser modulation is based on programming algorithms, which is normally complex and time-consuming. Thus, simple beam shaping methods without complex algorithm calculation could be useful. In this thesis, novel dynamic control of complex polarization and various shapes with SLMs are proposed to fill this gap in knowledge and understanding. Moreover, a simpler CGH generation method of laser multiple spot formation in a MATLAB environment is also proposed.

Chapter 3

Experimental Equipment and Techniques

3.1 Introduction

This is a chapter of reviewing the equipment and techniques for current research, including two picosecond pulsed laser systems, a SPI fibre laser system, three Spatial Light Modulators (SLMs), and a motion system with scanning galvanometers. The output test of the SLMs is introduced in this chapter. The method of synchronization of SLM with the laser system and motion system also is introduced in this chapter.

3.2 Laser systems

3.2.1 High-Q 10ps laser system

The mainly used laser source in this work was a custom made seeded Nd:VAN regenerative amplifier laser (Model: IC-355-800, High-Q) features 10 picosecond pulse duration and three optical wavelengths output : 1064nm, 532nm and 355nm. This laser system is able operating four different repetition rates 5k, 10k, 20k, 50kHz to a maximum output power of 2 Watts (pulse energy $E_p \sim 0.1mJ$) at the 1064nm wavelength and repetition rate of 20kHz. The High-Q picosecond laser is principally consist of three parts: laser head, laser controller with power unit and closed circuit water-air cooling system, as shown in Figure 3.1.

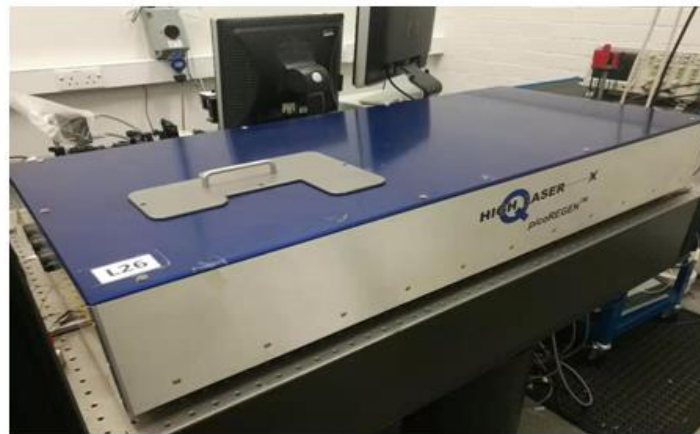

Figure 3. 1 Three mainly parts of the High-Q laser system: (top) laser head, (bottom left) laser controller with power unit and (bottom right) water-air cooling system.

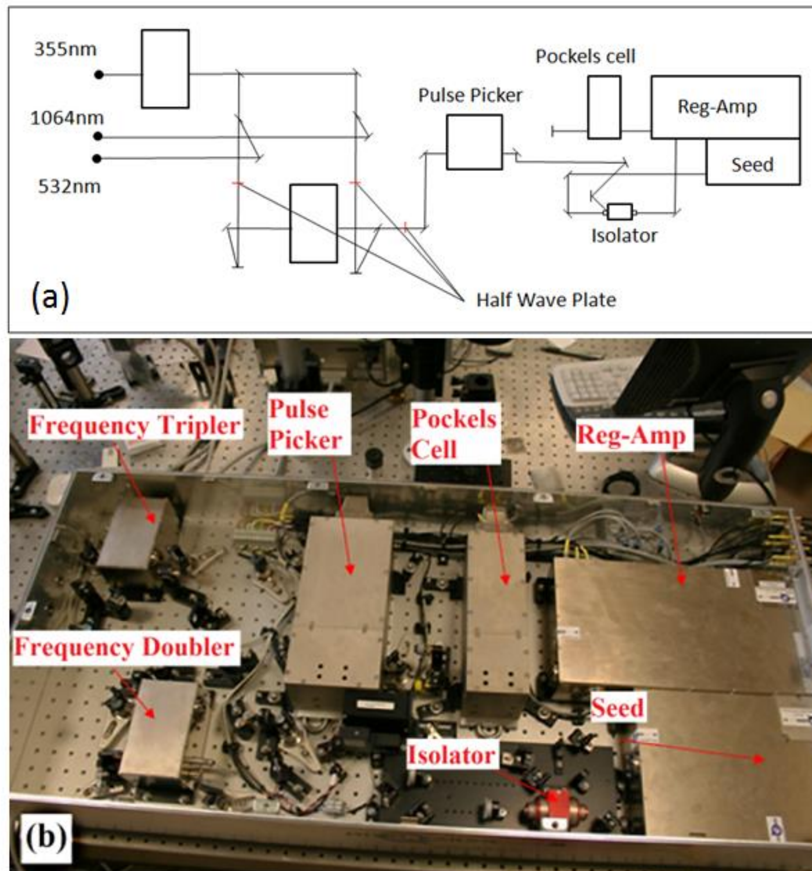

Figure 3. 2 (a) Schematic of optical setup inside of the High-Q laser head and (b) the corresponding image of laser head internals.

The details of optical set up of the High-Q laser head is shown in Figure 3.2. A low power seed beam at MHz level repetition is generated by a picosecond mode-locked seed oscillator. Through a Faraday isolator, all pulses are propagating to the regenerative amplifier for amplification. Due to the pulse picker, only certain pulses are trapped and amplified with high voltage (HV) pulses applied to the Pockel's cell. By adjusting the relevant polarizer in the Pockel's cell, the fundamental output wavelength of 1064nm can be frequency-doubled and tripled for 532nm or 355nm output wavelength generation.

Figure 3.3 presents an optical setup for polarization control. After the laser head, a half wave plate (HWP) and a polarizer has been used as an attenuator with polarization control. A beam expander has been used to magnify the laser spot to 3 times bigger. Mirrors were used to change to laser propagation to the spatial light modulator (SLM). Lens1 and Lens2 is a 4f system. A half wave plate (HWP) and a S-waveplate (SWP) between the Lens1 and SLM were used for particular study which will be discussed in chapter 6. For different studies, the HWP and SWP will be taken off or replaced. A periscope was used to change the laser propagation to a scanning galvanometer.

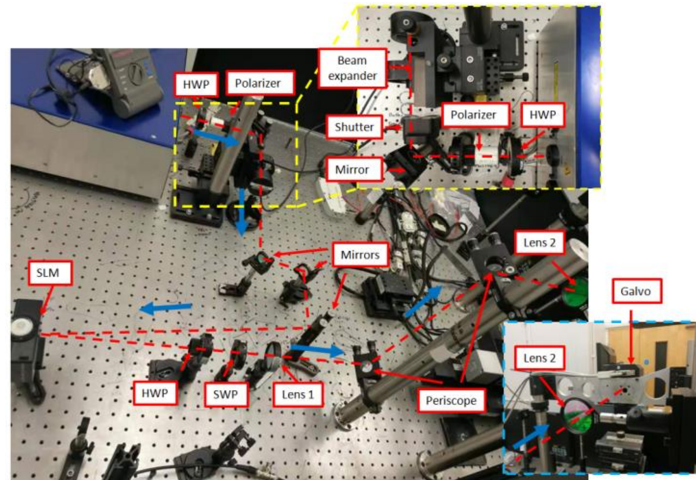

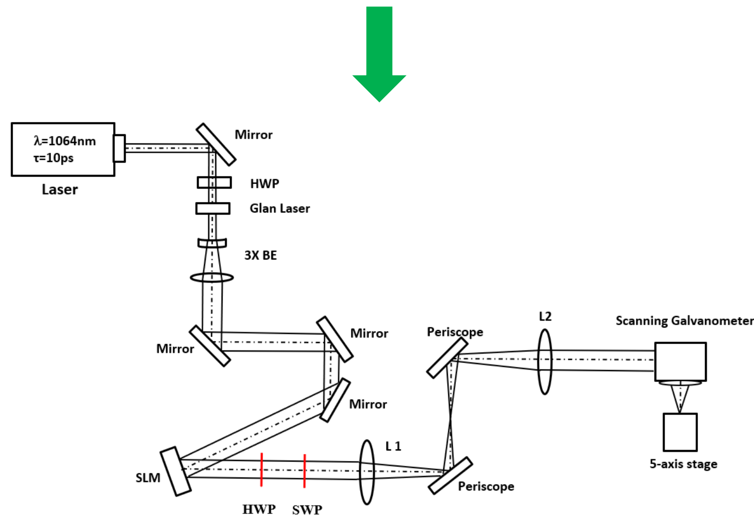

Figure 3. 3 A particular optical setup for laser polarization control. Blue arrows indicate the laser propagation direction.

The beam quality M^2 of the emitted laser beam from the High-Q picosecond laser system approximately to 1.3. In this research, the High-Q laser was configured to 1064nm wavelength output. Figure 3.4 shows the 1064nm output measured using a Thorlabs BC106 beam profiler, which was found to be approximately Gaussian distribution.

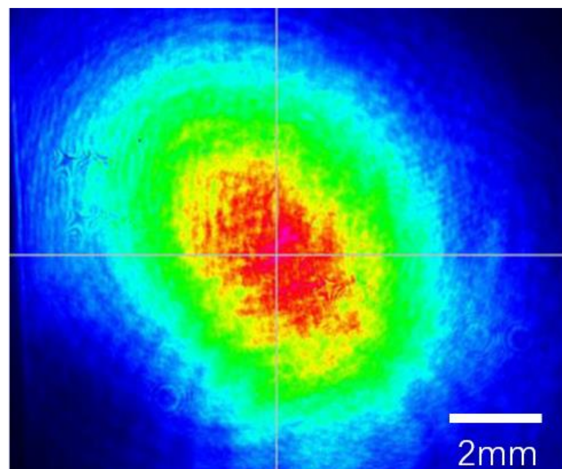

Figure 3. 4 Original beam profile measured using a CCD beam profiler of the High-Q laser system.

Figure 3.5 shows the interface of the control software. By clicking mouse, most of the laser parameters can be changed easily, e.g. switching the pulse repetition rate, varying the output and so on.

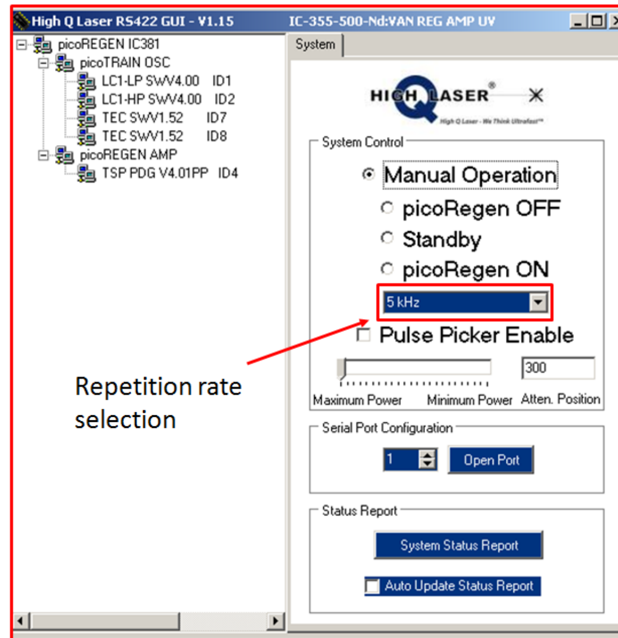

Figure 3. 5 Interface of High-Q laser system control software

3.2.2 Edgewave 10ps laser

A second higher power 10ps, InnoSlab laser (Edgewave Model PX400-3-GH, 10ps at 1064nm) was used in this work to test phase/temperature response (P>200W) of a liquid cooled LCOS spatial light modulator (SLM). This laser is different from the High-Q picosecond pulsed laser, the gain medium of a InnoSlab laser is formed of a slab which has a much wider aspect ratio compared to other solid state lasers. The laser output is generated by a multi-pass setup as shown in Figure.3.6.

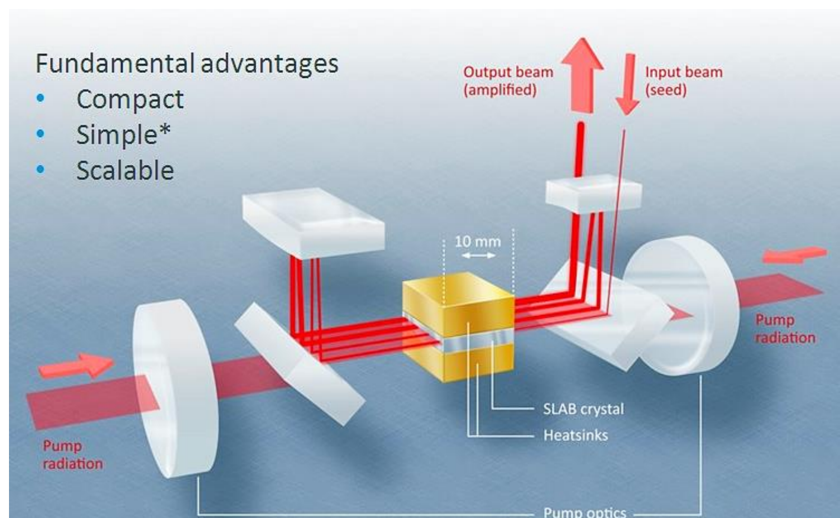

Figure 3. 6 The setup for an Innoslab laser [198]

The typical output beam intensity in near field is a Gaussian distributed rectangle shape. Then, by using a spatial filter or a telescope, the output beam can be symmetrized to a circle or an elliptical shape (M^2<1.5).

A spatial filter (aperture size =10mm) has been applied in this system to symmetry the beam shape. This laser operated with two trigger modes: internal trigger (low repetition rate, low average power output) and external trigger (high repetition rate, high average power output), the output maximum average power can is 300W at 2MHz repetition rate. The partial irradiation power respect to the system parameter setup is listed in Table 3.1.

Table 3. 1 Output power (Watts) of Edgewave laser with internal/external trigger.

	Int.Trig (kHz)			Ext.Trig (kHz)	
Freq.	10	20	30	404	1000
30%	2.1	4.1	6	22.6	44.3
40%	3.1	5.4	8	33	53.8
50%	4.6	9.4	13.4	61	100
60%	6.3	11.2	18.1	84.9	132
70%	7.2	14.4	21.1	96.4	163
80%	8.2	16.5	24.4	110	182
90%	8.6	17.8	26.6	117	194
100%	9.1	18.2	27.5	120	200

The Edgewave picosecond laser is mainly consists of three parts: laser head, laser controller with power unit and closed circuit water-air cooling system, as shown in Figure 3.7.

Figure 3. 7 Experimental device (a) A Edgewave laser indicated with a red rectangle (b) SCANLAB intelliSCAN 14 scan head with a F-theta lens, loaned from the University of Liverpool (c) SLM chiller (d) Hamamatsu X13138-03 SLM.

The laser mode was an ellipse with dimensions of ~12mm x 7mm (before the telescope) with horizontal major axis, where eccentricity (e) is ~1.7.

3.2.3 SPI fibre laser system

A SPI fibre laser (SPI G4 HS-L 20W, M^2 ~1.83) was used in this work to generate microstructures on the material surface for wettability modification. This laser system consists of a SPI fibre laser, a scanning

galvanometer with focal length f=160mm (Nutfield XLR-8-10), and a three-axis working stage (Thorlabs L490MZ/M). The laser setup is demonstrated in Figure 3.8.

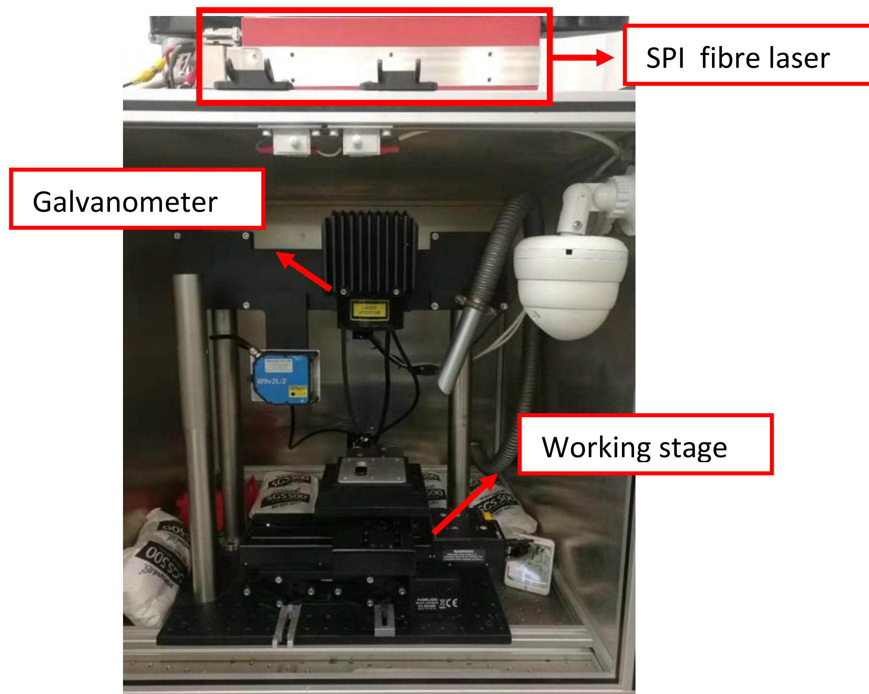

Figure 3. 8 Experimental setup for a SPI fibre laser system

With operating two modes of the SPI laser: nanosecond pulse duration and continuous wave (CW), the maximum average can be reached to 20W at 1064nm wavelength. The pulse duration ranges from 10ns to 220ns with repetition rate 1-1000kHz. The gain medium of a fibre laser is a glass fibre doped with rare earth ions. The SPI laser based on a PulseTune function which enables flexible control of pulse width and peak power. The SPI fibre laser with nanosecond pulses is mainly used to study the wettability behaviour by generating microstructures and subsequent nano scale structures on the material surface. The details of the surface wettability modification is discussed in chapter 6.

3.3 Spatial light modulators and diffractive optical element

Three Hamamatsu SLMs have been employed in current research with models X10468-03 (1064 nm, resolution 800x600 pixels), X13138-03 (1064nm, resolution 800x600 pixels) and X13138-5785(1064nm&532nm, resolution 1280x1024 pixels). For first two SLMs, both of them are electrically addressed reflective type PAL-SLMs with appropriate high reflective dielectric coatings. For X13138-5785 SLM, which has double high reflective dielectric coatings for 532nm and 1064nm, two wavelengths. The light utilization efficiency is very high for these PAL-SLMs, >90% [146]. Details of the three SLMs have been demonstrated in Table 3.2.

Table 3. 2 Structures and optical characters of the SLMs used in this current research

Model	Hamamatsu X10468-03	Hamamatsu X13138-03	Hamamatsu X13138-5785
LC Type	Parallel aligned nematic		
Number of input level	256 for 8-bit		
Resolution (pixels)	SVGA(800x600)	SVGA(800x600)	SVGA(1280X1024)
Pixel pitch (µm)	20	12.5	12.5
Effective area (mm^2)	15.8 x 12	15.9 x 12.8	15.9 x 12.8
Fill factor (%)	98	96	96
Mirror coating	Dielectric		
Light utilization efficiency(%)	97	97	96(532nm) 97(1064nm)
Readout wavelength (nm)	1050±50	1050±50	532±1 1064±5
Cooling	Passive	Active water	Active water

The ability of phase modulation of a Hamamatsu SLM is based on the liquid crystal direction that is controlled by applied corresponding voltage on the SLM. A bitmap CGH (800× 600 resolution or 1280x1024 resolution) can be sent to the SLM controller with a normal PC by connecting the digital visual interface (DVI). Then, the controller converts the received grey level (8-bit value) on each pixel to corresponding voltage, which precisely drives the corresponding liquid crystal (pixel) to a desired phase angle, inducing a phase delay to the light passed through it. Thus, the applied CGH on a PC will be addressed and displayed on the SLM display screen with desired corresponding phase angle of liquid crystal. Figure 3.9 shows the phase modulation level with input signal level of X10468 and X13138 series SLMs.

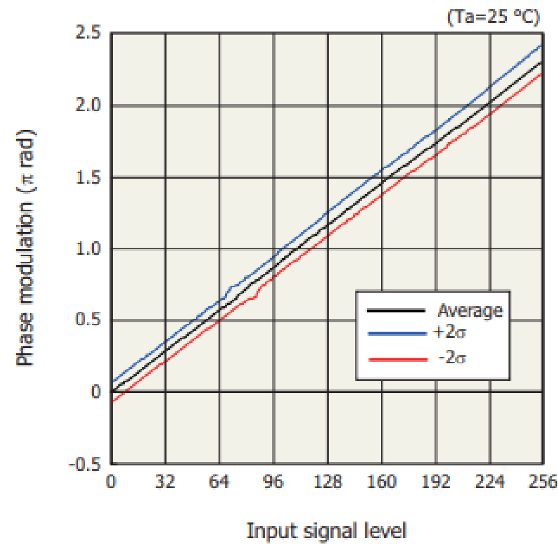

Figure 3. 9 Corresponding phase modulation with input grey level for X10468/X13138 series Hamamatsu SLMs [199].

Since the material of a SLM will absorbing power when a laser illuminating the SLM, the power handling of a SLM has been tested for next high average power affordable SLM generation. In addition, the power handling capability of Hamamatsu SLMs makes them outstanding since they have a ceramic cooling plate connected to the chip. Power handling tests of Hamamatsu SLMs were previously conducted in-house for both devices and found to easily handle 60W average powers involved with additional cooling [31]. In this research, power handling of a cooling SLM has been further tested.

3.3.1 Output test of X10468-03 SLM

In this research, the output of the X10468-03 SLM has been tested with a High-Q picosecond laser with repetition rate f=10kHz, power=1W. The optical setup for SLM testing is shown in Figure 3.10. This SLM has a single dielectric coating for 1064nm and is passively cooled with only a ceramic heat sink.

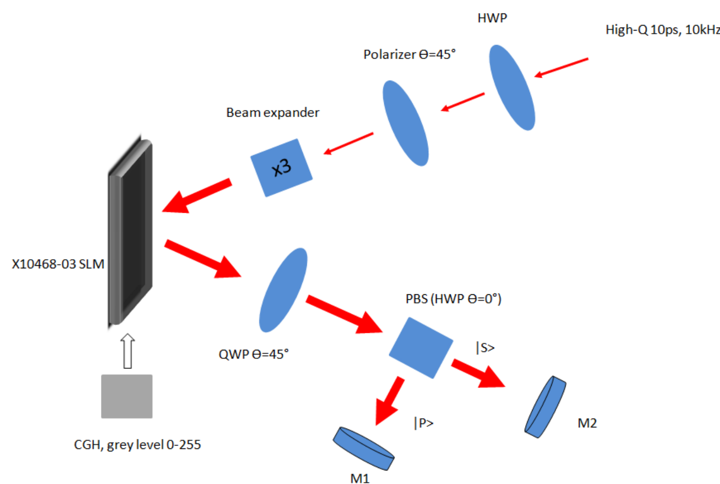

Figure 3. 10 Experimental setup for X10468 SLM output test. A beam expander was used to enlarge beam size.

As shown in Figure 3.10, the half wave plate (HWP) and a polarizer (Glan laser θ=45°) was used as an attenuator for laser output power adjustment. The polarization modulation properties of a SLM can be

described using a Jones matrix $\begin{pmatrix} e^{i\times\emptyset(x,y)} & 0 \\ 0 & 1 \end{pmatrix}$ by altering the polarization of the incident laser beam, where $e^{i\times\emptyset(x,y)}$ is the phase delay of an incident beam in horizontal (x) and vertical (y) direction. Therefore, the optical system can be described by Jones matrix $J(x,y)$=$\begin{pmatrix} 1 & 0 \\ 0 & 0 \end{pmatrix} \times \begin{pmatrix} \cos 2\theta & \sin 2\theta \\ \sin 2\theta & -\cos 2\theta \end{pmatrix} \times \frac{e^{i\pi/4}}{\sqrt{2}} \begin{pmatrix} 1 & -i \\ -i & 1 \end{pmatrix} \times \begin{pmatrix} e^{i\times\emptyset(x,y)} & 0 \\ 0 & 1 \end{pmatrix} \times \begin{pmatrix} \frac{1}{\sqrt{2}} \\ \frac{1}{\sqrt{2}} \end{pmatrix}$, here $\theta = 0°$ for the half wave plate. The output power from the attenuator was fixed at 1W with polarizer fast axis angle θ=45°. Then to a 3x beam expander and illuminated at X10468-03 SLM. Various grey level maps (grey level ranges from 0-255) has been applied on the SLM. The reflected beam from SLM was passed through a quarter wave plate (QWP, fast axis angle θ =45°). A polarization beam splitter (PBS, Thorlabs VBA05-1064) has been used to split the beam into s- and p- two directions. Power at M1 and M2 has been tested with a power meter (Coherent, Model LM-3 HTD). The tested results are demonstrated in Figure 3.11.

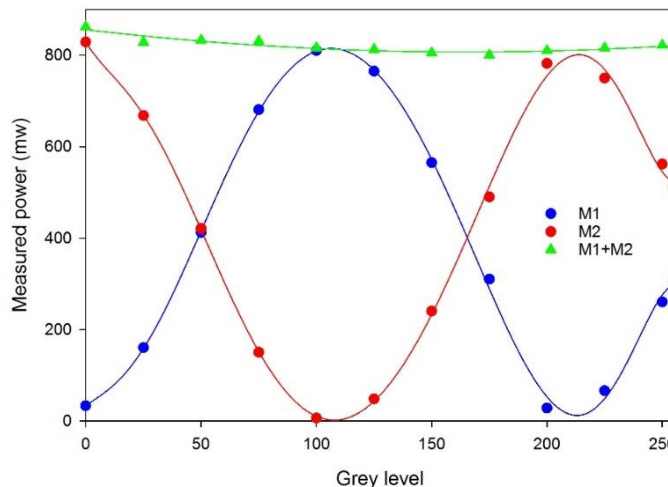

Figure 3. 11 Correspond measured power with input grey level applied on the SLM.

It can be seen that from Figure 3.10, the measured power with different grey level values were confirmed as a sine function. The phase modulation then can be reached at 2π for grey level 0-255. The measured results at M1 (p-state polarization, blue line) is $\frac{\pi}{2}$ delayed phase to s-state polarization (measured at M2) due to the s-state polarization is perpendicular to the p-state polarization. This SLM appear to perform well at this power level. No further higher power tests were performed on this SLM due to cooling restrictions.

3.3.2 Output test of X13138-5785 SLM

In this research, the output of the X13138-5785 SLM has been tested with a High-Q picosecond laser. This SLM has two high reflective dielectric coatings for 532nm and 1064nm and is actively water cooled via the ceramic heat sink. The optical setup for SLM testing is shown in Figure 3.12.

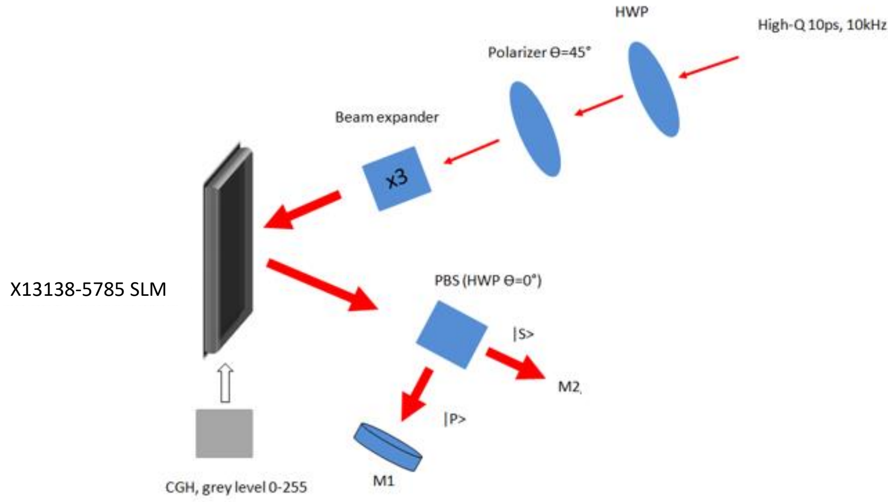

Figure 3. 12 Experimental setup for X13138-5785 SLM output test. A beam expander was used to enlarge beam size.

As shown in Figure 3.12, the half wave plate (HWP) and a polarizer (Glan laser, fast axis angle θ=45°) was used as an attenuator for laser output power adjustment. The output power from the attenuator was fixed at 1W with polarizer fast axis angle θ =45°. Next is a 3x beam expander then the X10468-03 SLM. Various grey level maps (grey level ranges from 0-255) were applied on the SLM. The reflected beam from SLM then passed through a polarization beam splitter (PBS) combined with a half wave plate (HWP). The polarization beam splitter (Thorlabs VBA05-1064) has been used to split the beam into s- and p-directions. For the output test, the s-polarization has been blocked and the power in p-polarization has then been measured at M1 by a power meter. Therefore, by describing all optical elements with Jones matrices, the theoretical achieved intensity output can be shown to be relative to the phase delay angle ($\emptyset(x, y)$). This can be expressed as in Figure 3.13.

Polarizer | Half wave plate | Hamamastu SLM | Laser 45 degree incident

$$J_{out}(x,y) = \begin{pmatrix} 1 & 0 \\ 0 & 0 \end{pmatrix} \times \begin{pmatrix} cos2\theta & sin2\theta \\ sin2\theta & -cos2\theta \end{pmatrix} \times \begin{pmatrix} e^{i\times\emptyset(x,y)} & 0 \\ 0 & 1 \end{pmatrix} \times \begin{pmatrix} \frac{1}{\sqrt{2}} \\ \frac{1}{\sqrt{2}} \end{pmatrix}$$

$$J_{out}(x,y) = \frac{1}{\sqrt{2}} \times \begin{pmatrix} cos2\theta e^{i\times\emptyset(x,y)} + sin2\theta \\ 0 \end{pmatrix}$$

$$\text{Intensity} = \frac{1}{2}\begin{pmatrix} cos2\theta e^{-i\times\emptyset(x,y)} + sin2\theta & 0 \end{pmatrix} \times \begin{pmatrix} cos2\theta e^{i\times\emptyset(x,y)} + sin2\theta \\ 0 \end{pmatrix}$$

$$= \frac{1}{2} + \frac{1}{2} sin4\theta cos\emptyset$$

Figure 3. 13 Calculations for theoretical intensity output with an SLM. All elements are expressed with corresponded Jones matrices and laser passes from right to left [186].

The calculated theoretical intensity is expressed as $\frac{1}{2} + \frac{1}{2}\sin 4\theta \cos \emptyset$, where θ is the fast axis angle of the half wave plate and $\emptyset$ is the input phase angle. Therefore, when θ is set to be $= \pm\frac{1}{8}\pi$, the output intensity

can be reached from minimum to maximum by adjusting the phase delay angle from 0 to $\frac{\pi}{2}$, then, the output intensity can be adjusted from 0 to maximum.

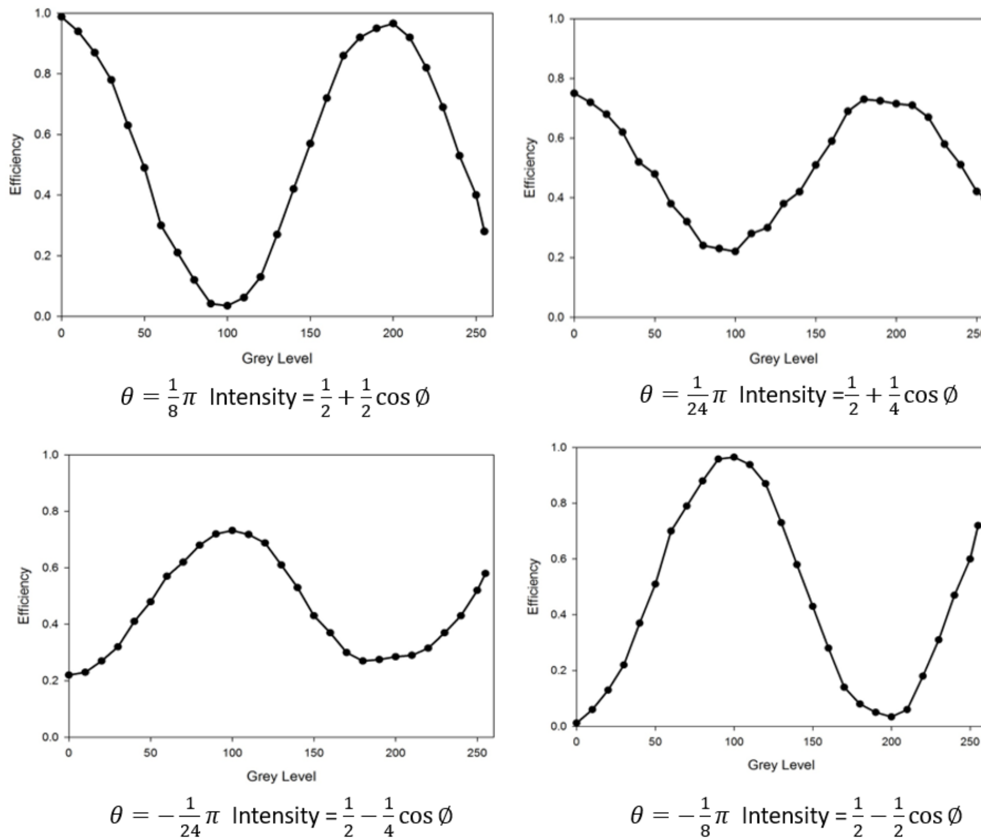

Figure 3. 14 Output intensity vs grey level with rotating half wave plate fast axis angle @ 0.2W,10kHz,10ps.

As the grey level applied on the SLM will change the phase delay of an output beam, the efficiency term in Figure 3.14 is the ratio of the input and output measured power. The trend line of efficiency at all fast axis angles can be fitted to a cosine function with different phases, which matches the equation below each image. Based on the theoretical intensity equation, the output intensity can be changed from 0 to maximum if the phase delay can be modulated from 0 to $\frac{\pi}{2}$. However, the experiment results showed that the phase delay of the SLM can be modulated to $\frac{5\pi}{4}$, which is greater than $\frac{\pi}{2}$, thus, the intensity modulate ability can be reached at maximum while the fast axis angle of a half wave plate is $\frac{\pi}{8}$ or $-\frac{\pi}{8}$. This means that the laser outputs can be adjusted by changing CGH grey levels on the SLM. Higher power performance of this dual wavelength device was found to be poor despite the active cooling. Further experimentation would be needed to confirm why this was the case.

3.3.3 Output test of X13138-03 SLM

The output performance of the X13138-03 SLM was then tested with a high average power picosecond laser (Edgewave, PX400-3-GH). The optical setup for SLM testing is shown in Figure 3.15. This SLM has only a single dielectric coating for 1064 and is actively water cooled via the ceramic heat sink.

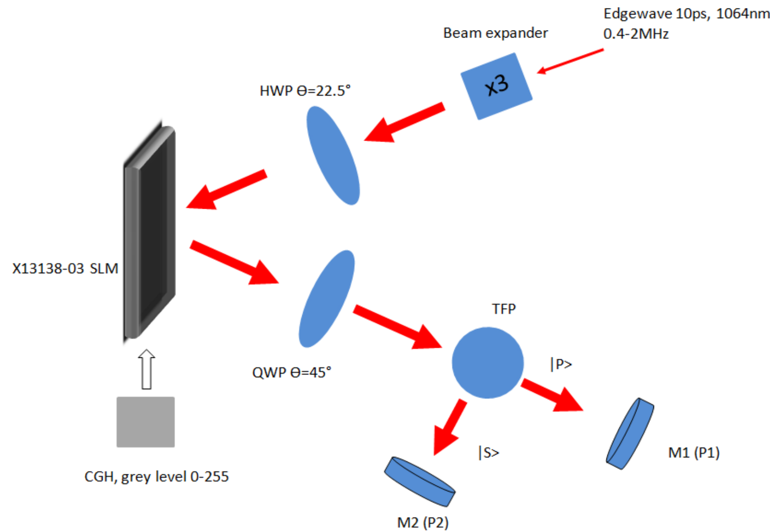

Figure 3. 15 Experimental setup for X13138-03 SLM output test. A beam expander was used to enlarge beam size.

As shown in Figure 3.15, the initial laser beam was expanded to 3 times and passed through a half wave plate (HWP, fast axis angle θ =22.5°) to illuminate the SLM. The reflected beam has elliptical polarization which was then passed through a quarter wave plate (QWP, fast axis angle θ =45°) to convert back to linear polarization. A thin film polarizer (TFP) was used to split the input beam into two different directions with s-polarization and p-polarization and the power was measured at M1 and M2. Hence, the optical system can be described with Jones matrix of optical elements $J(x,y) = \frac{e^{i\pi/4}}{\sqrt{2}}\begin{pmatrix} 1 & -i \\ -i & 1 \end{pmatrix} \times \begin{pmatrix} e^{i\times\emptyset(x,y)} & 0 \\ 0 & 1 \end{pmatrix} \times \begin{pmatrix} \frac{1}{\sqrt{2}} \\ \frac{1}{\sqrt{2}} \end{pmatrix}$. Different grey level maps (grey level ranges from 0-255) has been presented on the SLM. The tested results are demonstrated in Figure 3.16:

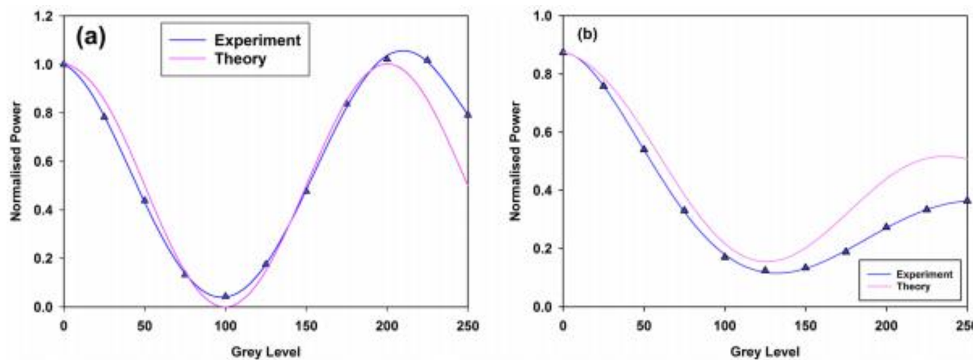

Figure 3. 16 The calculated phase response with incident average power at M2. (a) Experimental data at low average power, P=26.2W compared with a pure $\boldsymbol{cos^2\theta}$ function, (b) Experimental data at high average power, P=160W compared with a pure $\boldsymbol{cos^2\theta}$ function. [32].

It can be seen in Figure 3.16, the full phase modulation of the SLM is available with a low average power (Figure 3.16 (a)), but it did not recover a full phase modulation when the applied laser average power was increased to 160W (Figure 3.16 (b)).

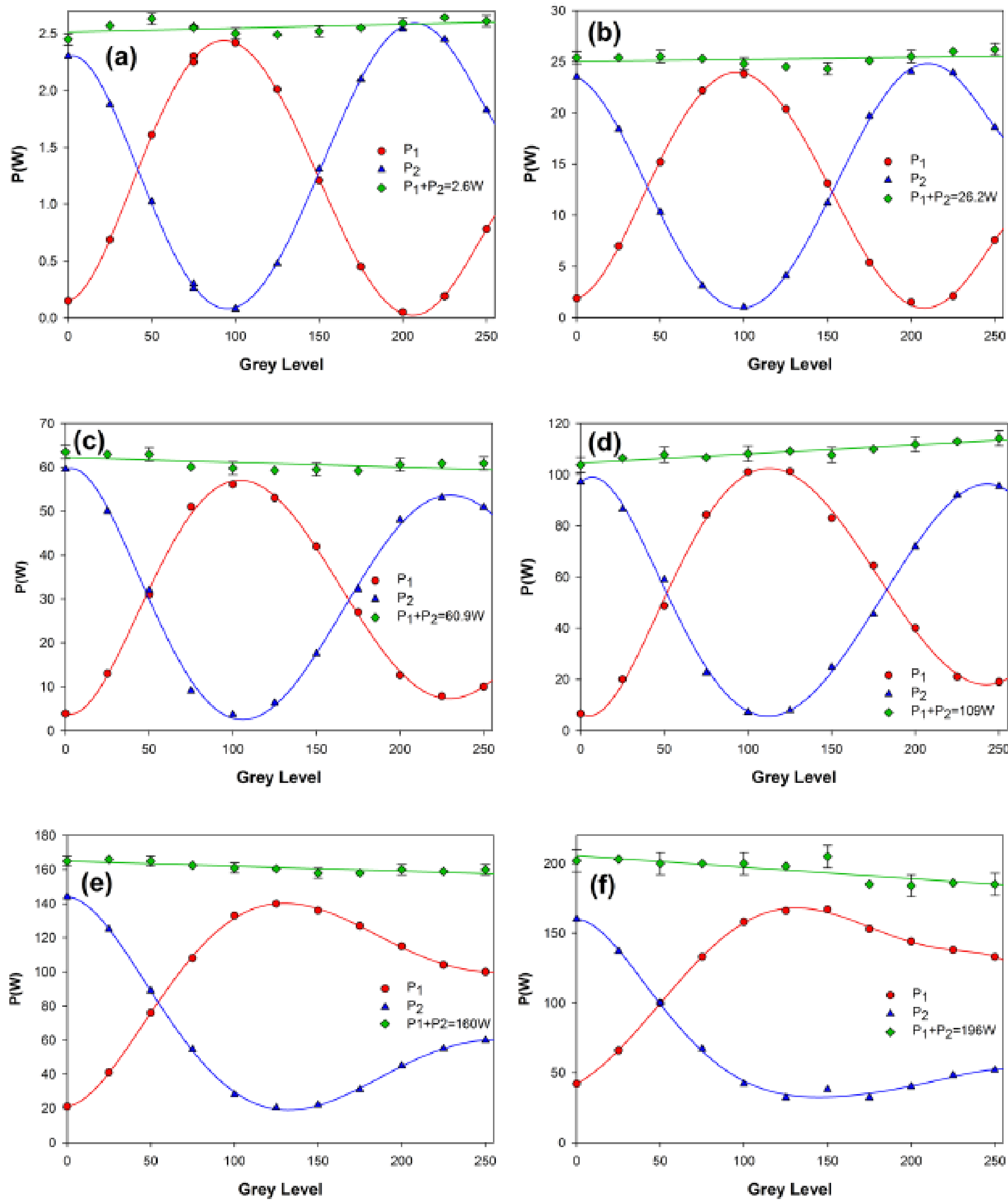

Figure 3. 17 Phase response of cooled X13138-03 SLM at M1(P1) and M2(P2). (a) P=2.6W, (b) P=26.2W, (c) P=60.9W, (d) P=109W, (e) P=160W, (f) P=190W. The phase response of the SLM only reaching over a π instead of 2π when applied power P≥ 160W [32].

It can be seen from Figure 3.16 and Figure 3.17, when the laser power on the SLM is over 160W, the SLM cannot produce a full phase modulation ability. This is likely due to the performance of the ceramic cooling plate on the SLM giving a reduced heat diffusion ability at high laser average power. The temperature response has been tested with a FLIR SC660 thermal camera. The temperature of the SLM was found to linearly increase when the applied power on the SLM is increasing. Measured results are demonstrated in Figure 3.18:

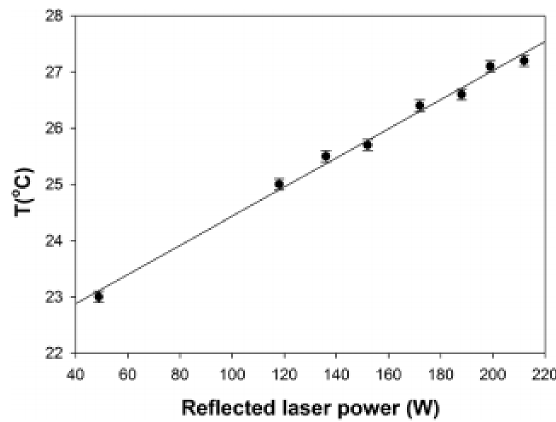

Figure 3. 18 Measured temperature rise with reflected laser power. Laser repetition f=1MHz. Temperature response with a gradient m=0.026° C W^{-1}. Errors represent 1σ and fit is least squares with high confidence, R=0.99, emissivity=0.73 [32].

It can be seen from Figure 3.18, the absorption of the SLM is constant throughout and the temperature on the SLM is linearly dependent in the power range (from 0W to 215W). The temperature response gradient of 0.026° C W^{-1} is also indicated that the SLM is cooled effectively.

3.3.4 S-waveplate

The polarization convertor used in this research is an S-waveplate (Altechna, RPC-1030-10-109, operation wavelength at 1030 ± 35nm,) which is a space variant polarization converter based on a nano-structured imprint inside a fused silica substrate. In this research, the S-waveplate converts incident linear to radial or azimuthal polarization. For optical configuration, the centre of the S-waveplate is aligned with the optic axis of the incident laser beam and then rotated to align the mark on the substrate parallel to the incident linear polarization orientation. In this case, the output will be radially polarized (fast axis angle θ =0°). If the incident linear polarization is perpendicular to the alignment mark, the output will be azimuthally polarized (fast axis angle θ =90°). The output loss test of an S-waveplate with an SLM (X10468-03) is shown in Figure 3.19:

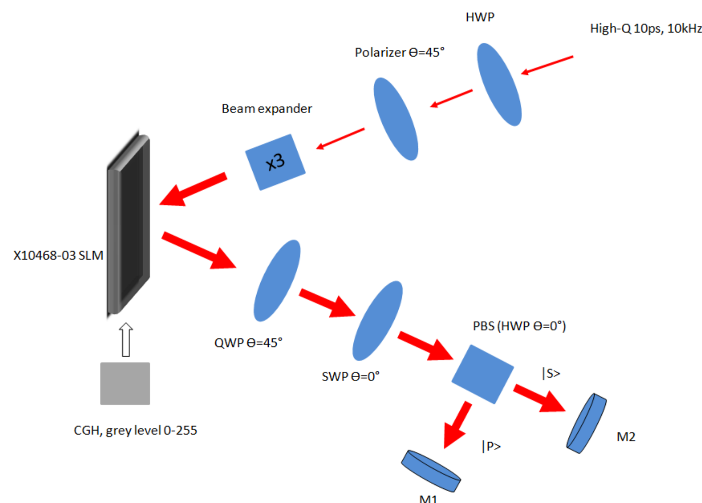

Figure 3. 19 Experimental setup for S-waveplate output loss test. A beam expander was used to enlarge beam size. Various grey level CGHs were applied on the SLM.

As shown in Figure 3.19, a half wave plate (HWP) and a polarizer (Glan laser, fast axis angle θ = 45°) was used as an attenuator for laser output power adjustment. The output power from the attenuator was fixed at 1W with polarizer fast axis angle θ = 45° to the fast axis of the SLM. The X10468-03 SLM was illuminated with a 3x beam spot (beam spot diameter is 8mm). Various grey level maps (grey level ranges from 0-255) have been applied on the SLM. The reflected beam from the SLM was passed through a quarter wave plate (QWP, θ = 45°). The S-waveplate (SWP, θ = 0°, radial polarization) was put after the quarter wave plate. A polarization beam splitter (PBS, Thorlabs VBA05-1064) has been used to split the beam into s- and p- states. The power at M1 and M2 has then been measured with a power meter. The output power after the SLM was measured before the S-waveplate (M1+M2). The results are shown in Figure 3.20:

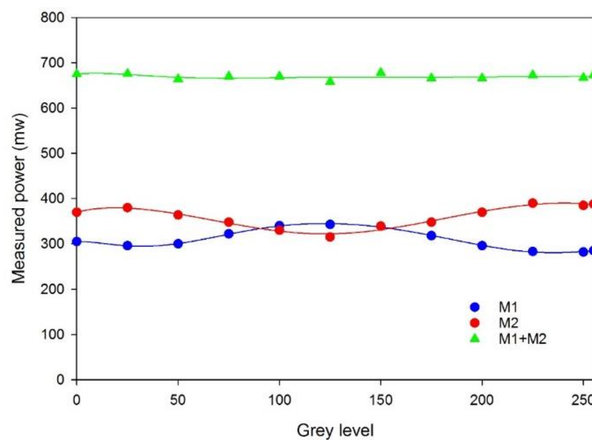

Figure 3. 20 Corresponding measured power with input grey level applied on the SLM @ 1W, 10ps, 10kHz.

It can be seen from Figure 3.20, the phase modulation ability of the SLM is still 2π. However, the measured power at M1 and M2 are closed to each other as the polarization after the S-waveplate is an inhomogeneous polarization which contains different electric field directions in a beam spot. The S-waveplate will cause approximately 15% energy losses. The polarization purity of the S-waveplate was measured using an additional half-wave plate and a polarizer analyser. Details of measured results are shown in Figure 3.21:

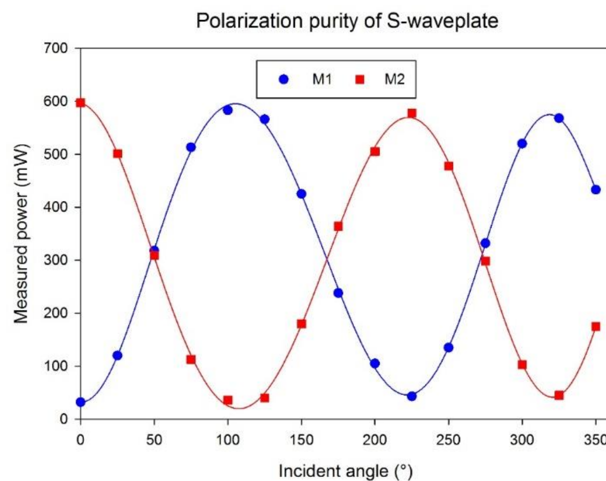

Figure 3. 21 Polarization purity measurement of CV beams by rotating a half wave plate from 0° to 360°.

It can be seen in Figure 3.21, that adjusting the half wave plate with an angle from 0° to 360°, the measured output power at M1 and M2 gives regular changes which are following a sine function. Based on the polarization purity equation $P_{purity} = \frac{Power_{max} - Power_{min}}{Power_{max} + Power_{min}}$, the polarization purity after an S-waveplate was measured to be ~ 88%. This shown that the output radial/azimuthal polarization has less power losses since the beam losses will be caused by a poor polarization due to parasitic light and heating [200].

3.4 Scanning equipment and multi-axis motion control system

3.4.1 Scanning galvanometer

3.4.1.1 High-Q laser system scan head

For manufacturing using the High-Q picosecond laser system, a Nutfield XLR-8-10 with a F-theta lens (f=100mm, Linos) has been employed for laser processing on a sample. The module consists of 2 galvanometer scanner (X and Y), two mirrors, two servo-amplifiers, and communication electronics. Figure 3.22 shows the setup of the scanning galvanometer. In High-Q laser system, the Nutfield XLR8-10 scanning galvanometer can be controlled by a Real Time Control (RTC) card (SCANLAB RTC4 card) combined with a graphical interface software, Lanmark-Winlase Pro. With the high accuracy of motion (micrometer level) and high scanning speed (up to 10m/s) of the galvanometer provided, laser precise processing is achievable.

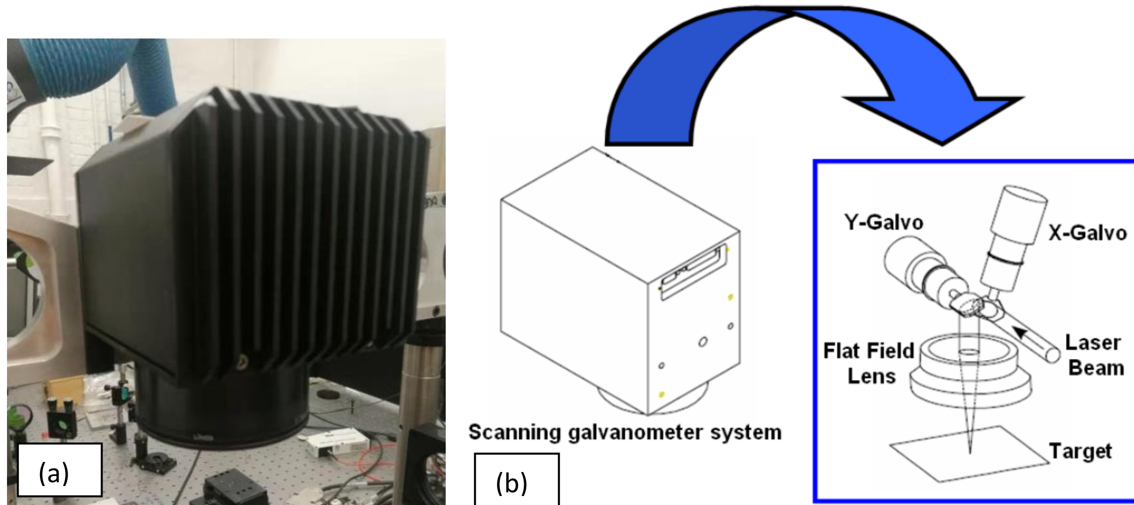

Figure 3. 22 (a) a scanning galvanometer system Nutfield XLR-8-10; (b)Structures of a scanning galvanometer system.

Since the two dielectric turning mirrors attached on the X-galvanometer and Y-galvanometer has highly synchronized under servo-controlled, the laser can be perpendicular directed to the specific locations on the target sample without edge effects via the F-theta lens. The motion of two synchronized turning mirrors is provided the flat field scanning area in a range of 60mm x 60mm.

3.4.1.2 Edgewave laser system scan head

For manufacturing using the Edgewave laser system, a SCANLAB intelliSCAN 14 with a F-theta lens (f=254mm, Thorlabs) has been employed for laser processing on a sample. The module also consists of 2 galvanometer scanner (X and Y), two mirrors, two servo-amplifiers, and communication electronics. The SCANLAB intelliSCAN 14 used in this work also can be controlled by a Real Time Control (RTC) card (SCANLAB RTC5 card) combined with a graphical interface software, SCAPS SAMLight. Same as the scanning galvanometer in the High-Q laser system, the high accuracy of motion (micrometre level) and high marking speed (up to 2m/s) of the galvanometer also provided for laser precise processing. The motion of two synchronized turning mirrors is provided the scanning area in a range of 95mm x 95mm.

3.4.2 Motion control system and control software

The key motion control system used in this research was an Aerotech multi-axis motion control system, as shown in Figure 3.23 (a). A five-axis motion control system (x, y, z three dimensional movement and u, v two tilting angles) with an Aerotech A3200 controller has been employed on High-Q picosecond laser system under the scan head for part indexing. A3200 uses Motion Composer to create motion trajectories. A resolution of 0.5μm in all directions. The working area ranges from 100 x 100mm in X, Y axis and 15mm in the Z direction. The maximum speed can be tuned to 230mm/s for X,Y direction and 50mm/s for Z direction.

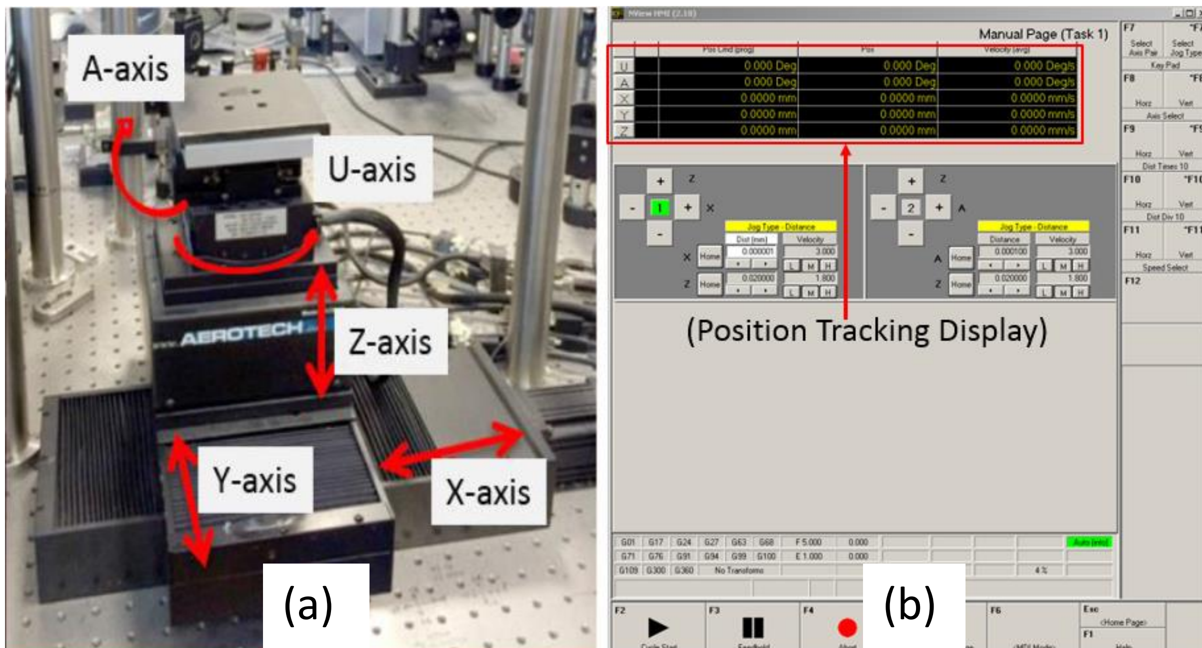

Figure 3. 23 Setup of 5 axis stage (a) The stage with X, Y, Z, U, A, five axis (b) interface of the stage control software.

The CNC stage is controlled by an Npaq driver and Nview GUI. Commands can be loaded to the CNC via the control software interface, which is shown in Figure 3.25 (b). This is allows for all X, Y, Z, U, A directions moving at the same time for a specific requirement. Furthermore, it is possible to define X, Y,

Z values for the traverse speed and vector speed, acceleration and deceleration. For this research, the Z axis was used to define the focal plane for processing.

3.5 Sychronization of ultrafast laser system

Studies of dynamic control of polarization and beam shapes for ultrashort laser processing is the focus of this current research. Thus, it is necessary to synchronize the SLM and the scanning galvanometer system. A method of synchronization is presented below:

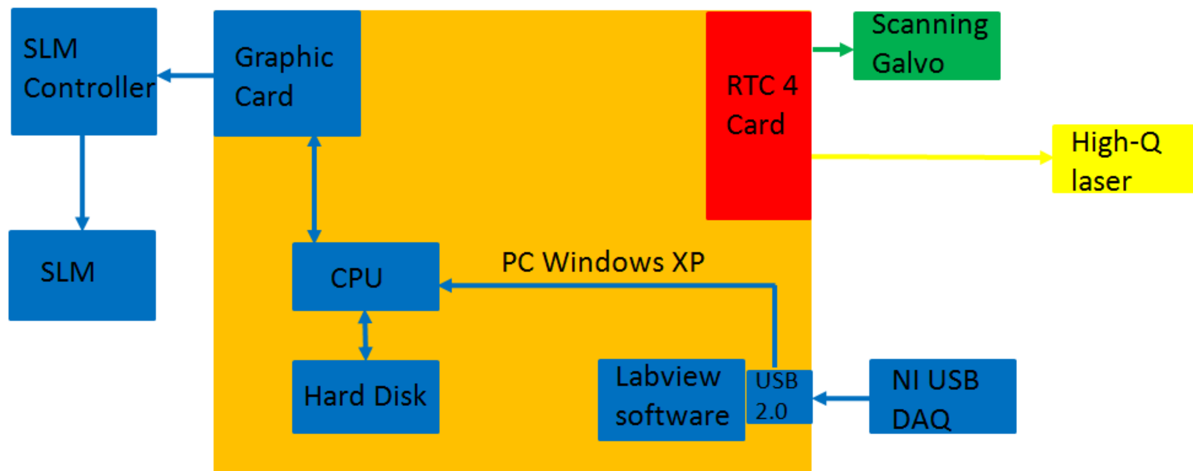

Figure 3. 23 a schematic of synchronization system for a laser and a computer.

Figure 3.24 shows the schematic of the synchronized HighQ laser system. Based on the controlling of the Nutfield- XLR-8-10 galvanometer and the shutter of the HighQ picosecond laser by a RTC 4 card in the PC with the galvanometer controlling software, Lanmark-Winlaser Pro, signals from the RTC 4 card trigger software based on a Labview environment to change a CGH on the SLM. Both the Lanmark-Winlaser Pro software and the SLM control software were running under a Windows XP environment. CGHs (8-bits) are displayed on the SLM via Labview. The delay time for CGH changing is also controlled by Labview. Figure 3.25 shows the interface of the Labview GUI, which was used to alter the CGHs and display the signals. Any 8-bit CGHs with 800x 600 pixels can be displayed. Displayed CGHs are pre-saved with sequence numbers in the hard disk on the PC. TTL signals are sent from the Aerotech controller and received by a National Instruments (NI) USB data acquisition device (NI USB-6501). After receiving the TTL signal from the Aerotech controller, the software immediately displays the pre-save CGH on the SLM in sequence number. Hence, the Aerotech controller has made a communication with the SLM control software. After the SLM control software is configured, it can be set to run in the background and wait for the trigger signals from the Aerotech controller. The trigger signals for CGH changing can be set with two ways: manually and automatically. The manual CGH changing method means the pre-save CGHs will be displayed after the trigger signals are received by the NI USB data acquisition device. The automatic CGH changing method means the pre-saved CGHs will be displayed automatically with user

defined delayed times. For high manufacturing processing efficiency achievement, the CGH refresh time should below 500ms (2Hz).

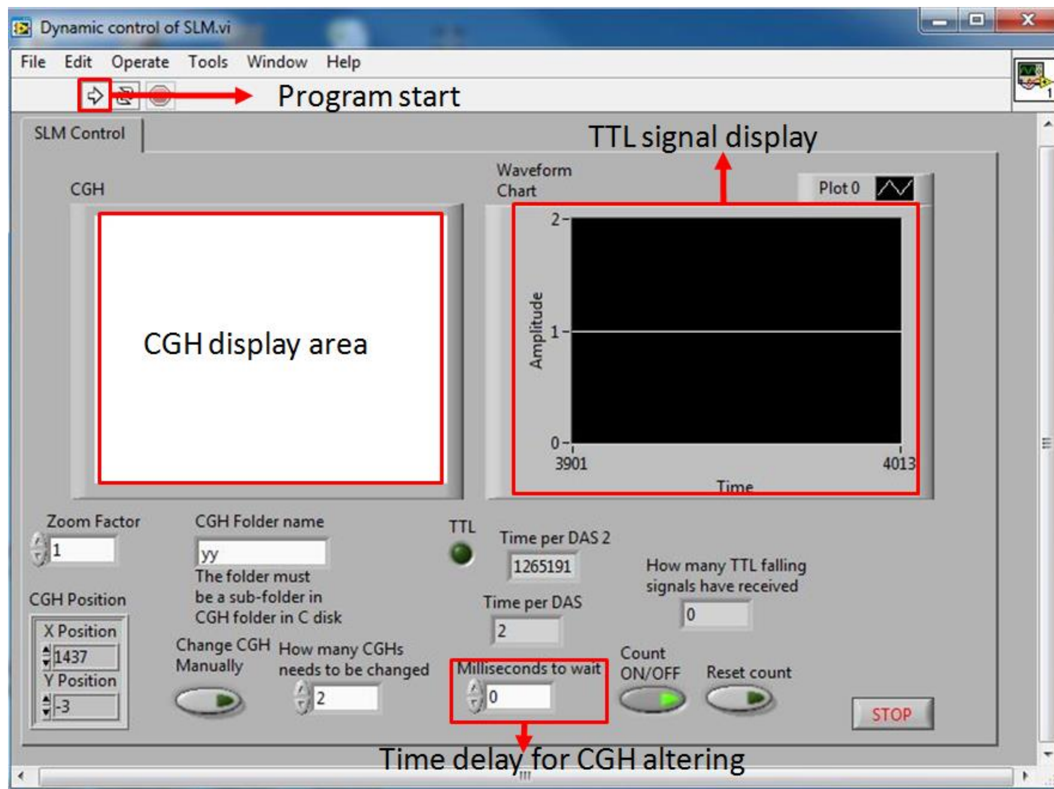

Figure 3. 24 Labview software interface for the dynamic control system

A block diagram of the Labview program is included in the Appendix for further detail.

3.6 Measurement and analysis equipment

3.6.1 Beam profiler

Two different beam profilers were employed in this research, a Thorlabs BC106-VIS and a Spiricon Model SP620U

- Thorlabs BC106-VIS

The Thorlabs BC106-VIS with pixel size of 6.45µm x 6.45µm, a working wavelength range of 350-1100nm, power range of 1fW-1W and the measured beam size range of 30µm - 6.6mm with a CW/pulsed laser source [201]. It consists of the following equipment: an embed optical sensor for measurement, a filter wheel with four absorptive neutral density (ND) filters (10dB, 20dB, 30dB and 40dB), a Mini B USB connector and a TTL Trigger input. A BC1M2 Extension mounted at the bottom of the profiler for M^2 measurement and further precision measurement. The assembled device is shown in Figure 3.26. The Thorlabs BC106-VIS provides all the essential features needed for laser beam analysis (see Figure 3.27). 2D and 3D beam profile can be displayed together at a high resolution. Important parameters of a beam

profile such as intensity, beam diameter and peak density can be monitored at a high speed. The detector area is 8.8mm×6.6mm.

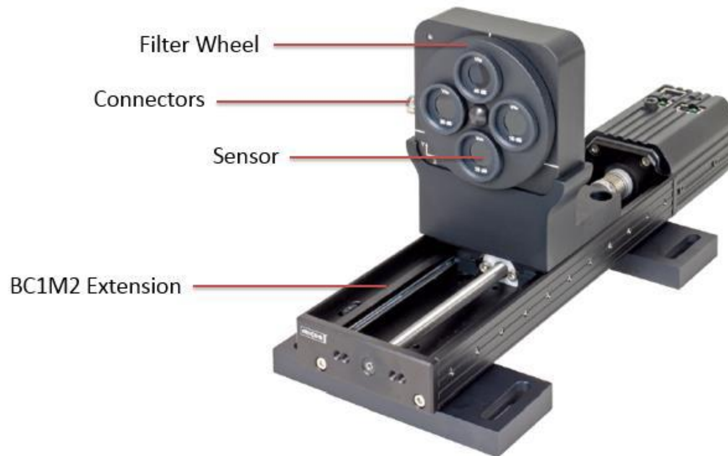

Figure 3. 25 Thorlabs BC106 camera. This camera consists of filter wheel (with four filters), computer-camera connector, sensor and an extension [4].

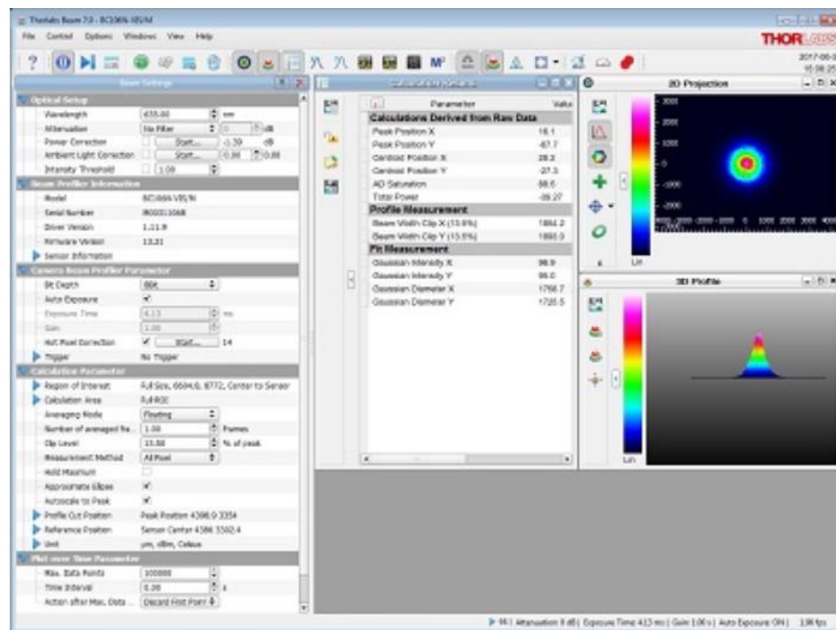

Figure 3. 26 BC106 beam profiler software interface [4].

- Spiricon SP620U

The second beam profiler employed in this research is a Spiricon SP620U, as shown in Figure 3.28 (a). This beam profiler system consists of a Spiricon frame grabber card with software and a CCD camera. The Spiricon SP620U has a pixel size of 4.40μm x 4.40μm, a working wavelength range of 190-1100nm, power range of 1fW-1W and the measured beam size range of 30μm - 6.6mm with a CW/ pulsed laser source [202]. A wedged fused silica plate was placed before the CCD chip near the Brewsters angle to

avoid a high power laser beam damaging the CCD camera. Due to the fused silica plate placed near the Brewsters angle, only the s-polarized beam will be reflected to the CCD chip and the rest of the beam transmitted. 2D and 3D beam profiles can be displayed with high speed, high resolution and intensity distribution. Figure 3.30 (b) shows the 2D image with intensity distribution of SP620U.

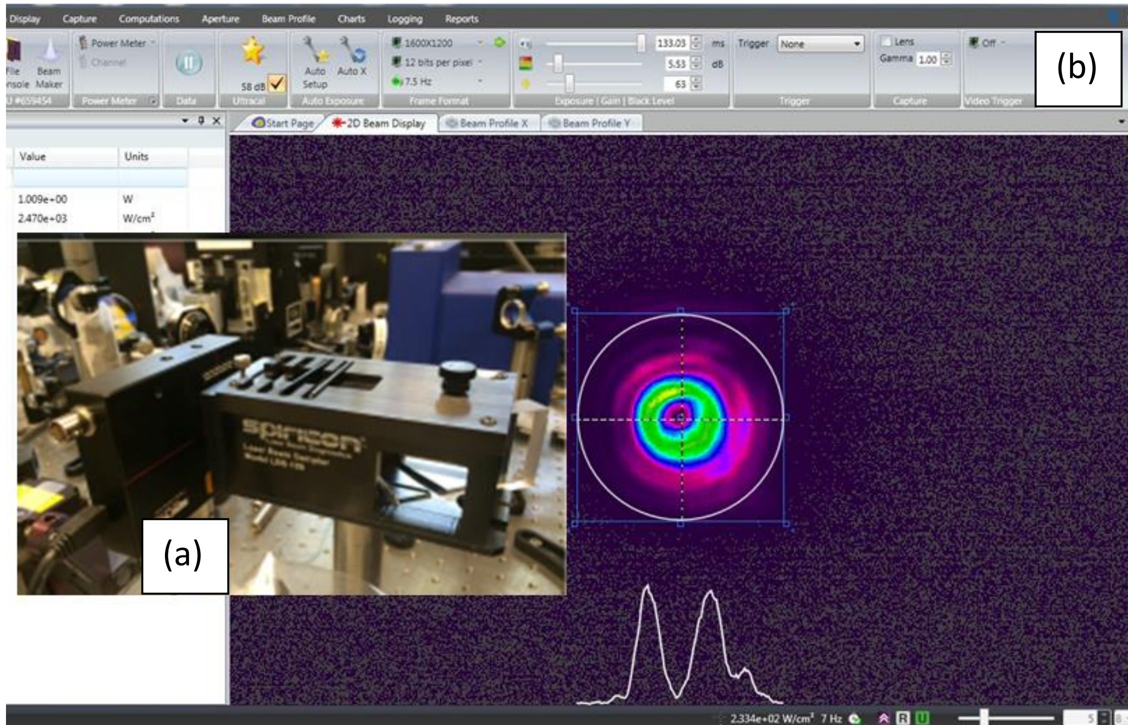

Figure 3. 27 (a) Spiricon SP620U beam profiler with wedge beam splitter and (b) its software (BeamGage) interface

3.6.2 Nikon Eclipse LV150NL optical microscope

The surface condition after laser treatment was checked by a Nikon optical microscope with various magnification of 2D images. The microscope provides detailed inspection of processed surface with magnification: x4, x10, x20, x50 and x100. The Nikon optical microscope consists of an optical microscope, a digital camera, and a software running in a Windows environment for operating the digital Camera. A 3-axis stage was integrated with the optical microscope for placing the sample and finding the focal plane of the microscope. Image J was used to take calibrated images and measurements using a pre defined scale.

3.6.3 WYKO NT1100 white light interferometer microscope

The surface condition after laser treatment can be checked by a WYKO NT1100 white light interferometer microscope with various magnification of 2D/3D images with vertical resolution 3nm (single measurement) and1nm (multiple measurement). The microscope provides detailed inspection of processed surface with magnification: x2.5, x5, x10, x20, x50 and x100. Achieved results can be analyzed using Vision 32 software. During the measurement, a white light illumination source splits into two beams, with one beam on the sample surface and reflected back to interfere with the reference beam generating fringe

patterns, giving a 3D profile of the sample surface. A 3-axis stage is integrated with the interferometer microscope for placing the sample and finding the focal plane of the microscope. Figure 3.29 shows the WYKO NT1100 white light microscope with an analysis PC.

Figure 3. 28 WYKO white light interferometer with a control PC

3.6.4 FLIR SC660 thermal camera

A FLIR SC660 thermal camera was employed to analyse the temperature response of a spatial light modulator (SLM) when illuminated with high average laser power. The FLIR thermal camera has a 640x480 image resolution for producing sharp images with high accuracy radiometric readings. This thermal camera has a spectral range from 7.5μm to 13μm

3.6.5 Scanning Electron Microscope (SEM)

The SEM used in this research was a JEOL JSM 6610 SEM with 4.0nm resolution (at 30kV), Tungsten filament and an Oxford INCA X-act EDX detector. The SEM enables magnification from x5 to 300,000, allowing imaging of 1.2nm. Table 3.3 shows the parameters of the SEM. The SEM used to obtain sub-micron and nano structures on metal surface that were produced with lasers.

Table 3. 3 parameters for the SEM6610

Resolution	4.0nm
Magnification	X5-300,000
Accel. Voltage	0.3-30kV
Image modes	SE,BSE,EDX
Max. Sample Size	200mm
Max. Sample Mass	1kg

3.6.6 Drop shape analysis system

A Krüss EasyDrop standard drop shape analysis system was used to measure the water contact angles. This equipment was used in the study of surface wettability modification in chapter 6. The drop shape analysis system mainly consists of 4 parts: an observation camera, microliter pipette holder, sample stage and an illuminator, as shown in Figure 3.30.

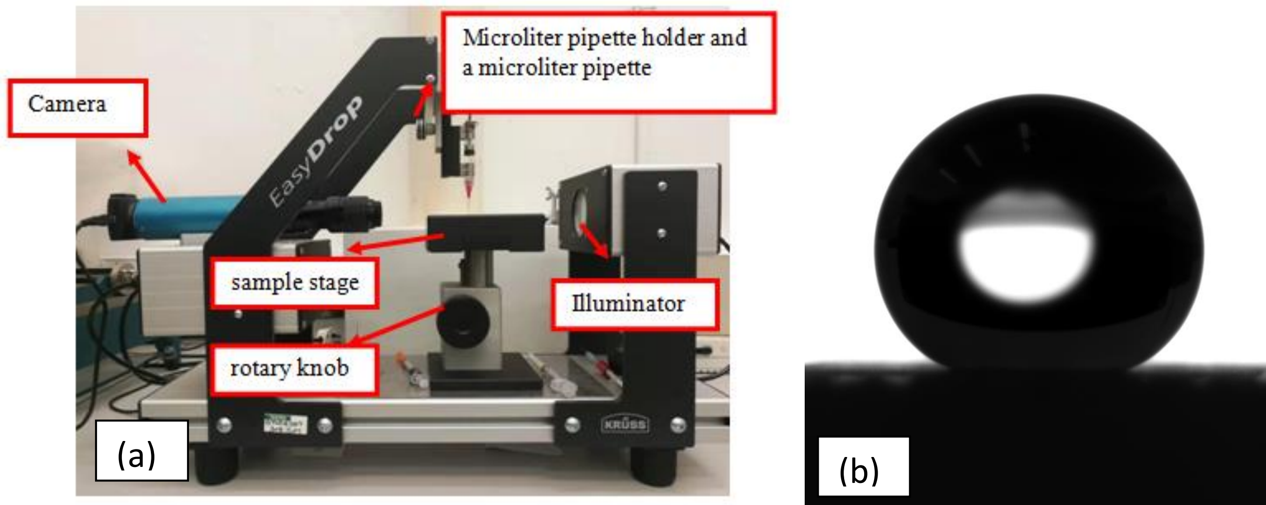

Figure 3. 29 (a) A Krüss EasyDrop standard drop shape analysis system. (b) A saved image which was observed by a camera.

Samples are placed on the stage for observation by using the illuminator. The height of the stage can be adjusted by rotating the rotary knob. The observation camera is connected with a PC, so the results can be observed and saved via the PC. One of the saved images as shown in Figure 3.32(b) and its will be analysed by the Image J with the drop-snake plugin for contract angle measurement. Details of the measurement are demonstrated in chapter 6.

3.7 Modelling and simulation software

3.7.1 ZEMAX

ZEMAX is a convenient software that can be used to perform analysis of optical systems, optimization, tolerance analysis as well as to analyze imaging systems such as camera lenses, and illumination systems. It works by ray tracing—modelling the propagation of rays through an optical system. It can be used to model the effect of optical elements, such as simple lenses, and some uncommon lens like aspheric lenses, gradient index lenses, mirrors, and diffractive optical elements, and can produce standard analysis diagrams such as spot diagrams and ray-fan plots. The optical system optimization functions of ZEMAX are flexible. Users can use those functions to optimize their optical system to find out the minimized beam size and also to achieve some optimum setting parameters by applying a known goal. In this work, ZEMAX optical studio 15 has been used to model the optical systems and to analyse results. Figure 3.31 shows the interface of ZEMAX optical studio 15.

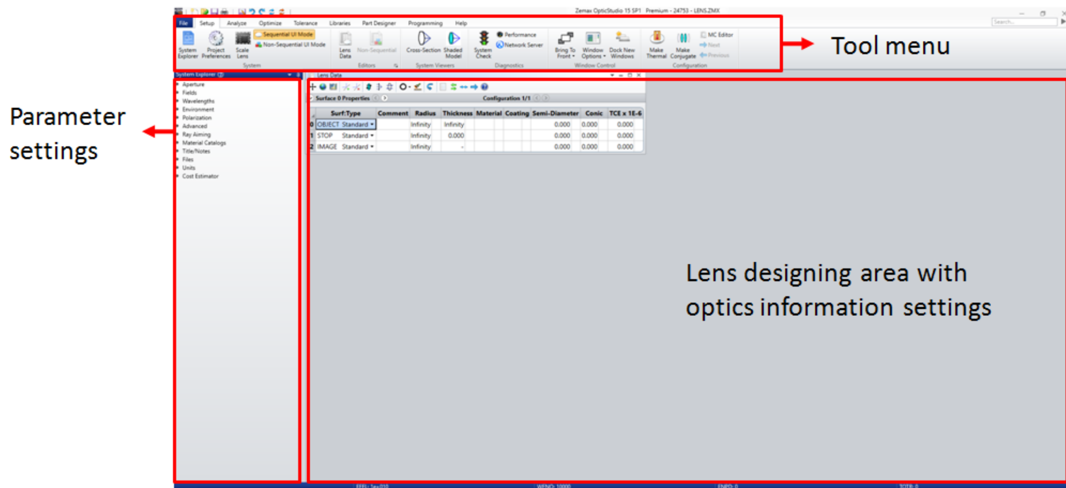

Figure 3. 30 The interface of ZEMAX optical studio 15

3.7.2 MATLAB

MATLAB is a widely used numerical computing and programming software developed by MathWorks. MATLAB allows matrix manipulations, plotting of functions and data, displaying corresponded computer generated holograms (CGHs) with programming languages, like C, C++, C#, Java and python. In this work, MATLAB has been used to generate a desired computer generated hologram (CGHs). Figure 3.32 shows the interface of MATLAB R2014a.

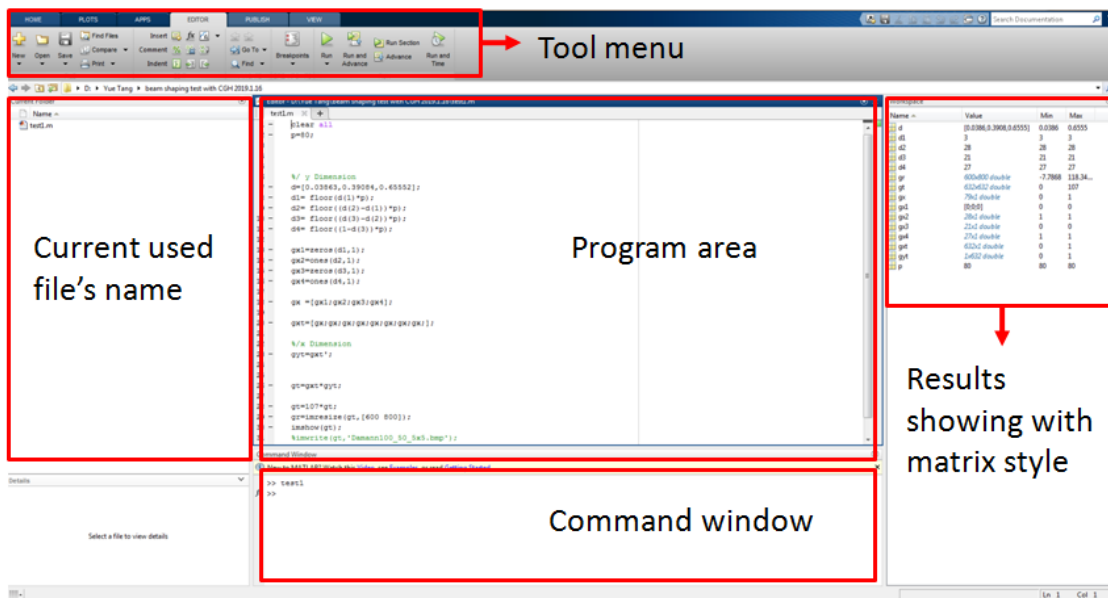

Figure 3. 31 The interface of MATLAB R2014a

3.8 Summary

In this chapter, the equipment used in this research were reviewed. This included two picosecond laser systems (High-Q and Edgewave), a SPI nanosecond pulsed fibre laser, motion control systems, scanning galvanometer systems, SLMs and measurement equipment, such as CCD beam profilers, SEM and white

light interferometer. Several SLMs were used in this research for different purposes. The SLMs used in the High-Q laser system have been mainly applied for micro processing and the SLM used on the Edgewave laser system has been mainly applied for high power tests of the SLM. The output power for each used SLM has been measured with relative optics. The polarization purity of an S-waveplate was measured using an additional half-wave plate and a polarizer analyser. The method of synchronization of the laser system with SLMs and the motion system was also reviewed. Software for modelling and simulation, such as ZEMAX and MATLAB were reviewed.

Chapter 4

Diffractive Dynamic Beam Shaping with Polarization Control at the Image Plane

4.1 Introduction

A specified laser beam irradiance distribution in the focal plane [203] or the image plane [204] has been developed for a number of laser industrial [205] and medical [206] applications to date. Beam shaping techniques based on lasers has been used in material microprocessing[185], optical tweezers [179] and laser iginition [207].

Ultra-short pulse laser beam shaping for material processing can lead to the improvement of different processes for material modification. From the use of ampulitude mask projection and diffractive optical elements (DOEs) [208] to deformable mirrors [209], different techniques have been attempted to shape ultra-short pulse laser beams for various applications.

Precision control of laser polarization offers a significant posibility to optimise laser material processing performance. For example, a radially polarized beam can double laser cutting speed compared with linearly polarized beam [210].

In this chapter, beam shaping with polarization control to generate various shaped beams with radial or azimuthal polarization is presented. Both binary geometric mask combined with an S-waveplate have been used to fully shape the input laser beam and polarization states control. Further multiple beam shaping by applying grey level masks with two SLMs is also demonstrated. The beam shapes and distribution were reconstructed at an image plane of an f-theta lens. The polarization states have been confirmed using Laser Induced Periodic Surface Structures (LIPSS). The observed pattern matched the beam pofile very well while the radial or azimuthal polarization states can be observed clearly.

4.2 Methodology of beam shaping at the image plane

Most of the beam shaping techniques by using SLM, such as diffractive beam splitting [154], beam intensity modulation [151] are directly focused on the focal plane to achieve highest efficiency and diffractive accuracy with desired Computer generated holograms(CGHs). In this work, a novel beam shaping method at the image plane is provided which is simpler than beam shaping at the focal plane avoiding complex computer generated holograms (CGHs) calculations.

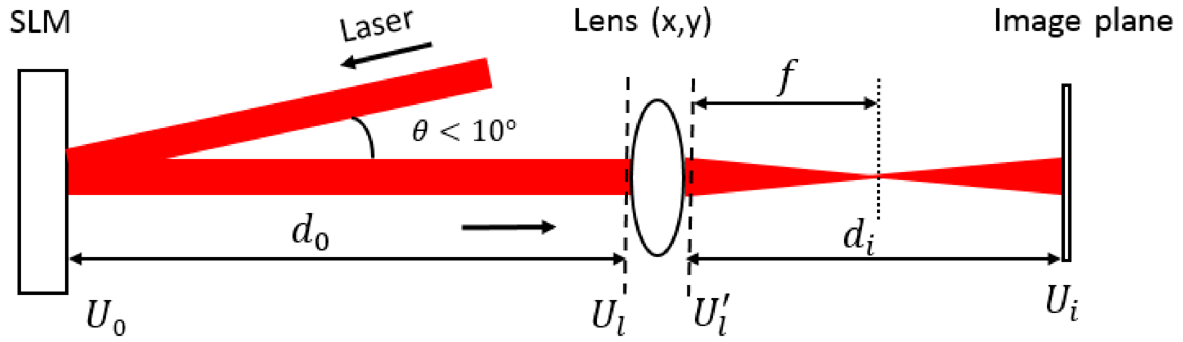

Figure 4. 2 Schematic of processing at the imaging plane

Figure 4.1 shows a schematic of laser processing at the imaging plane. A laser beam is illuminated onto a SLM, on which is displayed a geometric mask which can shape the beam at the imaging plane of a focusing lens. In this research, the SLM is used as an intensity modulator by employing various mask shapes. The reflected beam from the SLM passes through a thin focus lens and reaches the imaging plane with a desired shape and intensity. Since the SLM is using geometric masks for light modulation, the complex amplitude of the laser at the objective plane can be referred as U_0, with the light propagating to the focus lens, the complex amplitude before and after the focus lens can be referred as U_l and U_l' respectively. And U_i is the electric field diffraction pattern at the image plane. In practical terms, U_0, is a 256 bit matrix of grey level values to be displayed on the SLM.

The complex amplitude at U_l can be expressed as a complex equation based on the Fresnel diffractive integral [211, 212]:

$$U_l(x,y) = \frac{1}{1i\lambda d_0} \exp(ikd_0) \exp\left[i\frac{k}{2d_0}(x^2+y^2)\right] \times \iint_{-\infty}^{\infty} U_0(x_0,y_0) \times \exp\left[j\frac{k}{2d_0}(x_0^2+y_0^2)\right] \exp\left[-i\frac{2\pi}{\lambda d_0}(x_0 x + y_0 y)\right] dx_0 dy_0 \quad (4\text{-}1)$$

The complex amplitude of the lens, which is expressed below, can be described with Fourier Optics theory [211]:

$$T(x,y)=P(x,y)\exp\left[-i\frac{k}{2f}(x^2+y^2)\right] \quad (4\text{-}2)$$

where $P(x,y)$ is the pupil function of the lens. $P(x,y)$ can be approximately regarded as 1 due to the laser beam diameter (8mm) being much smaller than the size of the lens (50.8mm) used in this study.

While the light is passed through the focus lens, the complex amplitude of light after the lens can be expressed by multiplying U_l and lens complex amplitude function T(x,y) :

$$U_l' = U_l(x,y)T(x,y) \quad (4\text{-}3)$$

The laser beam then passes through the lens, and will be brought to the focal plane of the focus lens, which is considered a Fourier plane. Beam shaping at the Fourier plane needs to follow the Fourier Transformation. From Figure 4.1 the Fourier plane is at d_i and the image plane is at U_i, the electric field diffraction pattern can be calculated using the Fresnel diffraction integral as:

$$U_i(x_i, y_i) = \frac{1}{i\lambda d_0}\exp(ikd_i)\exp\left[i\frac{k}{2d_i}(x_i^2+y_i^2)\right] \times \iint_{-\infty}^{\infty} U_l'(x,y) \times \exp\left[j\frac{k}{2d_0}(x^2+y^2)\right]\exp\left[-i\frac{2\pi}{\lambda d_i}(x_i x + y_i y)\right]dxdy \quad (4\text{-}4)$$

A complex multiple integral equation can be derived by multiplying (4-1) (4-2) and (4-3) into (4-4):

$$U_i(x_i, y_i) = \frac{1}{\lambda^2 d_0 d_i}\exp(ikd_i)\exp\left[i\frac{k}{2d_i}\left(x_i^2+y_i^2\right)\right] \times \iint\iint_{-\infty}^{\infty} U_0(x_0,y_0) \times \exp\left[i\frac{k}{2}\left(\frac{1}{d_0}+\frac{1}{d_i}-\frac{1}{f}\right)(x^2+y^2)\right] \times$$
$$\exp\left[j\frac{k}{2d_0}(x_0^2+y_0^2)\right] \times \exp\left[-i\frac{2\pi}{\lambda d_0}(x_0 x + y_0 y)\right] \times \exp\left[-i\frac{2\pi}{\lambda d_i}(x_i x + y_i y)\right]dxdydx_0dy_0 \quad (4\text{-}5)$$

Because of the component exp $[\frac{k}{2d_i}(xi2+yi2)]$ does not affect the final intensity distribution, so it can be neglected. Thus, the complex multiple integral equation above can be simplified. Since for each point on imaging plane, there should be a small relating area on the objective plane, and the phase difference is relatively small. Therefore, we can also assume that:

$$\exp\left[j\frac{k}{2d_0}(x_0^2+y_0^2)\right] \approx \exp\left[i\frac{k}{2d_0}\left(\frac{x_i^2+y_i^2}{M^2}\right)\right] \quad (4\text{-}6)$$

where $M = \frac{d_i}{d_0}$ is the magnification factor. Therefore, the factor of x_0 and y_0 can be replaced by the magnification factor of M.

$$\frac{1}{d_0}+\frac{1}{d_i}-\frac{1}{f} = 0 \quad (4\text{-}7)$$

Applying the thin lens equation in geometric optics. The simplified electric field diffraction pattern U_i can be calculated as:

$$U_i(x_i,y_i) = \frac{1}{\lambda^2 d_0 d_i}\iint_{-\infty}^{\infty}\left\{\iint_{-\infty}^{\infty} U_0(x_0,y_0)\exp\left[-i\frac{2\pi}{\lambda d_0}(x_0 x + y_0 y)\right]dx_0dy_0\right\} \times \exp\left[-i\frac{2\pi}{\lambda d_i}(x_i x + y_i y)\right]dxdy$$
$$= \frac{1}{\lambda^2 d_0 d_i}\iint_{-\infty}^{\infty} G_0 \times exp\left[-i\frac{2\pi}{\lambda d_i}(x_i x + y_i y)\right]dxdy$$
$$= \frac{1}{M}U_0\left(-\frac{x_i}{M}, -\frac{y_i}{M}\right) \quad (4\text{-}8)$$

The electric field pattern on the imaging plane can be approximately derived as $U_i(x_i, y_i) = \frac{1}{M}U_0(-\frac{x_i}{M}, -\frac{y_i}{M})$ while applying a geometric mask U_0 on the SLM. This still remains the exact shape of U_0 but is reversed.

4.3 Experimental and methodology

4.3.1 Experimental setup

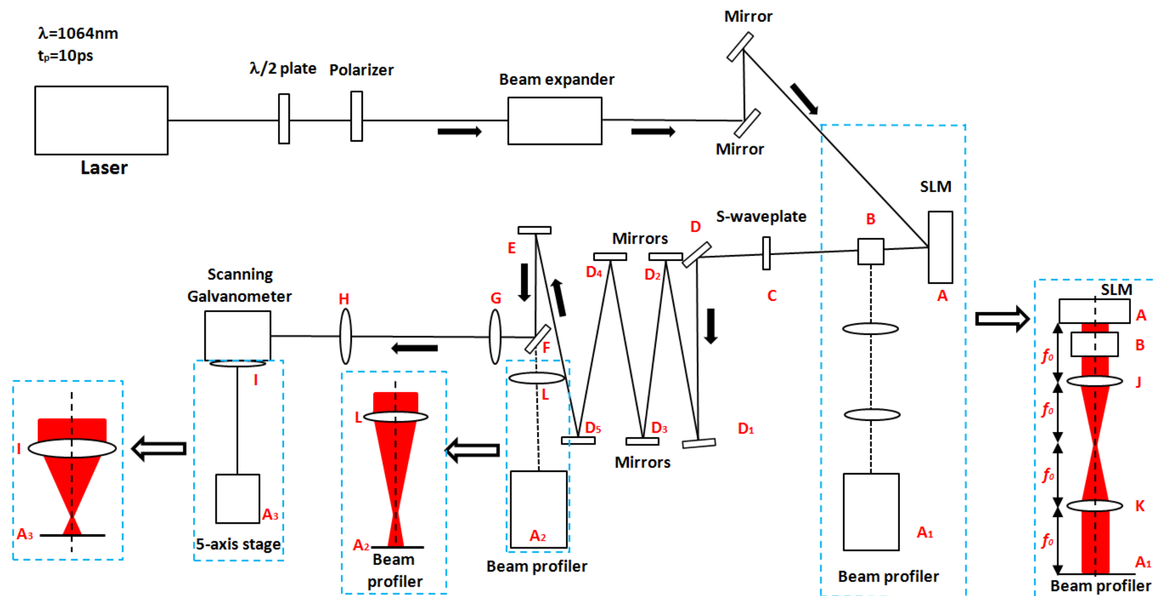

Figure 4. 3 Experimental setup

Figure 4.2 shows a schematic of the experimental setup. The ultrafast laser system used for this research is a custom made Nd:VAN seeded regenerative amplifier laser system(High-Q IC-355-800ps, Photonic solutions). A linearly polarized laser beam: τ =10ps, λ=1064nm and repetition rate *PRF*=10kHz passes through a half wave plate and polarizer which is used to adjust power and polarization direction, after that, the laser passes through a beam expander(M≈×3) then is directed to a phase only, reflective, liquid crystal SLM (A, Hamamatsu X13138-5785, 1280x1024 pixels).

At B there is a half wave plate and polarising beam splitter (VBA05-1064, Thorlabs). This is used as a pick off for laser beam profiling of the shaped beam via a 4f system with two positive lenses (lens J and lens K, focal length: f_0=200mm) and a CCD camera (BC106-VIS, Thorlabs). It is also as a polarization filter to be discussed later.

An uncoated nano-structured fused silica S-waveplate (C, Altechna) was added to adjust the output polarization state from radial to azimuthal. When processing, the beam traversed a long distance (≈5 meters) by multiple reflections on mirrors (D-E) to reach a scanning galvanometer with an f-theta lens (I, f_θ =100mm). Lens G and lens H (f=300mm) consists of a 4f system. Machining samples were mounted on a five-axis (x,y,z,u,v) motion control stage, placed under the f-theta lens (I). When observing the beam profile after beam shaping and polarization control, a flip mirror (F) was used for optical alignment to let the beam pass through a positive lens (L, focal length: f_o=500mm) to reach a CCD camera (BC106-VIS,

THORLABS) placed at the image plane. Hence the intensity profile during processing could be observed simultaneously.

4.3.2 Beam shaping using a SLM

By rotating the polariser before the beam expander, a beam has been produced with a 45° linear incident polarization state beam relative to the fast axis of the SLM (A), The SLM, half wave plate and a polarizer, can all be expressed as a Jones vector J(x,y), where x and y are the horizontal and vertical coordinates across the beam profiles. A full derivation using the optical properties of the setup gives:

$$J(x,y) = \begin{pmatrix} 1 & 0 \\ 0 & 0 \end{pmatrix} \times \begin{pmatrix} cos2\theta & sin2\theta \\ sin2\theta & -cos2\theta \end{pmatrix} \times \begin{pmatrix} e^{i\varphi(x,y)} & 0 \\ 0 & 1 \end{pmatrix} \times \begin{pmatrix} \frac{1}{\sqrt{2}} \\ \frac{1}{\sqrt{2}} \end{pmatrix} \quad (4\text{-}9)$$

Where φ(x,y) is the relative phase delay induced with the SLM, and θ is the angle of the fast axis of the half wave plate at B. We can derive the intensity of the output from equation 4-9:

$$I = \frac{1}{2}\begin{pmatrix} cos2\theta e^{-i\times\varphi(x,y)} + sin2\theta & 0 \end{pmatrix} \times \begin{pmatrix} cos2\theta e^{i\times\varphi(x,y)} + sin2\theta \\ 0 \end{pmatrix} = \frac{1}{2} + \frac{1}{2} sin4\theta cos\varphi \quad (4\text{-}10)$$

Where I is the beam pass efficiency. The laser beam will pass through the polarizer at B without energy loss when I=1 and the polarizer blocks all the energy while I=0. As shown in Equation 4-10, when $\theta = \frac{3}{8}\pi$, $I = \frac{1}{2} - \frac{1}{2} cos\varphi$, which means theoretically using this method, the intensity can be adjusted from 0 to 1. The intensity control based on this method will also demonstrated in section 4.6 for flat-top beam shaping at the image plane.

4.3.3 Polarization control using an S-waveplate

Linear or circular polarized beams can be used with polarization converters such as an S-waveplate. For the incident linearly polarized beam, the S-waveplate rotates the incident linear polarization by the angle necessary to produce a radial distribution of the electric field.

4.3.4 Polarization confirmation with ZEMAX modelling

Linear or circular polarized beams can be used for polarization converters such as a S-waveplate. For the incident linearly polarized beam, the S-waveplate rotates the incident linear polarization by the angle necessary to produce a radial distribution of the electric field. The polarization state of various CV beams have been confirmed with ZEMAX optical modelling software. For the ZEMAX simulation, the Jones matrix of an S-waveplate was employed with the fast axis set to Ø = 0°, 45°, 90° and -45° relative to an incoming linearly polarised beam. The Jones matrix was set to $\begin{pmatrix} 1 & 0 \\ 0 & 1 \end{pmatrix}$ in spatial coordinate (Z axis reference polarization method) in ZEMAX for Ø = 0° and corresponding Jones matrices were set in ZEMAX with Ø = ±45° and 90°. Radial polarization can be obtained when the angle of input polarization

with fast axis angle of the S-waveplate Ø = 0° while Azimuthal polarization is obtained for Ø = 90°. When intermediate angles, Ø = 45° and -45° were input, logarithmic spiral electric field distributions with opposite handedness result – first predicted by F. Gori [213] and observed in [131]. Figure 4.3 display the electric field of radial and azimuthal beams, the electric field direction of oscillation varies continuously with polar angle Ø. Thus, the S-waveplate was defined in ZEMAX with spatial coordinates but observed along the Z axis in ZEMAX. The simulated results are shown in Figure 4.4. Details of polarization confirmation setup in ZEMAX will be introduced in Appendix 3.

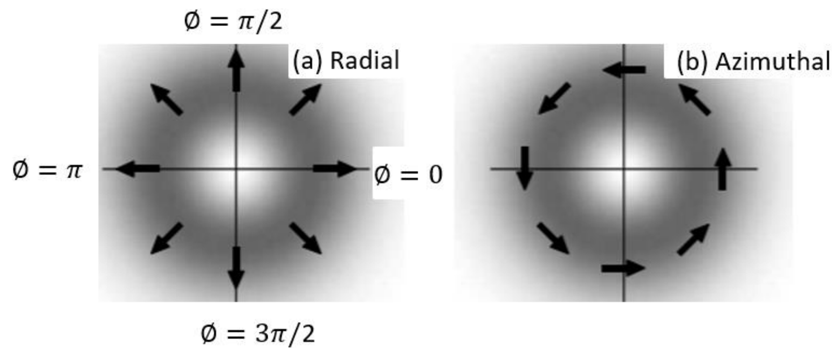

Figure 4. 3 Representation of the electric field of radial and azimuthal axially symmetric beams with polar angle Ø [131].

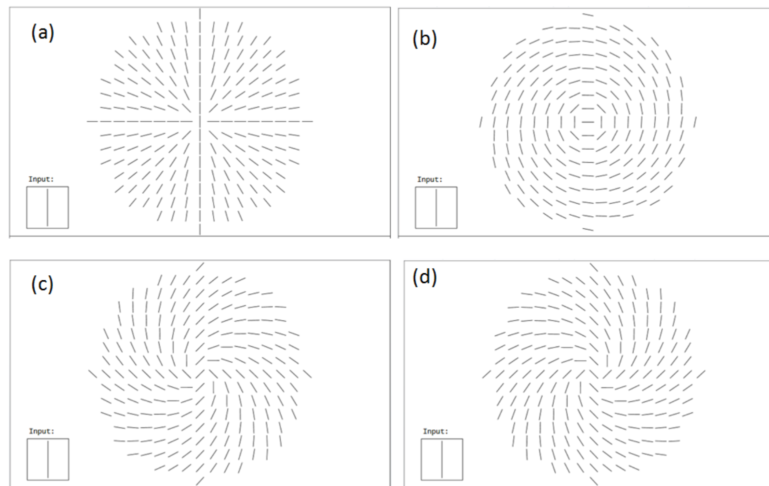

Figure 4. 4 Complex polarization states confirmation of the S-waveplate in ZEMAX. By defining different polar angle (Ø), different output polarization can be achieved with the same input polarization direction (a) Ø=0° (Radial) (b) Ø=90° (Azimuthal), (c) Ø=45° (d) Ø= -45°, (logarithmic spirals of opposite handedness).

4.3.5 Shaping reconstruction at the imaging plane

As shown in Figure 4.2, the generated mask will shape the incident beam in the near field after the SLM at A. The shape is also reconstructed after the 4f optical system at A_1. In addition, this is also reconstructed after a focusing lens at A_2 for observation. The beam then reaches the f-theta lens and is reconstructed at the imaging plane A_3. As shown in Figure 4.2, there are five mirrors, D_1-D_5, added into the beam path to significantly increase the distance from the SLM to the focusing f-theta lens, i.e. the object distance. The purpose of this was to reconstruct the shape to a small size comparable to the beam waist which is 34 μm

and the Rayleigh length is 852μm. The position of the imaging plane A_3 can be estimated, based on the thin lens imaging equation below:

$$\frac{1}{u}+\frac{1}{v}=\frac{1}{f} \tag{4-11}$$

where, $u \approx 5000mm$ is the object distance, i.e. the distance from the SLM(A) to the f-theta lens (I), $f = 100mm$ is the focal length of the f-theta lens and v is the image distance, i.e. the distance from the f-theta lens(I) to image plane(A_3). Due to the object distance is much longer than the focal length, so it is not necessary to calculate the image distance very precise.

$$v=\frac{fu}{u-f} \approx 102\text{mm} \tag{4-12}$$

$$d = v - f = 2mm \tag{4-13}$$

The magnification of the image system is M≈1/45. Therefore, when a 250 pixel side length mask is applied to the SLM with a side length approximately 1.5mm, the diameter of the reconstructed beam at A_3 can be calculated to be approximately 31μm, which is comparable to the beam waist at the focal plane M. The depth of focus is various due to the shaped beam size is various.

Since both the shape and interference pattern needs to be observed, the same method can be used at the beam profiler A_2. A positive lens (focal length: f_0=500mm) was placed after the flip mirror and a beam profiler was placed after the lens at the image plane.

4.4 Result and discussion

4.4.1 Polarized beam observed by a CCD camera

As shown in Figure 4.5, Figure 4.6 and Figure 4.7, three different shaped beams with radial or azimuthal polarization have been demonstrated. The first line shows the results of beam shapes using a SLM. The shapes of a square, star and triangle can be observed by applying a corresponding binary mask. The second line shows the method of beam shaping plus a polarization converter, S-waveplate. All of the outputs from the polarization converter have a similar shape and intensity distribution as their input beam. The reconstructed beam appears to be uniform due to the small shaping areas, however the beam is still Gaussian. Due to the long laser beam path, the reconstructed shapes at A_2 have some distortion and have diffracted edges.

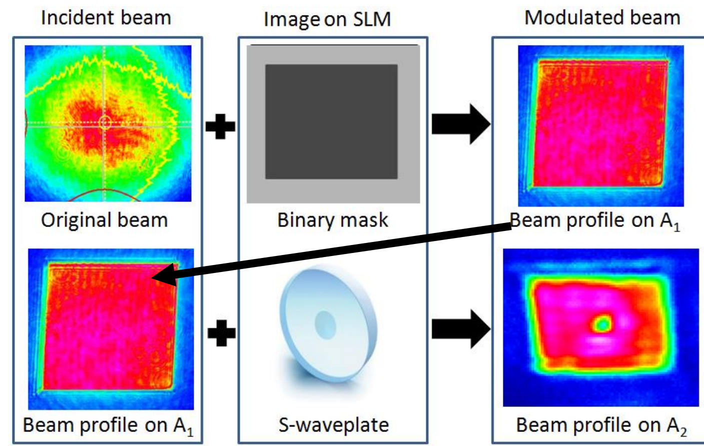

Figure 4. 5 Beam shaping with an S-waveplate. A shaped square beam can be achieved by an incident beam plus a binary mask at A1. An S-waveplate has been added to achieve a polarized beam at A2. The central hole at A2 indicates that the beam is aligned with the centre of the S-waveplate.

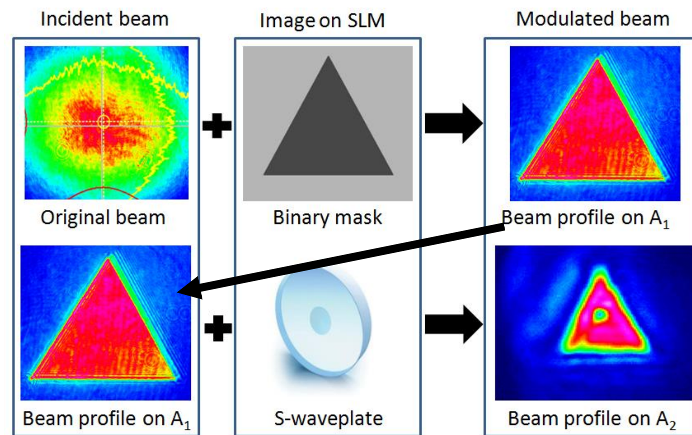

Figure 4. 6 Beam shaping with an S-waveplate. A shaped star beam can be achieved by an incident beam plus a binary mask at A1. An S-waveplate has been added to achieve a polarized beam at A2. The central hole at A2 indicates that the beam is aligned with the centre of the S-waveplate.

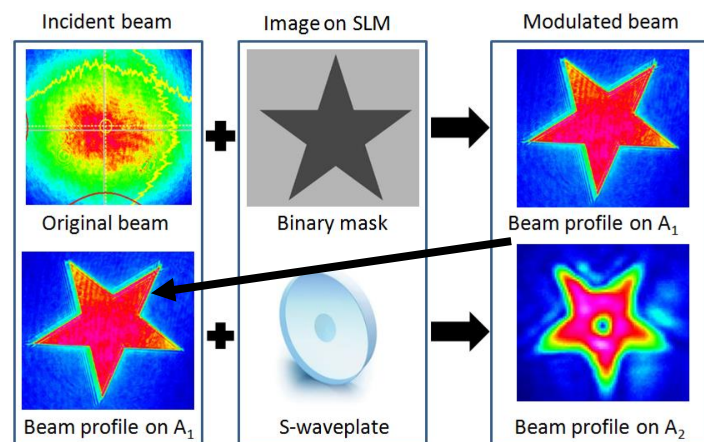

Figure 4. 7 Beam shaping with an S-waveplate. A shaped triangular beam can be achieved by an incident beam plus a binary mask at A1. An S-waveplate has been added to achieve a polarized beam at A2. The central hole at A2 indicates that the beam is aligned with the centre of the S-waveplate.

4.4.2 Dynamic beam shaping machining results

As the SLM is a display device the image can be changed rapidly. Despite the limits on the control and laser synchronisation system discussed in Chapter 3, a 5Hz refresh rate is possible. As shown in Figure 4.8 and Figure 4.9, machined beam footprints with dynamic control are presented. For processing, the laser repetition rate was set at 10kHz with approximately 2 μJ/pulse, measured before the scanning galvanometer aperture and exposure set to N=50pulses/spot. LIPSS structures with different polarization states were produced on a polished titanium surface. The time taken to process each spot was ~5ms including a 200ms delay for binary mask synchronization, all 9 spots with three different shapes were patterned in ~1.3 seconds. Both beam shaping with azimuthal and radial polarization are presented. Figure 4.8 presents the machined footprint of various beam shapes with a radial polarization state.

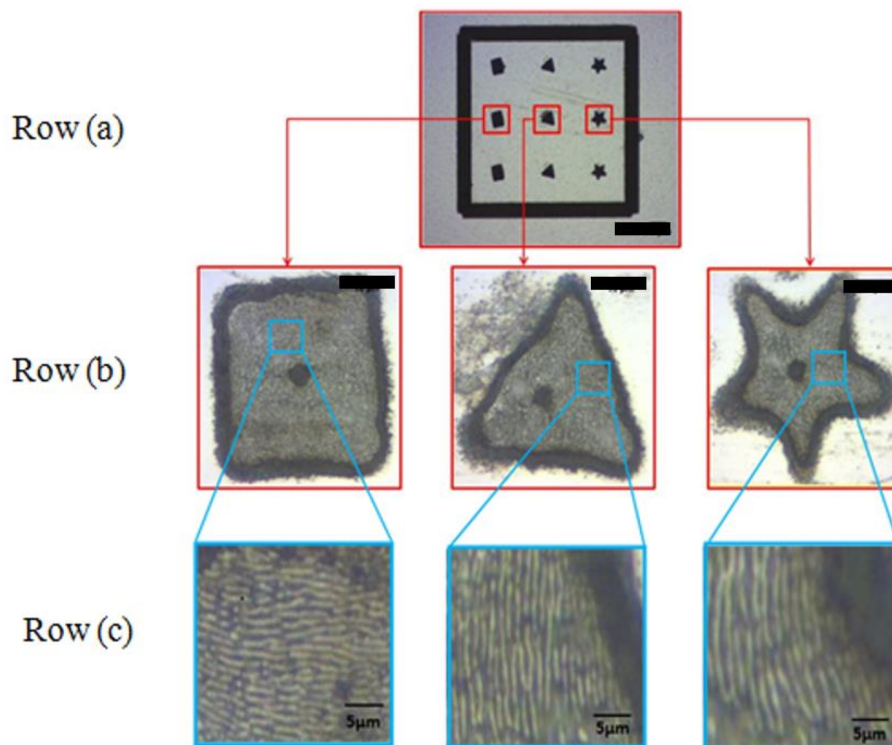

Figure 4. 8 Dynamic control of machined beam shapes with radial polarization. Row (a) shows three different shapes with radial polarization. Black scale bar is 150$\boldsymbol{\mu m}$. Row (b) shows a high magnification of each beam footprint. Black scale bar is 10$\boldsymbol{\mu m}$. Row (c) shows the radial polarization states for each beam confirmed by LIPSS orientation.

Figure 4.8 showed the machined footprint of various beam shapes with azimuthal polarization state.

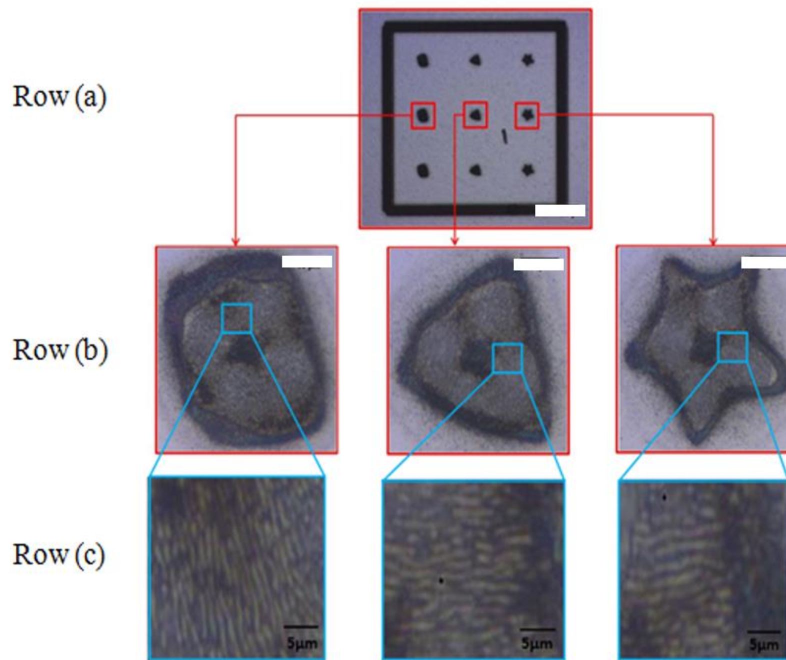

Figure 4. 9 Dynamic control of machined beam shapes with azimuthal polarization. Row (a) shows three different shapes with azimuthal polarization. White scale bar is 150μm. Row (b) shows a high magnification of each beam footprint. White scale bar is 10μm. Row (c) shows the azimuthal polarization states for each beam confirmed by LIPSS orientation.

As shown in Figure 4.10, a machined star beam shape with radial polarization has been generated. For processing, the laser repetition rate was set at 10kHz with approximately 2μJ/pulse, measured before the scanning galvanometer aperture and exposure set to N=50pulses/spot. Polished Ti6Al4V was used as a substrate. Fifteen laser spots with star shapes were patterned with a motion control system. The time taken to process each spot was ~5ms including a 200ms delay for binary mask synchronization. The total processing time for all fifteen spots was ~2.2s. It can be seen that the star shape are slightly distorted. This may be due to a discrepancy between the machining plane and the image plane. In practice, it can be difficult to find the precise image plane as it requires numerous iterations.

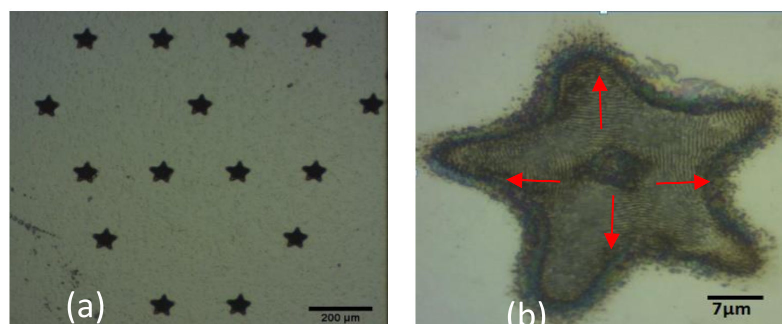

Figure 4. 10 Dynamic control of machined beam shapes with (a) radial polarization (10kHz, 2μJ/pulse, 50pulses) (b) A single magnified star shaped beam with radial polarization (10kHz, 2μJ/pulse, 50pulses). The red arrows indicate the direction of polarization states.

As shown in Figure 4.11, scanning electron microscope (SEM) results of a star shaped beam with radial and azimuthal polarization are presented. For the Figure 4.11 (a), the direction of the polarization state (red arrows) around the beam centre which indicate azimuthal polarization. For the Figure 4.11 (b), the direction of the polarization state (red arrows) is directed towards the beam centre which indicate radial polarization. LIPSS orientations in Figure 4.11 represent the polarization states which are expected. However, the LIPSS quality was found to be low due to the Gaussian beam mode, which causes over-exposure near the centre when processing.

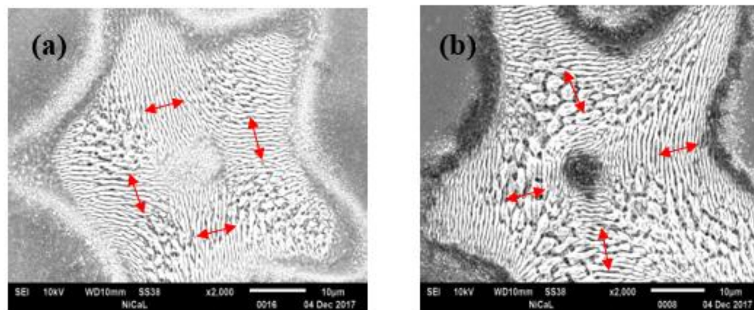

Figure 4. 4 SEM results. (a) The star shape with azimuthal polarization. (b) The star shape with radial polarization. Both shapes were machined by Gaussian type laser beam. The red arrows indicate the direction of polarization states. (10kHz, 2μJ/pulse, 50pulses).

As shown in Figure 4.12, machined results with binary mask were observed using a white light interferometer (WYKO NT1100).

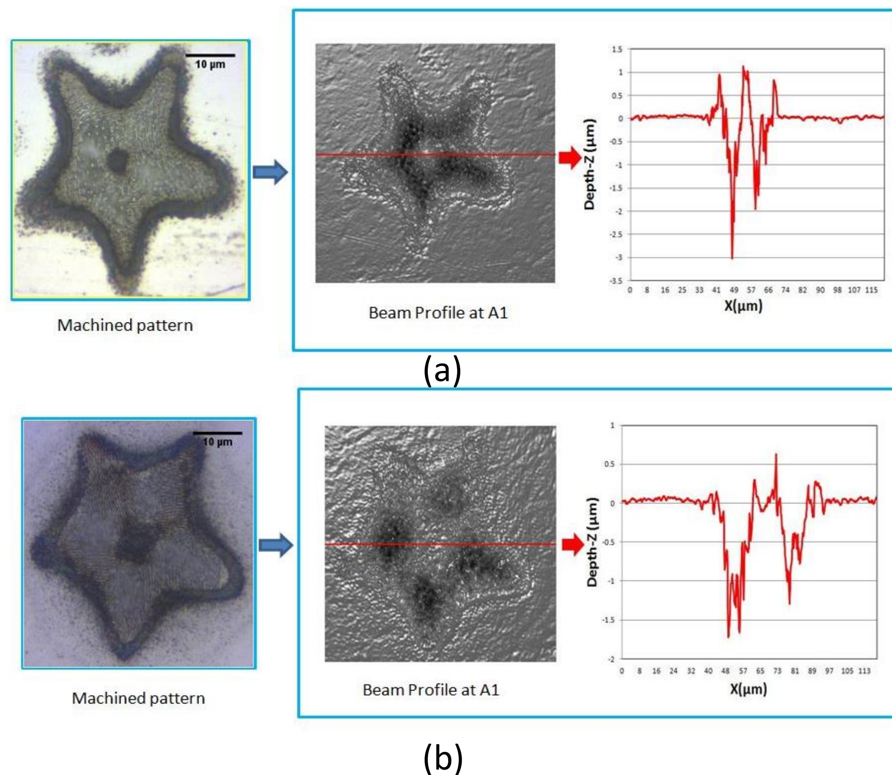

Figure 4. 5 Optical and WYKO images for star shapes with azimuthal and radial polarization states.(a) azimuthally polarized star shape. (b) radially polarized star shape. Both results were fabricated at the image plane with the same laser energy and processing time. (10kHz, 2μJ/pulse, 50pulses).

It can be seen that the processing depth of a radially polarized beam is deeper than an azimuthally polarized beam, which is expected. Weber et al [37] has reported that the radially polarized beam has higher absorptivity when drilling.

The shaped beam outlines produced by this method compare reasonably well to the other SLM based methods of beam shaping [17,18]. However, the diffraction efficiency appears to be lower. This is likely due to the mask size and the long beam propagation path.

4.4.3 Beam shaping efficiency-with Binary masks

Beam shaping quality and efficiency can be modified with different sizes of geometric masks. Equation 4-14 can be used to calculate the shaping efficiency:

$$\eta = \frac{\oint I_{shaped}\, ds}{\oint I_0\, ds} \times 100\% \tag{4-14}$$

Where $\oint I_{shaped}\, ds$ is the integral of the shaped beam intensity profile and $\oint I_0\, ds$ is the integral of the original beam intensity profile obtained at A_1 measured by the CCD beam profiler. The shaping efficiency can be seen to increase when the size of the mask is increased (Figure 4.13), as would be expected, as more of the original beam is being shaped and transmitted through the analyser.

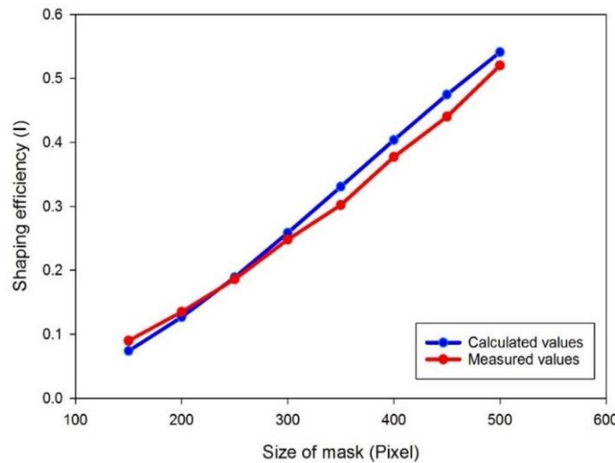

Figure 4. 6 Calculated and measured shaping efficiency with different sizes of binary masks.

Figure 4.13 shows the intensities of various mask sizes in the CCD camera observing the shaped area. A discrepancy between the calculated and measured values can be seen at higher mask sizes due to the intensity of the diffractive edge of the shaped beam is integrated for onward shaping efficiency calculation. With a binary mask, the outline of the input beam can be changed into any required shape, while the intensity distribution will remain the same as the original Gaussian distribution. Figure 4.14 shows a shaped beam with Gaussian distribution at the image plane. However, with a grey level mask added, the

intensity distribution can also be modified. Uniform power distribution of a laser beam, like a flat-top beam, can be obtained while applying grey level masks.

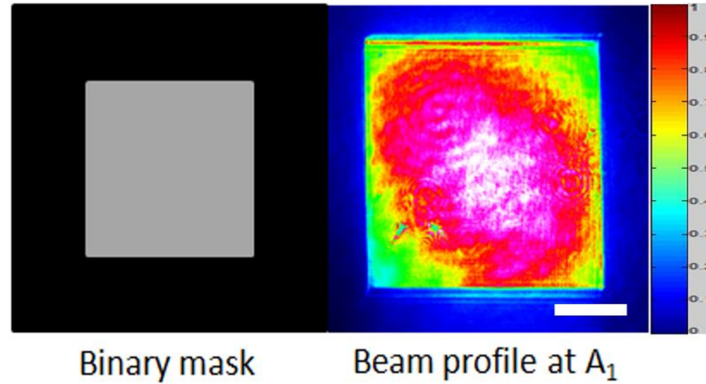

Figure 4. 7 The binary mask with continuous grey level (grey level =90) and its observed result on the CCD beam profiler with normalized colorscale. The white scale bar is 10 μm.

4.5 Beam shaping with grey level masks

By applying grey level masks, a flattop beam can be achieved. Assuming the target beam has a flat top distribution with intensity Y(m,n), where m,n is the pixel position relative to the SLM. The required intensity should therefore be proportional to the transmission efficiency $\mathrm{I(m,n)}$ multiplied by original near Gaussian intensity distribution O(m,n), as measured from the beam profiler and edited using Matlab to yield a constant spatial intensity. This is given in equation 4-15 where α is a factor to normalize the required intensity Y(m,n) between 0 and 1.

$$\mathrm{Y(m,n)} = \alpha \times \mathrm{I(m,n)} \times \mathrm{O(m,n)} \tag{4-15}$$

Thus, Y(m,n) can be achieved based on the pixel position of the shaped area.

The equation for I(m,n) can be derived from equation 4-10 when $\theta = \frac{3}{8}\pi$, where:

$$\mathrm{I} = \frac{1}{2} - \frac{1}{2}\cos\varphi \tag{4-16}$$

$$\mathrm{I(m,n)} = \frac{1}{2} - \frac{1}{2}\cos\left(\frac{2\pi}{190} \times [\mathrm{GL}]\right) \tag{4-16}$$

where [GL] is the grey level of a given point in the shaping area and the value is displayed on the SLM. The measured corresponding grey level on the SLM to 2π phase is 190 at beam profile A1 (in Figure.4.2) with various grey level maps on the SLM, then the measured results can be plot in Figure 4.14 with grey level versus transmission efficiency relative to the equation 4-17. When $\cos\varphi = 1$ ($\varphi = 2\pi$ or 0), transmission efficiency reaches at the minimum, the output intensity from the SLM will be minimum. Thus, the grey level which makes the transmission efficiency corresponded to 2π.

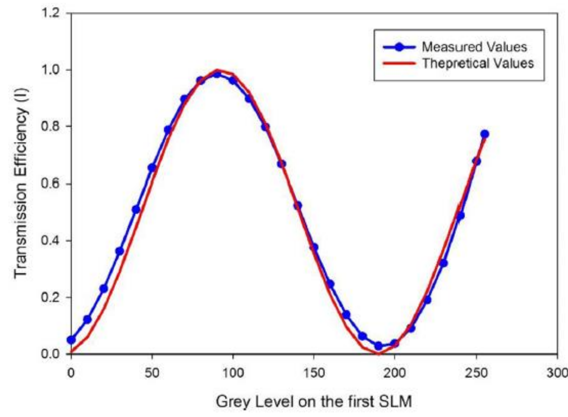

Figure 4. 8 Plotted measured and theoretical transmission efficiency of the SLM based on the equation 4-16.

As the input polarization is 45°, the output linear polarization state can therefore be rotated with the grey level on the SLM. The induced phase-delay has been found to be linearly related to [GL][204]. By combining equation 4-9 and 4-10, we can derive:

$$[\mathrm{GL}] = \frac{190}{2\pi}\arccos\left[\left(\frac{\mathrm{Y(m,n)}}{\alpha\mathrm{O(m,n)}} - \frac{1}{2}\right) \times 2\right] \qquad (4\text{-}18)$$

The equation 4-18 can therefore be used to shape the original beam into a flat-top distribution by altering grey level ([GL]) values on the SLM. Figure 4.16 shows a shaped beam with uniform distribution at the image plane.

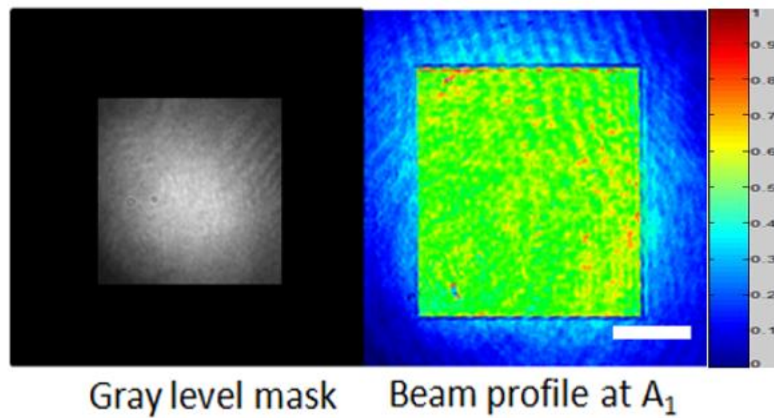

Figure 4. 9 The grey level mask with a grey level gradient (grey level: 0-255) and its observed result on the CCD beam profiler with normalized colorscale. The white scale bar is 10 μm.

4.6 Multiple parallel beam shaping with two SLMs

Further multiple parallel shaped beams can be produced by combining a second SLM (Hamamatsu X10468-03, 800x600 pixels) at the end of the long beam path (as shown in Figure 4.17). A half wave plate has been added before the SLM2 to modulate the polarization parallel relative to SLM2 fast axis for the onward multiple beam generation with the grey level CGHs. The first SLM is used to shape the Gaussian beam into different shapes and different distributions by applying binary or grey level masks as discussed,

the second SLM can be used for multiple spot generation with grey level CGHs. The grey level CGH used for multiple parallel spots generation was calculated by the Hamamatsu LcosControl software, as shown in Figure 4.18. This uses an Iterative Fourier-Transform Algorithm (IFTA) to generate an optimised CGH.

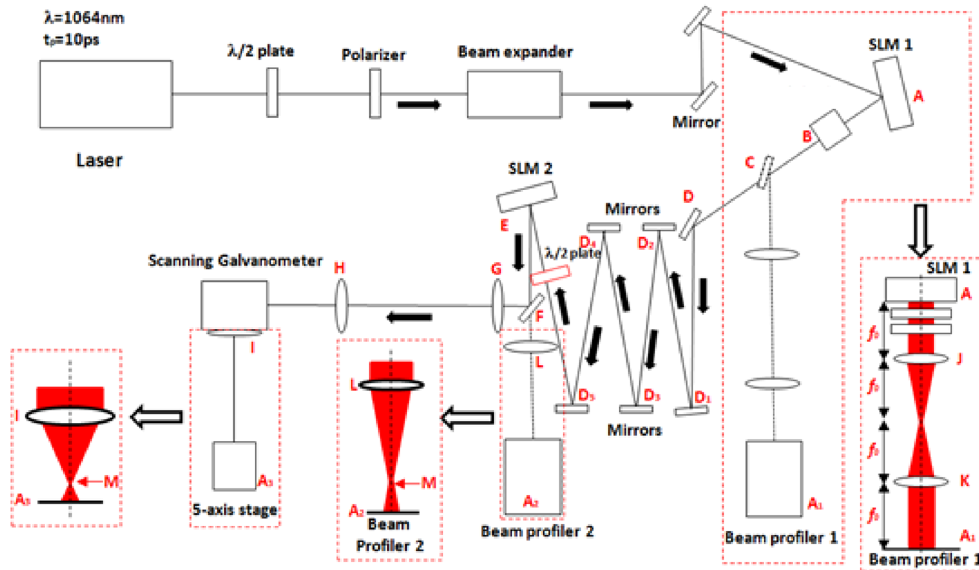

Figure 4. 10 Experimental setup for multipule shaped beam generation.

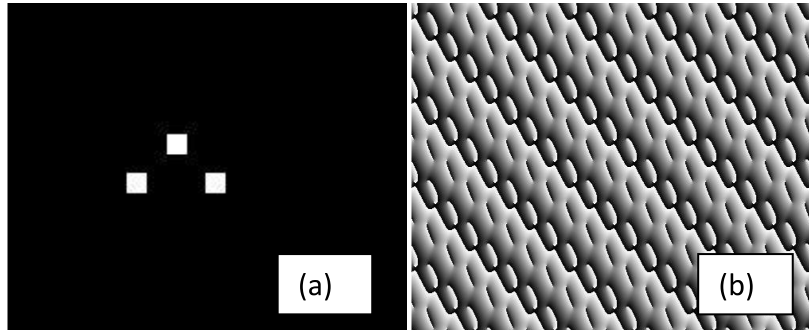

Figure 4. 11 Target multiple beam pattern and its CGH generating by Hamamatsu LcosControl (a) Target pattern (b) Generated CGH.

Further considering convolution theory, multiple complex light fields on the image plane depend on the Fourier Transformation of the applied grey level CGHs, FT (x_i, y_i), which can be expressed as:

$$\frac{1}{M} U_0 \left(-\frac{x_i}{M}, -\frac{y_i}{M}\right) * FT(x_i, y_i) = U_i(x_i, y_i) \quad (4\text{-}19)$$

where $U_i(x_i, y_i)$ is the amplitude at the image plane.

The advantage of using a grey level mask to achieve higher intensity uniformity can be seen in Figure 4.19.

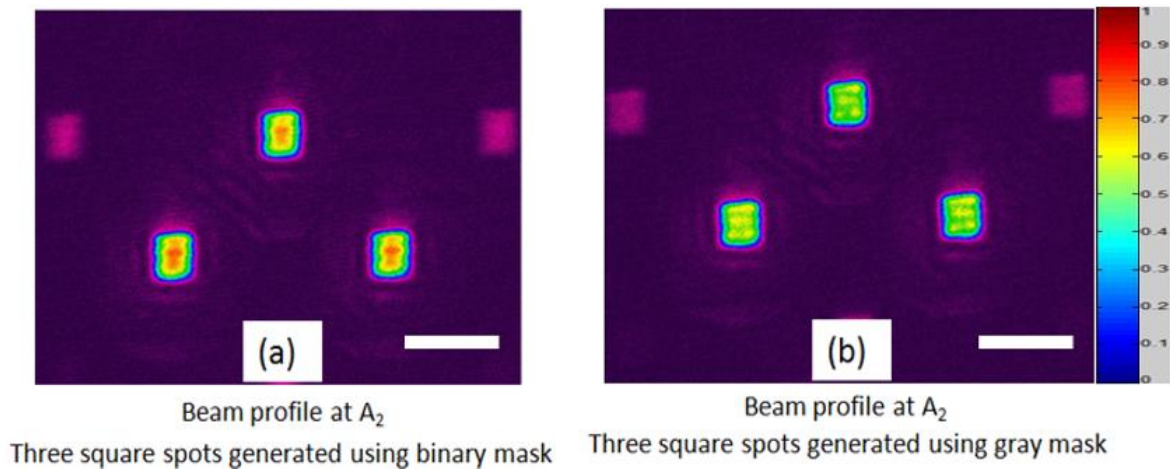

Figure 4. 12 Multiple squared beams produced at image plane with (a) binary mask (b) grey level mask with normalized colorscale. The white scale bar is 60 μm.

4.6.1 Beam shaping efficiency -with grey level masks

Using the same method of measuring beam shaping efficiency as with binary masks in section 4.4.3, the beam shaping efficiency with grey level masks can be obtained as shown in Figure 4.20.

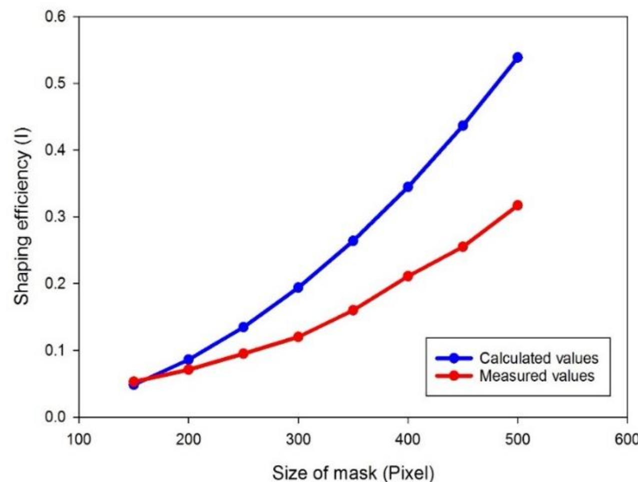

Figure 4. 13 Calculated and measured shaping efficiency of different size of grey level masks.

Comparing the beam shaping efficiency with binary masks (Figure 4.15) and grey level masks (Figure 4.20), the beam shaping efficiency with grey level masks was found to be lower. This is likely due to the limitation of the shaping capability of the SLM and the original distribution. For flat-top distribution generation using grey level masks, more energy at the beam centre has been removed, therefore a reduced usage of the available intensity.

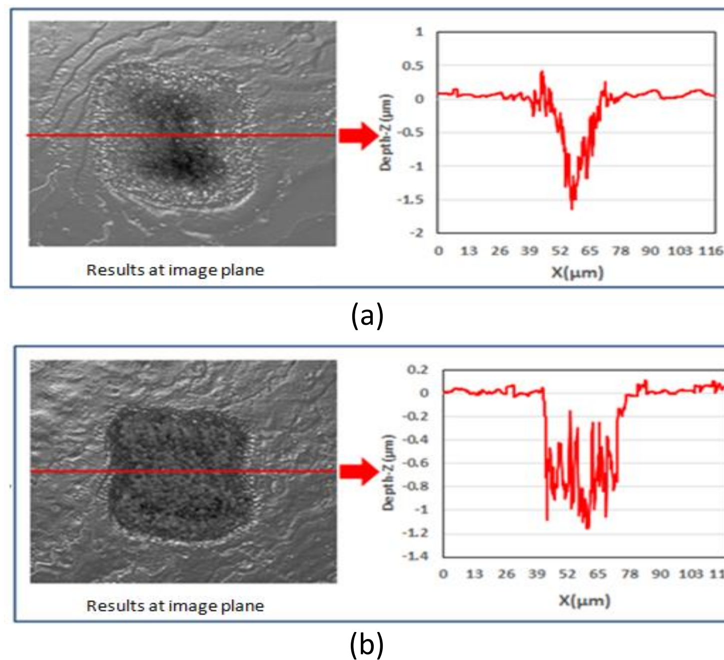

Figure 4. 14 WYKO image of machined footprints with binary and grey level masks at the image plane. (a) machined results with binary mask. (b) machined results with grey level mask. (10kHz, 10μJ, 1s, 0.19J/cm^2).

The shaping limitation using grey level masks can be demonstrated by measuring the intensities of all pixels in the CCD camera observed shaped area and compare with the original Gaussian beam (Figure 4.14). It can be seen in Figure 4.19 that the uniformity of the flat-top results on the image plane is not as well defined as the results observed at A_1. This is likely caused by knife-edge diffraction effects as the flattop beam is a diffracting beam. Most beam profiles can be produced if enough laser intensity is provided. However, there is a limitation between the shaped area and shaping quality, as the shaping area cannot be larger than the limitation of the 1/e^2 of the Gaussian distribution. Therefore, the beam shaping limitation with this technique is dependent on the beam mode or M^2 of the input laser.

4.7 Summary

This chapter demonstrated the radial or azimuthal polarization control with a beam shaping technique on the image plane. A spatial light modulator has been used for beam shaping with an applied a binary mask. A diffractive optical element, S-waveplate, has been used to control the output polarization from linear to radial or azimuthal. The output beam profile which has been converted effectively and observed at the lens image plane. A polished titanium sample was machined by the shaped beam at the imaging plane. The machined footprints have the corresponding shape and desired polarization state as confirmed by LIPSS structures. In addition, a novel ultrashort pulse laser beam-shaping technique to generate multiple geometric flattop beams has been demonstrated by combining grey level masks and grey level multiple spots generation CGHs. Beam shaping limitation is affected by the size and quality of the input Gaussian beam. The size of the footprint can be adjusted from the mask and comparable to the beam waist at the focal plane. The beam shaping method using binary masks and grey level masks presented in this chapter

is significantly more flexible and avoids complex CGH calculation. This technique potentially has applications in enhanced laser drilling, unique security marking and thin film processing.

Chapter 5
Generation of cylindrical vector beam arrays using binary CGHs

5.1 Introduction

Ultrafast laser processing with various polarization states have been widely studied and investigated in laser cutting [215], laser micro-drilling [216] and surface texturing [217]. Inhomogeneous polarization, such as radial and azimuthal polarization states are of increasing the interest in laser processing, such as laser cutting [37] and laser micro-processing [103] as they can improve the quality and efficiency. The methods of radial or azimuthal polarized beam generation include the use of diffractive optical elements (DOEs) [218] and spatial light modulators (SLM) [41]. More recently, a combination of a DOE with a SLM to generate tailored radial and azimuthal polarizations for laser material processing was demonstrated [131]. Azimuthal and radial polarization states are considered to be cylindrical vector (CV) states due to the polarized beams with cylindrical symmetry in polarization [219].

High processing throughput of ultrafast lasers can be achieved using diffractive multi-beam patterns generated by a spatial light modulator (SLM) for material surface processing [183, 220] and material inscription [184, 221]. Recently, multiple parallel spots have been employed using high average power at the 100W level (10ps) demonstrating multi- beam thin film patterning at 80cm^2/s [32]. For generating multi-beams using a SLM, a computer generated hologram (CGH) should be applied. There are many algorithms to generate CGHs, such as iterative Fourier transform algorithm (IFTA) [222], one being the Gerchberg-Saxton algorithm [193]. Diffraction efficiency is algorithm and geometry dependent. The CGHs are typically grey level phase holograms, in which the phase changes continuously from 0 to 2π. On the other hand , binary phase holograms, such as Dammann gratings, are much simpler and can produce equal-intensity spots at diffractive orders with good uniformity [223, 224] due to their phase changes involving only 0 and π. While laser generated parallel spots are often linearly polarized. Allegre et al, combined two SLMs with appropriate waveplates and grey level phase holograms to generate multiple vortex radial and azimuthal beam spots [41].

A method of multiple parallel beam shaping at the image plane with grey level CGHs was demonstrated in chapter 4. In this chapter, a SLM combined with a nanostructured S-waveplate have been used to generate multiple uniform laser beam arrays with plane wave radial and azimuthal polarization based on binary multiple spots generation CGHs. The binary CGH is also used for SLM performance tests under high average power (up to P=160W). LIPSS patterns have been used to indicate the polarization state of the laser beam on Titanium (Ti-6Al-4V) samples. A careful analysis of theoretically expected with experimentally measured ring and Gaussian mode intensity distributions allowed a comparison of ablation thresholds.

A scalable approach associated with light phase control has been applied for confirming the vector purity of multiple spots.

5.2 Experimental

5.2.1 Experimental setup

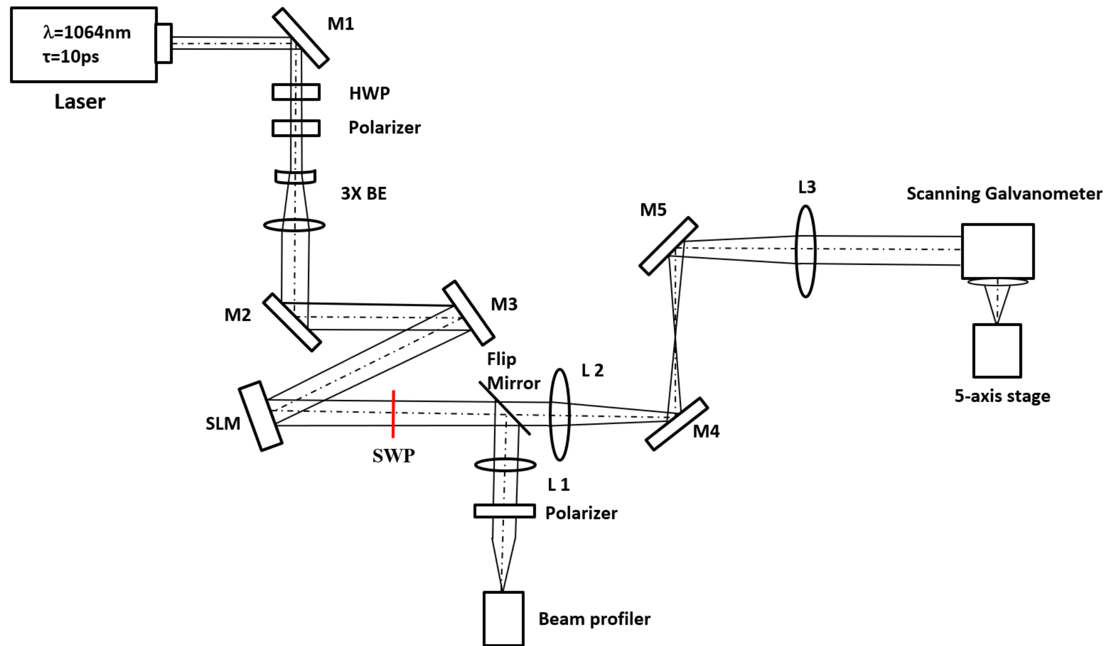

Figure 5. 1 Experimental setup with an S-waveplate

Figure 5.1 shows a schematic of the experimental setup. The ultrafast laser system used for this research is a custom made Nd: VAN seeded regenerative amplifier laser (High-Q IC-355-800ps, Photonic Solutions). A linear polarized laser beam (horizontal, parallel to long axis of SLM): τ=10ps, λ=1064nm, PRF=10kHz passes through a half wave plate and Glan-laser polarizer used for adjusting power and polarization direction, a beam expander (M ≈ ×3), and two plane mirrors (M2 and M3) for controlling the beam path and illuminated on a reflective phase only SLM. The beam size at the SLM is approximately 8mm. A Hamamatsu X10468-03 liquid crystal on silicon (LCoS) SLM was used with 800 × 600 pixels and dielectric coated for 1064 nm wavelength (reflectivity ≈ 95%, fill factor 98%). A combined hologram with a desired Dammann grating and Fresnel zone lens was applied on the SLM. The beam was then passed through a nanostructured S-waveplate (SWP, Altechna, RPC-1030-10-109) to modulate the polarization state to Radial or Azimuthal. A flip mirror has been placed after the S-waveplate to direct the beam to a CCD based beam profile (Spiricon, SP620U) for observation. A focusing lens (L1, f=500mm) and a polarizer were used to analyse and confirm the polarization states. With the flip mirror removed, 4f imaging system (L2 and L3, f=400mm) imaged the SLM complex field to the input aperture of a galvo scanner (Nutfield-XLR8-14) via periscope mirrors M4 and M5. The laser beam was focused with a flat field f-theta lens (f=100 mm, Linos). The focused Gaussian beam size is 25 μm in diameter.

For processing experiments, samples were mounted on a precision 5-axis (x, y, z, u, v) motion control system (A3200 Ndrive system, Aerotech) for precise location of the focal plane. Polished Ti-6Al-4V and thin film Chromium on glass were used as sample substrates.

The SLM in this work has been used to generate multiple beams with 1x5, 2x2 and 5 x 5 Dammann gratings. In order to defocus the zero order, a Fresnel zone lens has also been combined with the Dammann grating to tune the degree of defocusing at the processing plane. Calculation of the Dammann gratings was accomplished in MATLAB, with numerical data used from Zhou et al [156]. With the nano-structured S-waveplate positioned close to the SLM and low angles of diffraction, multi-cylindrical vector beam arrays were generated.

5.2.2 Polarization control using an S-waveplate

Linear or circular polarized beams can be used with polarization converters such as an S-waveplate. For the incident linearly polarized beam, the S-waveplate due to the spatially dependent birefringence rotates the incident linear polarization by the angle necessary to produce a radial distribution of the electric field. The Jones matrix can be used to describe the polarization transformations appropriately. The S-waveplate can be represented by a Jones matrix as [134]:

$$M_s=\begin{pmatrix}\cos\emptyset & -\sin\emptyset \\ \sin\emptyset & \cos\emptyset\end{pmatrix} \tag{5-1}$$

where $\emptyset$ is the polar angle, so the polarization states after the S-waveplate is position dependent. The horizontal linear polarization can be expressed as:

$$M_l=\begin{pmatrix}1 \\ 0\end{pmatrix} \tag{5-2}$$

The output polarization for radial polarization is then given by the Jones matrix:

$$J_{rad}=\begin{pmatrix}\cos\emptyset & -\sin\emptyset \\ \sin\emptyset & \cos\emptyset\end{pmatrix} \times \begin{pmatrix}1 \\ 0\end{pmatrix} = \begin{pmatrix}\cos\emptyset \\ \sin\emptyset\end{pmatrix} \tag{5-3}$$

The azimuthal polarized beam can be generated by rotating the fast axis of the S-waveplate 90°, giving:

$$J_{azi}=\begin{pmatrix}\cos\left(\emptyset+\frac{\pi}{2}\right) \\ \sin\left(\emptyset+\frac{\pi}{2}\right)\end{pmatrix} = \begin{pmatrix}-\sin\emptyset \\ \cos\emptyset\end{pmatrix} \tag{5-4}$$

These two polarisation states are orthogonal since the matrix product of these two states (transpose of 5-3) with 5-4 is zero:

$$J=\begin{pmatrix}\cos\emptyset & \sin\emptyset\end{pmatrix} \times \begin{pmatrix}-\sin\emptyset \\ \cos\emptyset\end{pmatrix} = -\cos\emptyset\sin\emptyset + \sin\emptyset\cos\emptyset = 0 \tag{5-5}$$

By combining the use of a half wave plate, an S-waveplate and a polarization analyzer, the polarization purity of the generated CV beam has measured to be approximately 88%. The details of the S-waveplate polarization purity measurement is discussed in chapter 3.

5.3 Results and discussion

5.3.1 Cylindrical vector (CV) beams generation

For single CV beam generation, a reflective mirror was used instead of the SLM and the results were observed on the CCD beam profiler. Figure 5.2(a) shows a single cylindrical vector azimuthally polarized beam can been observed on the Spiricon CCD beam profiler without a polarizer. The radial and azimuthal polarization purity was measured to be approximately 88%. This was confirmed using a polarizer. Figure 5.2(b) shows an SEM image of the surface processing of Ti-6Al-4V with CV polarization state, confirming that is indeed azimuthal polarized. With polarizer added, Figure 5.2 (c-f) show the intensity profile observed when rotating the polarizer transmission axis, confirming the azimuthal state.

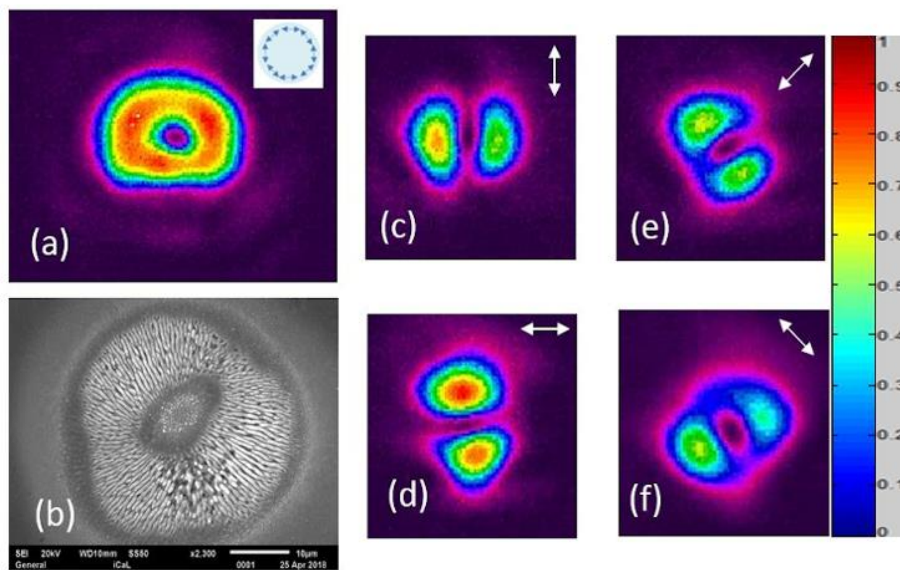

Figure 5. 2 Azimuthally polarized single beam observed on a Spiricon CCD beam analyzer. (a) The beam profiler image. The small image on the right top is the electric field direction. (b) SEM image to confirm the azimuthal polarization state (Ti-6Al-4V,10kHz, 4μJ/pulse, 50pulses). The scale bar is 10 μm. (c)-(f) The beam profile images with a polarizer analyser. The white arrows represent the direction of the fast axis of the polarizer analyser. The double lobe intensity distribution rotates as expected with the polariser fast axis but also highlights some non-uniformity in the ring intensity mode due likely to residual wavefront aberration of the incident Gaussian beam.

Figure 5.3 (a) shows a single cylindrical vector radially polarized beam can been observed on the Spiricon CCD beam profiler without a polarizer. Figure 5.3 (b) shows an SEM image of the surface processing of Ti-6Al-4V with CV polarization state, confirming that is indeed radially polarized. With polarizer added,

Figure 5.3 (c-f) show the intensity profile observed when rotating the polarizer transmission axis, confirming the radial state.

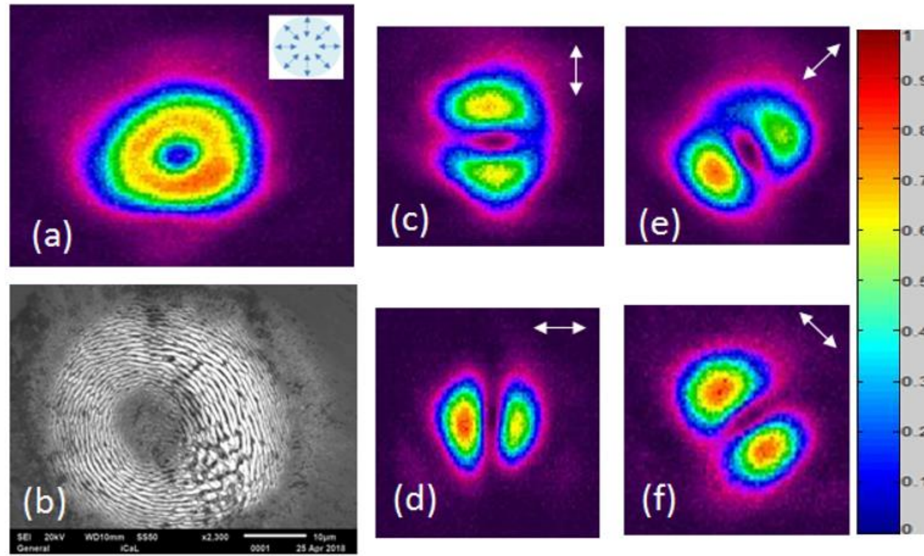

Figure 5. 3 Radially polarized single beam observed on a Spiricon CCD beam analyzer. (a) The beam profiler image, radial polarization. The small image on the right top is the electric field directions. (b) SEM image to confirm the polarization state (10kHz, 4μJ/pulse, 50pulses). The scale bar is 10 μm. (c)-(f)The beam profile images with a polarizer analyser. The white arrows represent the direction of the fast axis of the polariser. Again, the double lobe intensity distribution rotates as expected with the polariser fast axis but highlights some non-uniformity in the ring mode possibly due to the non-perfect Gaussian beam.

5.3.2 Ablation test on Ti-6Al-4V and Cr thin film with Gaussian and CV beam

The ablation threshold fluence for a Gaussian beam can be obtained from the equation [225]:

$$D^2 = 2{w_0}^2 \ln(F_0 / F_{th}) \tag{5-6}$$

where D is the ablated crater diameters, w_0 is the beam waist radius, F_0 is the applied peak fluence and F_{th} is the threshold fluence for a material. The near Gaussian laser beam was focused by a flat field f-theta lens (f=100mm), the measured beam diameter was $2\omega_0 = 22.0 \pm 0.2\mu m$.

5.3.2.1 Intensity comparison of Gaussian and CV beams

The intensity of Gaussian and CV beams have been modelled and compared with calculations using MATLAB. The equation used to describe the ring beam amplitude is that used for describing a vortex beam given by [226]:

$$E(r, \theta, 0) = E_0 \frac{1}{\sqrt{m!}} \left(\sqrt{2} \frac{r}{\omega_0}\right)^m \exp\left(-\frac{r^2}{\omega_0^2}\right) \exp(im\theta) \tag{5-7}$$

where E_0 and ω_0 refer to the amplitude of the normalized electric field and Gaussian beam waist, respectively; m is the topological charge, θ is the phase angle ranging from 0 to 2π. By setting m = 0, one obtains the Gaussian amplitude distribution while setting m =1, the ring mode amplitude for CV

beam profiles is obtained. The intensity distribution for m = 1 is given by $I = E^* * E$ which immediately yields,

$$I(r) = E^* * E = 2I_0(\frac{r^2}{\omega_0^2})\exp(-2(\frac{r^2}{\omega_0^2})) \tag{5-8}$$

where I_0 is the peak intensity of the Gaussian from which the CV beam is transformed. This function goes to zero at r = 0 as expected. To find the ring maxima, differentiating (8) and setting the derivate to zero, we find the simple solutions:

$$r = \pm\omega_0/\sqrt{2} \tag{5-9}$$

for the position of the ring maxima where ω_0 is the $1/e^2$ Gaussian beam radius. Setting this value of r into equation (8), we arrive at the absolute peak intensity of the ring beam given by $I(r = \omega_0/\sqrt{2}) = I_0/e$ where e = 2.718 is the natural logarithm. By integrating (8) round 2π to obtain the total pulse power P, we obtain

$$P(\text{ring}) = 4\pi I_0 \int r\,(r/\omega_0)^2 \exp(-2(r/\omega_0)^2)\,dr = I_0(\pi\omega_0)^2/2 \tag{5-10}$$

Similarly, $P(\text{Gauss}) = 2\pi I_0 \int r \exp(-2(r/\omega_0)^2)\,dr = I_0(\pi\omega_0)^2/2$ confirming that these beams have the same total power or pulse energy.

Figure 5.4 shows the shows the simulated intensity distributions of the Gaussian and ring CV beams in MATLAB.

The simulated ratio of peak intensities $\frac{\text{Intensity}_{PG}}{\text{Intensity}_{PCV}} = 2.7(\sim e)$ in agreement with that expected. Hence, if ablation threshold is unaltered by the ring intensity distribution, the pulse energy of the CV beam should be 2.7 times higher than the Gaussian beam for the same effect. The simulation in Matlab will be used for onward comparison with experimental results.

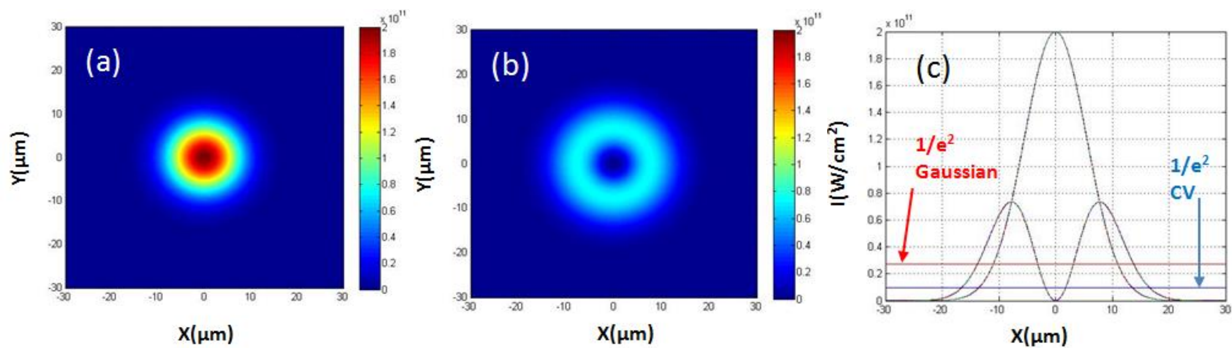

Figure 5.4 The simulated intensity distribution in MATLAB: (a) a Gaussian distribution, m = 0. (b) a CV beam distribution, m=1 with the same total pulse energy. (c) Cross section view of a Gaussian distribution and a CV beam distribution. The two lines show the $1/e^2$ intensity levels, red line for the Gaussian distribution beam and blue line for the CV beam distribution.

The Gaussian beam waist ω_0 used in this case is 11.0μm. After calculation, the CV beam diameter is approximately 36μm at $1/e^2$. Experimental comparison was made of the Gaussian and CV beams generated with the S-wave plate using a spiricon camera (SP620U), as shown in Figure 5.5.

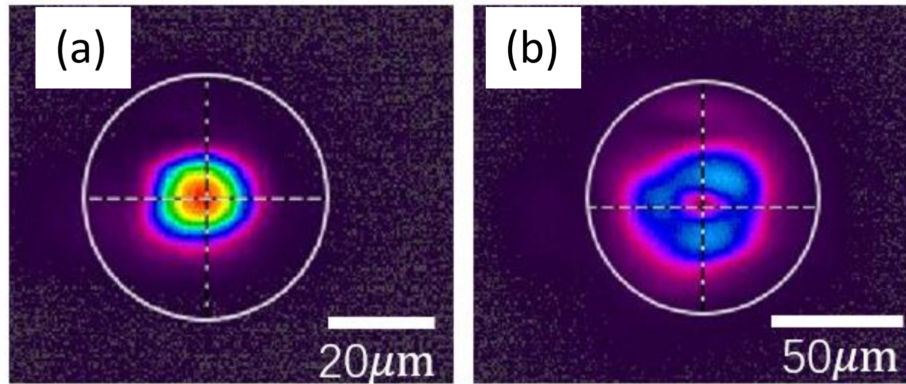

Figure 5. 5 Measured beam intensity using Spiricon SP602U. (a) the intensity of a Gaussian beam. (b) the intensity of a CV beam with S-waveplate. A focus lens with focal length of 500mm was used to ensure more pixels were activated for measurement. Intensities are measured with the same input power. Both images are with the same scale when measuring.

Measured data is shown in table 5.1 with total integrated powers of a Gaussian beam and corresponding CV beam and peak intensities. Powers agree within 2% and the ratio of peak intensity $\frac{\text{Intensity}_{\text{PG}}}{\text{Intensity}_{\text{PCV}}}$ =2.74 close to e = 2.72.

Table 5. 1 Measured results using the Spiricon camera

	Gaussian beam	CV beam
Total power (mW)	74.2	75.8
Peak intensity (W/cm^2)	35.16 x10^4	12.84 x10^4

These results support the view that the theoretical intensity distributions and those calculated in MATLAB for Gaussian and ring CV beams for m=1 are in agreement.

5.3.2.2 Single beam Surface Ablation with Gaussian and Ring modes

An issue with CV beams is being able to define the beam size and peak intensity in the same terms as a Gaussian beam. A comparison was made with vortex beams generated by the SLM without S-waveplate. Peak intensity and effective of vortex beams can be calculated from Eq 5-7. CV beams could be therefore be defined in similar terms it shown to give similar results. Figure 5.6 presents optical and SEM images of the ablated Cr thin film surface with radially polarised single pulse with the centre region (below ablation threshold) remaining.

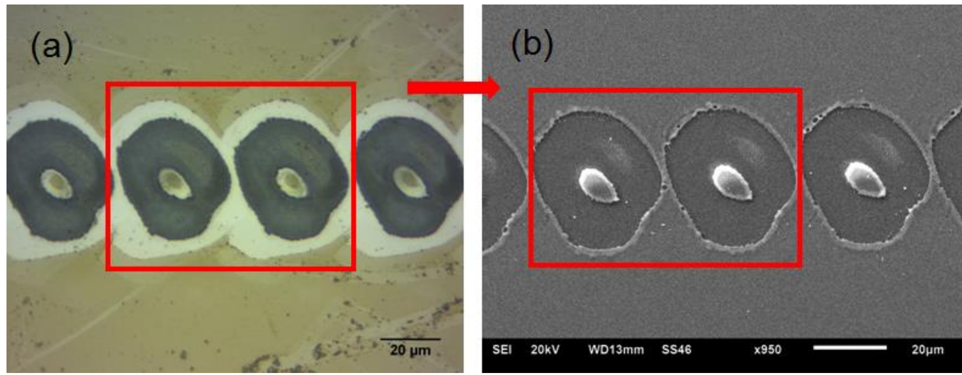

Figure 5. 6 (a) optical image of ablated Cr thin film with CV single pulse. (b) SEM image of ablated Cr thin film with CV single pulse. (22µJ/pulse,10kHz,400mm/s), showing the ring structure.

Figure 5.7 compares the ablated beam size for an m=1 vortex beam (using spiral CGH) and Radially polarised (with same pulse energy) on thin film Chromium on glass. These have similar dimensions as expected.

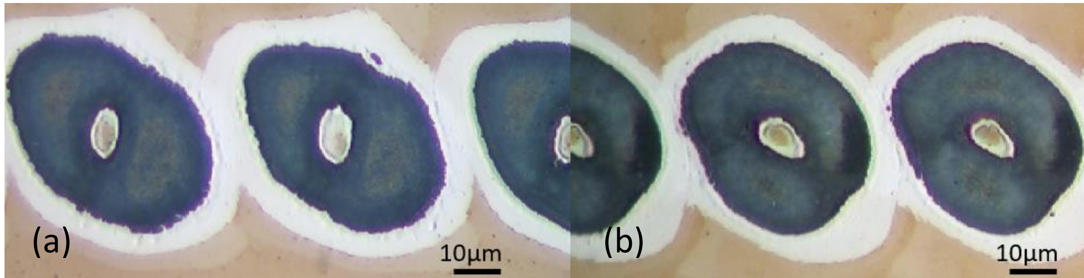

Figure 5. 7 Single pulse ablation with (a) vortex beam (m=1) and (b) CV beam (Radial) on Cr coated thin film. By overlapping two images, the beam size for m=1 and CV beam are similar (30µJ,10kHz, 500mm/s).

Figure 5.8 shows the relevant plots for obtaining the threshold energies required for modification on both Titanium and Chromium thin film. With the Gaussian beam, D^2 versus ln E yields the gradient m = $2(\omega_0)^2$ allowing the peak fluence to be calculated. However, for the ring mode, at fluence threshold, a thin ring with diameter $D_0 = \sqrt{2}\omega_0$ would be ablated while above this, the ring width will expand with increasing fluence. Hence, a plot of $D^2 - D_0^2 = D^2 - 2\omega_0^2$ versus ln E yields the threshold ablation energy for the ring mode at the cut off.

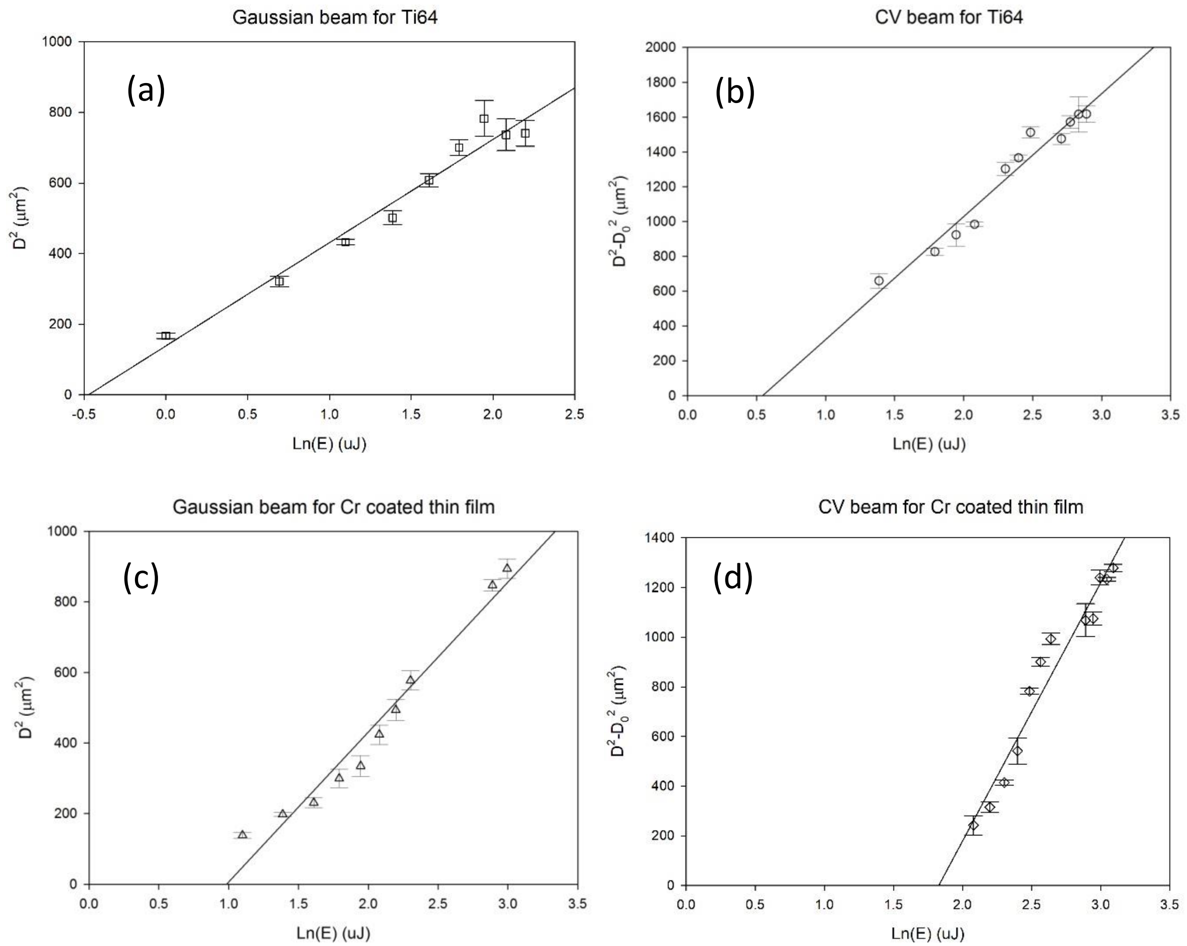

Figure 5. 8 (a) Plot of squared diameter $\mathbf{D^2}$ versus ln(E) for Gaussian beam ablation threshold fluence calculation of Ti-6Al-4V with single pulse (b) Plot of $\mathbf{D^2 - D_0^2}$ versus ln(E) for radially polarised CV beam ablation threshold energy calculation of Ti-6Al-4V with single pulse (c) Plot of squared diameter $\mathbf{D^2}$ versus ln(E) for Gaussian beam ablation threshold fluence calculation of Cr coated thin film with single pulse (d) Plot of $\mathbf{D^2 - D_0^2}$ versus ln(E) for CV beam ablation threshold fluence calculation of Ti-6Al-4V with single pulse.

From Figure 5.8, the threshold ablation energies for Ti-6Al-4V with a Gaussian beam mode and CV beam mode are 0.63μJ and 1.77μJ respectively. The ratio of the cut-off energy is $\frac{1.77\mu J}{0.63\mu J} = 2.81{\pm}0.03$, close to the value e = 2.72 calculated above required to bring peak intensity in the ring and corresponding peak fluence to that of the Gaussian. As the single pulse threshold fluence of the Gaussian and CV beams from above is Fth = 0.32 ± 0.02 J/cm^2 and 0.31 ±0.02 J/cm^2 respectively, in excellent agreement. The cut-off energy for Cr coated thin film with a Gaussian beam mode and CV beam mode is 2.67μJ amd 6.22μJ respectively, the ratio of the cut-off energy is $\frac{6.22\mu J}{2.67\mu J} = 2.32{\pm}0.03$, lower than expected. The ablation thresholds of Cr thin film with Gaussian and CV single pulse are 1.38±0.02J/cm^2 and 1.73±0.02J/cm^2 respectively. This was surprising but this substrate may be more sensitive to beam aberrations.

We have modelled ring beams with higher m values and the resulting intensity distributions, details are in Table 2. These functions show that peak ring intensities drop with increasing m – while the peak radii increase. Integrating these functions round 2π all yield the same power ($P = I_0\ \pi\omega_0^2/2$) and pulse energy. Again, ω_0 is the Gaussian beam $1/e^2$ radius from which these intensity profiles are generated and I_0 the Gaussian peak intensity.

Table 5. 2 Peak intensity with different topological charge m and corresponded maximum r where $\boldsymbol{\omega_0}$, $\mathbf{I_0}$ is beam waist and peak intensity of a Gaussian mode.

Topological charge m	max r	Peak intensity expression	Peak intensity
1	$\omega_0/\sqrt{2}$	$2I_{peak} * \frac{r^2}{\omega_0^2} * \exp\left(-2\frac{r^2}{\omega_0^2}\right)$	I_0/e
2	ω_0	$2I_{peak} * \frac{r^4}{\omega_0^4} * \exp\left(-2\frac{r^2}{\omega_0^2}\right)$	$2I_0/e^2$
3	$\sqrt{3}\omega_0/\sqrt{2}$	$\frac{4}{3}I_{peak} * \frac{r^6}{\omega_0^6} * \exp\left(-2\frac{r^2}{\omega_0^2}\right)$	$9I_0/2e^3$
4	$\sqrt{4}\omega_0/\sqrt{2}$	$\frac{2}{3}I_{peak} * \frac{r^8}{\omega_0^8} * \exp\left(-2\frac{r^2}{\omega_0^2}\right)$	$32I_0/3e^4$

Figure 5.9 shows the ablation plots of ln(E) vs $D^2 - D_0^2$ for m=1 and m=2 vortex beam.

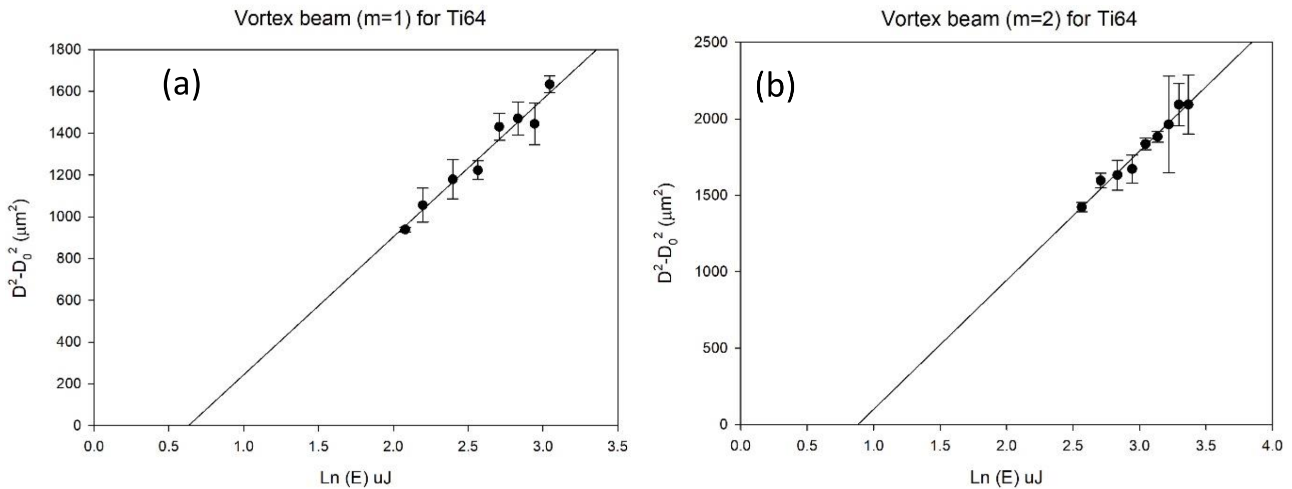

Figure 5. 9 (a) Plot of squared diameter $\mathbf{D^2 - D_0^2}$ versus ln(E) for vortex beam (m=1) ablation threshold fluence calculation of Ti-6Al-4V with single pulse (b) Plot of $\mathbf{D^2 - D_0^2}$ versus ln(E) for vortex beam (m=2) ablation threshold energy calculation of Ti-6Al-4V with single pulse.

The threshold ablation energy for Ti-6Al-4V with a vortex beam (m=1) and vortex beam (m=2) is 1.87μJ and 2.41μJ respectively, the ratio of the cut-off energy is $\frac{2.41\mu J}{1.87\mu J} = 1.29\pm0.03$. This is very close to the

value e/2 = 1.35 that is calculated from table 2 so that ablation threshold for m=2 is similar to that for m=1 and the Gaussian beam. The ratio of the cut-off energy for comparing m=1 and Gaussian beam is $\frac{1.87\mu J}{0.63\mu J} = 2.96 \pm 0.03$, slightly higher than expected (e ≈ 2.7) ration from table 2. The ratio of the cut-off energy for comparing m=2 and Gaussian beam is $\frac{2.41\mu J}{0.63\mu J} = 3.82 \pm 0.03$, slightly higher than expected ($e^2/2 \approx 3.7$) ratio from table 2. With the same peak intensities of Gaussian, the m=1 and m=3 ring beams were used to ablate a polished Ti-6Al-4V sample with clear surface LIPSS, shown in Figure 5.10. The ablated widths were 20μm, 45μm and 82μm with scan speeds s=20mm/s, 33mm/s and 36mm/s respectively. Processing rates or area coverage were therefore increased by a factor of 3.7(m=1) and 7.4 (m=3) respectively.

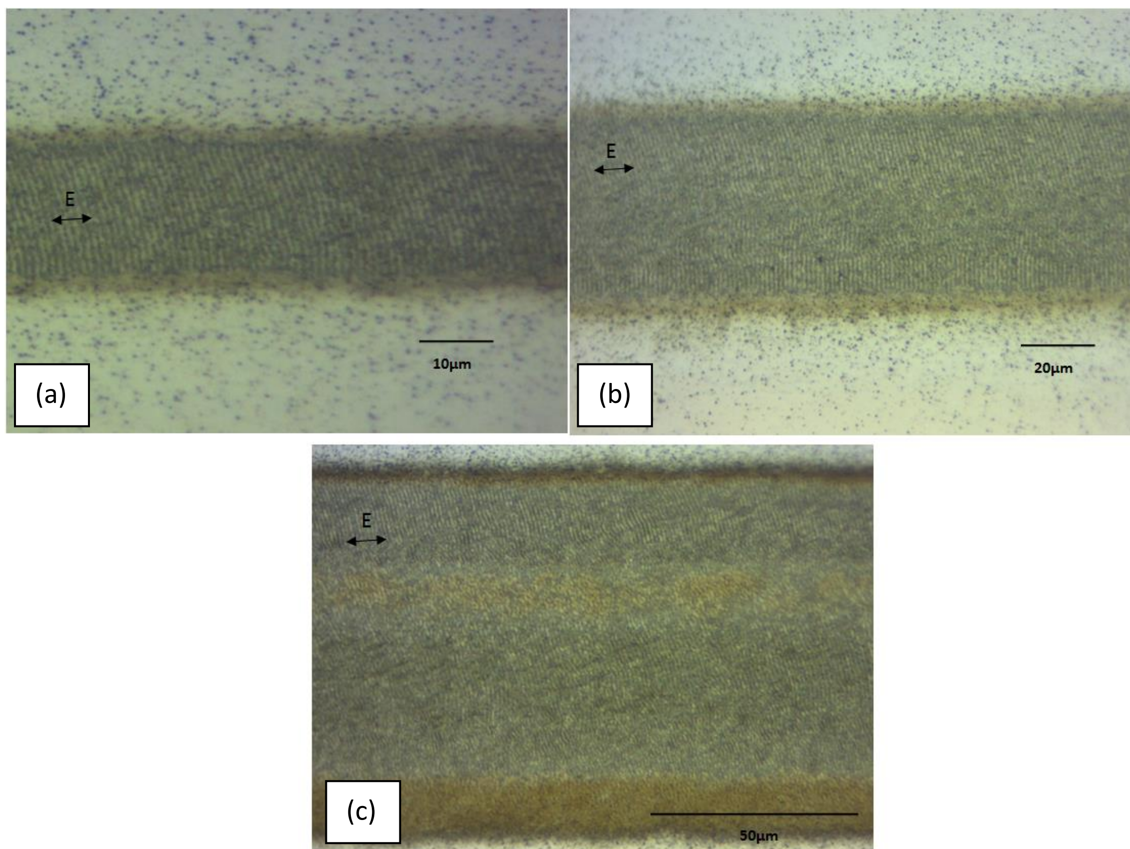

Figure 5. 10 Laser ablated polished Ti-6Al-4V with (a) Gaussian beam, 15mW (b) m=1 vortex beam, 42mW (c) m=3 vortex beam, 70mW. All beams have the same peak intensities (fluence).

5.4 Multiple cylindrical vector (CV) beam generation

Two binary gratings on the SLM, 1x5 and 2x2 Dammann gratings were generated by Matlab and have been used to create uniform multiple cylindrical vector beams with the S-waveplate. The transition points (the minimum distance between two different continuous transition points is the feature size of a Dammann grating, as shown in figure 5.11.) within a single period of 0.03863, 0.39084, 0.6555 and 0.5 as described in [156] have been used for the 1x5 Dammann grating and 2x2 Dammann grating generation

respectively. Figure 5.11 shows the details of the generated Dammann gratings. A Dammann grating consists of many grating unit cells, each having two grey levels (normally white and black, corresponding to 0 and π). The intensity and uniformity of the output beam arrays based on a Dammann grating will be affected by the grey level values of the grating unit cell. The uniformity of the parallel spots generated have been measured with equation of $\eta = \frac{\sigma_i}{a_i}$, where σ_i and a_i are the standard deviation and the arithmetic mean of the ablated spot diameters. The results of a study at various grey levels on Ti-6Al-4V can be seen in Figure 5.12. The uniformity of the spots reached the highest at the grey level of 107(for the Hammatsu 10468-03, the full 2π phase modulation corresponds to grey level 212). Thus, the grey level value of 107which corresponds closely to π has been selected for both Dammann gratings used in this study to achieve the highest uniformity. The measured diffraction efficiency of the calculated 1x5 Dammann grating and 2x2 Dammann grating with a grey level value of 107 are 77% and 81% respectively.

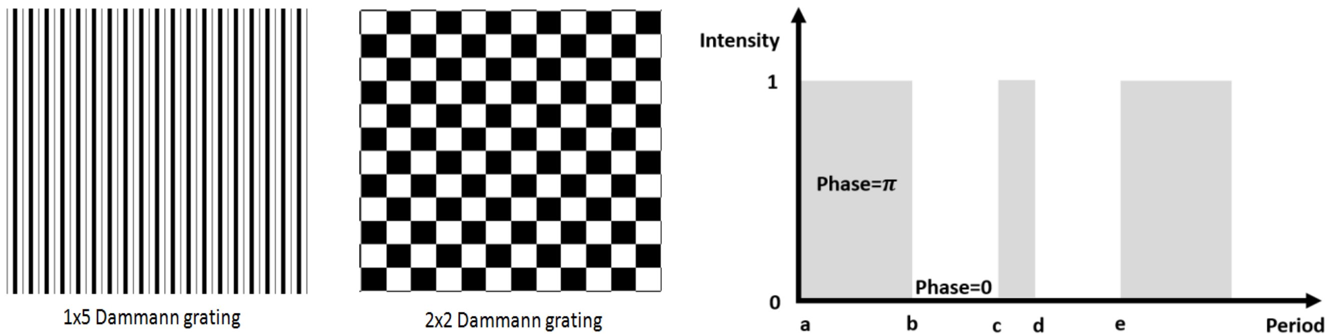

Figure 5. 11 1x5(left) and 2x2 (middle) Dammann gratings and a Dammann grating with transition points, a-e (right).

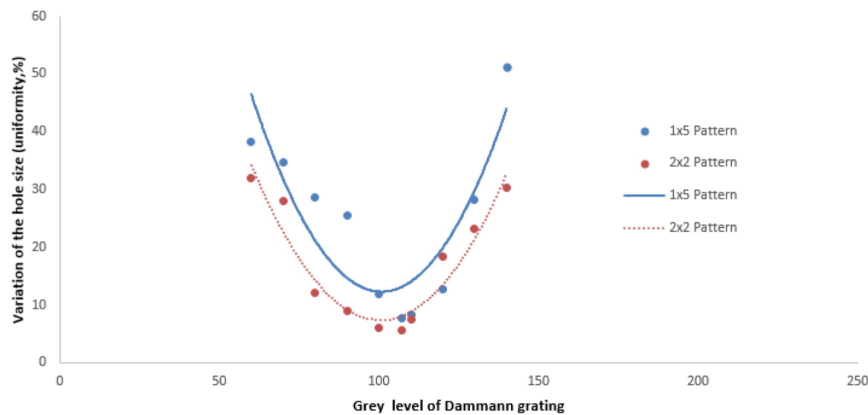

Figure 5. 12 Uniformity η of the ablated spot diameters on Ti-6Al-4V with variation of grey level of the binary Dammann grating. (10kHz, 20μJ/pulse, 100pulses).

Multiple cylindrical vector beams can then be generated by combining the optimized binary Dammann grating on the SLM with the S-waveplate. A schematic of multiple vector beam generation can be seen in Figure 5.13, where the 0th order is present at the centre of in the beam profiler images. In order to reduce the 0th order intensity, a Fresnel zone lens hologram can be used.

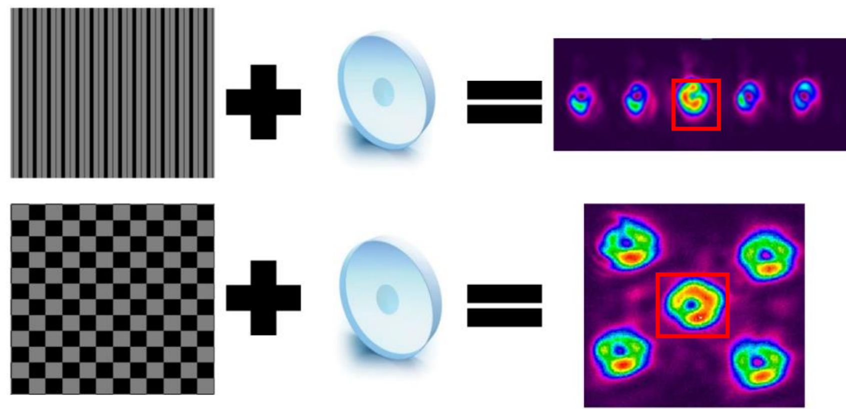

Figure 5. 13 Multiple vector beam generation, by combing binary Dammann gratings with an S-waveplate. The red squares indicate the 0-th order.

5.5 Reducing intensity of zero order

The zero order (0-th order) of a diffractive pattern will degrade the uniformity of a parallel machined pattern as it will typically have higher power compared with the other diffractive orders. Generally, if the 0-th order can be removed before processing, the uniformity of the machined results will be improved. Here, a Fresnel zone lens (FZL) has been used to defocus the 0-th order away from the generated beam array centre. Figure 5.14 shows a schematic for the mechanism of 0-th order optimisation. The FZL applied to the SLM can be used to achieve the defocus diffractive pattern. The separation: $|\Delta d| = |f_0 - d2| = |f0 - (f_{FZL}f_0 - f_0 d1)/(f_{FZL} + f_0 - d1)|$ can be used to calculate the space between 0-th order and diffractive pattern, where d1 is the distance between FZL and f-theta lens, d2 is the distance between f-theta lens and sample plane. When $\Delta d > 0$ the added FZL works as a positive lens, and when $\Delta d < 0$ it works as a negative lens.

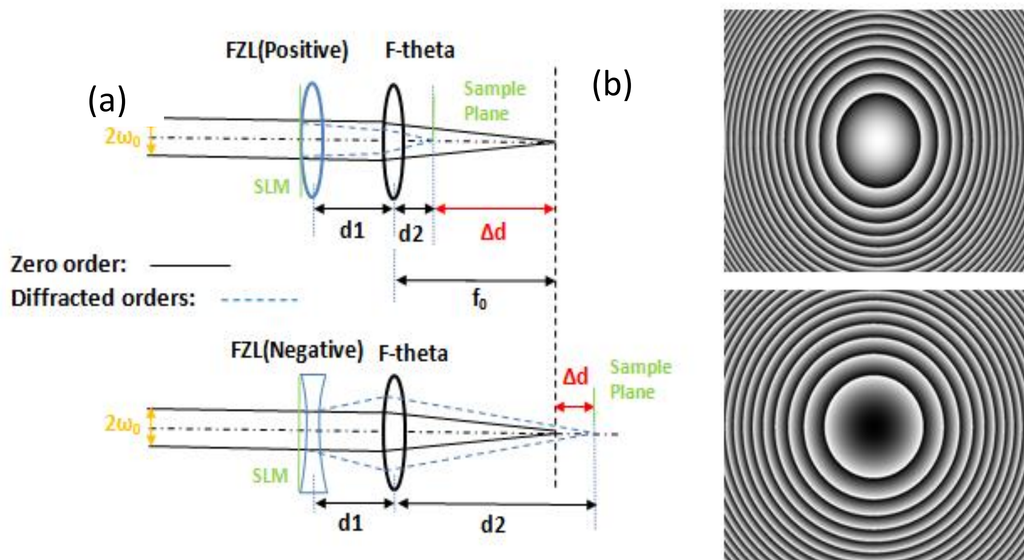

Figure 5. 14 (a)Schematic showing the method of 0-th order removal with a Fresnel zone lens (FZL). (b) The upper is the hologram of a positive FZL and the lower image is the hologram of a negative FZL.

5.6 Measuring cylindrical vector beams

5.6.1 Measuring of single CV beam

There is increasing current interest in cylindrical vector beams which exhibit a polarization singularity at their centre [219] and when scalar with a uniform polarization, carry Orbital Angular Momentum, (OAM) quantized in terms of $\hbar/2\pi$ [219]. These states can be represented on a High Order Poincare sphere (HOPS) with right and left hand polarized vortex beams at the poles while vector vortex beams appear around the equator of the sphere with Radial and Azimuthal polarisations on opposite sides [219, 227]. The quality of scalar laser beams with fixed polarization and Gaussian like intensity profile is generally defined in terms of the beam quality M^2 [228]. Therefore, measuring the quality of a vector mode is very important and useful to identify the quality of a vector beam. Bienvenu Ndagano et al [229] applied a quantum tool to measure the vector quality factor (ranging from 0 (scalar, uniform polarisation) to 1 (complete vector, inhomogeneous polarization)) of a single vector/scalar vortex beam. Ebrahim Karimi et al [230] presented a measurement of correlated photon pairs with hybrid entanglement between spin and orbital angular momentum. Due to the coupling of the polarization and spatial modes of a CV beam, these degrees of freedom (DOF) are nonseparable. Therefore, measuring the Bell inequality of a CV beam will indicate the correlation of the degree of polarization and spatial mode [231]. The creation of multi-beams is important for increasing throughput of any given application of structured light, for example, in optical tweezers or laser processing hence there is a need to measure vector quality factor (VQF) for multi-beam vector vortex states.

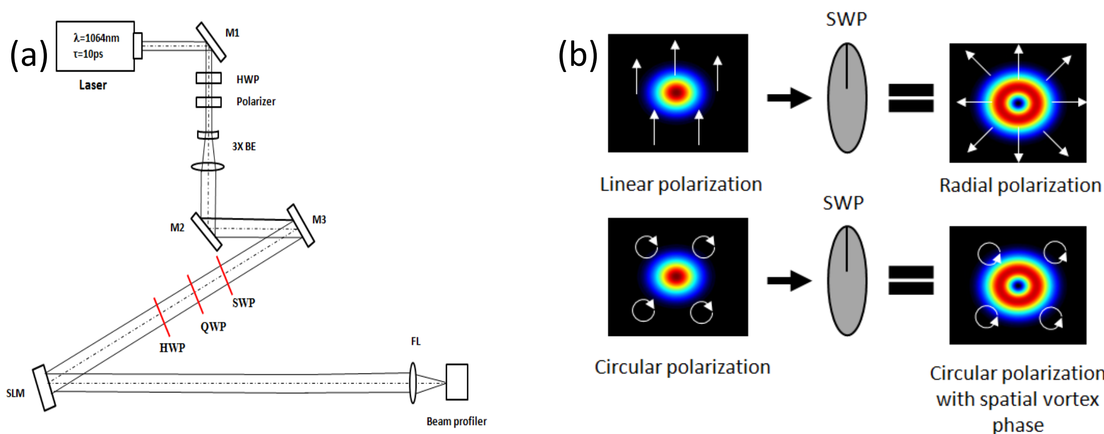

Figure 5. 15 (a) Experimental setup for a single CV beam measurement (b) Summarization of polarization selection of an S-waveplate. The polarization state on the SLM is mixed and dependent on the fast axis angle of the QWP and HWP.

First, we measured the concurrence and entanglement entropy of a single vector vortex beam with necessary optics and devices. Experimental setup as shown in Fig 5.15 (a) with a quarter wave plate (QWP). The QWP was inserted to achieve full state tomography in including both polarization and orbital angular momentum (OAM) states. The superposition states and pure states (left and right circular

polarizations with associated QWP fast axis angle ±45°) of polarizations and OAM modes ($l \pm 1$) will be invloved. On-axis intensity was recorded using a CCD camera (Spiricon SP620) by rotating the half wave plate angle (θ_1) and encoded hologram angle (θ_2, six OAM states, as shown in Figure 5.16). The S-waveplate employed in this work with a polarization selection ability as summarized in Figure 5.15 (b). If the orientation of the input polarization state is parallel to the fast axis of the SWP, then the output polarization state is radial, otherwise the output polarization is azimuthal. If the input beam is circularly polarized, then output beam is circularly polarized but with vortex phase.

The vector quality factor (VQF) of a beam can be determined by entropy of entanglement (E) or concurrence (C) [229]. The concurrence C can be calculated by

$$VQF = Re(C) = Re(\sqrt{1 - s^2}) \quad (5\text{-}11)$$

where Re means real part. For the on-axis intensities measured on a CCD camera, the Re is not necessary in here. Thus, Eq.(5-11) can be simplified to $C = \sqrt{1 - s^2}$. Where the s is the length of the Bloch vector, which is defined as

$$s = (\sum_i \langle \sigma_i \rangle^2)^{1/2} \quad (5\text{-}12)$$

Here i=1,2,3 and σ_i are the expectation values of the Pauli operators, representing a set of normalized intensity measurements. The Pauli operators $\langle \sigma_i \rangle$ are computed from I can be derived from:

$$\langle \sigma_1 \rangle = (I_{13} + I_{23}) - (I_{15} + I_{25}) \quad (5\text{-}13)$$

$$\langle \sigma_2 \rangle = (I_{14} + I_{24}) - (I_{16} + I_{26}) \quad (5\text{-}14)$$

$$\langle \sigma_3 \rangle = (I_{11} + I_{21}) - (I_{12} + I_{22}) \quad (5\text{-}15)$$

where I_{ij} is the measured intensity on the CCD camera with associated polarization and OAM basis state. The details of the I_{ij} are summarized in Table 5.3. Therefore, the bloch vector s can be calculated with the measured on-axis intensities on a CCD camera and then used to calculate the concurrence C.

Table 5. 3 shows the projective measured intensity and its respective basis state for a vector vortex mode.

Basis State	$l = 1$	$l = -1$	$\theta_2 = 0$	$\theta_2 = \pi/2$	$\theta_2 = \pi$	$\theta_2 = 3\pi/2$
L	I_{11}	I_{12}	I_{13}	I_{14}	I_{15}	I_{16}
R	I_{21}	I_{22}	I_{23}	I_{24}	I_{25}	I_{26}

The entropy of entanglement (E) can be expressed as:

$$E = h(\tfrac{1+s}{2}) \quad (5\text{-}16)$$

where $h(x) = -x\log_2(x) - (1 - x)\log_2(1 - x)$ is the binary entropy [232]. Thus, the bloch vector s also can be employed for E calculation.

Based on Eq.(5-11) and Eq.(5-16), the concurrence (C) and entanglement entropy (E) of a single vector vortex beam was found to be C = 0.95 ± 0.02 and E= 0.93 ± 0.02 respectively and so has a high degree of vector purity.

The experimental normalized intensity measurements have been carried for six polarization states and six OAM states for a single diffractive mode. Six polarization states (left, right, horizontal, vertical, diagnal and antidiagonal) were executed with six different holograms: $|l = 1 >, |l = -1 >, |l = 1 > +exp\ (i\theta_2)|l = -1 >$ for $\theta_2 = 0, \frac{\pi}{2}, \pi, \frac{3\pi}{2}$. The normalized measured intensity by a CCD camera with associated polarization and OAM states for a single beam as shown in Figure 5.16.

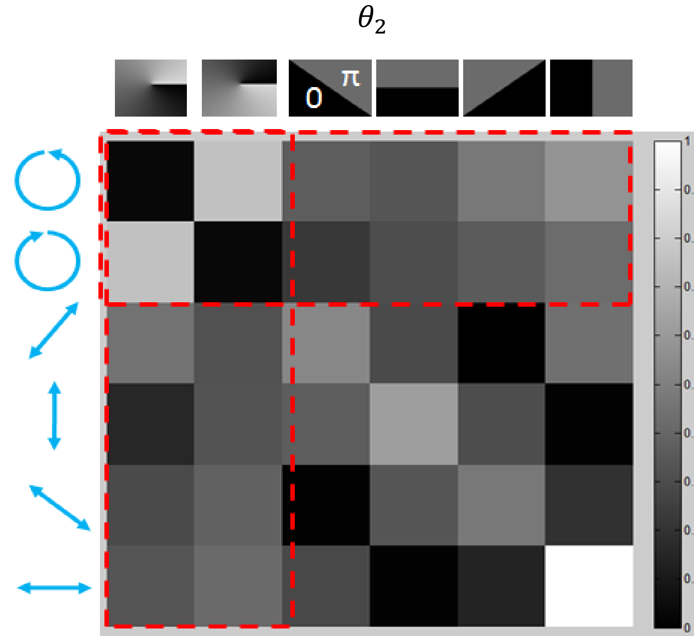

Figure 5. 16 Normalized experimental measured intensities with a combination of a quarter wave plate and half wave plate. The entanglement entropy of the vector beam was calculated by the measurements in outlined red dash lines.

A measurement of Clauser-Horne-Shimonu-Holt-Bell (CHSH-Bell) inequality is to demontrate a violation of Bell's inequality of a single vector vortex beam. Typically, a CHSH-Bell inequality is measured with a single degree of freedom of a pair of photons separately, e.g. polarization [233, 234] or OAM [230]. In our experiment, we measured two degree of freedom (DOF) locally instead of measuring a DOF nonlocally. The Bell parameter S can be defined as

$$S = E(\theta_1, \theta_2) - E(\theta_1, \theta_2') + E(\theta_1', \theta_2) + E(\theta_1', \theta_2') \tag{5-17}$$

where $E(\theta_1, \theta_2)$ can be calculated by measuring the on-axis intensity $I(\theta_1, \theta_2)$ on a CCD camera:

$$E(\theta_1, \theta_2) = \frac{I(\theta_1,\theta_2)+I\left(\theta_1+\frac{\pi}{2},\theta_2+\frac{\pi}{2}\right)-I\left(\theta_1,\theta_2+\frac{\pi}{2}\right)-I\left(\theta_1,\theta_2+\frac{\pi}{2}\right)}{I(\theta_1,\theta_2)+I\left(\theta_1+\frac{\pi}{2},\theta_2+\frac{\pi}{2}\right)+I\left(\theta_1,\theta_2+\frac{\pi}{2}\right)+I\left(\theta_1,\theta_2+\frac{\pi}{2}\right)} \tag{5-18}$$

where $\theta_1$and $\theta_2$are the angles of the half wave plate and the encoded hologram, respectively. For the Bell parameter measurement of each diffractive beam spot, the quarter wave plate (QWP) was taken off. Four different orientations of the half wave plate: $\theta_1 = 0$ rad (0°), : $\theta_1 = \pi/8$ rad (22.5°), $\theta_1 = -\pi/4$ rad (-45°),: $\theta_1 = 3\pi/8$ rad (67.5°) have been selected. For each orientation of the half wave plate, the holograms were rotated from $\theta_2 = 0$ to $\theta_2 = \pi$, and the on-axis intensity was recorded for each diffractive beam. Normalized intensity measurement as shown in Figure 5.17.

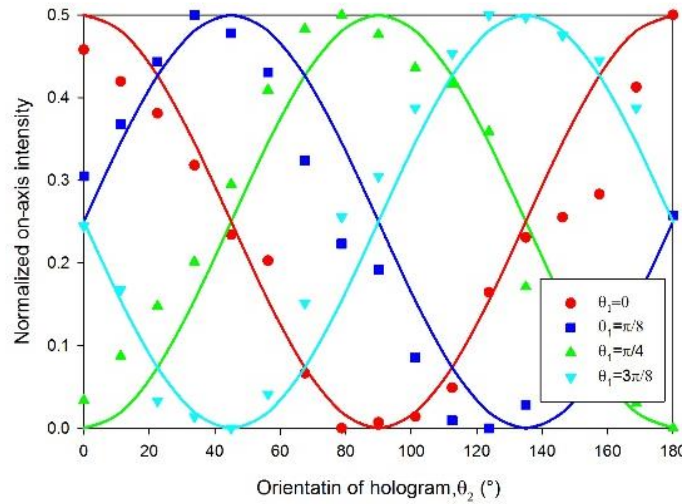

Figure 5. 17 Bell curve for a single CV with four different orientations of the half wave plate ($\boldsymbol{\theta_1}$) and associated hologram angle ($\boldsymbol{\theta_2}$). Curves are fitted with pure $\mathbf{cos^2\theta}$ function.

By placing a quarter wave plate (QWP) ahead of the S-wave plate with the fast axis angle $\alpha = \pm 45°$, the output beam from the S-waveplate are left- and right- handed circularly polarized scalar vortex beam [235]. The beam mode from vector to scalar can be obtained by rotating the QWP fast axis angle from 0° to 45°. Therefore, we measured the concurrence from a single scalar vortex beam (C=0.14) to vector beam (C=0.95). Results as shown in Figure 5.18, fitting the theoretical curve well.

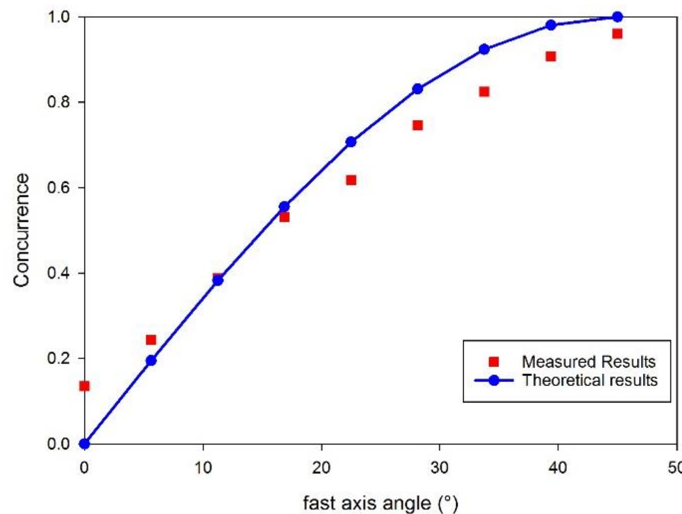

Figure 5. 18 Measured concurrence of a single beam from scalar mode (C=0.14) to vector mode (C=0.95). Fitted with a pure $\boldsymbol{cos^2\theta}$ function.

5.6.2 Measuring of Multiple CV beams

For the Multiple CV beams measurement, the experimental setup was updated, as shown in Figure. 5.19.

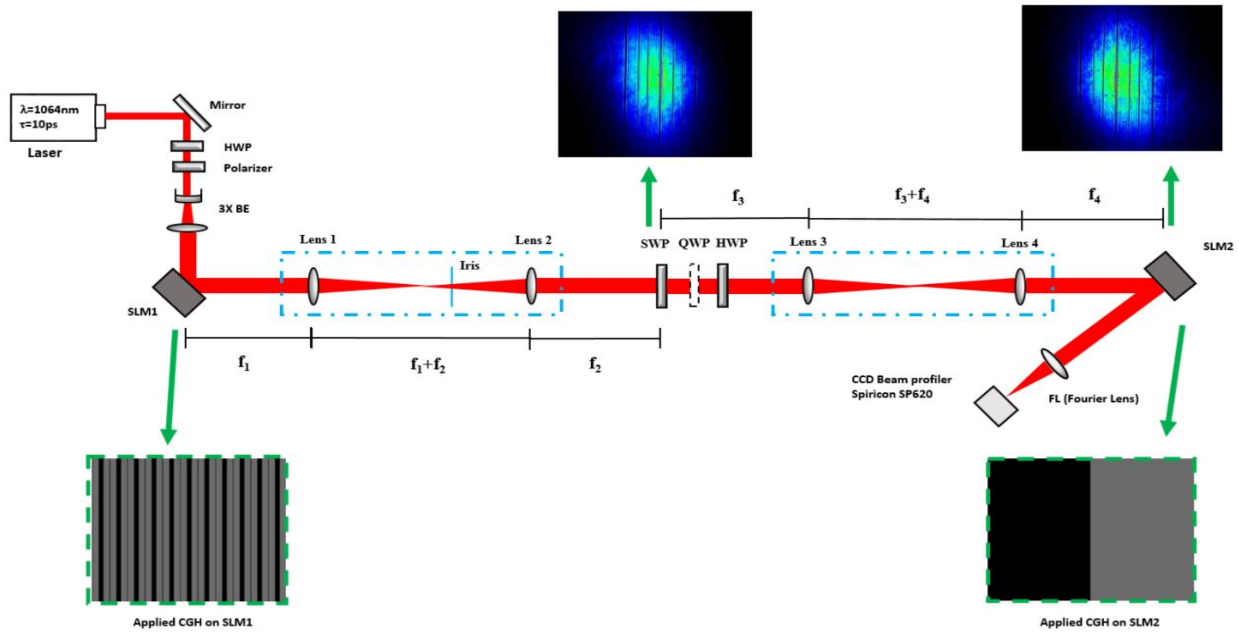

Figure 5. 19 Experimental setup. Two spatial light modulators were applied (SLM1 and SLM2). Two 4f systems (highlighted with blue rectangle dash box) were applied to re-constructer the image plane of SLM 1 to SLM 2. The re-constructured image (1x5 Damann grating) plane of each 4f system were highlight with green rectangle dash box. The reconstructured images were captured by using a CCD camera (Thorlabs, BC106-VIS).

A Hamamatsu X13138-5785 liquid crystal on silicon (LCoS) with 1280 × 1024 pixels and dielectric coating for 1064 nm wavelength was used (SLM1). A computer-generated hologram of a desired Dammann grating was applied to SLM1 (with SLM correction file). The beam was then passed through a 4f system (f_1=f_2=300mm) so that the image plane of SLM1 will be reconstructed on the nanostructured S-waveplate (SWP, Altechna, RPC-1030-10-109) with all diffracted beams precisely overlapped and centred. The S-waveplate was used to modulate the polarization state to radial or azimuthal. Then, a second 4f system (f_3=f_4=100mm) was placed after the SWP with the SWP plane reconstructed on SLM2 (Hamamatsu X10468-03 LCoS, 800 × 600 pixels) for further beam analysis (without SLM correction file). There was no SLM correction file applied on SLM2 as the SLM2 was applied on phase holograms. A quarter wave plate (QWP) and a half wave plate (HWP) were placed after the SWP for projections and state tomography with the aid of SLM2 which was encoded with a series of symmetric CGH's, [0,π] and rotated with a given phase angle around the centre. The QWP was inserted only for circular polarization states (left and right) generation. The reflected beam was then directed to a CCD based beam profiler (Spiricon, SP620U) for observation and measurement. A plano-convex lens (FL, f=500mm) was used to focus the resulting beams to CCD camera was placed at the lens Fourier plane. The necessary projections and state tomography can be obtained by rotating the half wave plate and changing the phase angle holograms on the SLM 2.

Thus, based on the Eq. (5-17) and Eq. (5-18), the Bell parameter S for each diffractive spot in a 1x5 Damann grating beam array can be calculated and as shown in Table 5.4.

Table 5. 4 Measured Bell parameter S for each diffraction spots in 1x5 spots array

Diffractive spots	1	2	3(0th order)	4	5
Bell Parameter S	2.32±0.03	2.33±0.03	2.36±0.02	2.36±0.02	2.36±0.02

A maximal |S| is $2\sqrt{2}$ for any quantum state with polarization-entangled photons [235]. Thus, the polarization and spatial mode of each spot in a 1x5 spots exceeds the Clauser-Horne-Shimony-Holt (CHSH) inequality $|S| \leq 2$ by more than 17 standard deviations with $<|S|> = 2.35\pm0.02$.

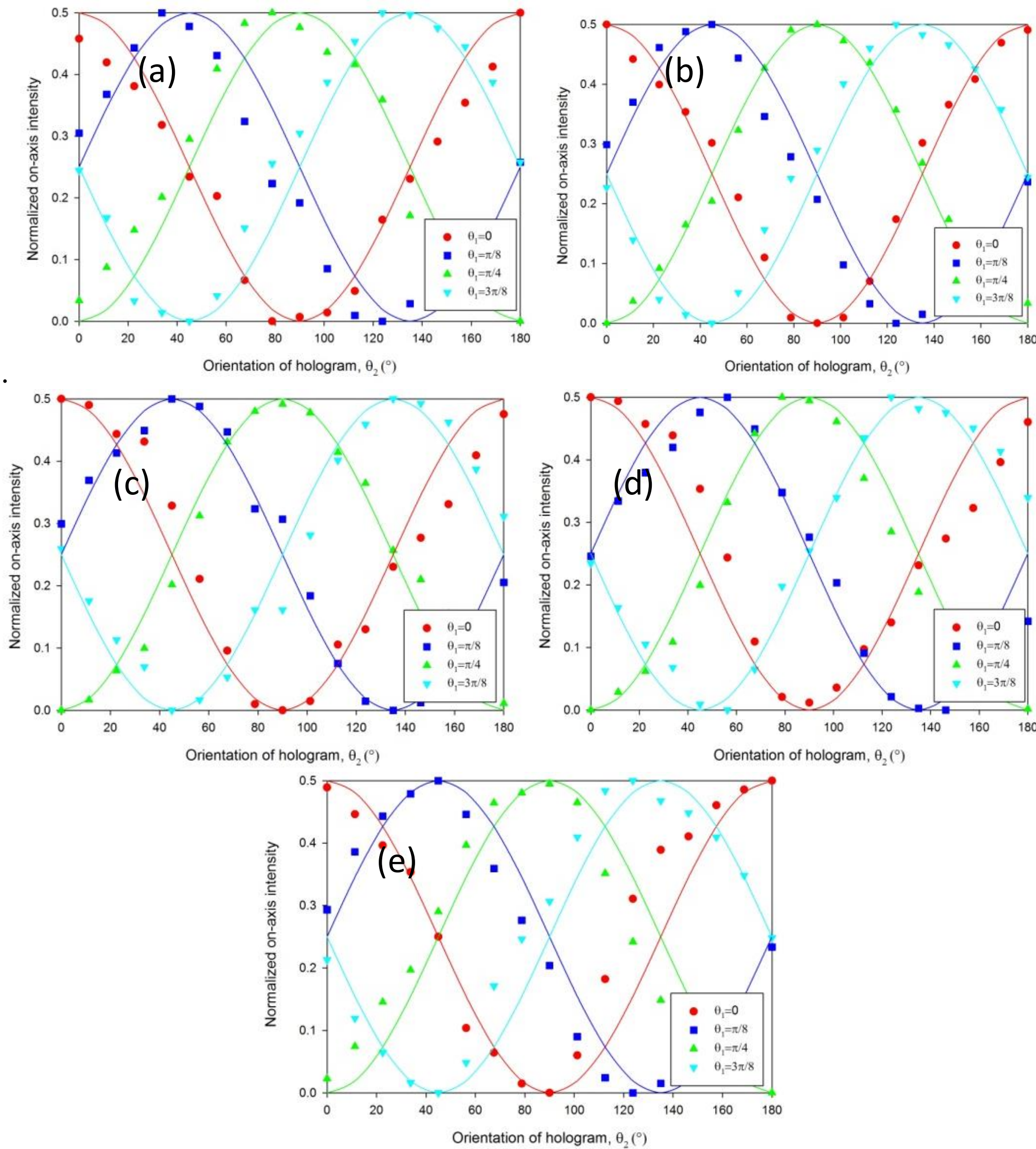

Figure 5. 20 Bell curve for each diffractive spot in a 1x5 spot array with four different orientations of the half wave plate (θ_1) and associated hologram angle (θ_2). (a-d) Bell curves for four diffractive orders with pure $\cos^2\theta$ function fit. (e) Bell curve for the 0th order with pure $\cos^2\theta$ function fit.

There seems to be difference between data and solid lines in Figure 5.20, this may due to the phase aberration caused by the SLM2. For a multiple spot array, we measured the diffractive spot one by one. The normalized measured intensity with associate polarization and OAM states as shown in Figure 5.21.

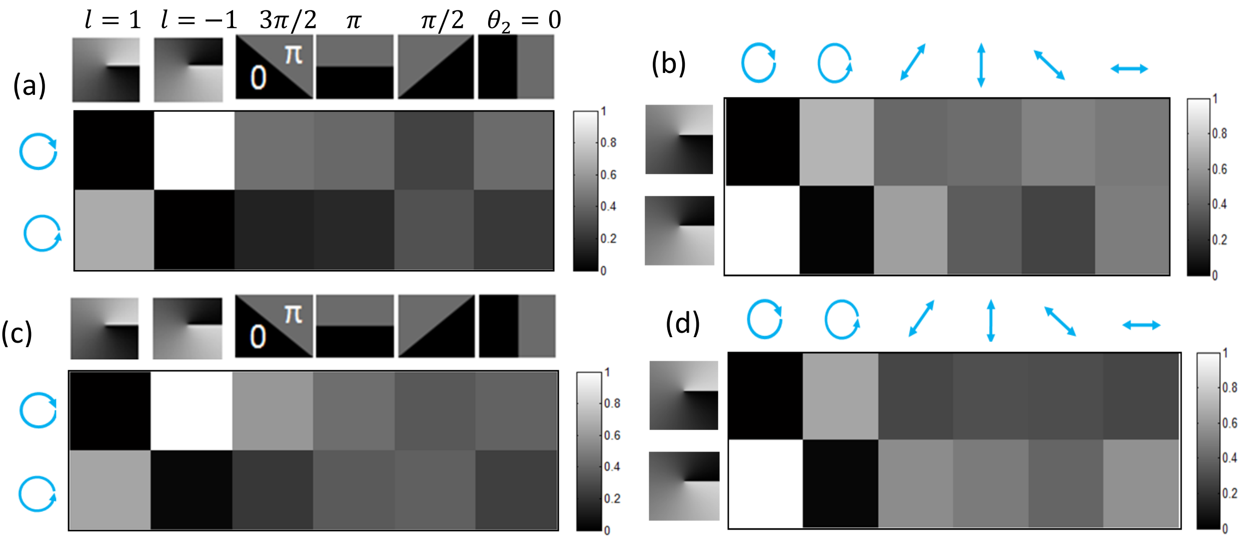

Figure 5. 21 Typical graphical depiction of intensity measurement of a vector vortex mode in multiple spot arrays (a) measured intensity of a beam in 1x5 spots array with six OAM states; (b) measured intensity of a beam in 1x5 spots array with six polarization states;(c) measured intensity of a beam in 2x2 spots array with six OAM states;(d) measured intensity of a beam in 1x5 spots array with six polarization states . Either the measuements with OAM states or polarization states can be chosen as the basis state forward to calculate concurrence and entanglement entropy.

Therefore, using Eq.(5-11) and Eq.(5-13), the concurrence and entanglement entropy of each diffractive vector vortex beam was found to be $C_{1x5} = 0.95 \pm 0.01, 0.96 \pm 0.01, 0.95 \pm 0.01, 0.94 \pm 0.01, 0.96 \pm 0.01$ and $E_{1x5} = 0.93 \pm 0.02, 0.95 \pm 0.01, 0.94 \pm 0.01, 0.92 \pm 0.02, 0.95 \pm 0.01$ respectively respectively. The concurrence and entanglement of each diffractive vector vortex beam in a 2x2 array were found to be $C_{2x2} = 0.96 \pm 0.02$ (0th order), $0.87 \pm 0.03, 0.87 \pm 0.03, 0.84 \pm 0.03, 0.87 \pm 0.03$ and $E_{2x2} = 0.94 \pm 0.02, 0.83 \pm 0.02, 0.82 \pm 0.02, 0.78 \pm 0.02, 0.82 \pm 0.02$ respectively. The measured concurrence and entanglement entropy of multiple spots are concluded in Table 5.5 and Table 5.6. The vector purity of the 2x2 array (apart from zero order) is therefore significantly lower than the linear 1x5 array.

Table 5. 5 Measured Concurrence and Entanglement entropy of a 1x5 spot array

Diffractive spots	1	2	3(0th order)	4	5
Concurrence	0.95±0.01	0.96±0.01	0.95±0.01	0.94±0.01	0.96±0.01
Entanglement entropy	0.93±0.02	0.95±0.01	0.94±0.01	0.92±0.02	0.95±0.01

Table 5. 6 Measured Concurrence and Entanglement entropy of a 2x2 spot array

Diffractive orders	0(0th order)	1	2	3	4
Concurrence	0.96±0.02	0.87±0.03	0.87±0.03	0.84±0.03	0.87±0.03
Entanglement entropy	0.94±0.02	0.83±0.02	0.82±0.02	0.78±0.02	0.82±0.02

By placing a quarter wave plate (QWP) ahead of the S-wave plate with fast axis angle = $\pm 45°$, the output beam from the S-waveplate are left- and right- handed circularly polarized scalar vortex beam. herefore, we measured the concurrence and entanglement entropy of 1x5 scalar vortex beams. A typical intensity map for the scalar vortex beam as shown in Figure 5.22. The measured concurrence for each diffractive scalar spot as shown in Table.5.7.

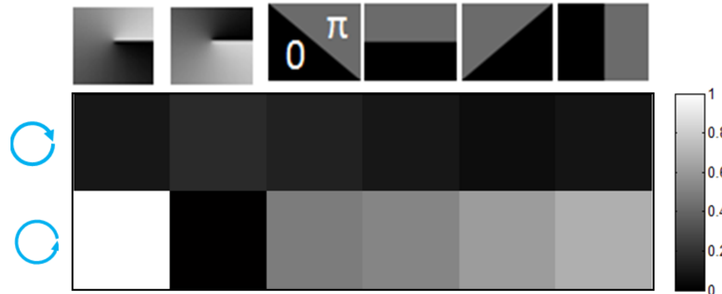

Figure 5. 22 A typical graphical depiction of intensity measurement of a scalar vortex mode (with fix fast axis angle of the QWP=45°). Calculated concurrence C=0.14.

Table 5. 7 Measured concurrence of a 1x5 scalar vortex beams

Diffractive orders	0(0th order)	1	2	3	4
Concurrence	0.14	0.14	0.13	0.13	0.14

5.6.3 Measurement with Stokes projections

Stokes parameters were measured replacing the SLM 2 with a reflective mirror and adding a polarizer in the setup of Fig.1. Based on this new setup, the measurements can be carried with Stokes projections [21]. The concurrence of spots in the 1x5 and 2x2 spot arrays were measured by using a CCD camera (Spiricon SP620U) one by one with total intensity. The laser beam comes after the S-waveplate is radially polarized. Hybrid polarization states after the quarter wave plate (QWP) are shown in Figure 5.23.

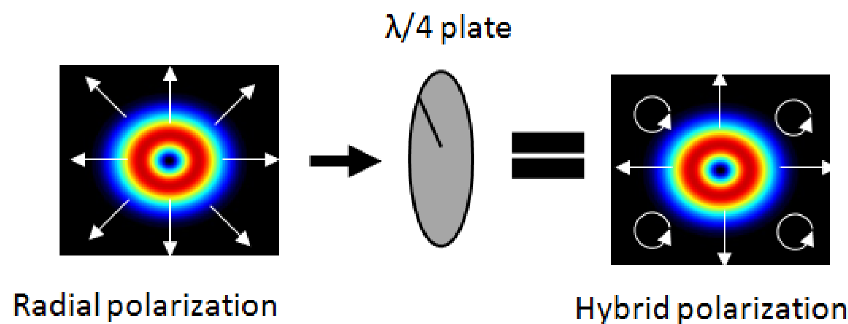

Figure 5. 23 Polarization states after the QWP used in measurement with Stokes parameter.

The entanglement state of a given beam is associated with spatially local Stokes parameters as shown in below:

$$\vec{S}(\vec{r}_\perp)=\begin{pmatrix} I_h(\vec{r}_\perp)+I_v(\vec{r}_\perp) \\ I_h(\vec{r}_\perp)-I_v(\vec{r}_\perp) \\ I_d(\vec{r}_\perp)-I_a(\vec{r}_\perp) \\ I_r(\vec{r}_\perp)-I_l(\vec{r}_\perp) \end{pmatrix} \tag{5-19}$$

where $I_h, I_v, I_d, I_a, I_r, I_l\ (\vec{r}_\perp)$ are the intensity of the horizontal, vertical, diagonal, antidiagonal, right and left circular polarization component respectively. The Eq. (5-11) for the concurrence calculation can be updated to the analogue formulation:

$$C=\sqrt{1-\left(\frac{I_h-I_v}{I_h+I_v}\right)^2-\left(\frac{I_d-I_a}{I_d+I_a}\right)^2-\left(\frac{I_r-I_l}{I_r+I_l}\right)^2} \tag{5-20}$$

With this definition, the measured the concurrence of single spot, 1x5 and 2x2 multiple spots with Stokes projection are tabulated shown in Table.6.

Table 5. 8 Measured concurrence of a single beam, 1x5 and 2x2 multiple beams with Stokes Projections.

Diffractive orders	0(0th order)	1	2	3	4
Concurrence (single spot)	0.97±0.01	-	-	-	-
Concurrence (1x5)	0.95±0.02	0.95±0.02	0.94±0.02	0.94±0.02	0.95±0.02
Concurrence (2x2)	0.96±0.02	0.95±0.02	0.94±0.01	0.96±0.01	0.94±0.02

While the concurrence of the 1x5 spot array is similar to that measured previously, that of the 2x2 array has improved significantly. This is possibly due to the SLM CMOS chip being not perfectly flat and as the generated 2x2 spots array requires two diffraction angles (vertical and horizontal) on the second SLM, a poorer result will be obtained.

5.7 Parallel processing on a Ti-6Al-4V surface using uniform multiple cylindrical vector beam arrays

Uniform multiple vector beams have been generated by the combination of binary Dammann gratings with a Fresnel zone lens optimising the 0th order spot. This is included on the 5x5, 2x2 and 1x5 multiple CV beam arrays on CCD camera. Figure 5.24 (a,c) shows uniform 5x5 arrays with radial and azimuthal polarizations and confirming by the polarization analyser (Figure 5.24 (b,d)).

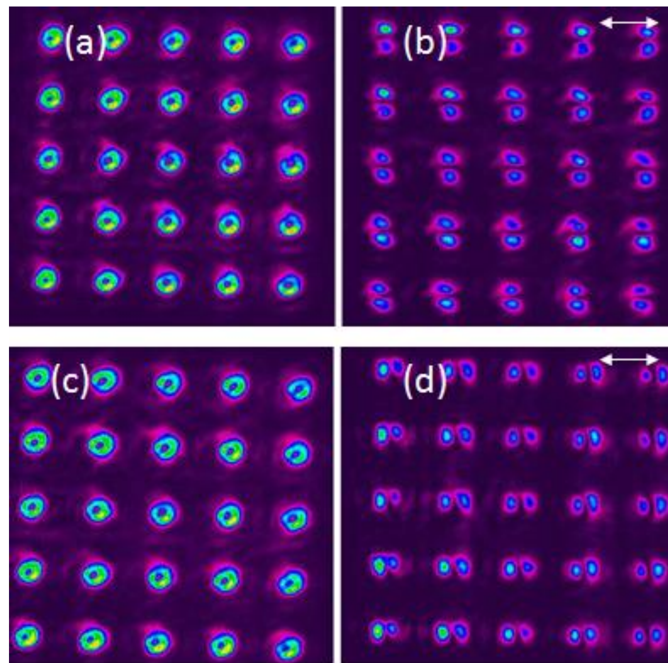

Figure 5. 24 5x5 CV beam arrays on CCD beam profiler (a) 5x5Radially polarized beam arrays (b). 5x5 Radially polarized beam arrays with a analyse polarizer. The white arrow represents the direction of the fast axis (c) 5x5 Azimuthally polarized beam arrays. (d) 5x5 Azimuthally polarized beam arrays with a analyse polarizer. The white arrow represents the direction of the fast axis.

while 5x5 array uniformity was excellent, the pulse energy/spot was too low to machine the surface, hence arrays with lower spot numbers were used for micro machining. As shown in Figure 5.25 to Figure 5.28, multiple laser beam spots (1x5 and 2x2 arrays) have been machined on polished Ti-6Al-4V with radial polarization and azimuthal polarization. For processing, the laser repetition rate was set at 10kHz with 40 μJ/pulse and 45 pulses per spot.

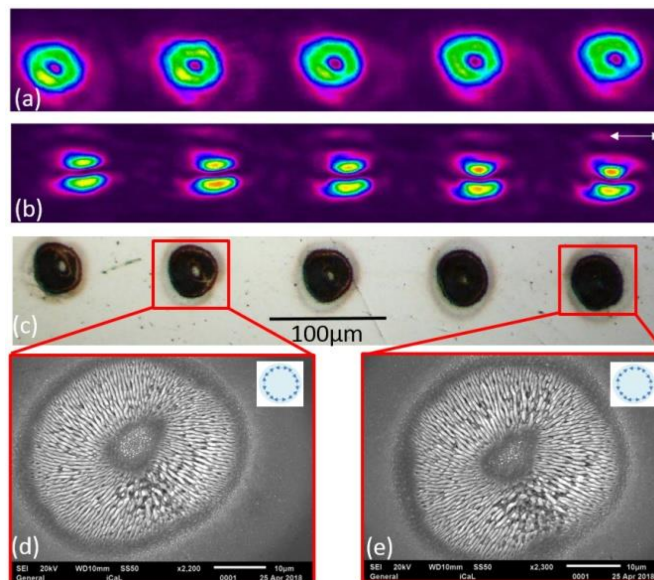

Figure 5. 25 Azimuthally polarized uniform 1x5 vector beam array. (a) Beam profiler image. (b) Beam profiler image with a polarizer analyser. The white arrow represents the direction of the fast axis of the polarizer analyser. (c) Machined uniform

1x5 vector beam arrays on a Ti-6Al-4V sample. The diameter of each spot is approximately 40µm. (d)-(e) The SEM images. (10kHz, 40µJ/Pulse, 45 pulses).

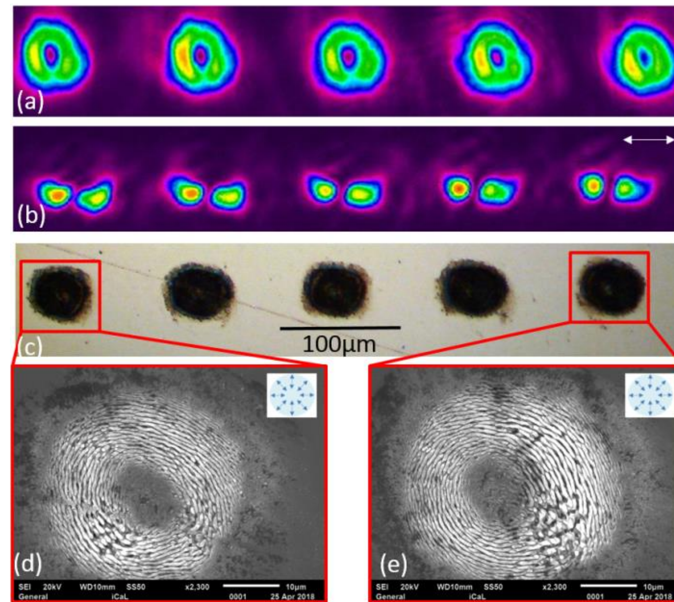

Figure 5. 26 Radially polarized uniform 1x5 vector beam array. (a) Beam profiler image. (b) Beam profiler image with a polarizer analyser. The white arrow represents the direction of the fast axis of the polarizer analyser. (c) Machined uniform 1x5 vector beam arrays on a Ti-6Al-4V sample. The diameter of each spot is approximately 40µm. (d)-(e) SEM images. (10kHz, 40µJ/Pulse, 45 pulses) with azimuthal LIPSS confirming the radial polarization state.

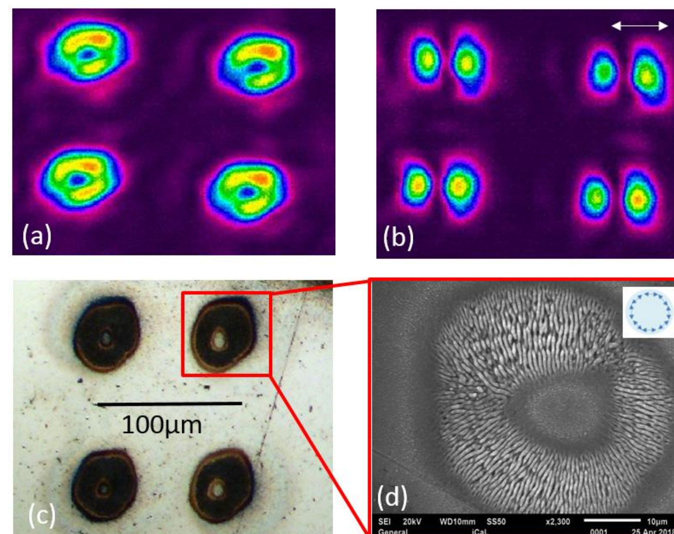

Figure 5. 27 Azimuthally polarized uniform 2x2 vector beam array. (a) Beam profiler image. (b) Beam profiler image with a polarizer analyser. The white arrow represents the direction of the fast axis of the polarizer analyser. (c) Machined uniform 2x2 vector beam arrays on a Ti-6Al-4V sample. The diameter of each spot is approximately 40µm. (d) SEM images. (10kHz, 40µJ/Pulse, 45 pulses) with radial LIPSS confirming azimuthal polarization state.

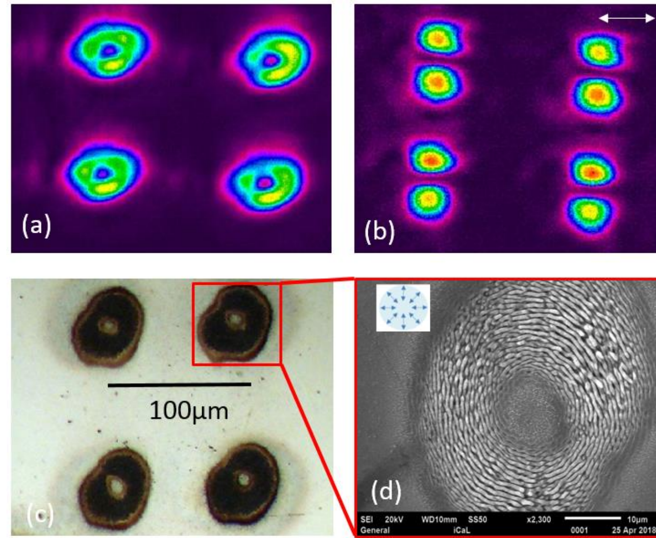

Figure 5. 28 Radially polarized uniform 2x2 vector beam array. (a) Beam profiler image. (b) Beam profiler image with a polarizer analyser. The white arrow represents the direction of the fast axis of the polarizer analyser. (c) Machined uniform 2x2 vector beam arrays on a Ti-6Al-4V sample. The diameter of each spot is approximately 40μm. (d) SEM images. (10kHz, 40μJ/Pulse, 45 pulses).

The above LIPSS generation and analysis confirmed clearly successful generation of the desired polarization states. The multiple CV spots produced by this method compare reasonably well to other SLM based methods of parallel CV spot generation [41]. However, perfect LIPSS structures were not achieved in this work. Probably due to the beam mode issue not perfectly Gaussian combined with alignment errors. The method presented in this work however is significantly more flexible and avoids complex CGH calculation for multiple CV beam generation. The uniformity of each spot depended on the spot separation in a beam array and has been determined

5.8 Similarity of each spot - Cosine Similarity

Cosine similarity is a method to measure the similarity between two non-zero vectors of a product or image. If the cosine angle of two non-zero vectors of 0° for an image is 1 this would mean the vectors are the same, so compared images are the same. In this work, in order to compare the similarity of the generated diffractive spots, a MATLAB code based on cosine similarity method has been used. The main equation used (Eq. 5-19) is given below:

$$\text{Similarity} = \cos(\theta) = \frac{\vec{A}\cdot\vec{B}}{||\vec{A}||\,||\vec{B}||} = \frac{\sum_{i=1}^{n} A_i B_i}{\sqrt{\sum_{i=1}^{n} A_i^2}\sqrt{\sum_{i=1}^{n} B_i^2}} \quad (5\text{-}19)$$

where A and B are two vectors of attributes of the image, Ai and Bi are components of vector A and B respectively. As the SEM images are grey level, a MATLAB code has been used to generate a grey scale histogram of the images. These grey scale histograms can be compared using MATLAB to create cosine similarity.

In order to decrease the measurement error, each machined spot image was taken with the same magnification factor to ensure the details were clearly presented. The first spot of each kind of polarization has been selected as a reference in the 1x5 and 2x2 spot arrays. Then, the other spots were compared the reference spot. For example, the results of comparison of the reference spot with the second spot will be group1, the results of reference spot with the third spot will be group 2 and so on. Therefore 10 result groups can be achieved in the comparison of 1x5 spot arrays and 6 result groups can be achieved in 2x2 spot arrays. The details of the spots similarity results are shown in Figure 5.29 and Figure 5.30.

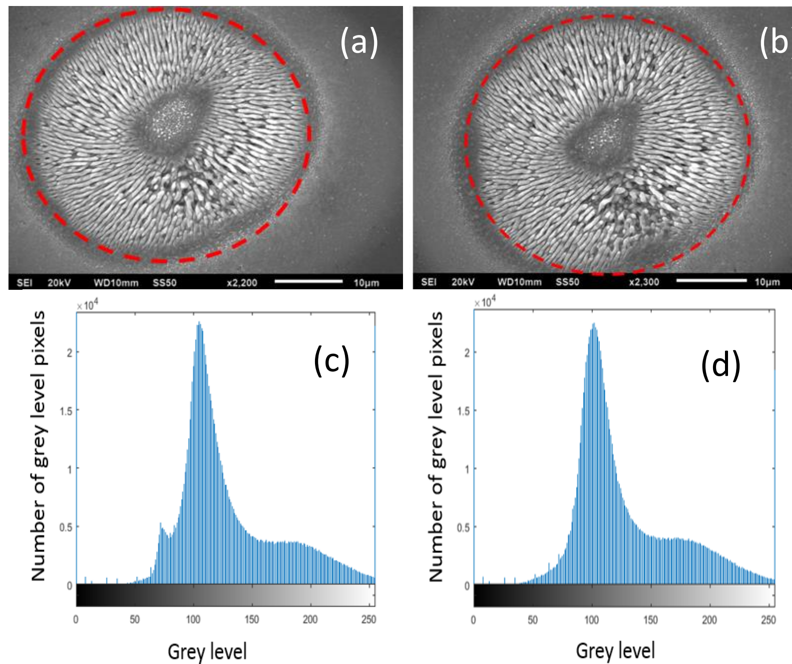

Figure 5. 29 Examples of grey scale histograms that can be extracted from the SEM images for azimuthal polarization (a) Measured area (inside of the red dash line) (c) The grey scale histogram extracted from (a). (d) The grey scale histogram extracted from (b). The area of the red dash in (a) and (b) are same and can be defined in MATLAB environment.

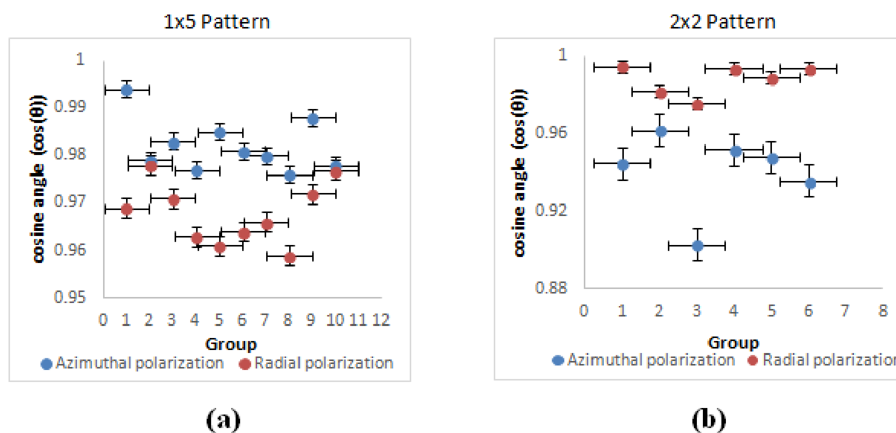

Figure 5. 30 (a) Line graph of cosine similarity for 1x5 cylindrical vector beams. (b) Line graph of cosine similarity for 2x2 cylindrical vector beams.

For high similarity, the cosine angle should be close to 1 and values should have a small spread. Based on the histogram data in Figure 5.29, the similarity of each spot in the 1x5 cylindrical vector beam arrays and the 2x2 cylindrical vector beam arrays are high with cosine similarity $0.9 \leq \cos\theta \leq 0.995$. As the cosine angle is > 0.9, the compared spots can be regarded as almost the same. By comparing with the machined spot size of polished material surface, the beam arrays produced were found to have a good similarity with spots within 10% of each other in terms of structure.

5.9 High power processing with cooled SLM / Dammann gratings

Recently, Guangyu Zhu et al [32] reported the phase range of a cooled SLM cannot reach 2π while using high laser power (P≥120W). The diffraction efficiency of the generated multispots were found to decrease with increasing laser powers as the zero order increased with exposure, as shown in Figure 5.31.

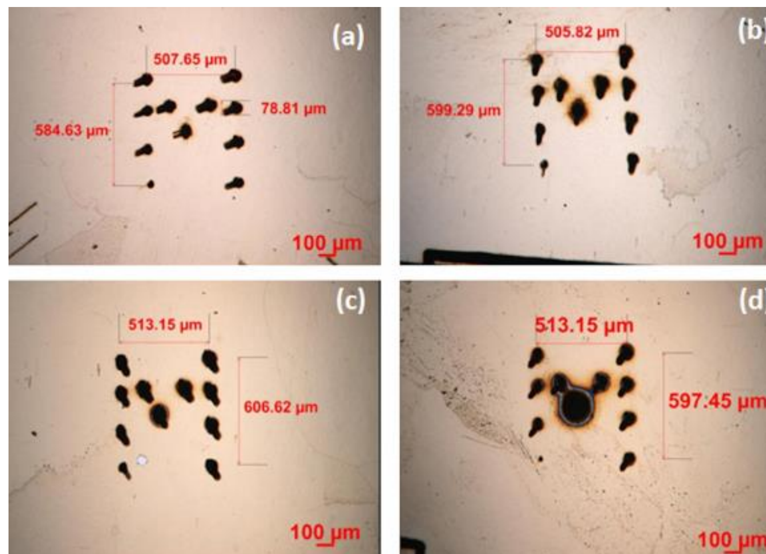

Figure 5. 31 Optical images of machined "M" pattern on a polished brass plate with increasing laser powers (a) 30W (b) 120W (c) 160W and (d) 250W. Diffraction efficiency drops while applying P≥ 120W [32].

Therefore, a simple binary phase CGH is an alternative option as the full 2π modulation is not required. In this work, a generated Dammann grating was also applied using the same high output laser system (Edgewave 10ps @1064nm, Model PX400-3-GH) for testing. Observed generated 5x5 beam arrays at Fourier plane and machined results on stainless steel foil are shown in Figure 5.32. It can be seen that the uniformity of generated spot is high. However, the zero order is still remaining.

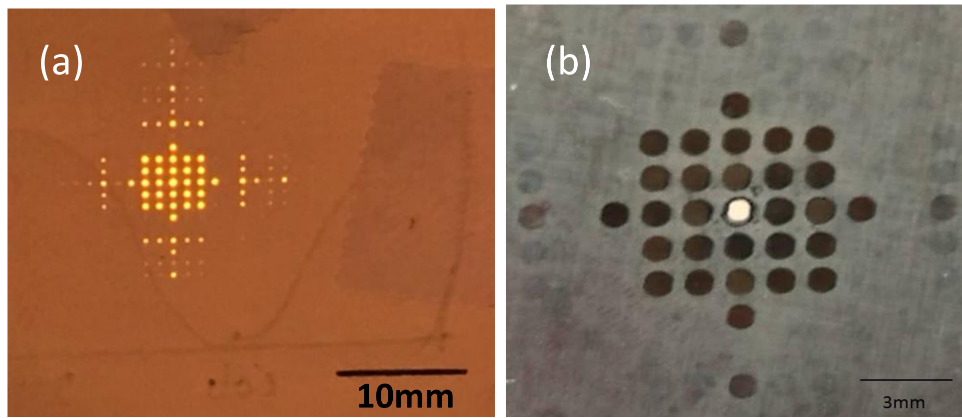

Figure 5. 32 Generated 5x5 beam array using Edgewave picosecond laser. (a) 5x5 beam arrays at Fourier plane and (b) machined 5x5 arrays on stainless steel foil (2kHz, 0.64W). The ghost diffraction spots can be observed in (a). The diffractive zero order in centre of the beam array has high intensity.

By keeping same processing time of 5.6s (100 repetitions), different frequencies and powers have been applied to machine the beam arrays on stainless steel foil. Results are shown in Figure 5.33.

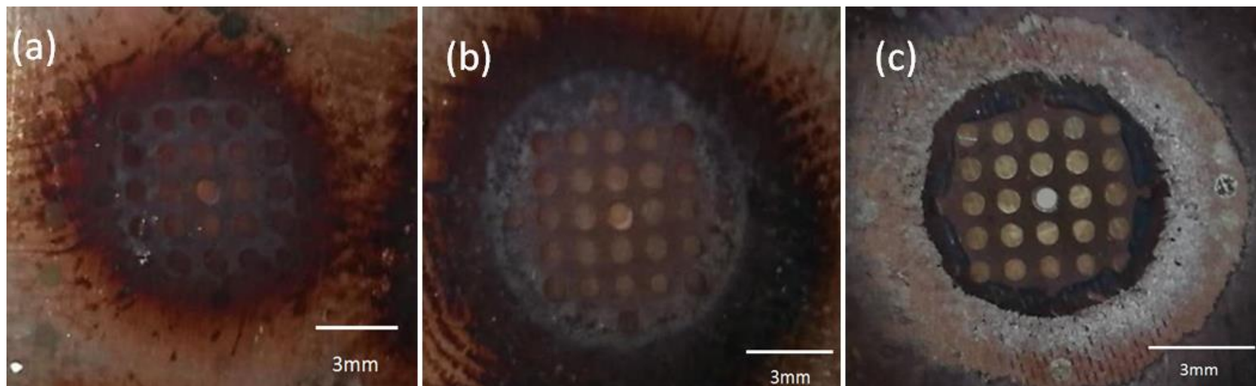

Figure 5. 33 Machined 5x5 beam arrays on stainless steel foil with (a) 404kHz, 96.4W (b) 404kHz, 130W (c) 1MHz, 160W. Diffraction efficiency remains at higher level as expected.

Compared to the results shown in Figure 5.32, the machined results shown in Figure 5.33, the diffraction efficiency remains higher as would be expected when applying CGHs requiring only a 0 to π phase range. These CGHs are not affected as significantly by the loss of performance of the SLM at higher powers.

5.10 Laser surface patterning and texturing

5.10.1 Dynamic laser surface patterning with multiple CV beams

Two 1x5 Dammann gratings (vertical direction and horizontal direction) have been synchronized with a motion control system for dynamic processing on a polished Ti-6Al-4V sample. For processing, the laser repetition rate was set at 10kHz with 40μJ/pulse and exposure set to N=100pulses/spot. 45 laser spots with "UOL" pattern were patterned with a motion control system, as shown in Figure 5.34. The time taken to process each array was ~10ms and required a 400ms delay for Dammann grating synchronization.

The total processing time for all 45 spots was ~3.3s. Laser multi-spot patterning with a dynamic synchronized methodology can be used to improve manufacturing efficiency.

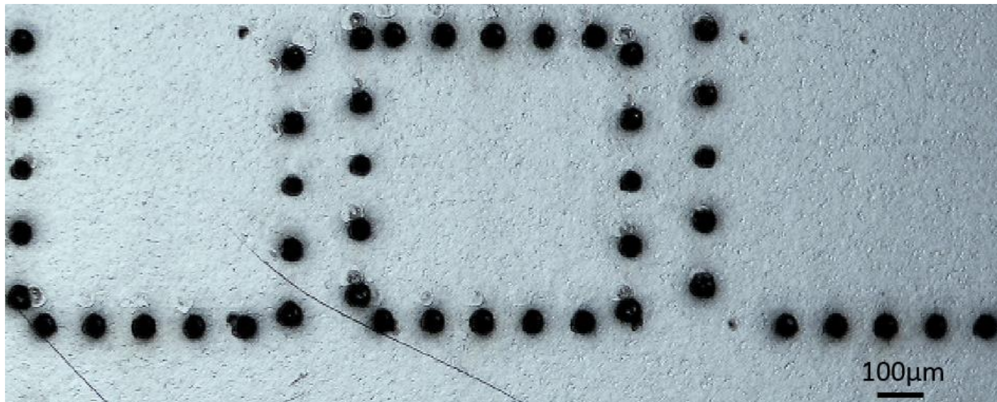

Figure 5. 34 Dynamic control of multiple parallel spots with azimuthal polarization. "UOL" shaped pattern has been demonstrated with multiple 5 spot groups synchronised with galvo movement (10kHz, 40µJ/pulse, 100pulses).

5.10.2 Arrays of laser spots with different polarization states

The states of polarization can be modulated by rotating the S-waveplate. The experimental setup was configured to produce discrete patterns of 2x2 laser spots arranged in a T-shape, each with desired LIPSS orientation, as shown in Figure 5.35.

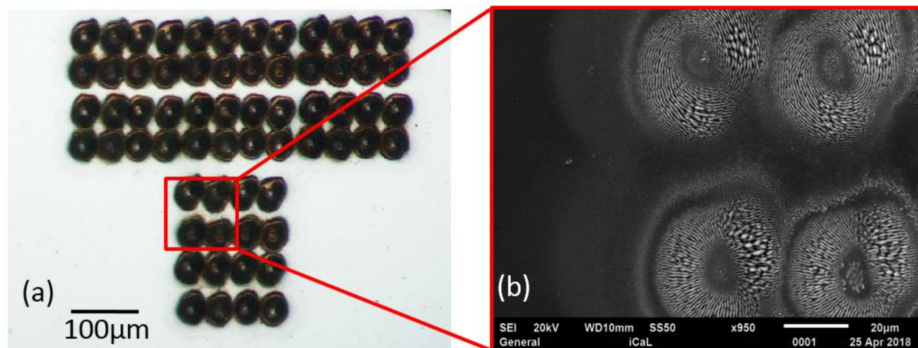

Figure 5. 35 Optical micrograph showing the produced T-shape array of laser spots. (a) Machined T-shapes pattern on a Ti-6Al-4V sample at 10kHz, 40µJ/Pulse, 45 pulses. (b) SEM results with different polarizations states for each spot.

5.10.3 Continuous scanning with different polarization states

The setup was configured to scan a series of line patterns, where polarization was sequentially changed per line during scanning. Figure 5.36 shows optical micrographs of the surfaces produced and confirms once more that synchronization is complete. The SEM microscopic analysis confirmed that the expected LIPSS orientations.

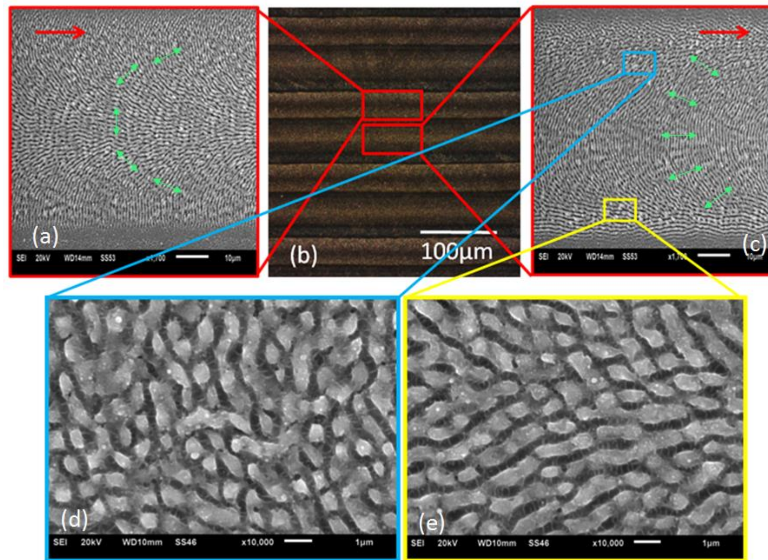

Figure 5. 36 Continuous scanning results with different polarization states. (a)The SEM result of azimuthal polarization (10kHz, 40μJ/pulse, 10mm/s,). (b) Optical micrograph of line patterns with side illumination (c) SEM result of radial polarization (10kHz, 40μJ/pulse,10mm/s). The red arrows represent the laser scanning direction. The green arrows represent the E field. (d-e) Images at higher magnifications of areas inside the blue and red squares, showing shark skin-like morphologies.

5.11 Summary

The generation of uniform multiple radial or azimuthal polarized beam arrays have been demonstrated in this study by combining a nano-structured waveplate with a spatial light modulator addressed with Dammann gratings. Consequently, ring beam arrays with 1x5 and 2x2 and 5 x5 uniform beams were generated by combining binary Dammann gratings with Fresnel zone lens holograms to defocus zero order intensity. A nano-structured diffractive optic element, S-waveplate, has been used to convert the output polarization from linear to radial and azimuthal with high purity ~88%. Ablation threshold measurements typically assume a Gaussian beam profile. This method was modified to accommodate ablation with ring modes which demonstrated that when absolute intensity (fluence) is matched, the single pulse ablation thresholds are essentially unaltered. For example, the measured ablation threshold of Ti-6Al-4V with Gaussian and CV single pulse was 0.32±0.02J/cm^2 and 0.31±0.02J/cm^2 respectively while the ratio of pulse energies was found to be 2.8, close to the theoretically expected value of e = 2.72. In the case of Chromium thin film on glass, the ratio was 2.3, lower than expected by 15%. This difference likely arises from the sensitivity of the thin film substrate to resident beam aberrations. The Cr thin film single pulse ablation thresholds with Gaussian and CV single pulse is 1.38±0.02J/cm^2, 1.73±0.02J/cm^2 respectively. The expected ring intensity distribution (radial/azimuthal polarisation) created from a Gaussian has been modelled and indicates that the ring peak intensity reaches I_0/e where I_0 is the Gaussian peak intensity and e is the natural logarithm. The ring maximum also occurs at r = $\omega_0/\sqrt{2}$. The threshold

ablation energy for Ti-6Al-4V for vortex beams with m=1and m=2 was 1.87μJ and 2.41μJ respectively hence the ratio of the cut-off energy is $\frac{2.41\mu J}{1.87\mu J} = 1.3\pm\ 0.1$ allowing for experimental error, this is close to the value e/2 ≈ 1.35 expected theoretically hence ablation thresholds are therefore similar to that for the Gaussian beam. Relative to the Gaussian beam, the ratio of the cut-off energy for comparing m=1 is $\frac{1.87\mu J}{0.63\mu J} = 3.0 \pm 0.3$, slightly higher than expected ($e \approx 2.7$) while for m=2, the ratio is $\frac{2.41\mu J}{0.63\mu J} = 3.8 \pm 0.1$, close to that expected ($e^2/2 \approx 3.7$). Hence ablation threshold on Ti-6Al-4V with ring beams of different m are very similar. Physically, this is to be expected since peak intensity and fluence (along with material physical properties) determine ablation threshold. If ablation threshold was dependent on intensity distribution, this would infer a change in the light- matter coupling, which appears unlikely. With ultrafast pulses, heat diffusion is minimised along with melting so that ablation becomes a deterministic process dependent on the peak intensity (fluence) and material physical properties. Ashkenasi et al demonstrated the equivalence of ablation thresholds independent of Gaussian beam diameter [88]. A method of cosine similarity has been used to analyse the comparison of each spot. The beam arrays produced were found to have a good similarity with spots within 10% of each other in terms of structure. This indicates that good repeatability has been achieved. The machined footprints have the desired polarization state as confirmed by LIPSS structures. Complex shark skin-like LIPSS appear with specific laser parameters during beam scanning due to the overlap of vector fields. 5x5 or even more ring mode spots can be machined if enough laser energy is applied. Diffraction efficiency of the Dammann grating [0,π] CGHs keeps at a high level when applying laser power up to 160W.

Scanning polished titanium samples (Ti-6Al-4V) with ring modes with identical peak intensities of a Gaussian accelerated LIPPS surface processing significantly so that beam shaping, using higher available powers can increase surface processing speed. The method used in this research has potential applications in large area LIPSS generation for laser security marking, material wettability modification as well as multiple spots micro drilling.

The concurrence, entanglement entropy and Bell parameter of single and multiple vector/scalar beam spots have been confirmed by applying a quantum tool kit. Measured results have been presented with associated polarization and OAM projections locally. The concurrence and entanglement entropy in a linear 1x5 multiple spot array are higher than those in a 2x2 multiple spot array, likely due to the fact that the 2x2 array requires two diffraction angles (horizontal and vertical). It was found that the concurrence, entanglement entropy and Bell inequality of each diffractive order in the same multiple spot array are similar. The vector quality factor measurement for multiple vector/scalar vortex beams is a very new technique used here for the first time. Based on the measurement with Stokes projection, a significant improvement of the concurrence of the 2x2 multiple spots has been observed. This is likely due to the

wavefront error introduced by the second SLM. The correction file of the SLM can be used to improve the flatness of the SLM, the addition of correction file will also affect the polarization and phase of the light. With the increasing interests in the application with multiple vector beams, such as laser micro processing and optical trapping, the purity of the multiple vector beams is important significant to investigate. while arrays have been created by interferometric approaches, here, a much more robust and versatile approach using fan-out grating approaches is demonstrated. Importantly, high purity vector arrays with little to no degradation as the array size is increased was shown, suggesting that this approach is scalable.

.

Chapter 6

Dynamically controlled cylindrical vector beams and applications in surface processing

6.1 Introduction

Presented in this chapter is a dynamic CV polarization control method for Ti64 surface modification. Laser surface modification on materials with polarized ultrashort pulsed lasers can improve the properties of a treated surface by improved corrosion resistance[236], thermal and mechanical effects[237], and morphological effects [3-5]. Laser polarization state is always regarded as an important parameter for linear and non-linear laser irradiation under high laser input intensities. Normally the laser polarization state can be classified into spatially homogeneous and spatially inhomogeneous polarization states, depending on the beam polarization direction. Cylindrical vector (CV) polarization, a cylindrically symmetric spatially inhomogeneous polarization state, is different from the spatially homogeneous states of polarization (i.e. linear, circular and elliptical polarization) as the CV beams are tangentially polarized with a polarization singularity at the electric field centre. A typical cylindrical vector polarization includes radial and azimuthal polarization state variants. Many optical plates and devices have been demonstrated to generate CV beams, such as diffractive optical elements (DOEs) [238]or spatial light modulators (SLM) [41]. A number of applications for CV beams range from optical trapping [239] to laser processing [240] and charged particle acceleration[241].

To date, ultrafast laser processing with picosecond pulses has aroused great interests in surface property modification by the generation of nano-scaled Laser Induced Periodic Surface Structures (LIPSSs) for self-cleaning [242], enhanced cell attachment [243] and material security colour marking [5]. Recently, Yang Jin et al [244] has presented a dynamic control method to generate various linear polarization directions for material processing. In addition, Ouyang. J et al [131] have reported tailored optical vector/ vortex field generation using an S-waveplate with a picosecond laser. Impressive spiral plasmons have been generated by altering an S-waveplate with horizontal linear polarization. The LIPSS orientations produced by the CV polarizations are not linear. Thus, it is of interest to investigate the laser-material surface properties with CV polarization states. More Recently, E. Skoulas et al [245] have demonstrated a novel strategy to fabricate a hydrophobic biomimetic surface with CV femtosecond pulsed beams. The LIPSS were produced under a variety of laser scanning speeds, laser input fluences and the effective number of pulses.

Laser-induced periodic surface structure (LIPSS) can be produced on a material surface with the fluence of a laser close to the damage threshold of the material [8]. However, many factors, such as laser scanning speed (number of overlapped pulses), material thermal properties will affect LIPSS formation. According to the different spatial period of the LIPSS, they can be categorised to low spatial frequency LIPSS (LSFL) and high spatial frequency LIPSS (HSFL) LIPSS[246]. The spatial period of the LIPSS is also determined by the light incident angle [15]. Although, the material surface modification with linear and CV

polarization states have been reported in various literatures [247] no comprehensive study of dynamically modulated CV polarizations with one SLM has been performed to date.

In this chapter, dynamic modulating CV polarization states allow the possibility to further control laser light for flexible and desirable laser-material interaction. This work includes method of altering cylindrical vector polarizations dynamically for ultrashort laser material processing by combining only one phase Spatial Light Modulator (SLM) and a nano-structured polarization converter, S-waveplate (Athena). Consequently, the polarization state between radial and azimuthal can be dynamically switched with a motion control system at a frequency f=5Hz. This real-time control allows material surface colour marking by producing the Laser Induced Periodic Surface Structures (LIPSS) on polished Ti6Al4V samples with a picosecond pulsed laser. In addition, by covering a nanosecond laser treated surface with LIPSS nanostructures, the surface hydrophobicity can be explored. The LIPSS with a lateral period of approximately 1μm can also be used to verify the state of polarization at the focal plane. A scanning electron microscope (SEM) and white light interferometer microscope (WYKO NT1100) have been used to characterize and quantify the effects of the surface modification. ZEMAX opticstudio 15 was used to confirm the complex output polarization states.

6.2. Experimental

6.2.1 Experimental setup

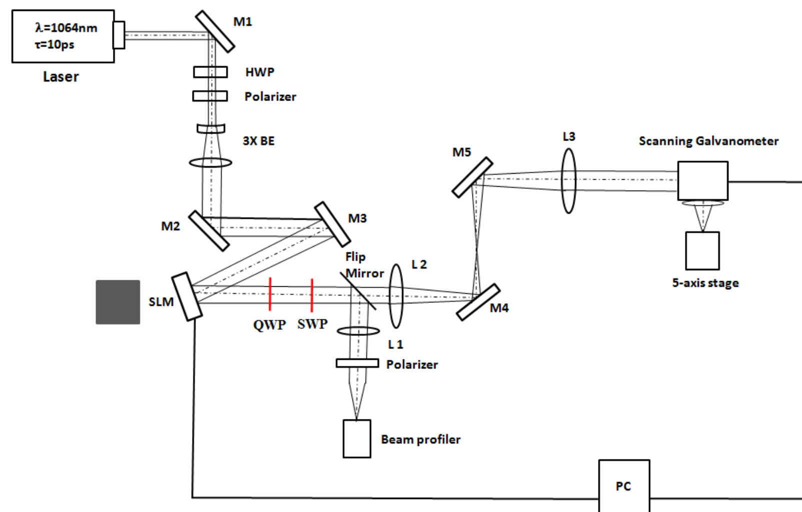

Figure 6. 1 Modified experimental setup

Figure 6.1 shows a schematic of the modified experimental setup. The ultrafast laser system used for the results presented in this chapter is a custom made Nd: VAN seeded regenerative amplifier laser system (High-Q IC-355-800ps, Photonic Solutions). A horizontal linear polarized laser beam output (beam diameter: Dia.≈2.7mm, pulse duration: τ=10ps, wavelength: λ=1064nm, and repetition rate =10kHz) passes through a half wave plate (HWP) and polarizer (Glan laser) which was used to adjust power and

polarization direction (45° relative to the SLM fast axis), a beam expander (M ≈ ×3) has been placed after the polarizer, and two plane mirrors (M2,M3) for controlling the beam path and illuminated on a reflective, liquid crystal phase only SLM (Hamamatsu X10468-03, 800x600 pixels, fill factor 98%). Then, a quarter waveplate (QWP) placed after the SLM has been used to modulate linear polarization direction to a nano-structured diffractive optical element, S-waveplate (SWP). The S-waveplate has been added behind the quarter waveplate for the onward CV beams generation. Computer generated holograms (CGHs) with various continuous grey level (GL) maps were applied on the SLM and used to alter the direction of the incident polarization. A flip mirror has been placed after the S-waveplate, to a CCD based beam profiler (Thorlab, BC106-VIS) for observation. A focusing lens (L1, f=500mm) and a polarizer have been used to analyse and confirm the polarization states. A 4f imaging system (L2 and L3) was placed after the flip mirror to reconstruct the beam to the input aperture of a galvo scanner (Nutfield XLR8-10) via periscope mirrors M4 and M5. At the galvo output, the laser beam was focused with a flat field f-theta lens (f=100 mm, Linos). A PC was used to synchronize the SLM with the scanning galvometer.

For processing experiments, samples were mounted on a precise 5-axis (x,y,z,u,v) motion control system (A3200 Ndrive system, Aerotech) for precise location of the focal plane. Polished Ti6Al4V samples were used in this work. Samples were cleaned with acetone (99.99%) before laser processing.

6.2.2 Polarization control using an S-waveplate

Linear or circular polarized beams can used in conjunction with polarization converters, such as an S-waveplate, for output polarization modification. For an incident linearly polarized beam, an S-waveplate rotates the incident linear polarization by the angle necessary to produce a radial /azimuthal distribution of the electric field. The radial polarization can be get when the orientation of the linear polarization is parallel to the S-waveplate fast axis and perpendicular to get azimuth polarization.

Therefore, table 6.1 shows the output polarization with different incident angle of linear polarization.

Table 6. 1 Jones matrixes of single beam polarization control using an S-waveplate

S-waveplate	Linear polarization at incident angle θ	Output polarization
$\begin{pmatrix} cos\emptyset & -sin\emptyset \\ sin\emptyset & cos\emptyset \end{pmatrix}$	$\theta = 0°, \begin{pmatrix} 0 \\ 1 \end{pmatrix}$	$\begin{pmatrix} -sin\emptyset \\ cos\emptyset \end{pmatrix}$
$\begin{pmatrix} cos\emptyset & -sin\emptyset \\ sin\emptyset & cos\emptyset \end{pmatrix}$	$\theta = 90°, \begin{pmatrix} 1 \\ 0 \end{pmatrix}$	$\begin{pmatrix} cos\emptyset \\ sin\emptyset \end{pmatrix}$
$\begin{pmatrix} cos\emptyset & -sin\emptyset \\ sin\emptyset & cos\emptyset \end{pmatrix}$	$\theta = +45°, \frac{1}{\sqrt{2}}\begin{pmatrix} 1 \\ 1 \end{pmatrix}$	$\frac{1}{\sqrt{2}}\begin{pmatrix} cos\emptyset - sin\emptyset \\ sin\emptyset + cos\emptyset \end{pmatrix}$
$\begin{pmatrix} cos\emptyset & -sin\emptyset \\ sin\emptyset & cos\emptyset \end{pmatrix}$	$\theta = -45°, \frac{1}{\sqrt{2}}\begin{pmatrix} 1 \\ -1 \end{pmatrix}$	$\frac{1}{\sqrt{2}}\begin{pmatrix} cos\emptyset - sin\emptyset \\ sin\emptyset - cos\emptyset \end{pmatrix}$

The output polarization will be a spiral rotation when applying $\pm 45°$ linear polarization to the S-waveplate. The symbol of " $\pm$" in table 1indicates the spiral rotation direction for a logarithmic spiral LIPSS structure. Figure 6.2 represents the operations of a S-Waveplate with different input polarization states. If the linear polarization direction is parallel to the fast axis angle of the angle, the output beam polarization is radial. The output azimuthal polarization state can be achieved while the input linear polarization direction is perpendicular to the fast axis of the S-waveplate. Spiral polarization states can be obtained while the S-waveplate fast axis has a certain angle (such as $45°$) to the input linear polarization direction.

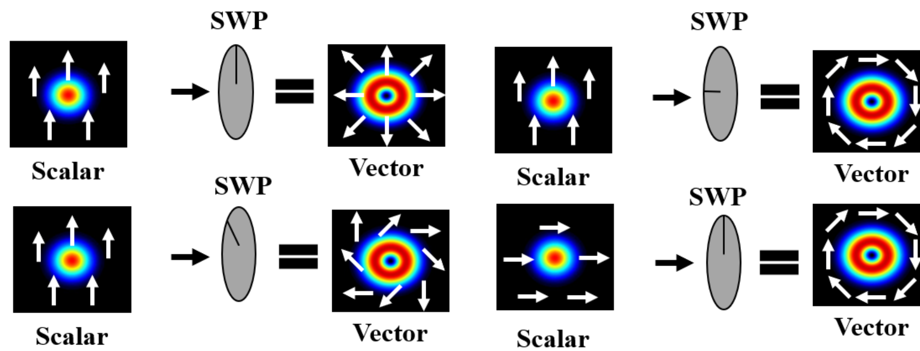

Figure 6. 2 Operations of a S-waveplate with different fast axis angle and various input polarization states.

6. 3 Cylindrical vector polarization states confirmed with ZEMAX

ZEMAX opticstudio 15 has used to confirm the complex output polarization states. The Jones matrix of an S-waveplate was defined in ZEMAX sequential mode with fixed $\emptyset = 0°$ (defined Jones matrix J=$\begin{pmatrix} 1 & 0 \\ 0 & 1 \end{pmatrix}$ in spatial coordinate (Z axis reference polarization method) in ZEMAX), which means the fast axis of the S-waveplate is kept at 0°. The output polarization states from the S-waveplate combined with various linear polarization incident angles are shown in Figure 6.3. The details of the ZEMAX model is demonstrated in Appendix 3.

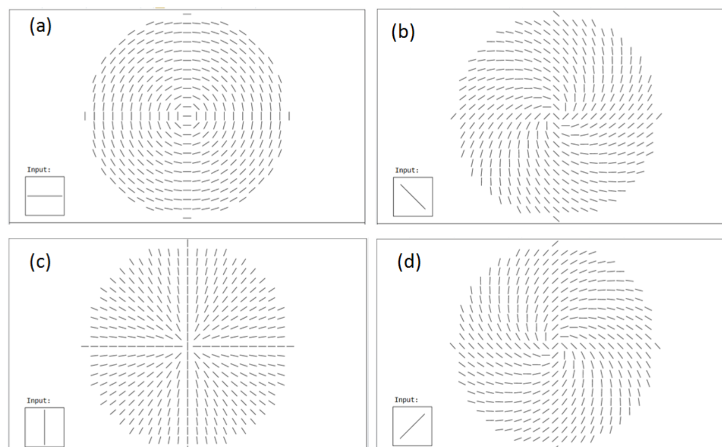

Figure 6. 3 By keeping the fast axis of the S-waveplate equal to 0° in ZEMAX, the output CV polarization will be related to the input linear polarization orientations: (a) radial polarization achieved with horizontal linear polarization, (b) anti-clockwise

spiral polarization achieved with -45° linear polarization, (c) Azimuthal polarization achieved with vertical linear polarization and (d) Clockwise spiral polarization achieved with +45° linear polarization.

6.4 Results and discussion

6.4.1 Dynamic controlled linear polarization

An experiment was configured to identify the initial linear LIPSS orientations by applying grey level CGHs on the SLM. Results were machined on the polished Ti6Al4V samples with 3mm x 3mm squares, partial results are shown in Figure 6.4. The input polarization to the SLM has been altered to 45° relative to the SLM fast axis, the output polarization from the SLM is then elliptical. A quarter wave plate (QWP) was used to change the elliptical polarization to linear polarization for onward radial/azimuthal polarization generation. The output linear polarization from the QWP is sensitive to the grey level of the displayed CGHs on the SLM. By switching to different grey levels dynamically, different orientations of linear polarization will be produced. LIPSS have been produced at the processing focal plane to confirm the polarization orientations with the grey level CGHs. For processing, the laser was set to 10kHz with 8μJ/pulse while the laser was scanned with 100mm/s on the sample. The scanned line spaces (hatch distance) was set to 10μm. An array of 3x3mm squares 18 in total, was produced. The array was produced in ~35 seconds including ~2 second per square with a 200ms delay to synchronise each grey level map.

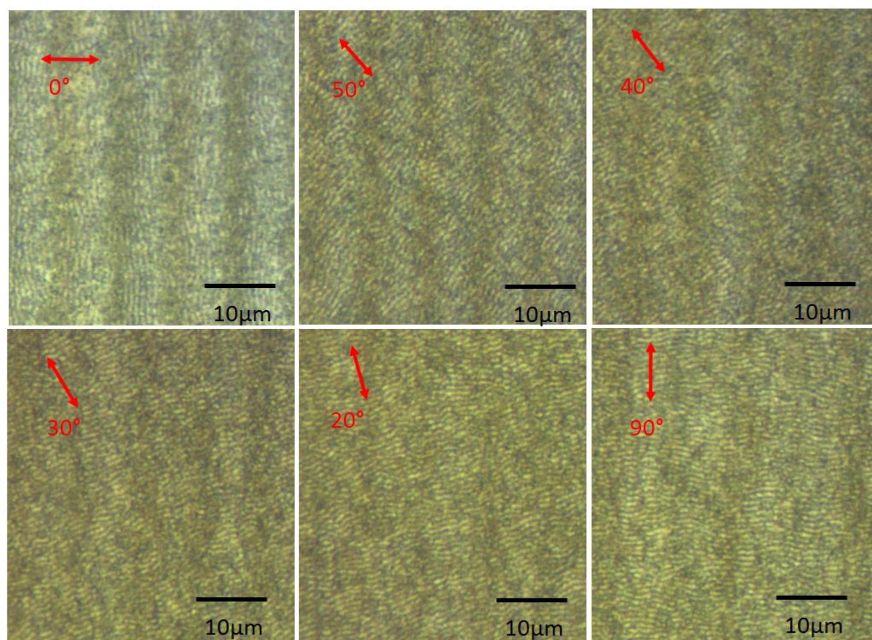

Figure 6. 4 Optical images of linear LIPSS orientations with dynamic grey level CGHs on polished Ti-6Al-4V. LIPSS orientations are switched with the grey levels of the CGHs. Red arrows indicate the direction of the incident linear polarization angle (**θ**) (10kHz, 100mm/s, 8μJ). LIPSS orientation is perpendicular to polarization state.

The produced LIPSS orientations are switching when the grey level of the CGHs are changed. This is as expected and can be effectivity linked with the polarization control works by a SLM in Chapter 3. Therefore, we can obtain the corresponding grey level values for horizontal ($\theta = 0°$), vertical ($\theta = 90°$)

and tilted ($\theta = \pm 45°$) LIPSS generation are 187, 61, 37, 131 respectively. These four grey level CGHs are used for onward corresponding CV polarization state generation.

6.4.2 Dynamic controlled cylindrical vector polarization

6.4.2.1 Synchronized CV polarized beams generation

The horizontal and vertical polarization can be converted to azimuthal and radial polarization respectively when the fast axis angle of an S-waveplate is 0°. Figure 6.5 shows SEM images of selected linear polarizations with S-waveplate removed.

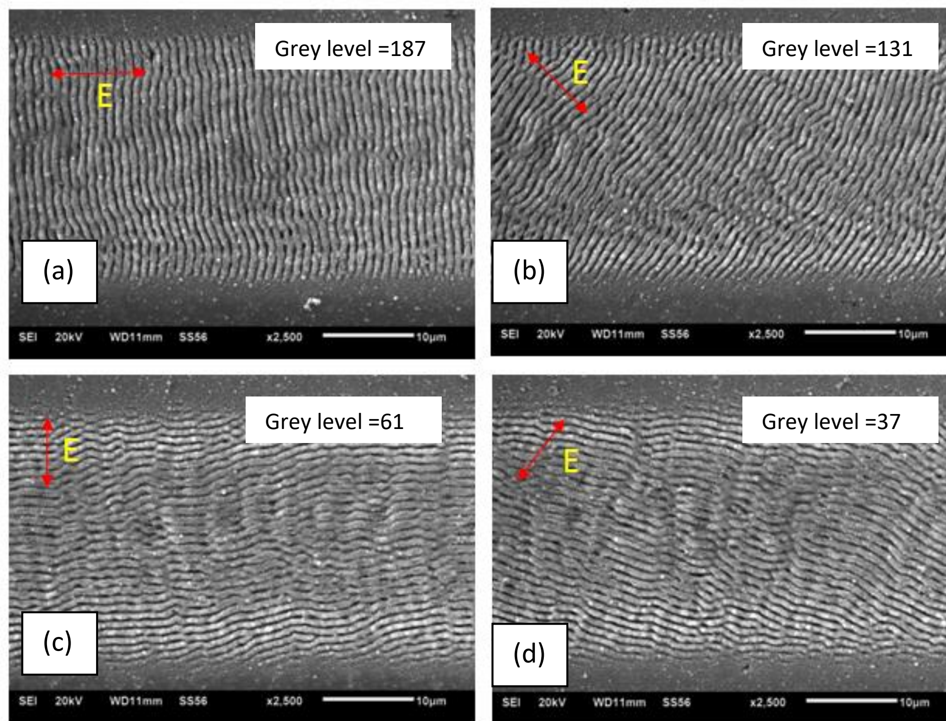

Figure 6. 5 SEM images of laser processing with generated corresponded linear polarization. (a) LIPSS orientation angle horizontal (b) LIPSS orientation angle -45° (c) LIPSS orientation angle vertical (d) LIPSS orientation angle 45° (d). 10kHz, 25mm/s, 5.5μJ. LIPSS spatial period ~1μm.

The linear polarization states that are demonstrated in Figure 6.5 can be synchronized with the motion control system and then passed through the S-waveplate to generate the corresponding cylindrical vector polarization states. Therefore, linear polarization states are dynamically converted to the corresponded cylindrical vector polarizations. The machined results as shown in Figure 6.6. An array of 4 spots have been generated with different CV states with a synchronised grey level on the SLM from section 6.4.1. The laser repetition rate was set to 10kHz with 2.5μJ/pulse, 50pulses for each spot. It can be seen from Figure 6.6, the desired LIPSS orientations are matched well with machined spot footprints on the polished Ti64 surface.

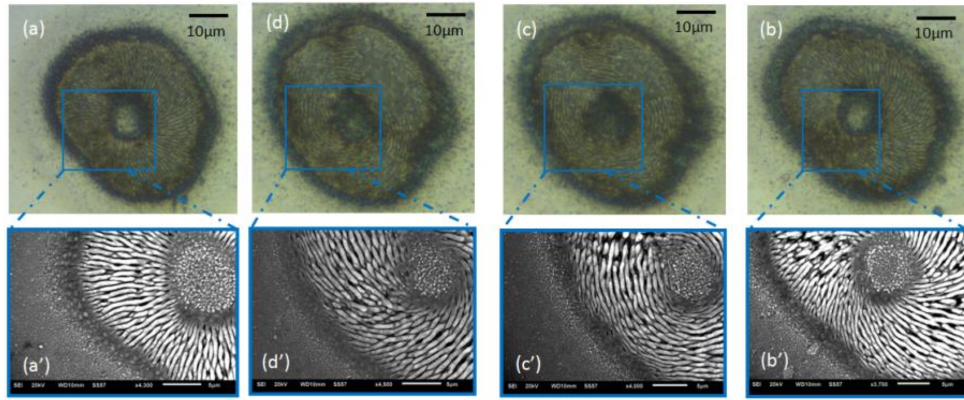

Figure 6. 6 Top line: Optical images of cylindrical vector polarizations created from desired input linear polarization orientations. (a) Azimuthal polarization (b) Spiral (anti-clockwise) polarization (c) radial polarization (d) Spiral (clockwise). (a'-d') SEM images of cylindrical vector polarization states. LIPSS spatial period ~1μm. The scale bar in a SEM image is 10μm. (10kHz, 5μJ, 50pulses).

The laser wavelength λ, the polarization of the laser electric field, laser pulse numbers and the laser incident angle are influencing factors in LIPSS generation with a typical spatial period Λ ($\Lambda_{LSFL}=\lambda/[1\pm\sin\theta]$) [24]. For our particular case, the Ti64 is absorbing 1064 nm radiation, and taking into account the use of polarization at normal angle of incidence, the expected low spatial frequency periodicity is Λ_{LSFL} ~1064nm. The measured spatial period is ~1μm. The period of the lower spatial frequency LIPSS (LSFL) which is close to the wavelength ($\Lambda_{LSFL} \approx \lambda$) on the Ti64 metal surface, are also usually oriented perpendicular to the laser beam local field vector polarization.

6.4.2.2 Scanned lines using synchronized CV beams

The fabricated precisely controlled structures on the material surface present more than one morphology as the polarization of the CV polarized beam is spatially inhomogeneous. Changing scanning velocity to produce the LIPSS structures on the polished Ti6Al4V surface demonstrated various characteristics. The ring mode laser spot was focused on the sample with an outer ring diameter of 50μm. The laser fluence was adjusted to 0.6J/cm^2 for three different scanning velocities, 7mm/s, 10mm/s and 15mm/s to generate LIPPS. The CV beams have cylindrical symmetry in polarization without energy at the polarization centre. Figure 6.7 presents SEM images of the scanned lines using cylindrical vector polarization with various scanning speeds, producing complex LIPSS orientations. The ripples have an average periodicity close to the laser wavelength. These tracks are essentially produced by a series of cylindrical vector polarized overlapping spots repeated over the whole area, for a given speed, repetition rate and pulse overlap. Thus, for laser scanning with CV beams, the scanned path will have with various different direction of LIPSS, from the edges to the centre depending on vector beam. This variation in spatial LIPSS pattern can be seen in Figure 6.7. The scanned ring modes produces a very uniform exposure at the surface.

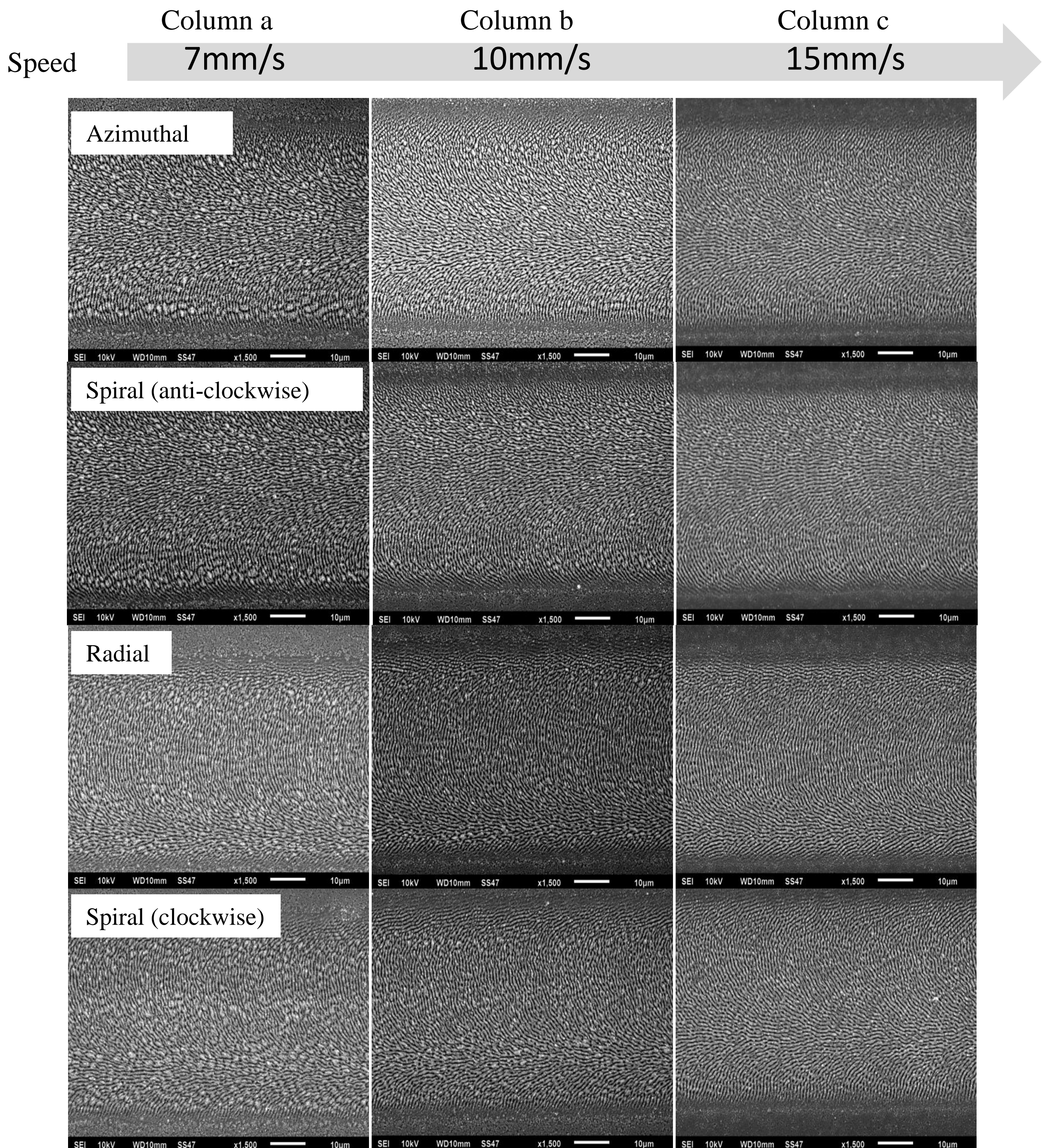

Figure 6. 7 SEM images of scanned lines using generated CV beams with a range of scanning speeds from 7mm/s to 15mm/s. The used polarization direction from top line to bottom line is azimuthal, spiral (anti-clockwise), radial and spiral (clockwise). (Column a) Schematic of beam overlap process at 7mm/s with four CV beams (Column b) Schematic of beam overlap process at 10mm/s with four CV beams (Column c) Schematic of beam overlap process at 15mm/s with four CV beams. All of the scans used peak fluence=0.6J/cm^2.

Scan speed has a significant effect on developing surface morphologies. As can be seen in Figure 6.7 deep grooves parallel to the scanning direction can be observed at the edge of the scanned line when the laser speed was set to 7mm/s and 10mm/s, but the grooves tend to disappear when the scanning speed is

increasing. This is likely due to a higher overlap rate at low scanning speed with increased thermal effects, causing thermal stress induced cracks and melting. Higher scanning speeds would therefore be preferred. However, LIPSS formation is dependent on specific material properties and laser fluence. The fluence used for LIPSS formation should be close to the material ablation threshold, the scanning speed is then the key factor for large area LIPSS formation. The quality of produced LIPSS was found to be dependent on the scanning speed on Nickel (Ni) surfaces as well [245].

6.4.2.3 Overlaid CV polarization states

By overlaying two polarization states, it is possible to obtain complex surface nanostructures with different spatial pattern and periods. Figure 6.8 presents the different spatial periods of the ripples by overlaying two CV polarization states in scanned lines. A scanned line of one CV state is first produced, then a second scan line of another CV state is overlaid on top of this.

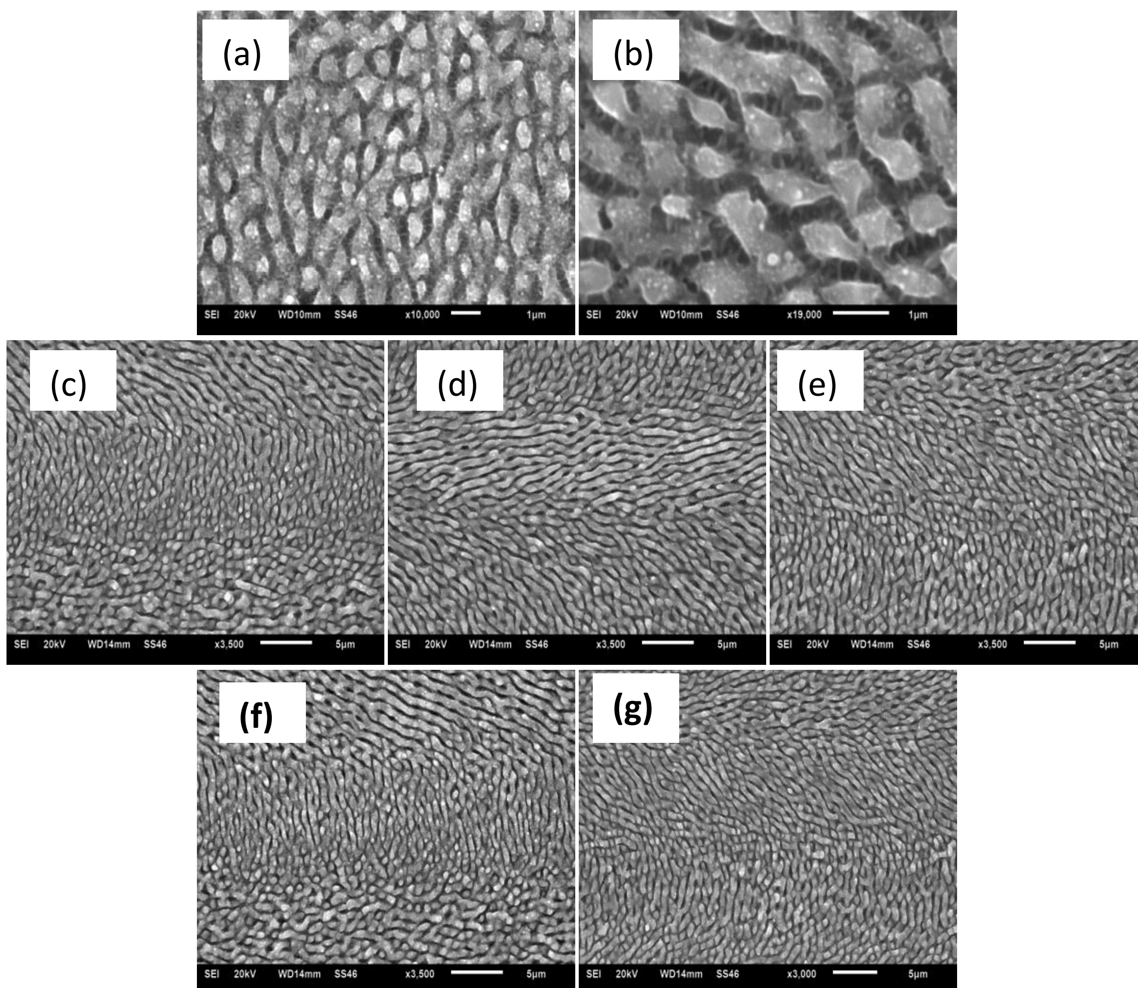

Figure 6. 8 Schematic and SEM images with overlaid polarization states. Top line: LIPSS of overlaid radial and azimuthal polarizations (a) at the centre of the scanned line (b) at the edge of the scanned line. Middle line: (c) Overlaid azimuthal and clockwise spiral (SP1) polarizations. (d) Overlaid radial and clockwise spiral polarizations. (e) Overlaid azimuthal and counter clockwise spiral (SP2) polarizations. Bottom line: (f) Overlapped radial and counter clockwise spiral polarizations. (g)

Overlaid clockwise spiral and counter clockwise spiral polarizations. The Image (c-g) are measured at the scanned line centre. (0.2J/cm^2, 10mm/s).

As shown in Figure 6.8, two distinct spatial period of are evident due to overlaid polarizations. The spatial period at the centre (^~0.6μm) of the scanned line is lower than the two sides (^~0.9μm). This is due to less energy contained in the beam centre. Overlaid LIPSS spatial periods with three or four polarization states could be even more complex. Different LIPSS orientations are also presented. For example, comparing the LIPSS in Figure 6.8 (c) with the LIPSS produced by clockwise spiral or azimuthal polarization states in Figure 6.6, the LIPSS in Figure 6.8 (c) presents a different orientation. This confirms that complex LIPSSs generated by overlaid polarization states are a composite topography rather being wiped and reset by each other. Different spatial periods of the ripples in Figure 6.8 (c-g) can also be observed. Shark-skin like structures can also be seen in Figure 6.8(a) and (b). These could have potential applications in engineering and biomedical devices due to self-cleaning and anti-bacterial properties[95, 248].

6.4.2.4 Fabrication of large surface area structures using a single synchronized CV beam

For volume-produced items, the use of holographic patterning for surface security is of significant interest for brand protection. However, holographic surface security patterning is not flexible because each pattern would require a redesign of the hologram. Compared with the holographic patterning, laser induced surface patterning on metal surfaces are both permanent and highly flexible. For high-value products, such as precious metals and banknotes, each item could have a unique polarization coded pattern, barcode or company logo on the surface, making the security level even higher than imprinting a single product design surface security pattern on every item. Figure 6.9 shows the result of security colour marking based on the CV polarization generated LIPSSs.

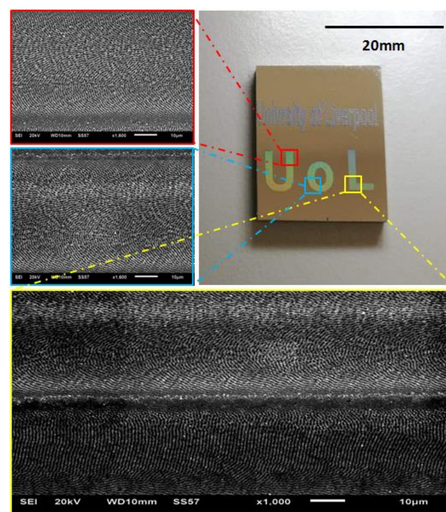

Figure 6. 9 Optical and SEM images of “University of Liverpool” (top) and “UoL” (bottom). Patterns were fabricated by azimuthally polarized CV beams with different hatch distance (100μm for the top pattern and 50μm for the bottom UOL

pattern). The top pattern is not as clear due to the large hatch distance. Practising speed v=15mm/s and fluence=0.6J/cm^2. Processing time for "UOL" pattern ≈37s.

The colour display on the UOL pattern can be observed clearly by illuminating with a white light. This is due to the complex LIPSS structures on the surface are regarded as diffractive gratings, the light will be diffracted based on the diffraction formula.

A pie chart based on the work presented in section 6.4.1, 18 segments have been used to configure the CV beams with 18 different grey level CGHs. The aim was to produce a pie chart fully covered with LIPSS but with different complex LIPSS orientations on each segment. 18 linear polarizations were synchronised by the motion control system, rotating from 0° (Horizontal linear polarization) to 180°clockwise with an incremental change of 10°. Using the S-waveplate the generated CV beams from the linear polarizations have been used for laser processing on the Ti64 surface, as shown in Figure 6.9. The processing scanning speed was v=15mm/s, the laser repetition rate was set at 10 kHz with the fluence=0.6J/cm^2. The spacing between scanned lines (hatch distance) was set at 52 µm to ensure each scanned line can be identified clearly under the optical microscope. These parameters produced clear LIPSS on the polished Ti6Al4V samples (cleaned with acetone (99.99%)). The processing started from the top-centre segment and each segment was produced one by one in a clockwise sequence while the cylindrical vector polarization orientation was synchronised automatically, changing from segment to segment. The time taken to process each segment was ~5.2 seconds, including a 200 ms delay for CGH change. The whole disc was patterned in ~93 seconds. As shown in Figure 6.10, various iridescent colours can be seen on the laser fabricated pie chart pattern.

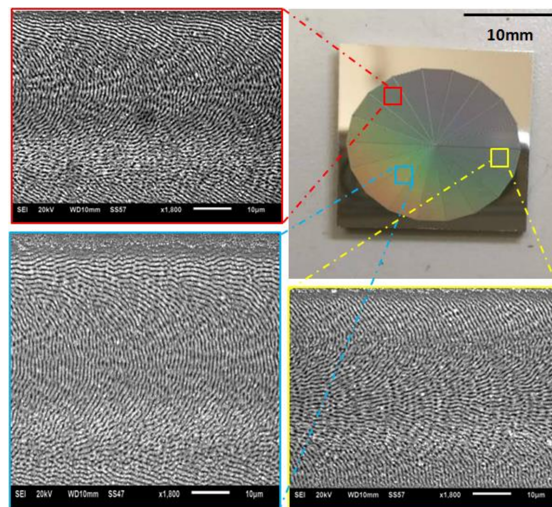

Figure 6. 10 Optical and SEM images of 18 segments pie chart with various CV beams. Structural coloration exhibited on an 18 segments pie chart, fabricated by 18 linearly-corresponding polarized CV beams with fluence = 0.6J/cm^2 at velocity =15mm/s, hatch distance=27µm. Total processing time s≈93s, includes 200ms delay for each grey level map switching.

6.5 Wettability properties

Among all the techniques that can be used to fabricate structures in the micro or nanoscale, picosecond laser machining has been demonstrated to be an effective technology to modify the wetting properties of a large list of material surfaces[245, 249]. In some research, the LIPSS generation process is accompanied by a chemical treatment in order to obtain extreme wetting properties such as superhydrophobicity [250]. However, even with only a LIPSS nano-patterning the wetting properties of a surface are changed [251]. Research has also shown that the orientation of LIPSS will give different wetting behaviour contact angles of the laser-processed surface [252]. In this work, a nanosecond pulsed fibre laser (SPI G4 HS-L 20W, M^2=1.83) was used to modify the wettability of polished Ti64 samples with spot by spot laser irradiation to form a 3x3 mm^2 consistent Cassie-Baxter state area (Figure 6.11), as described in [253] by Rico et al. Then, a picosecond laser (High-Q) was used to form complex LIPSS on the prepared microstructured specimen surface. The Ti64 sample surface produced has Gaussian-like craters, as shown in Figure 6.11, this is due to the nanosecond laser is Gaussian distribution. In this particular case, the nanosecond laser has been set to 33kHz, 5.09J/cm^2, overlap rate =15% for initial microstructure formation and a picosecond pulsed laser with 10kHz, 10mm/s, 0.6J/cm^2 has been set for LIPSS formation. After laser processing, the treated specimens were put in an oven for annealing with 200°C for 20 hours and cooled in the air for 3 hours. This was found by Rico Sierra et al [253] to stabilise the oxide formation and enhance the effect. The machined surface topography with a nanosecond laser was confirmed by a scanning electron microscope (SEM), as shown in Figure 6.11. It can be seen that a significant effect is present but this has been used to rapidly generate the micro scale spikes effectively.

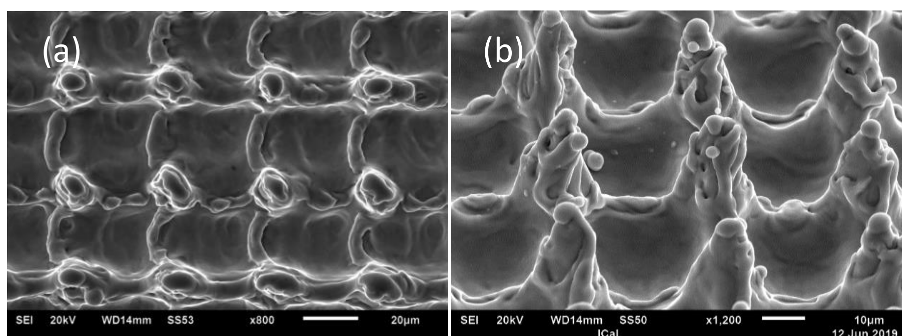

Figure 6. 11 Treated material surface with SPI nanosecond fibre laser. Spikes on the surface are presented. (a) Top view. (b) Tilt view. The applied Gaussian beam size was approximately 50μm, 15% overlap rate for processing, 5.09J/cm^2.

By dynamic altering of the cylindrical vector polarization states, different oriented LIPSS have been produced on the microstructured material surface for subsequent water contact angle tests. The contact angle images was carried by a Krüss EasyDrop standard Drop Shape Analysis System. The contact angle measurement was performed with a plug-in of Image J, DropSnake. The volume of a water droplet was controlled by a microliter pipette (V~10μL). The measured contact angle is approximately 57° for an untreated polished Ti64 sample. The microstructured sample using only the SPI nanosecond pulsed fibre

laser in air without thermal treatment changed the contact angle to 82°, an increase of 25°. After thermal treatment this stabilized to 112°.

Multiple CV states have been produced using a SLM and an S-waveplate at a refresh rate of 5Hz. Figure 6.12 and Figure 6.13 show the microstructures covered with different oriented LIPSS. Structures in Figure 6. 12 are only formed with one kind of CV polarization state and in Figure 6.13, structures were formed with two kinds of CV polarization states (Two different CV polarization states for alternating scan lines in sequence) on altering scan lines. For large area surface processing of LIPSS, the hatch distance was set to 40μm for the one-state polarized LIPSS and the dual-state polarized. In order to compare the surface wettability with more complex structures, the microstructured sample surface was covered with four-state polarized LIPSS (Repeating radial, clockwise spiral, azimuthal and counter-clockwise spiral direction CV polarization states for each scanned line in sequence, with 40μm hatch distance). The details of the CV polarization direction and LIPSS orientation can be seen in Figure 6.3 and Figure 6.6.

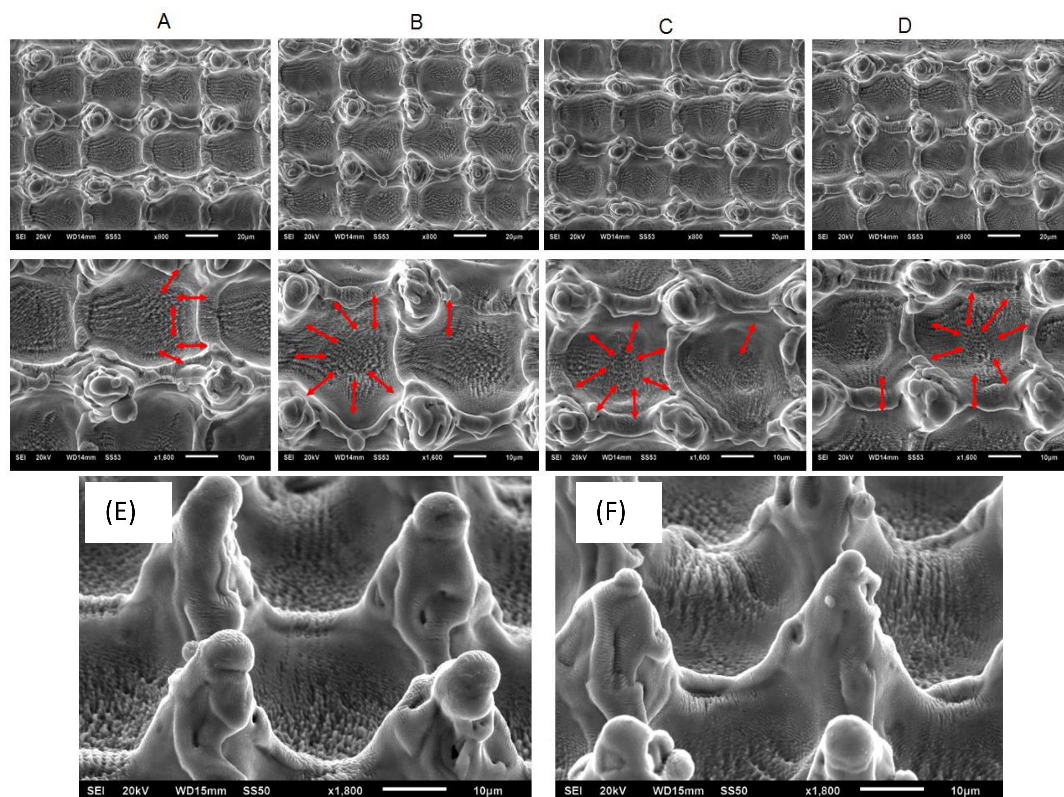

Figure 6. 12 SEM images of combining polarization dependent nanostructures and microstructures. (column A) microstructures with radial polarization; (column B) microstructures with spiral polarizations (clockwise LIPSS orientation); (column C) microstructures with azimuthal polarization; (column D) microstructures with spiral polarizations (counter clockwise). (E) Tilt view of column A. (F) Tilt view of column B. Red arrows represent the electric field E. The scale bar is 20μm for top line and 10μm for middle line.

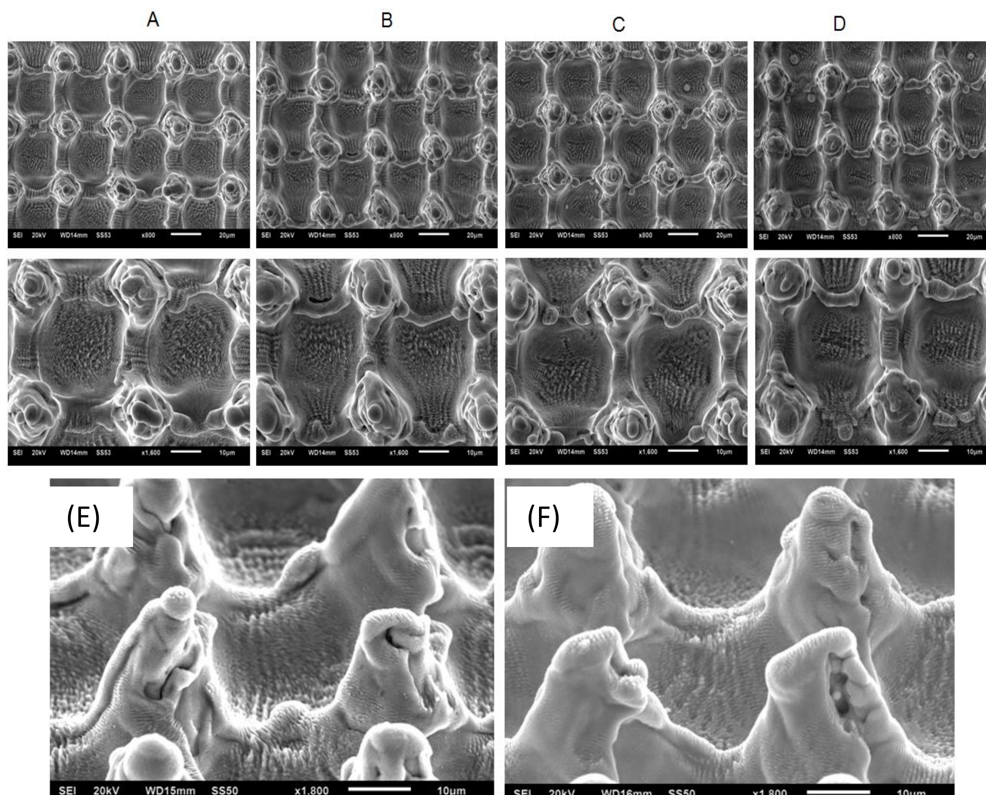

Figure 6. 13 SEM images of combining polarization dependent nanostructures and microstructures. (column A) microstructures with radial polarization plus azimuthal polarization; (column B) microstructures with azimuthal polarization and counter-clockwise spiral LIPSS orientation; (column C) microstructures with clockwise and counter-clockwise LIPSS orientation; (column D) microstructures with radial, azimuthal clockwise and counter-clockwise polarizations. (E) Tilt view of column A. (F) Tilt view of column B. The scale bar is 20μm for top line and 10μm for middle line.

It can be seen from Figure 6.12 and Figure 6.13 (E) and (F), the height of the connection between two spikes is almost same, therefore, the contact area of a water droplet on the treated surfaces will remain the same essentially. However, it is very difficult to identify the major difference in the results from Figure 6.12 and Figure 6.13, the surface roughness as measured using a WYKO NT1100 interferometer. The surface roughness of the structures with dual-state LIPSS (Ra~8.2±0.2μm) was found to be higher than the one-state structure (Ra~7.2 ±0.3 μm). The surface roughness of the sample with four-state CV LIPSS was measured as Ra~8.3 ±0.2 μm, which is close to the dual -state LIPSS surface with Ra~8.2μm. The increased surface roughness is likely due to the longer laser exposure time for a dual- and four-state LIPSS formation.

After an oven annealing of 20 hours at 200°C, all the LIPSS covered surfaces showed a superhydrophobic behaviour (contact angle >150°) on the first day of measurement. Depending on the complex surface structures and LIPSS orientations, the contact angle was found to be fluctuate however they all remained above 130° after 31 days, with some contact angles remaining >150°.

The decrease of superhydrophobic behaviour with time is attributed to the oxidation of the surface in an air atmosphere [254]. In addition, samples only covered with LIPSS were also annealed in the oven at 200°C for 20 hours. However, the contact angles were observed to decrease significantly for nanostructures (LIPSS) covered samples. All measurements are shown in Figure 6.14. All of the samples are superhydrophobic on the first day with a contact angle ⩾155°. It can be seen from Figure 6.14 (a), (b) and (c), all of the contact angle (CA) are stable within 31 days but with CA less than 140°, those samples were covered with only one kind of CV polarization. Dual-state polarized LIPSS covered structures present to have higher CA (CA~150°)) than one-state LIPSS covered structures (CA~ 135°). However, the CA of the four-state LIPSS covered surface was measured above 140° but lower than 150°, as shown in Figure 6.14 (c), although it has a close surface roughness to the sample covered with dual-state LIPSS. In addition, the surfaces with only microstructures have the lowest CA, seen in Figure 6.14 (c). Samples only covered with nanostructures (LIPSS) were superhydrophobic at the beginning, but this behaviour only lasted 2 days, then the CA shows a rapid decrease, as shown in Figure 6. 14 (d) and (e). However, superhydrophobic behaviour of samples covered with complex nano and microstructures combined with a thermal treatment was stable for at least 31 days. This is likely due to the space between scanned lines being small, and the water droplet not being able to fall down the complex surface structures. The sharp LIPSS structures covering the microstructured surface (Figure 6.13) does exhibit akin to the typical Cassie-Baxter state[255].

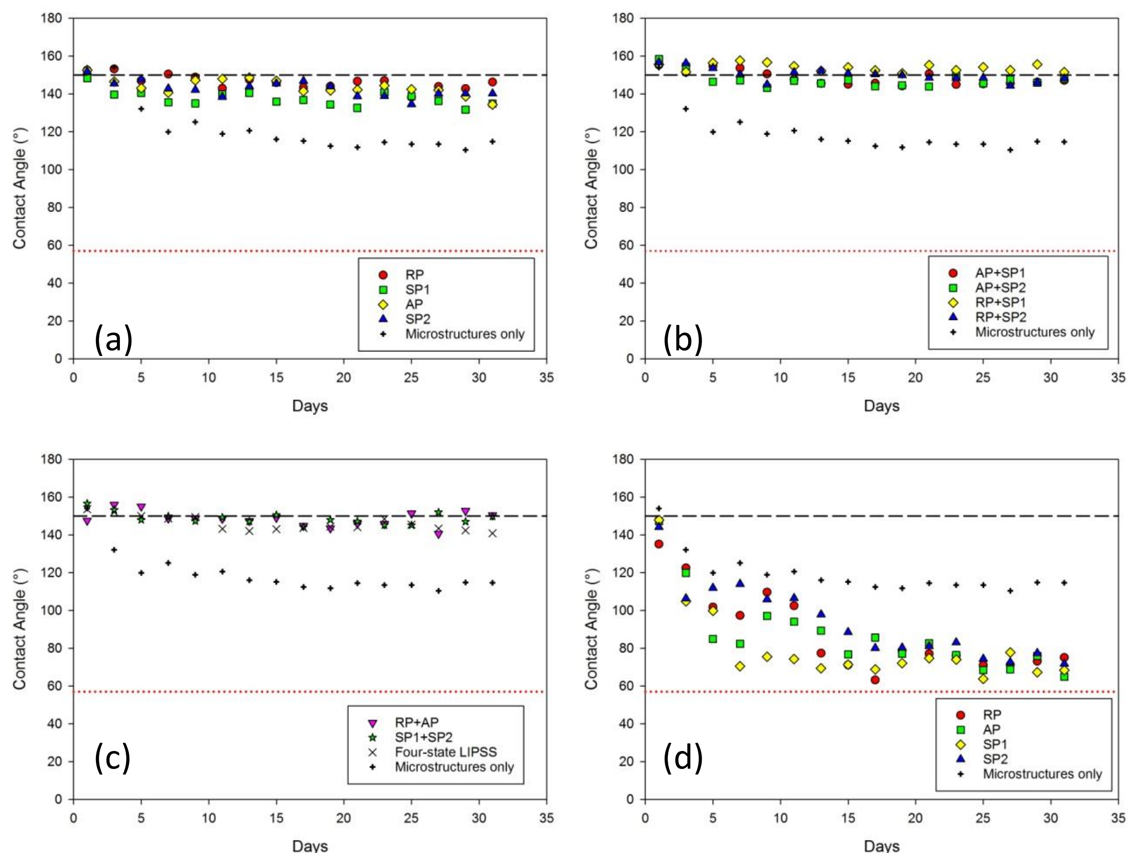

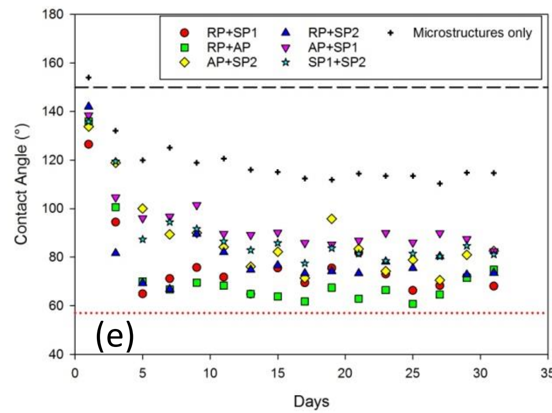

Figure 6. 14 contact angle measurements for (a-c) LIPSS covered microstructures or only microstructures surfaces (no LIPSS), (d-e) only LIPSS covered surfaces. Black dash line indicates 150° (superhydrophobic point). Red dotted line indicates 57° (the CA for an untreated sample). LIPSS produced with various polarization states. RP: radial polarization, SP1: clockwise spiral polarization, AP: azimuthal polarization, SP2: counter-clockwise spiral polarization. The laser parameters was set to 33kHz, 5.09J/cm^2 for microstructures formation and 10kHz, 0.6J/cm^2 for LIPSS formation.

Figure 6.15 presents the water CA on different surface structures. RP represents radial polarization, SP1 represents clockwise spiral polarization, AP represents azimuthal polarization and SP2 represents counter-clockwise spiral polarization, the details of each polarization states are shown in Figure 6.3 and corresponding LIPSS orientations are shown in Figure 6.6. Figure 6.15 (a) shows the CA of an untreated sample surface and (b-j) are the images of CA on the surface with microstructures combined with two or four polarized LIPSS nanostructures at Day 31. The contact angle with microstructures covered with four-state polarization was found to drop. This is likely due to the height of the spike is relative higher to the space between two LIPSSs (because of the four-state LIPSS has more complex structures), a small capillary has been generated at the surface makes the water droplet wetting easier [256]. The oxidation on the certain samples could be played a role in water contact angle measurement with time, however, this should be further investigated.

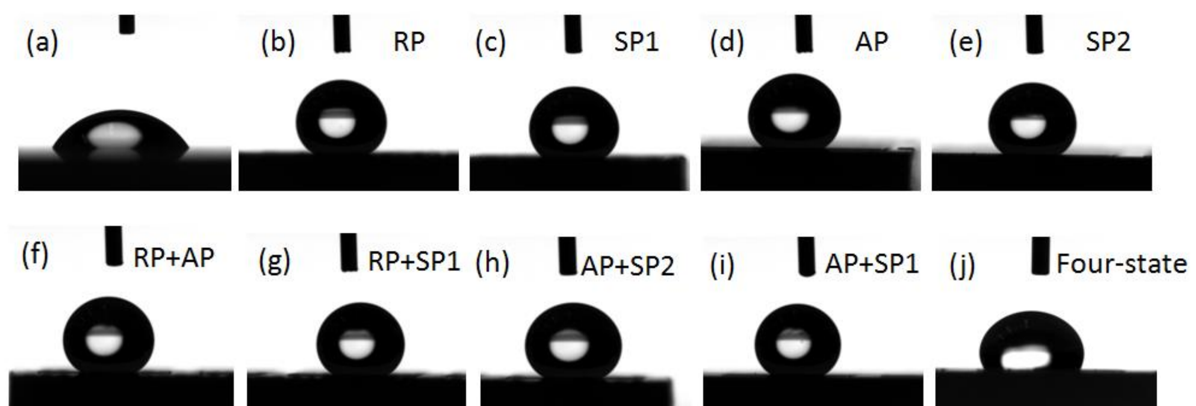

Figure 6. 15 Contact angles for different laser induced structures on Ti64 at day 31. (a) Untreated Ti64 surface. (b-e) Microstructure plus one-state polarization LIPSS. (f-i) Microstructure plus dual-state polarization LIPSS. (j) Microstructure plus four-state polarization LIPSS.

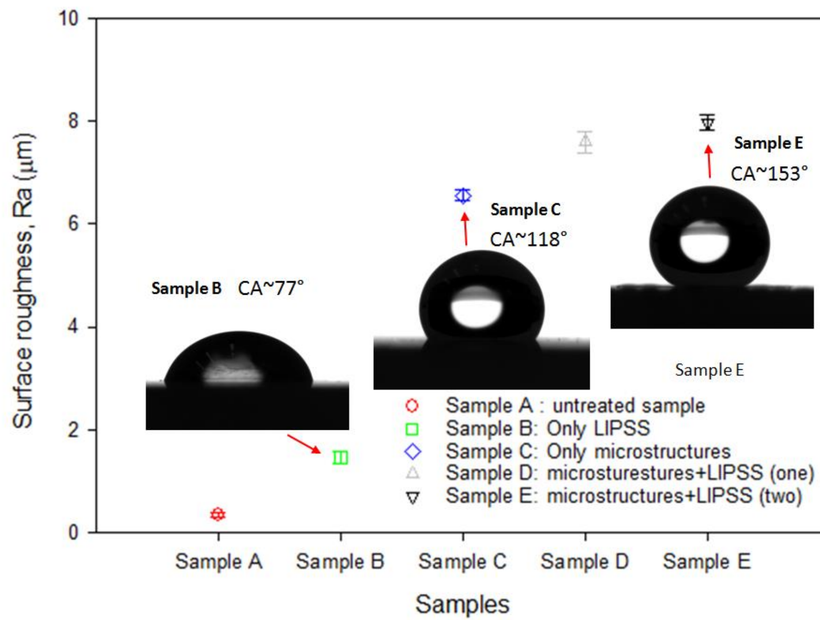

Figure 6. 16 Water contact angle changes with different surface roughness after the thermal treatment.

The thermal treatment was applied on the sample A to the sample E. It can be seen from Figure 6.16, the contact angle increases as the surface roughness is increasing.

The rolling-off angle is another important factor in surface wettability measurements. The LIPSS orientation impact on the water droplet contact angle on stainless steel with linear and circular polarization were discussed in [252]. The contact angles were performed from 135° to 150° with different orientated LIPSS structures. The measured contact angle (CA) with linearly polarized LIPSS (CA~150°, LIPSS orientations were vertical and horizontal) were found to be higher than circularly polarized LIPSS (CA~135°, LIPSS orientations were between vertical and horizontal). The CA for most of the treated surface in this study were over 140° at day 31, which means the surface wettability appears to be stable. However, the rolling-off angle of the treated samples were found to be different by performing with a Krüss EasyDrop standard Drop Shape Analysis System. The sample was put on a tilting stage, the water droplet on the sample surface will be rolling off by tilting the stage. Typical measured rolling-off angle results are shown in Figure 6.17. Differences in rolling off angle are likely due to surface structure orientations. A lower following off angle indicates a better superhydrophobic performance.

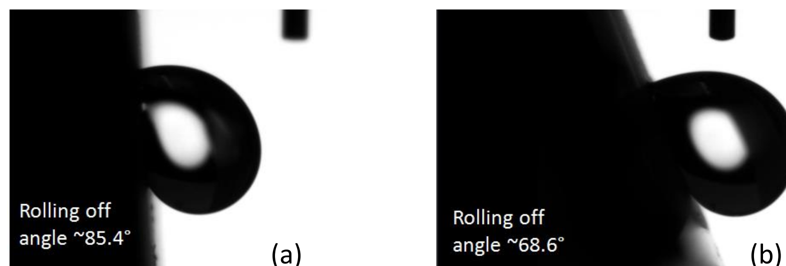

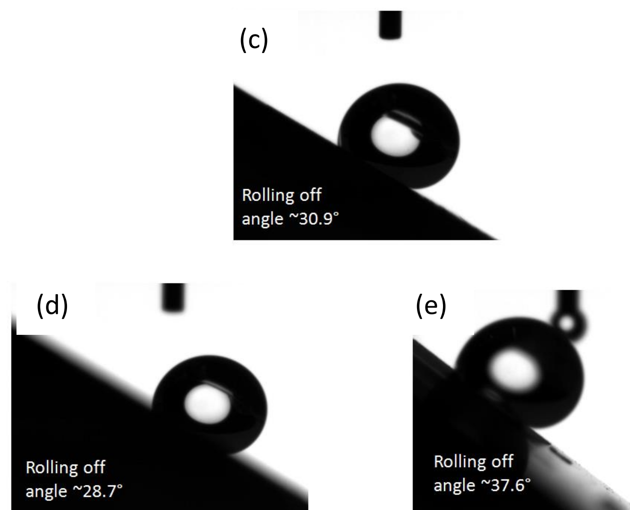

Figure 6. 17 The rolling off angle of samples covered with microstructures plus (a-b) one-state CV polarization LIPSS, (c-e) dual-state CV polarization LIPSS.

Figure 6.17 (a) and (b) shows the rolling-off angle with microstructures plus one-state polarization. The rolling-off angle were found to be >68°. Figure 6.17 (c), (d) and (e) shows the rolling-off angle with microstructures plus dual-state polarizations. The rolling-off angle were found to be~35°. The altering of the LIPSS orientation does appear to have an effect on rolling-off angle. Lower rolling-off angles were achieved by employing dual-state polarizations. This is likely due to the higher surface roughness compared with one-state polarization, where the water droplet has been more supported. This is likely due to the dual-state polarized nanostructures possibly provide less resistance than one-state nanostructures when the water droplet is rolling off due to the lower capillary action of the higher roughness. Figure. 6.18 displaying the contact angle hysteresis as the function of the tilting angle of one-state and dual-state CV LIPSS covered samples, where $\Delta\alpha$ represents the difference between advancing angles and receding angles.

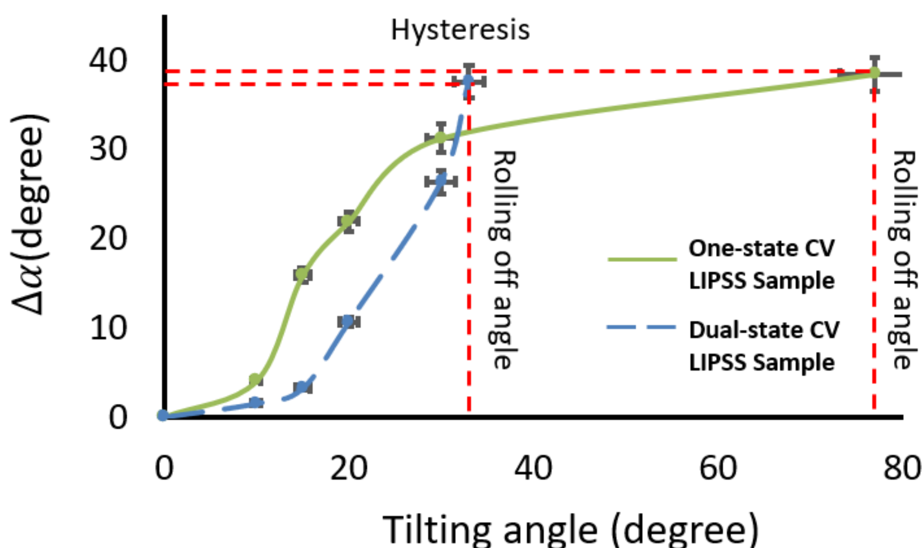

Figure 6. 18 Contact angle hysteresis and rolling off angle for one-state and dual-state CV LIPSS covered samples.

The microstructures of the samples play an important role in the spreading of the water droplet along the direction of the spikes, the nanostructures (LIPSS) provide a support for the water droplet. Therefore, the treated sample surface with two-level structures (microstructures combined with complex nanostructures) were found to perform with a good wettability behaviour, in which the two structures resemble the natural structure of the lotus leaf (Cassie-Baxter state). The comparison of the lotus leaf structures with the structures presented in this study is shown in Figure 6.19.

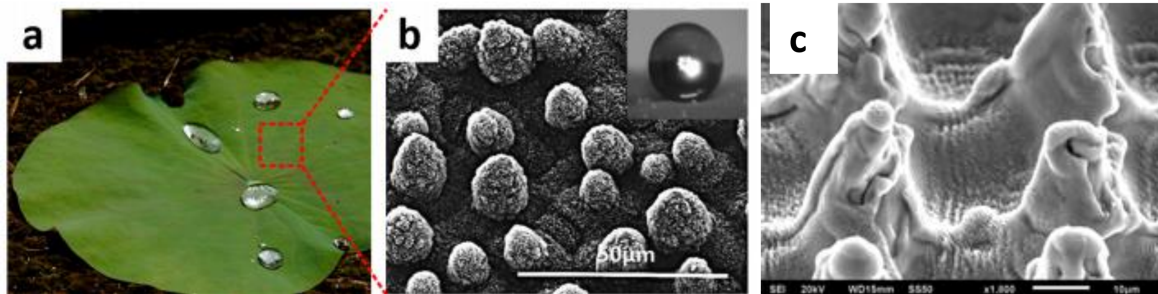

Figure 6. 19 (a) Image of a lotus leaf (b) the SEM image of the lotus leaf showing the hierarchical structures with papillose cells; (c) SEM image a two level structures which was formed by combining a nanosecond pulsed laser and a picosecond pulsed laser. Image (a) and (b) are taken from [257].

6.6 Summary

To summarize, presented in this chapter is a novel method of dynamically switching the cylindrical vector polarization of a picosecond pulsed laser by combining a phase-only SLM and a polarization converter (S-waveplate) for material surface processing. The SLM was used to switch the output polarization in real-time by changing a number of grey level holograms on the SLM with a frequency f=5Hz. The S-waveplate was used to modify the various input linear polarization states to different output cylindrical vector polarization states. Material surface structuring was realized with laser area scanning of radially, azimuthally and spirally polarized beams for unique surface colour marking and wettability modification. The laser scanning with complex CV polarization states on the material surface have produced shark skin-like morphologies. A method of overlaying and integrating complex polarizations dynamically for Ti64 surface processing with potential applications in surface marking, self-cleaning have been presented in this chapter. By combing the microstructures produced by a SPI nanosecond fibre laser and LIPSS formation with a picosecond pulsed laser, different wettability contact angles (CA) from 156° (dual-state polarized LIPSS structures on microstructures) to 135° (single-state polarized LIPSS structures on microstructures) have been displayed. The difference in the CA on the treated samples were likely due to the dual-state polarized LIPSS producing a more complex nanostructure pattern which leads lower capillary action for surface adhesive modification. Surfaces with combined nanostructures and microstructures were found to have a strong impact on the contact angle. The rolling-off angle for the dual-state LIPSS covered surface (~35°) is lower than the one-state LIPSS covered surface (>68°). The

rolling off angle are however very high, this is likely due to the surface energy of a treated sample is different. The investigation of employing several polarizations-dependent LIPSS on the microstructure surface could be useful for precision surface wettability behaviour control.

Chapter 7

Conclusions and future work

7.1 Conclusions

This thesis presents several novel methods of optimizing ultrafast lasers for material micro processing by using spatial light modulators (SLMs).

In Chapter 4, a novel method of beam shaping with polarization control and intensity modification at the image plane for material processing has been demonstrated. Arbitrary shapes with desired polarization states of single output beam were achieved with one SLM by employing binary geometric masks. An S-waveplate was used for spatial and polarization transformation to ring mode with vector beam. In addition, multiple shaped beams with a uniform intensity distribution were achieved with two SLMs by employing grey level geometric masks. Shaped beam results were reconstructed at the imaging plane of an optical system with expected shapes and intensities/polarization states.

By applying binary geometric masks on an SLM (Hamamatsu 10468-03), the output beam was shaped to simple geometries, such as square, star and triangular, with a Gaussian intensity distribution. In order to get sufficient intensity at the imaging plane for material processing, the thin lens equation was used. Therefore, a long objective distance (~5m) was set to minimize the distance between the focal plane and the imaging plane to obtain the reconstructed beam size which is approximately 31μm. The output beam was still linearly polarized. By employing a nano-structured polarization converter, S-waveplate, the output polarization after the S-waveplate at the imaging plane was radial or azimuthal, which is dependent on the fast axis angle of the S-waveplate. Polished Ti64 samples were machined by the shaped beams with desired polarization states. Laser induced Periodic Surface Structures (LIPSS) were used to confirm the polarization states. The machined footprints well matched the corresponding masks with desired LIPSS orientations. Both shaping quality and efficiency therefore depended on the size of the input beam with smaller mask sizes providing a better beam shaping quality due to the shaping ability of the SLM. In other words, higher shaping ability of the SLM will result in correspondingly lower shaping efficiency. This is due to the limitation of the shaping ability of the SLM and the original distribution of an input beam. A good balance between beam shaping quality and beam shaping efficiency can be achieved by selecting a mask with an appropriate size compared to the input beam size. For this work, a mask size of 250 pixels (1 pixel = 6.45μm) for an input beam size of 8mm was found to give the best results. Using this technique, arbitrary beam shapes can be obtained with desired masks and a complex Fourier transformation for beam shaping was avoided. By adding a polarization control optical element, the input linear polarization can be easily converted to complex radial or azimuthal polarization with various beam shapes for flexibility and efficiency improvement in laser applications. However, due to the Gaussian intensity distribution, this technique is limited, producing an uneven depth of machined footprints.

Grey level masks were then employed for both output beam outline profile and intensity distribution control. As with the binary masks, the grey level masks kept the same outline profile with similar geometric masks. However, by applying various grey level values in the grey level masks, the output beam intensity was modified according to the applied grey levels. Grey level masks were designed based on the original beam profile and the shaping ability of the used SLM. A near Gaussian beam was shaped to a near uniform square with desired outline and intensity distribution using a grey level mask.

With the benefits of shaped uniform laser beams, the beam shaping technique in this thesis was combined with parallel processing to improve manufacturing efficiency. Two SLMs were used to obtain multiple shaped beams at the imaging plane. The first SLM (Hamamatsu X10468-03) was used to shape the beam outline and intensity. The second SLM (Hamamatsu X13138-5785) was used to split the input beam into a desired multiple spots pattern. The grey level masks applied on the first SLM were for beam shaping at the objective plane. After a long distance propagation, the shaped beam was split into multiple beams on the second SLM. The grey level computer generated holograms (CGH, grey level phase changes from 0 to 2π) were applied on the second SLM for multiple laser spots generation. The multiple shaped beams were reconstructured on the imaging plane. The patterns at the imaging plane were the results of the convolution of the applied geometric masks and the CGHs for multiple beam generation. The machined footprints well matched the corresponding masks with desired intensity of multiple laser spots. By combining the beam shaping techniques with laser parallel processing, this allows laser-material interaction to be further improved using accurate and flexible shaped beams at a relatively high efficiency.

The generation of grey level CGHs are always difficult because of the complex calculations for the Fourier transformation algorithm. In Chapter 5, a simple, binary phase CGH, Dammann grating, was used in this study for multiple beam generation. The Dammann grating was produced by MATLAB code developed as part of the work. This was found to be a simpler algorithm when compared with the algorithms, such as iterative Fourier transformation algorithm (IFTA). The Dammann grating is much simpler and can produce equal-intensity spots, however these generally will have a lower diffraction efficiency (≤ 88%) due to the phase change involving only 0 and π. The uniformity of the spots reached the highest at the grey level of 107 on the SLM (for the Hamamatsu 10468-03, the full 2π phase modulation corresponds to grey level 212). Thus, the grey level value of 107 which corresponds closely to π was selected in this research. However, the generated arrays from a Dammann grating will lead to different beam size/intensity as the diffractive 0th order in the beam arrays carries higher intensity than other diffractive orders. By conjugating a Fresnel lens hologram with a Dammann grating on the SLM, the 0th diffractive order can be defocused to obtain a better uniform pattern.

Novel beam arrays with complex cylindrical vector (CV) polarization were achieved by employing an S-waveplate for multiple CV polarization control with one SLM. A machine learning method, cosine similarity, was used to compare the uniformity of generated arrays in MATLAB using SEM images.

An issue with CV beams (ring mode beams) is being able to define beam size and peak intensity in the same terms as a Gaussian beam. A novel method of defining the ablation threshold with a ring mode beam was presented. The single pulse ablation threshold on a material occurs when the radial/azimuthal polarized ring mode pulse energy is 2.7 times higher than the Gaussian pulse energy or when their peak intensities (and fluence) are the same.

A very recent new approach to defining the beam vector quality factor (VQF) [231] of ring vector beams with non-unifrom polarizations has been imprimented, This has been applied for the first time to beam arrays generated by Dammann (1x5 and 2x2) gratings, with concurrence C and entanglement entropy E measured to be $<C_{1x5}> = 0.95\pm0.01$, $<E_{1x5}> = 0.94\pm0.01$ respectively. However, on the 2x2 array, results were significantly lower in yielding $<C_{2x2}> = 0.86\pm 0.02$ and $<E_{2x2}> = 0.82\pm0.02$ respectively. The source of this discrepancy may lie in the flatness limitation of the SLM and angle dependent aberrations at the S-waveplate when beams arrive with both vertical and horizontal angles of incidence (AOI). From the 1x5 array results, the Bell-type test of single photon local entanglement of spatial mode and polarization state was carried out (state tomography) yielding $|S_{1x5}|= 2.35 \pm 0.02$, while beyond the classical limit $|S|\leq 2$. In addition, stokes projections were carried out on both arrays by removing the second SLM and replacing with a polarization analyzer. In this case, a significant improvement in the concurrence of the 2x2 array was observed inferring that the flatness limitation of the second SLM is more likely the source.

In addition, due to limitations of the cooled SLM (Hamamatsu X13138-03) high average powers greater than 120W are not possible with complex grey level CGHs [32]. Thus, the power handling ability of a cooled SLM was tested with a Dammann grating in this work. An average power of 160W was possible when using a binary Dammann grating CGH. The machined results with Dammann grating CGHs at high power were found to have good output diffractive efficiency .

In Chapter 6, the cylindrical vector (CV) polarization states were modified by a dynamic polarization control method with a combination of a SLM, quarter wave plate (QWP) and a polarization converter, S-waveplate. Various grey level CGHs were applied on the SLM (Hamamatsu X10468-03) with input linear polarization set to 45° polarization to generate different output elliptical polarizations. After passing through the QWP, rotated linear polarizations resulted. Then, the rotated linear polarizations passed through an S-waveplate with a fixed fast axis angle (0°) creating vector vortex beams. Hence, the output polarizations can be dynamically rotated from radial to azimuthal and their superpositions. LIPSS

were used to confirm the polarization state on polished Ti64 samples. The LIPSS on the Ti64 sample surfaces produced various iridescent colours under different viewing angles by white light diffraction. By overlaying several CV polarization states, the LIPSS were found to have two periods in a processed line. Shark-skin like LIPSS morphology was produced with a specific laser fluence. This technique allows dynamic altering of complex CV polarization states for applications such as security colour marking on high-value components. Altered complex CV polarization states were also applied for wettability modification of Titanium alloy. Firstly, a surface spike microstructure was created using a SPI nanosecond laser under galvo control and low pulse overlap of 15% and fluence 5.09J/cm^2. Secondly, the 10 ps pulsed laser was then used to produce the LIPSSs on the microstructured surface while dynamically altering CV polarization states with hatch distance between each scanned line set to 40μm. After laser processing, the samples were thermally treated at 200°C for 20 hours to control the oxidation on the Ti64. The microstructures plus one-state LIPSS, two-state LIPSS and four-state LIPSS were used to investigate the wettability behaviours of the processed samples. The water droplet contact angle (CA) of the samples with microstructures plus dual-state LIPSS (CA≥ 150°) were found to be higher than the samples only with microstructures plus one-state LIPSS (CA≤ 135°). The rolling off angle for the surface of the microstructure plus dual-state LIPSS (~35°) is significantly lower than the surface with one state LIPSS (>70°). Note that the maximum contact angle with only laser nanosecond processing was only 112°, hence the addition of complex LIPSS was very effective in making the surface superhydrophobic. This was likely due to the surface pattern of the dual-state LIPSS nanostructures being more complex than the one-state LIPSS reducing surface tension.

Overall, the work presented here has achieved the objectives as follows:

1. Generation of single shaped beams using mask imaging with desired polarization states at the optical imaging plane for laser micro processing. This is a novel method of beam shaping with polarization control for investigation of laser-material interactions.
2. Generation of multiple shaped beams with a uniform intensity distribution and linear polarization at the optical imaging plane for laser micro processing using two SLMs with excellent results. This method avoids the complex calculations of the Fourier Transform algorithms for generation of the computer generated holograms (CGH).
3. Multiple cylindrical vector (CV) polarized beams were obtained by using a binary CGH (Dammann grating) and a polarization converter (S-waveplate). The single pulse ablation threshold of CV polarized ring mode beam was found to occur when the pulse energy is 2.7 times higher than the equivalent Gaussian beam or when their peak intensities (and fluence) are the same. Higher order ring modes (m = 3) also showed the same ablation threshold indicating that the ablation threshold is independent of laser mode with 10 ps pulses.

4. The vector beam quality factor (VQF, concurrence and entanglement entropy) and Bell inequality of single and multiple beams have been measured, the latter for the first time leading to a scalable approach for multi-beam applications of vector vortex beams.
5. A novel method of dynamic control of CV polarization states using a spatial light modulator and an S-waveplate for laser surface modification was demonstrated. Shark skin-like Laser Induced Period Surface Structures (LIPSS) structures were observed with the CV polarizations. More complex LIPSS structures were achieved by overwriting scans with different CV polarizations generating a composite surface topography rather being wiped and reset by each other. The water contact angle and rolling off angle are affected by the direction of the CV polarized LIPSS.
6. The phase modulation of a cooled SLM used with binary CGHs was found to have a better performance than the SLM used with grey level CGHs at high average laser input power ($P \geq 120W$) extending the exposure range to $P \geq 160W$.

7.2 Recommendations for future work

The beam shaping technique can be improved further to achieve higher shaping efficiency and accuracy by combining machine learning models, such as Artificial Neural Networks (ANNs) and support vector machines (SVMs). The parameters of the geometric masks applied in the beam shaping optical system were found by comparing a rang of experimental tests. This can be achieved by a supervised machine learning method to optimize the geometric size and grey level values in the masks for precision beam shaping quality improvement. The original beam intensity was measured from a CCD beam profiler camera as an initial data for onward grey level masks generation, the quality of the image is low and still has noise, which affect the quality of the generated grey level masks hence affecting the generated beam quality in experiments. This can be improved by using a computer vision algorithm to generate a better CGH image with lower noise for geometric masks formation. CGHs created using binary Dammann gratings often have a higher intensity zero order. A feedback system using Spiricon camera could be used to reduce the zero order intensity and hence improve uniformity. Multiple spots generation using CGHs in this study was limited to 2D patterns as the spots were focused on the material surface. However, 3D multiple spots patterns could be investigated for 3D materials processing.

Multiple spots beam shaping at the image plane has been demonstrated in this study. However, all of the multiple spots are with the same shapes, therefore, multiple beam shaping with different shapes can be further investigated by modifying the geometric masks on the SLM.

The Bell's inequality measurement could be tested while splitting the incident beam into two paths and comparing photon polarizations in one channel with spatial modes in the other channel. In addition, multi-beam vector quality tests at high average laser powers $P > 100W$ would be very interesting.

Binary CGHs (0, π) were used to investigate the phase modulation ability of a cooled SLM under high laser power exposure. The thermal effects due to light absorption limit the phase modulation range to below 2π with average power P>120W. The use of Dammann binary gratings requiring only 0 and π modulation allowed the efficient diffraction up to 160W, a significant increase. This could be increased further by for example, using a flat-top beam instead of the Gaussian beam so reducing peak intensity on the SLM chip.

While I used only normal incidence for LIPSS generation, additional control of LIPSS could be investigated by varying the angle of incidence to the metal substrates. The LIPSS are useful for controlling for example, cell adhesion on biomedical polymers and thin films, however, most of the biomedical polymers and thin films are transparent or semi-transparent, hence difficult to inscribe surface LIPSS. CV polarized LIPSS printed on a metal mould could be hot-pressed on polymer or thin films for applications in research and industry.

References

1. Sugioka, K. and Y. Cheng, Femtosecond laser three-dimensional micro- and nanofabrication. Applied Physics Reviews, 2014. **1**(4): p. 041303.
2. Sagisaka, Y., et al., Micro Parts Processing Using Laser Cutting and Ultra-short-pulse Laser Peen Forming. Procedia Engineering, 2014. **81**: p. 2367-2372.
3. Sugioka, K. and Y. Cheng, Ultrafast lasers—reliable tools for advanced materials processing. Light: Science & Applications, 2014. **3**(4): p. e149-e149.
4. Courvoisier, F., R. Stoian, and A. Couairon, [INVITED] Ultrafast laser micro- and nano-processing with nondiffracting and curved beams. Optics & Laser Technology, 2016. **80**: p. 125-137.
5. Rekštytė, S., et al. Advances of Additive Laser Based Micro-Manufacturing Technologies for Cartilage Tissue Engineering: a Pre-Clinical Study. in 2015 European Conference on Lasers and Electro-Optics - European Quantum Electronics Conference. 2015. Munich: Optical Society of America.
6. Efficient Metal Processing Using High Average Power Ultrafast Laser. Journal of Laser Micro/Nanoengineering, 2017. **12**(3).
7. Ou, Z., M. Huang, and F. Zhao, Colorizing pure copper surface by ultrafast laser-induced near-subwavelength ripples. Opt Express, 2014. **22**(14): p. 17254-65.
8. Yao, J., et al., Selective appearance of several laser-induced periodic surface structure patterns on a metal surface using structural colors produced by femtosecond laser pulses. Applied Surface Science, 2012. **258**(19): p. 7625-7632.
9. Dusser, B., et al., Controlled nanostructrures formation by ultra fast laser pulses for color marking. Optics Express, 2010. **18**(3): p. 2913-2924.
10. Carter, R.M., et al., Picosecond laser welding of similar and dissimilar materials. Appl Opt, 2014. **53**(19): p. 4233-8.
11. Boyd, R.W., Nonlinear Optics. [electronic book]. Online access with subscription: Proquest Ebook Central. Amsterdam : Elsevier Science, 2008. 3rd ed.
12. Khorkov, K.S., et al., Processing materials in the mode of multiple filamentation of femtosecond laser radiation. Bulletin of the Russian Academy of Sciences: Physics, 2018. **81**(12): p. 1438-1441.
13. Xie, C., et al., Tubular filamentation for laser material processing. Sci Rep, 2015. **5**: p. 8914.
14. Ye, L., et al., NUV femtosecond laser inscription of volume Bragg gratings in poly(methyl)methacrylate with linear and circular polarizations. Laser Physics, 2013. **23**(12): p. 126004.

15. Theodosiou, C.E. and L. Armstrong, Two-photon ionisation of caesium. Journal of Physics B: Atomic and Molecular Physics, 1979. **12**(3): p. L87-L91.
16. Delone, N.B., Multiphoton ionization of atoms. Soviet Physics Uspekhi, 1975. **18**(3): p. 169-189.
17. Carman, H.S. and R.N. Compton, High ‐ order multiphoton ionization photoelectron spectroscopy of nitric oxide. The Journal of Chemical Physics, 1989. **90**(3): p. 1307-1312.
18. Fomin, V.M., et al., Mechanical characteristics of high-quality laser cutting of steel by fiber and CO2 lasers. Journal of Applied Mechanics and Technical Physics, 2015. **56**(4): p. 726-735.
19. Gu, B., et al., Optics to control thermal effects in selective laser melting. 2018: p. 48.
20. Chen, G. and X. Xu, Experimental and 3D Finite Element Studies of CW Laser Forming of Thin Stainless Steel Sheets. Journal of Manufacturing Science and Engineering, 2000. **123**(1): p. 66-73.
21. Dickey, F.M., Laser beam shaping : theory and techniques. 2nd ed. ed. 2014: CRC Press, Taylor & Francis Group.
22. Duerr, F. and H. Thienpont, Refractive laser beam shaping by means of a functional differential equation based design approach. Opt Express, 2014. **22**(7): p. 8001-11.
23. Laskin, A. and V. Laskin, πShaper– Refractive Beam Shaping Optics for Advanced Laser Technologies. Journal of Physics: Conference Series, 2011. **276**: p. 012171.
24. De Sio, L., et al., Beam shaping diffractive wave plates [Invited]. Appl Opt, 2018. **57**(1): p. A118-A121.
25. Ji, W., et al., Meta-q-plate for complex beam shaping. Sci Rep, 2016. **6**: p. 25528.
26. Frieden, B.R., Lossless Conversion of a Plane Laser Wave to a Plane Wave of Uniform Irradiance. Applied Optics, 1965. **4**(11): p. 1400-1403.
27. Kreuzer, J.L., COHERENT LIGHT OPTICAL SYSTEM YIELDING AN OUTPUT BEAM OF DESIRED INTENSITY DISTRIBUTION AT A DESIRED EQUIPHASE SURFACE. 1969, PERKIN ELMER CORP: United States.
28. Kato, J.-i., et al., Multiple-spot parallel processing for laser micronanofabrication. Applied Physics Letters, 2005. **86**(4): p. 044102.
29. Kuang, Z., et al., Fast parallel diffractive multi-beam femtosecond laser surface micro-structuring. Applied Surface Science, 2009. **255**(13-14): p. 6582-6588.
30. Kuang, Z., et al., Ultrashort pulse laser patterning of indium tin oxide thin films on glass by uniform diffractive beam patterns. Applied Surface Science, 2012. **258**(19): p. 7601-7606.
31. Beck, R.J., et al., Application of cooled spatial light modulator for high power nanosecond laser micromachining. Optics Express, 2010. **18**(16): p. 17059-17065.

32. Zhu, G., et al., Investigation of the thermal and optical performance of a spatial light modulator with high average power picosecond laser exposure for materials processing applications. Journal of Physics D: Applied Physics, 2018. **51**(9).
33. Bonse, J., M. Munz, and H. Sturm, Structure formation on the surface of indium phosphide irradiated by femtosecond laser pulses. Journal of Applied Physics, 2005. **97**(1): p. 013538.
34. Hnatovsky, C., V.G. Shvedov, and W. Krolikowski, The role of light-induced nanostructures in femtosecond laser micromachining with vector and scalar pulses. Opt Express, 2013. **21**(10): p. 12651-6.
35. Öktem, B., et al., Nonlinear laser lithography for indefinitely large-area nanostructuring with femtosecond pulses. Nature Photonics, 2013. **7**(11): p. 897-901.
36. Allegre, O.J., et al., Laser microprocessing of steel with radially and azimuthally polarized femtosecond vortex pulses. Journal of Optics, 2012. **14**(8): p. 085601.
37. Weber, R., et al., Effects of Radial and Tangential Polarization in Laser Material Processing. Physics Procedia, 2011. **12**: p. 21-30.
38. Beresna, M., et al., Radially polarized optical vortex converter created by femtosecond laser nanostructuring of glass. Applied Physics Letters, 2011. **98**(20): p. 201101.
39. Beresna, M. and P.G. Kazansky, Polarization diffraction grating produced by femtosecond laser nanostructuring in glass. Optics Letters, 2010. **35**(10): p. 1662-1664.
40. Wang, X.-L., et al., A new type of vector fields with hybrid states of polarization. Optics Express, 2010. **18**(10): p. 10786-10795.
41. Allegre, O.J., et al., Complete wavefront and polarization control for ultrashort-pulse laser microprocessing. Opt Express, 2013. **21**(18): p. 21198-207.
42. Han, W., et al., Vectorial optical field generator for the creation of arbitrarily complex fields. Opt Express, 2013. **21**(18): p. 20692-706.
43. Maurer, C., et al., Tailoring of arbitrary optical vector beams. New Journal of Physics, 2007. **9**(3): p. 78-78.
44. Allegre, O.J., et al., Real-time control of polarisation in ultra-short-pulse laser micro-machining. Applied Physics A, 2012. **107**(2): p. 445-454.
45. Hahne, S., B.F. Johnston, and M.J. Withford, Pulse-to-pulse polarization-switching method for high-repetition-rate lasers. Applied Optics, 2007. **46**(6): p. 954-958.
46. Gräf, S. and F.A. Müller, Polarisation-dependent generation of fs-laser induced periodic surface structures. Applied Surface Science, 2015. **331**: p. 150-155.
47. Yang, J., et al., Advanced Laser Patterning for Security Marking of High Value Metal Components. Procedia Engineering, 2017. **183**: p. 363-368.

48. Vogel, M., Principles of Lasers, 5th edn., by O. Svelto. Vol. 53. 2012. 1-1.
49. Lyubomirsky, I. and Q. Hu, Energy level schemes for far-infrared quantum well lasers. Applied Physics Letters, 1998. **73**(3): p. 300-302.
50. Sholokhov, E.M., et al., All-fiber Q-switched holmium laser. Laser Physics Letters, 2011. **8**(5): p. 382-385.
51. Liu, X., D. Du, and G. Mourou, Laser ablation and micromachining with ultrashort laser pulses. IEEE Journal of Quantum Electronics, 1997. **33**(10): p. 1706-1716.
52. Ma, S., et al., Efficient high repetition rate electro-optic Q-switched laser with an optically active langasite crystal. Sci Rep, 2016. **6**: p. 30517.
53. Liu, G., et al. Acousto-optic Q-switched pulse fiber laser with the peak power of 17.33kW. in 2012 International Conference on Optoelectronics and Microelectronics. 2012.
54. course, O.O. Laser : Fundamentals. 2019 [cited 2019 18 Mar]; Available from: http://www.optique-ingenieur.org/en/courses/OPI_ang_M01_C01/co/Contenu_12.html.
55. Rullière, C., Femtosecond laser pulses. [electronic book] : principles and experiments. Advanced texts in physics. 2005: New York : Springer, ©2005. 2nd ed.
56. Uesaka, M., Femtosecond beam science. [electronic book]. Online access with subscription: Proquest Ebook Central. 2005: London : Imperial College Press, 2005.
57. Krueger, A., Getting Practical. 2004.
58. Ducasse, A., C. Rullière, and B. Couillaud, Methods for the Generation of Ultrashort Laser Pulses: Mode-Locking, in Femtosecond Laser Pulses: Principles and Experiments, C. Rullière, Editor. 2005, Springer New York: New York, NY. p. 57-87.
59. Hammond, P.R., Saturable absorber properties of a laser dye; stimulated propagation of the pump flux. Applied Optics, 1979. **18**(4): p. 536-539.
60. Keller, U., et al., Solid-state low-loss intracavity saturable absorber for Nd:YLF lasers: an antiresonant semiconductor Fabry–Perot saturable absorber. Optics Letters, 1992. **17**(7): p. 505-507.
61. Hoffmann, M.C. and D. Turchinovich, Semiconductor saturable absorbers for ultrafast terahertz signals. Applied Physics Letters, 2010. **96**(15).
62. Spence, D.E., P.N. Kean, and W. Sibbett, 60-fsec pulse generation from a self-mode-locked Ti:sapphire laser. Optics Letters, 1991. **16**(1): p. 42-44.
63. Ell, R., et al., Generation of 5-fs pulses and octave-spanning spectra directly from a Ti:sapphire laser. Optics Letters, 2001. **26**(6): p. 373-375.
64. Treacy, E., Optical pulse compression with diffraction gratings. IEEE Journal of Quantum Electronics, 1969. **5**(9): p. 454-458.

65. Strickland, D. and G. Mourou, Compression of amplified chirped optical pulses. Optics Communications, 1985. **55**(6): p. 447-449.
66. Lemonick, S. Innovations in laser pgysics win the 2018 Nobel Prize in physics. 2018 [cited 2019 18 Mar]; Available from: https://cen.acs.org/physical-chemistry/Innovations-in-laser-physics-win-the-2018-Nobel-Prize-in-Physics/96/web/2018/10.
67. Kuang, Z., Parallel diffractive multi-beam ultrafast laser micro-processing, in Department of Engineering. 2010, University of Liverpool
68. Lasers, S. redENERGY® Pulsed Fiber Lasers. 2018 [cited 2019 April]; Available from: https://www.spilasers.com/industrial-fiber-lasers/redenergy-g4/.
69. Paschotta, R., Field guide to lasers. SPIE field guides: FG12. 2008: SPIE.
70. Quantum, L. taccor power. 2018 [cited 2019 April]; Available from: https://www.laserquantum.com/products/detail.cfm?id=98.
71. Phipps, C.R., Laser ablation and its applications. [electronic book]. Springer Series in Optical Sciences: 129. 2007: Boston, MA : Springer Science+Business Media, 2007.
72. Reid, D., Ultrafast Lasers - Technology and Applications. Vol. 211. 2003. 101-101.
73. Chichkov, B.N., et al., Femtosecond, picosecond and nanosecond laser ablation of solids. Applied Physics A, 1996. **63**(2): p. 109-115.
74. Steen, W.M. and J. Mazumder, Laser material processing. London : Springer, [2010] 4th ed.
75. Kiran Kumar, K., G.L. Samuel, and M.S. Shunmugam, Theoretical and experimental investigations of ultra-short pulse laser interaction on Ti6Al4V alloy. Journal of Materials Processing Technology, 2019. **263**: p. 266-275.
76. Förster, D., et al., Energy transfer mechanisms during laser pulsed processing of metals. 2015.
77. LaFratta, C.N., et al., Multiphoton fabrication. Angew Chem Int Ed Engl, 2007. **46**(33): p. 6238-58.
78. Le Harzic, R., et al., Pulse width and energy influence on laser micromachining of metals in a range of 100fs to 5ps. Applied Surface Science, 2005. **249**(1-4): p. 322-331.
79. Momma, C., et al., Short-pulse laser ablation of solid targets. Optics Communications, 1996. **129**(1): p. 134-142.
80. Fujimoto, J.G., et al., Femtosecond Laser Interaction with Metallic Tungsten and Nonequilibrium Electron and Lattice Temperatures. Physical Review Letters, 1984. **53**(19): p. 1837-1840.
81. Stafe, M., A. Marcu, and N. Puscas, Pulsed Laser Ablation of Solids. Vol. 53. 2014.
82. Hamad, A.H., Effects of Different Laser Pulse Regimes (Nanosecond, Picosecond and Femtosecond) on the Ablation of Materials for Production of Nanoparticles in Liquid Solution, in High Energy and Short Pulse Lasers. 2016.

83. Gharbi, M., et al., Influence of a pulsed laser regime on surface finish induced by the direct metal deposition process on a Ti64 alloy. Journal of Materials Processing Technology, 2014. **214**(2): p. 485-495.
84. Hamad, A., L. Li, and Z. Liu, A comparison of the characteristics of nanosecond, picosecond and femtosecond lasers generated Ag, TiO2 and Au nanoparticles in deionised water. Applied Physics A, 2015. **120**(4): p. 1247-1260.
85. Lonnie Lucas, J.Z. Femtosecond laser micromachining: A back-to-basics primer. 2012; Available from: https://www.industrial-lasers.com/articles/2012/06/femtosecond-laser-micromachining-a-back-to-basics-primer.html.
86. Le Harzic, R., et al., Comparison of heat-affected zones due to nanosecond and femtosecond laser pulses using transmission electronic microscopy. Applied Physics Letters, 2002. **80**(21): p. 3886-3888.
87. Oosterbeek, R.N., et al., Measuring the ablation threshold fluence in femtosecond laser micromachining with vortex and Bessel pulses. Opt Express, 2018. **26**(26): p. 34558-34568.
88. Ashkenasi, D., et al., Surface damage threshold and structuring of dielectrics using femtosecond laser pulses: the role of incubation. Applied Surface Science, 1999. **150**(1): p. 101-106.
89. Birnbaum, M., Semiconductor Surface Damage Produced by Ruby Lasers. Journal of Applied Physics, 1965. **36**(11): p. 3688-3689.
90. Bonse, J., et al., Femtosecond laser-induced periodic surface structures. Journal of Laser Applications, 2012. **24**(4).
91. Gnilitskyi, I., et al., High-speed manufacturing of highly regular femtosecond laser-induced periodic surface structures: physical origin of regularity. Sci Rep, 2017. **7**(1): p. 8485.
92. Höhm, S., et al., Dynamics of the formation of laser-induced periodic surface structures (LIPSS) upon femtosecond two-color double-pulse irradiation of metals, semiconductors, and dielectrics. Applied Surface Science, 2016. **374**: p. 331-338.
93. Borowiec, A. and H.K. Haugen, Subwavelength ripple formation on the surfaces of compound semiconductors irradiated with femtosecond laser pulses. Applied Physics Letters, 2003. **82**(25): p. 4462-4464.
94. Wu, B., et al., Superhydrophobic surfaces fabricated by microstructuring of stainless steel using a femtosecond laser. Applied Surface Science, 2009. **256**(1): p. 61-66.
95. Martínez-Calderon, M., et al., Femtosecond laser fabrication of highly hydrophobic stainless steel surface with hierarchical structures fabricated by combining ordered microstructures and LIPSS. Applied Surface Science, 2016. **374**: p. 81-89.

96. Jin., Y., Dynamic polarization control using spatial light modulators for advanced ultrafast laser surface-structuring, in Department of Engineering. 2016, University of Liverpool.
97. Lutey, A.H.A., et al., Towards Laser-Textured Antibacterial Surfaces. Sci Rep, 2018. **8**(1): p. 10112.
98. Chang, H.W., et al., Nanostructured Ag surface fabricated by femtosecond laser for surface-enhanced Raman scattering. J Colloid Interface Sci, 2011. **360**(1): p. 305-8.
99. Buividas, R., P.R. Stoddart, and S. Juodkazis, Laser fabricated ripple substrates for surface-enhanced Raman scattering. Annalen der Physik, 2012. **524**(11): p. L5-L10.
100. Nemanich, R.J., D.K. Biegelsen, and W.G. Hawkins, Aligned, coexisting liquid and solid regions in laser-annealed Si. Physical Review B, 1983. **27**(12): p. 7817-7819.
101. Hendrikson, W., et al., Mold-Based Application of Laser-Induced Periodic Surface Structures (LIPSS) on Biomaterials for Nanoscale Patterning. Macromol Biosci, 2016. **16**(1): p. 43-9.
102. Romano, J.-M., et al., Triangular laser-induced submicron textures for functionalising stainless steel surfaces. Applied Surface Science, 2018. **440**: p. 162-169.
103. Skoulas, E., et al., Biomimetic surface structuring using cylindrical vector femtosecond laser beams. Sci Rep, 2017. **7**: p. 45114.
104. Emmony, D.C., R.P. Howson, and L.J. Willis, Laser mirror damage in germanium at 10.6 μm. Applied Physics Letters, 1973. **23**(11): p. 598-600.
105. Barb, R.A., et al., Laser-induced periodic surface structures on polymers for formation of gold nanowires and activation of human cells. Applied Physics A, 2014. **117**(1): p. 295-300.
106. Bonse, J., et al., Laser-Induced Periodic Surface Structures— A Scientific Evergreen. IEEE Journal of Selected Topics in Quantum Electronics, 2017. **23**(3).
107. Costache, F., S. Kouteva-Arguirova, and J. Reif, Sub–damage–threshold femtosecond laser ablation from crystalline Si: surface nanostructures and phase transformation. Applied Physics A, 2004. **79**(4-6): p. 1429-1432.
108. Miyaji, G. and K. Miyazaki, Origin of periodicity in nanostructuring on thin film surfaces ablated with femtosecond laser pulses. Optics Express, 2008. **16**(20): p. 16265-16271.
109. Dong, Y. and P. Molian, Coulomb explosion-induced formation of highly oriented nanoparticles on thin films of 3C–SiC by the femtosecond pulsed laser. Applied Physics Letters, 2004. **84**(1): p. 10-12.
110. Ruiz de la Cruz, A., et al., High speed inscription of uniform, large-area laser-induced periodic surface structures in Cr films using a high repetition rate fs laser. Opt Lett, 2014. **39**(8): p. 2491-4.
111. Liu, D., et al., Picosecond laser beam shaping using A Spatial Light Modulator. 2012. 735-738.
112. Fauchet, P.M. and A.E. Siegman, Surface ripples on silicon and gallium arsenide under picosecond laser illumination. Applied Physics Letters, 1982. **40**(9): p. 824-826.

113. Fraggelakis, F., et al., Generation of micro- and nano-morphologies on a stainless steel surface irradiated with 257 nm femtosecond laser pulses. RSC Advances, 2018. **8**(29): p. 16082-16087.
114. Zuhlke, C.A., T.P. Anderson, and D.R. Alexander, Formation of multiscale surface structures on nickel via above surface growth and below surface growth mechanisms using femtosecond laser pulses. Opt Express, 2013. **21**(7): p. 8460-73.
115. Gurevich, E.L. and S.V. Gurevich, Laser Induced Periodic Surface Structures induced by surface plasmons coupled via roughness. Applied Surface Science, 2014. **302**: p. 118-123.
116. Ran, L. and S. Qu, Structure formation on the surface of alloys irradiated by femtosecond laser pulses. Applied Surface Science, 2010. **256**(8): p. 2315-2318.
117. Ardron, M., N. Weston, and D. Hand, A practical technique for the generation of highly uniform LIPSS. Applied Surface Science, 2014. **313**: p. 123-131.
118. Mezera, M., M. van Drongelen, and G.R.B.E. Römer, Laser-Induced Periodic Surface Structures (LIPSS) on Polymers Processed with Picosecond Laser Pulses. Journal of Laser Micro Nanoengineering, 2018. **13**: p. 105-116.
119. Kietzig, A.M., S.G. Hatzikiriakos, and P. Englezos, Patterned superhydrophobic metallic surfaces. Langmuir, 2009. **25**(8): p. 4821-7.
120. Uhlig, S., Self-Organized Surface Structures with Ultrafast White-Light: First Investigation of LIPSS with Supercontinuum. 2015: Springer Fachmedien Wiesbaden.
121. WIKIPEDIA. Phase (waves). [cited 2019 March]; Available from: https://en.wikipedia.org/wiki/Phase_(waves).
122. O'Shea, D.C., Elements of Modern Optical Design. 1985: Wiley.
123. Linear, Circular and Elliptical Polarization Animation in a Single Shot. 2011.
124. Jones, R.C., A New Calculus for the Treatment of Optical SystemsI. Description and Discussion of the Calculus. Journal of the Optical Society of America, 1941. **31**(7): p. 488-493.
125. Hall, D.G., Vector-beam solutions of Maxwell’s wave equation. Optics Letters, 1996. **21**(1): p. 9-11.
126. Novotny, L. and B. Hecht, Principles of Nano-optics. 2006: Cambridge University Press.
127. Zhan, Q., Cylindrical vector beams: from mathematical concepts to applications. Advances in Optics and Photonics, 2009. **1**(1).
128. Roxworthy, B.J. and K.C. Toussaint, Optical trapping with π-phase cylindrical vector beams. New Journal of Physics, 2010. **12**(7).
129. Donato, M.G., et al., Optical trapping of nanotubes with cylindrical vector beams. Optics Letters, 2012. **37**(16): p. 3381-3383.

130. Drevinskas, R., et al., Laser material processing with tightly focused cylindrical vector beams. Applied Physics Letters, 2016. **108**(22).
131. Ouyang, J., et al., Tailored optical vector fields for ultrashort-pulse laser induced complex surface plasmon structuring. Opt Express, 2015. **23**(10): p. 12562-72.
132. Allegre, O.J., et al., Laser microprocessing of steel with radially and azimuthally polarized femtosecond vortex pulses. Journal of Optics, 2012. **14**(8).
133. Ouyang, J., Tailored optical vector fields for ultrashort-pulse laser mirco-processing, in Department of Engineering. 2016, University of Liverpool.
134. Matsuo, S., Matrix calculus for axially symmetric polarized beam. Optics Express, 2011. **19**(13): p. 12815-12824.
135. Fowles, G.R., Introduction to modern optics. 2nd ed. ed. 1975.
136. Vorobyev, A.Y. and C. Guo, Direct femtosecond laser surface nano/microstructuring and its applications. Laser & Photonics Reviews, 2013. **7**(3): p. 385-407.
137. Boyd, R.W., Nonlinear Optics. 3rd ed. ed. Online access with subscription: Proquest Ebook Central. Elsevier Science.
138. Panov, N.A., et al., Filamentation of arbitrary polarized femtosecond laser pulses in case of high-order Kerr effect. Optics Letters, 2013. **38**(4): p. 537-539.
139. Fox, R.A., R.M. Kogan, and E.J. Robinson, Laser Triple-Quantum Photoionization of Cesium. Physical Review Letters, 1971. **26**(23): p. 1416-1417.
140. Temnov, V.V., et al., Multiphoton ionization in dielectrics: comparison of circular and linear polarization. Phys Rev Lett, 2006. **97**(23): p. 237403.
141. Reiss, H.R., Polarization Effects in High-Order Multiphoton Ionization. Physical Review Letters, 1972. **29**(17): p. 1129-1131.
142. Tuchin, V.V., Polarized light interaction with tissues. J Biomed Opt, 2016. **21**(7): p. 71114.
143. Austin, D.R., et al., Laser induced periodic surface structure formation in germanium by strong field mid IR laser solid interaction at oblique incidence. Opt Express, 2015. **23**(15): p. 19522-34.
144. Gawelda, W., et al., Ultrafast imaging of transient electronic plasmas produced in conditions of femtosecond waveguide writing in dielectrics. Applied Physics Letters, 2008. **93**(12).
145. Zhu, G., Experimental Studies on Ultrafast Laser-Materials Micro-Structuring with Phase Only Spatial Light Modulators, in Department of Engineering. 2018, University of Liverpool.
146. Yamada, K., et al., Anisotropic refractive-index change in silica glass induced by self-trapped filament of linearly polarized femtosecond laser pulses. Journal of Applied Physics, 2003. **93**(4): p. 1889-1892.
147. Rung, S., et al., Laserscribing of Thin Films Using Top-Hat Laser Beam Profiles. Vol. 8. 2013. 309.

148. Gillen-Christandl, K., et al., Comparison of Gaussian and super Gaussian laser beams for addressing atomic qubits. Applied Physics B, 2015. **122**.

149. Michigami, N., et al, High-performance printed circuit board production equipment for ultra-high density multi-layer wiring. Hitachi Review, 2011. **60**(5): p. 217.

150. Han, W., W. Cheng, and Q. Zhan, Flattop focusing with full Poincaré beams under low numerical aperture illumination. Optics letters, 2011. **36**: p. 1605-7.

151. Li, J., et al., Imaging-based amplitude laser beam shaping for material processing by 2D reflectivity tuning of a spatial light modulator. Applied Optics, 2016. **55**(5): p. 1095-1100.

152. Hasegawa, S. and Y. Hayasaki, Polarization distribution control of parallel femtosecond pulses with spatial light modulators. Optics Express, 2013. **21**(11): p. 12987-12995.

153. Ambrosio, A., et al., Light-induced spiral mass transport in azo-polymer films under vortex-beam illumination. Nature Communications, 2012. **3**: p. 989.

154. Silvennoinen, M., et al., Parallel femtosecond laser ablation with individually controlled intensity. Optics Express, 2014. **22**(3): p. 2603-2608.

155. Zhu, G., et al., Investigation of the thermal and optical performance of a spatial light modulator with high average power picosecond laser exposure for materials processing applications. Journal of Physics D: Applied Physics, 2018. **51**(9): p. 095603.

156. Zhou, C. and L. Liu, Numerical study of Dammann array illuminators. Applied Optics, 1995. **34**(26): p. 5961-5969.

157. Yu, J., et al., Three-dimensional Dammann array. Applied Optics, 2012. **51**(10): p. 1619-1630.

158. Liu, Y., et al., Generation of perfect vortex and vector beams based on Pancharatnam-Berry phase elements. Scientific Reports, 2017. **7**: p. 44096.

159. Ruffato, G., M. Massari, and F. Romanato, Diffractive optics for combined spatial- and mode-division demultiplexing of optical vortices: design, fabrication and optical characterization. Scientific Reports, 2016. **6**: p. 24760.

160. Khonina, S., R.V. Skidanov, and O.Y. Moiseev, Airy laser beams generation by binary-coded diffractive optical elements for microparticles manipulation. Vol. 33. 2009. 138-146.

161. Agrawal, G.P. and E. Wolf, Propagation-induced polarization changes in partially coherent optical beams. Journal of the Optical Society of America A, 2000. **17**(11): p. 2019-2023.

162. Porfirev, A.P., A.V. Ustinov, and S.N. Khonina, Polarization conversion when focusing cylindrically polarized vortex beams. Scientific Reports, 2016. **6**(1): p. 6.

163. Jin, Y., et al., Dynamic modulation of spatially structured polarization fields for real-time control of ultrafast laser-material interactions. Opt Express, 2013. **21**(21): p. 25333-43.

164. Zhu, L. and J. Wang, Arbitrary manipulation of spatial amplitude and phase using phase-only spatial light modulators. Sci Rep, 2014. **4**: p. 7441.
165. Ye, X., et al., Generation of a terahertz collimated top-hat beam by using two thin diffractive phase plates. OSA Continuum, 2018. **1**(4).
166. Forbes, A., et al., The generation of flat-top beams by complex amplitude modulation with a phase-only spatial light modulator, in Laser Beam Shaping XIII. 2012.
167. Kudryashov, A.V., et al., Gaussian-to-top-hat beam shaping: an overview of parameters, methods, and applications, in Laser Resonators, Microresonators, and Beam Control XIV. 2012.
168. Račiukatis, G., Laser Processing by Using Diffractive Optical Laser Beam Shaping Technique. Journal of Laser Micro/Nanoengineering, 2011. **6**(1): p. 37-43.
169. Goffin, N., J. Tyrer, and E. Woolley, Complex beam profiles for laser annealing of thin-film CdTe photovoltaics. Journal of Laser Applications, 2018. **30**(4).
170. Volpp, J., Investigation on the Influence of Different Laser Beam Intensity Distributions on Keyhole Geometry During Laser Welding. Physics Procedia, 2012. **39**: p. 17-26.
171. Duocastella, M. and C.B. Arnold, Bessel and annular beams for materials processing. Laser & Photonics Reviews, 2012. **6**(5): p. 607-621.
172. Sokolovskii, G.S., et al., Optical trapping with Bessel beams generated from semiconductor lasers. Journal of Physics: Conference Series, 2014. **572**.
173. Ren, O. and R. Birngruber, Axicon: a new laser beam delivery system for corneal surgery. IEEE Journal of Quantum Electronics, 1990. **26**(12): p. 2305-2308.
174. Laskin, A. and V. Laskin, πShaper– Refractive Beam Shaping Optics for Advanced Laser Technologies. Journal of Physics: Conference Series, 2011. **276**.
175. David, S., et al., Design of single and two-lens laser flat-top reshaping systems, in Illumination Optics V. 2018.
176. Tang, Y., et al., Dynamic beam shaping with polarization control at the image plane for material processing. Procedia CIRP, 2018. **74**: p. 581-584.
177. Liu, D., et al., Dynamic laser beam shaping for material processing using hybrid holograms. Optics & Laser Technology, 2018. **102**: p. 68-73.
178. Jin, Y., et al., WAVEFRONT AND POLARIZATION STRUCTURING FOR SHAPING THE FOCAL FIELDS OF ULTRASHORT-PULSE LASER BEAMS. 2015.
179. Woerdemann, M., et al., Advanced optical trapping by complex beam shaping. Laser & Photonics Reviews, 2013. **7**(6): p. 839-854.
180. Porfirev, A.P. and R.V. Skidanov, Dark-hollow optical beams with a controllable shape for optical trapping in air. Opt Express, 2015. **23**(7): p. 8373-82.

181. Bowman, D., et al., High-fidelity phase and amplitude control of phase-only computer generated holograms using conjugate gradient minimisation. Opt Express, 2017. **25**(10): p. 11692-11700.
182. Kuang, Z., et al., High throughput diffractive multi-beam femtosecond laser processing using a spatial light modulator. Applied Surface Science, 2008. **255**(5): p. 2284-2289.
183. Silvennoinen, M., et al., Parallel femtosecond laser ablation with individually controlled intensity. Opt Express, 2014. **22**(3): p. 2603-8.
184. Mauclair, C., et al., Dynamic ultrafast laser spatial tailoring for parallel micromachining of photonic devices in transparent materials. Optics Express, 2009. **17**(5): p. 3531-3542.
185. Osawa, K., et al., Beam shaping by spatial light modulator and 4f system to square and top-flat for interference laser processing. SPIE LASE. Vol. 10091. 2017: SPIE.
186. Li, J., et al., Multi imaging-based beam shaping for ultrafast laser-material processing using spatial light modulators. Optics and Lasers in Engineering, 2019. **112**: p. 59-67.
187. Klerksa, T. and S.E. , Flexible beam shaping system for the next generation of process development in laser micromachining in 9th International Conference on Photonic Technologies LANE 2016 2016, Bayerisches Laserzentrum GmbH: Furth Germany.
188. Hendriks, A., et al., The generation of flat-top beams by complex amplitude modulation with a phase-only spatial light modulator. SPIE Optical Engineering + Applications. Vol. 8490. 2012: SPIE.
189. Kuroiwa, Y., et al., Arbitrary micropatterning method in femtosecond laser microprocessing using diffractive optical elements. Optics Express, 2004. **12**(9): p. 1908-1915.
190. Brott, L.L., et al., Ultrafast holographic nanopatterning of biocatalytically formed silica. Nature, 2001. **413**: p. 291.
191. Born, M. and E. Wolf, Principles of Optics: Electromagnetic Theory of Propagation, Interference and Diffraction of Light. 1997: Cambridge University Press.
192. O'Shea, D.C., et al., Diffractive Optics: Design, Fabrication, and Test. 2004: Society of Photo Optical.
193. Chen, C.-Y., et al., 3-D modified Gerchberg–Saxton algorithm developed for panoramic computer-generated phase-only holographic display. Journal of the Optical Society of America B, 2017. **34**(5): p. B42-B48.
194. Liesener, J., et al., Multi-functional optical tweezers using computer-generated holograms. Optics Communications, 2000. **185**(1): p. 77-82.
195. Mikhaylov, D., et al., High accuracy beam splitting using spatial light modulator combined with machine learning algorithms. Optics and Lasers in Engineering, 2019. **121**: p. 227-235.
196. Chung, F.J.W.a.P.S., Design of Circular Dammann Grating: Fabrication and Analysis Advances in Unconventional Lithography, 2010.

197. Zhao, S. and P.S. Chung, Design of a circular Dammann grating. Optics Letters, 2006. **31**(16): p. 2387-2389.
198. AMPHOS. Technology. Available from: https://www.amphos.de/technology/.
199. HAMAMATSU. LCOS-SLM(Liquid Crystal on Silicon-Spatial Light Modulator). X10468/X13267/X13138 series 2018 [cited 2019 01/06/2019]; Available from: https://www.hamamatsu.com/resources/pdf/ssd/x10468_series_etc_kacc1172e.pdf.
200. Rosenkrantz, E., et al., High-power laser diodes with high polarization purity. SPIE LASE. Vol. 10086. 2017: SPIE.
201. THORLABS. CCD Camera Beam Profiler. 2019 [cited 2019 01/06/2019]; Available from: https://www.thorlabs.com/newgrouppage9.cfm?objectgroup_id=3483&pn=BC106N-VIS/M.
202. Photonics, O. Cameras. 2015; Available from: https://www.ophiropt.com/user_files/laser/beam_profilers/USB-Silicon-CCD-camera.pdf.
203. Ma, H., et al., Near-diffraction-limited annular flattop beam shaping with dual phase only liquid crystal spatial light modulators. Optics Express, 2010. **18**(8): p. 8251-8260.
204. Kuang, Z., et al., Ultrafast laser beam shaping for material processing at imaging plane by geometric masks using a spatial light modulator. Optics and Lasers in Engineering, 2015. **70**: p. 1-5.
205. Tanigawa, D., et al., Suppression of dilution in Ni-Cr-Si-B alloy cladding layer by controlling diode laser beam profile. Optics & Laser Technology, 2018. **99**: p. 326-332.
206. Yu, H., et al., Recent advances in wavefront shaping techniques for biomedical applications. Current Applied Physics, 2015. **15**(5): p. 632-641.
207. Kuang, Z., et al., Multi-location laser ignition using a spatial light modulator towards improving automotive gasoline engine performance. Optics and Lasers in Engineering, 2017. **90**: p. 275-283.
208. Sudrie, L., et al., Study of damage in fused silica induced by ultra-short IR laser pulses. Optics Communications, 2001. **191**(3): p. 333-339.
209. König, K., O. Krauss, and I. Riemann, Intratissue surgery with 80 MHz nanojoule femtosecond laser pulses in the near infrared. Optics Express, 2002. **10**(3): p. 171-176.
210. Niziev, V.G. and A.V. Nesterov, Influence of beam polarization on laser cutting efficiency. Journal of Physics D: Applied Physics, 1999. **32**(13): p. 1455-1461.
211. Goodman, J.W., Introduction to Fourier optics. 3rd ed. ed. 2005: Roberts & Co.
212. Sheppard, C.J.R. and M. Hrynevych, Diffraction by a circular aperture: a generalization of Fresnel diffraction theory. Journal of the Optical Society of America A, 1992. **9**(2): p. 274-281.
213. Gori, F., Polarization basis for vortex beams. Journal of the Optical Society of America A, 2001. **18**(7): p. 1612-1617.

214. Kikuchi, H., A. Mizutani, and H. Kikuta, Fourfold rotationally symmertrically polarized laser beam for drilling a square hole. Japanese Jounal of Applied Physics, 2016. **55**: p. 042701.
215. Rodrigues, G.C. and J.R. Duflou, Effects of Different Polarization Strategies on Laser Cutting with Direct Diode Lasers. Physics Procedia, 2016. **83**: p. 302-309.
216. Nolte, S., et al., Polarization effects in ultrashort-pulse laser drilling. Applied Physics A, 1999. **68**(5): p. 563-567.
217. Granados, E., et al., Enhancement of surface area and wettability properties of boron doped diamond by femtosecond laser-induced periodic surface structuring. Optical Materials Express, 2017. **7**(9): p. 3389.
218. Erdélyi, M. and Z. Bor, Radial and azimuthal polarizers. Journal of Optics A: Pure and Applied Optics, 2006. **8**(9): p. 737-742.
219. Zhan, Q., Cylindrical vector beams: from mathematical concepts to applications. Advances in Optics and Photonics, 2009. **1**(1): p. 1-57.
220. Hayasaki, Y., et al., Variable holographic femtosecond laser processing by use of a spatial light modulator. Applied Physics Letters, 2005. **87**(3): p. 031101.
221. Choudhury, D., J.R. Macdonald, and A.K. Kar, Ultrafast laser inscription: perspectives on future integrated applications. Laser & Photonics Reviews, 2014. **8**(6): p. 827-846.
222. Mei-Li, H. and L. Chun-Cheng. Design of computer generated phase holograms by using iterative Fourier transform algorithm. in CLEO/Pacific Rim 2003. The 5th Pacific Rim Conference on Lasers and Electro-Optics (IEEE Cat. No.03TH8671). 2003.
223. Zou, H., et al. The Study of Various Dammann Grating. in 2010 Symposium on Photonics and Optoelectronics. 2010.
224. Kuang, Z., et al., Ultrafast laser parallel microprocessing using high uniformity binary Dammann grating generated beam array. Applied Surface Science, 2013. **273**: p. 101-106.
225. Liu, J.M., Simple technique for measurements of pulsed Gaussian-beam spot sizes. Optics Letters, 1982. **7**(5): p. 196-198.
226. Ju, L.B., et al., Controlling multiple filaments by relativistic optical vortex beams in plasmas. Phys Rev E, 2016. **94**(3-1): p. 033202.
227. Leach, J., et al., Violation of a Bell inequality in two-dimensional orbital angular momentum state-spaces. Optics Express, 2009. **17**(10): p. 8287-8293.
228. Siegman, A., Defining, measuring, and optimizing laser beam quality. OE/LASE'93: Optics, Electro-Optics, and Laser Applications in Scienceand Engineering. Vol. 1868. 1993: SPIE.
229. Ndagano, B., et al., Beam quality measure for vector beams. Opt Lett, 2016. **41**(15): p. 3407-10.

230. Karimi, E., et al., Spin-orbit hybrid entanglement of photons and quantum contextuality. Physical Review A, 2010. **82**(2): p. 022115.

231. McLaren, M., T. Konrad, and A. Forbes, Measuring the nonseparability of vector vortex beams. Physical Review A, 2015. **92**(2).

232. Wei, T.-C., et al., Maximal entanglement versus entropy for mixed quantum states. Physical Review A, 2003. **67**(2): p. 022110.

233. Gadway, B.R., E.J. Galvez, and F. De Zela, Bell-inequality violations with single photons entangled in momentum and polarization. Journal of Physics B: Atomic, Molecular and Optical Physics, 2009. **42**(1): p. 015503.

234. Matsukevich, D.N., et al., Bell Inequality Violation with Two Remote Atomic Qubits. Physical Review Letters, 2008. **100**(15): p. 150404.

235. Gecevičius, M., et al., Single beam optical vortex tweezers with tunable orbital angular momentum. Applied Physics Letters, 2014. **104**(23): p. 231110.

236. Valette, S., et al., Influence of femtosecond laser marking on the corrosion resistance of stainless steels. Applied Surface Science 2006(252): p. 4696-4701.

237. Valette, S., et al., X-ray analysis of mechanical and thermal effects induced by femtosecond laser treatment of aluminum single crystals. Applied Surface Science, 2006(252): p. 4691-4695.

238. Liu, Y., et al., Generation of perfect vortex and vector beams based on Pancharatnam-Berry phase elements. SCIENTIFIC REPORTS, 2017: p. 1-8.

239. Roxworthy, B.J. and K.C.T. Jr, Optical trapping with π-phase cylindrical vector beams. New Journal of Physics, 2010(12): p. 1-10.

240. Niziev, V.G. and A.V. Nesterov, Influence of beam polarization on laser cutting efficiency. J. Phys. D: Appl. Phys., 1999. **32**: p. 1455-1461.

241. Carbajo, S., et al., Direct longitudinal laser acceleration of electrons in free space. PHYSICAL REVIEW ACCELERATORS AND BEAMS, 2016. **021303**(19): p. 1-7.

242. Huerta-Murillo, D., et al., Fabrication of multi-scale periodic surface structures on Ti-6Al-4V by direct laser writing and direct laser interference patterning for modified wettability applications. Optics and Lasers in Engineering, 2017(98): p. 134-142.

243. Nuutinen, T., et al., Control of cultured human cells with femtosecond laser ablated patterns on steel and plastic surfaces. Biomed Microdevices, 2013(15): p. 279-288.

244. Jin, Y., et al., Dynamic modulation of spatially structured polarization fields for real-time control of ultrafast laser-material interactions. Optics Express, 2013. **21**(21): p. 25333-25343.

245. Skoulas, E., et al., Biomimetic surface structuring using cylindrical vector femtosecond laser beams. SCIENTIFIC REPORTS, 2017(7): p. 1-11.

246. Bonse, J., et al., Femtosecond laser-induced periodic surface srtuctures. J. Laser Appl., 2012(24): p. 1-8.
247. Razi, S., K. Madanipour, and M. Mollabashi, Laser surface texturing of 316L stainless steel in air and water: A method for increasing hydrophilicity via direct creation of microstructures. Optics & Laser Technology, 2016(80): p. 237-246.
248. Wen, L., J.C. Weaver, and G.V. Lauder, Biomimetic shark skin: design, fabrication and hydrodynamic. The Journal of Experimental Biology 2014. **217**: p. 1656-1666.
249. Chen, L., et al., Superhydrophobic micro-nano structures on silicone rubber by nanosecond laser processing. J. Phys. D: Appl. Phys, 2018(51): p. 1-12.
250. Zhang, D., et al., A Simple Way To Achieve Pattern-Dependent Tunable Adhesion in Superhydrophobic Surfaces by a Femtosecond Laser. APPLIED MATERIAL & INTERFACES, 2012(4): p. 4905-4912.
251. Bizi-Bandoki, P., et al., Modifications of roughness and wettability properties of metals induced by femtosecond laser treatment. Applied Surface Science, 2011. **257**(12): p. 5213-5218.
252. Florian, C., et al., Controlling the Wettability of Steel Surfaces Processed with Femtosecond Laser Pulses. APPLIED MATERIAL & INTERFACES, 2018(10): p. 36564-36571.
253. Rico Sierra, D., S.P. Edwardson, and G. Dearden, Laser surface texturing of titanium with thermal post-processing for improved wettability properties. Procedia CIRP, 2018. **74**: p. 362-366.
254. MacDonald, D.E., et al., Thermal and chemical modification of titanium–aluminum–vanadium implant materials: effects on surface properties, glycoprotein adsorption, and MG63 cell attachment. Biomaterials, 2004. **25**(16): p. 3135-3146.
255. Alnaser, A.S., et al., Recent Advances in Femtosecond Laser-Induced Surface Structuring for Oil–Water Separation. Appl.Sci., 2019. **9**(1554): p. 22.
256. Kubiak, K.J., et al., Wettability versus roughness of engineering surfaces. Wear, 2011. **271**(3-4): p. 523-528.
257. Shin, S., et al., Bio-Inspired Extreme Wetting Surfaces for Biomedical Applications. Materials, 2016. **9**(116): p. 26.

Appendix 1

The CGH generation and optical simulation in MATLAB environment

A self-programmed MATLAB code for Dammann grating generation is presented as below:

```
%% For Dammann grating generation. Applied in Chapter5
close all;
clear all;
clc;
p=100; %scale number
ImRx=800; %image resolution x=800 pixels
ImRy=600; %image resolution y=600 pixels

%------------------/ y Dimension
d=[0.5];
d1= floor(d(1)*p);
%d2= floor((d(2)-d(1))*p);
%d3= floor((d(3)-d(2))*p);
d2= floor((1-d(1))*p);
%d4= floor((1-d(3))*p);

gx1=zeros(d1,1);
gx2=ones(d2,1);
%gx3=zeros(d3,1);
%gx4=ones(d4,1);
gx11=ones(d1,1);
gx22=zeros(d2,1);
%gx33=ones(d3,1);
%gx44=zeros(d4,1);
gx =[gx1,gx11;gx2,gx22;];
gxt=gx;
gyt=gx'; %y direction

%----------------------/x Dimension
gt=gxt*gyt;
gt1=repmat(gt,13,16);
gr=imresize(gt1,[600 800]);
data1=uint8(gr);
data2=data1*107;
imshow(data2);
imwrite(data2,'Damann100_2x2_GL107.bmp');
```

Figure A1.1 presents an example of Dammann grating CGH by using the MATLAB code

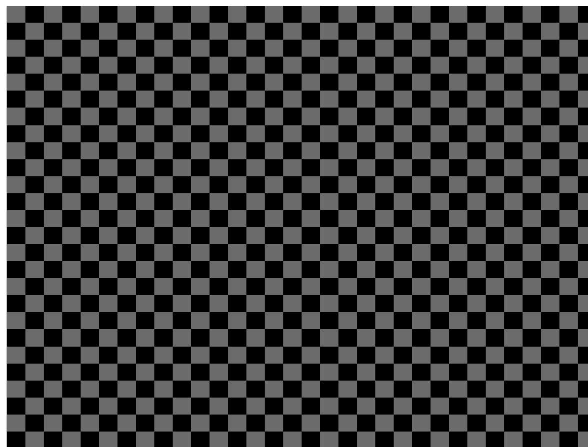

Figure A1.1 A binary Dammann grating CGH generated in MATLAB environement

A MATLAB code for ring mode beam generation is presented as below. This MATLAB code can also be used to compare the intensity distribution of a ring mode beam and a Gaussian beam.

```
%% For ring mode beam generation. Applied in chapter 6
close all;
clear all;
clc;
r0=11; % defining beam waist(radius) of the Gaussian beam
p=linspace(-30,30,1000);%p=-30e-3:1000:30e-3
q=linspace(-30,30,1000);%q=-30e-3:1000:30e-3
[x,y]=meshgrid(p,q); % Defining meshgrid for p and q coordinates
[theta,r]= cart2pol(x,y); % converting cartesian to polar coordinates

m=0;  % topological charge
a0=sqrt(1e11);% normolized field amplitude,
e0=a0.*(1/sqrt(factorial(m))).*(sqrt(2).*(r./r0).^abs(m)).*exp(-
(r.^2)/(r0.^2)).*exp(1i.*m.*theta);
I1=e0.*conj(e0);

m1=1; % topological charge
a1=sqrt(2)*sqrt(1e11);% normolized field amplitude,
e1=a1.*(1/sqrt(factorial(m1))).*(sqrt(2).*(r./r0).^abs(m1)).*exp(-
(r.^2)/(r0.^2)).*exp(1i.*m1.*theta);
I2=e1.*conj(e1);

%----------------------------optional m
%m2=2;
%a2=sqrt(4)*sqrt(2e11);% normolized field amplitude,
%e2=a2.*(1/sqrt(factorial(m2))).*(sqrt(2).*(r./r0).^abs(m2)).*exp(-
(r.^2)/(r0.^2)).*exp(1i.*m2.*theta);
%I3=e2.*conj(e2);

%m3=3;
%a3=sqrt(8)*sqrt(2e11);% normolized field amplitude,
%e3=a3.*(1/sqrt(factorial(m3))).*(sqrt(2).*(r./r0).^abs(m3)).*exp(-
(r.^2)/(r0.^2)).*exp(1i.*m3.*theta);
%I4=e3.*conj(e3);

%m4=4;
%a4=sqrt(16)*sqrt(2e11);% normolized field amplitude,
%e4=a4.*(1/sqrt(factorial(m4))).*(sqrt(2).*(r./r0).^abs(m4)).*exp(-
(r.^2)/(r0.^2)).*exp(1i.*m4.*theta);
%I5=e4.*conj(e4);
%------------------------------------------images
figure;
imagesc(I1); % intensity Gaussian
yticklabels = -30:10:30;
yticks = linspace(1,size(I1,1),numel(yticklabels));
set(gca, 'YTick', yticks, 'YTickLabel', flipud(yticklabels(:)))
xticklabels = -30:10:30;
xticks = linspace(1,size(I1,2),numel(xticklabels));
set(gca, 'XTick', xticks, 'XTickLabel', xticklabels)
axis on
caxis([0 2e11]);
colorbar
figure;
```

```
imagesc(I2); % intensity CV m=1
yticklabels = -30:10:30;
yticks = linspace(1,size(I2,1),numel(yticklabels));
set(gca, 'YTick', yticks, 'YTickLabel', flipud(yticklabels(:)))
xticklabels = -30:10:30;
xticks = linspace(1,size(I2,2),numel(xticklabels));
set(gca, 'XTick', xticks, 'XTickLabel', xticklabels)
axis on
caxis([0 2e11]);
colorbar;
%-----------------------------------------plots
line=0.135*max(max(I1));  % 1/e2 line of Gaussian beam, red
line2=0.135*max(max(I2)); % 1/e2 line of CV beam,blue
%line3=0.135*max(max(I3));
hold off

plot(-r,I1,-r,I2);hold on
plot(r,I1,r,I2);
pp=linspace(30,30,100);
plot(p,line,'r');
axis on;
grid on;
axis ([-30 30 0 2e11]);
plot(p,line2,'b');
axis on;
grid on;
axis ([-30 30 0 2e11]);
%-----------------------------------------------statics
IG=max(I1(:)); %peak intensity Gaussian beam in polar coordinate
ICV=max(I2(:)); %peak intensity CV beam in polar coordinate, m=1
%ICV11=max(I3(:));%peak intensity CV beam in polar coordinate, m=2
%ICV22=max(I4(:));%peak intensity CV beam in polar coordinate, m=3
%ICV33=max(I5(:));%peak intensity CV beam in polar coordinate, m=4
factor=IG/ICV;% peak intensity factor
%factor22=ICV/ICV11;
%factor33=IG/ICV22;
%factor44=IG/ICV33;

IG1=sum(I1(:)); %integral GA
ICV1=sum(I2(:));%integral CV m=1
%ICV2=sum(I3(:));%integral CV m=2
%ICV3=sum(I4(:));%integral CV m=3
%ICV4=sum(I5(:));%integral CV m=4
factor2=IG1/ICV1;% factor ga/m1
%factor3=IG1/ICV2; % ga/m2
%factor4=IG1/ICV3; %ga/m3
%factor5=IG1/ICV4; %ga/m4
```

Appendix 2

Table of ring mode beam peak intensity with topological charge

Topological charge m	max r	Peak intensity expression	Peak intensity
1	$\omega_0/\sqrt{2}$	$2I_{peak} * \frac{r^2}{\omega_0^2} * \exp\left(-2\frac{r^2}{\omega_0^2}\right)$	I_0/e
2	ω_0	$2I_{peak} * \frac{r^4}{\omega_0^4} * \exp\left(-2\frac{r^2}{\omega_0^2}\right)$	$2I_0/e^2$
3	$\sqrt{3}\omega_0/\sqrt{2}$	$\frac{4}{3}I_{peak} * \frac{r^6}{\omega_0^6} * \exp\left(-2\frac{r^2}{\omega_0^2}\right)$	$9I_0/2e^3$
4	$\sqrt{4}\omega_0/\sqrt{2}$	$\frac{2}{3}I_{peak} * \frac{r^8}{\omega_0^8} * \exp\left(-2\frac{r^2}{\omega_0^2}\right)$	$32I_0/3e^4$
5	$\sqrt{5}\omega_0/\sqrt{2}$	$\frac{2^5}{5!}I_{peak} * \frac{r^{10}}{\omega_0^{10}} * \exp\left(-2\frac{r^2}{\omega_0^2}\right)$	$625I_0/22e^5$
6	$\sqrt{6}\omega_0/\sqrt{2}$	$\frac{2^6}{6!}I_{peak} * \frac{r^{12}}{\omega_0^{12}} * \exp\left(-2\frac{r^2}{\omega_0^2}\right)$	$6^6I_0/6!\,e^6$
7	$\sqrt{7}\omega_0/\sqrt{2}$	$\frac{2^7}{7!}I_{peak} * \frac{r^{14}}{\omega_0^{14}} * \exp\left(-2\frac{r^2}{\omega_0^2}\right)$	$7^7I_0/7!\,e^7$
8	$\sqrt{8}\omega_0/\sqrt{2}$	$\frac{2^8}{8!}I_{peak} * \frac{r^{16}}{\omega_0^{16}} * \exp\left(-2\frac{r^2}{\omega_0^2}\right)$	$8^8I_0/8!\,e^8$
9	$\sqrt{9}\omega_0/\sqrt{2}$	$\frac{2^9}{9!}I_{peak} * \frac{r^{18}}{\omega_0^{18}} * \exp\left(-2\frac{r^2}{\omega_0^2}\right)$	$9^9I_0/9!\,e^9$
10	$\sqrt{10}\omega_0/\sqrt{2}$	$\frac{2^{10}}{10!}I_{peak} * \frac{r^{20}}{\omega_0^{20}} * \exp\left(-2\frac{r^2}{\omega_0^2}\right)$	$10^{10}I_0/10!\,e^{10}$
11	$\sqrt{11}\omega_0/\sqrt{2}$	$\frac{2^{11}}{11!}I_{peak} * \frac{r^{22}}{\omega_0^{22}} * \exp\left(-2\frac{r^2}{\omega_0^2}\right)$	$11^{11}I_0/11!\,e^{11}$
12	$\sqrt{12}\omega_0/\sqrt{2}$	$\frac{2^{12}}{12!}I_{peak} * \frac{r^{24}}{\omega_0^{24}} * \exp\left(-2\frac{r^2}{\omega_0^2}\right)$	$12^{12}I_0/12!\,e^{12}$
13	$\sqrt{13}\omega_0/\sqrt{2}$	$\frac{2^{13}}{13!}I_{peak} * \frac{r^{26}}{\omega_0^{26}} * \exp\left(-2\frac{r^2}{\omega_0^2}\right)$	$13^{13}I_0/13!\,e^{13}$
14	$\sqrt{14}\omega_0/\sqrt{2}$	$\frac{2^{14}}{14!}I_{peak} * \frac{r^{28}}{\omega_0^{28}} * \exp\left(-2\frac{r^2}{\omega_0^2}\right)$	$14^{14}I_0/14!\,e^{14}$
15	$\sqrt{15}\omega_0/\sqrt{2}$	$\frac{2^{15}}{15!}I_{peak} * \frac{r^{30}}{\omega_0^{30}} * \exp\left(-2\frac{r^2}{\omega_0^2}\right)$	$15^{15}I_0/15!\,e^{15}$
16	$\sqrt{16}\omega_0/\sqrt{2}$	$\frac{2^{16}}{16!}I_{peak} * \frac{r^{32}}{\omega_0^{32}} * \exp\left(-2\frac{r^2}{\omega_0^2}\right)$	$16^{16}I_0/16!\,e^{16}$
17	$\sqrt{17}\omega_0/\sqrt{2}$	$\frac{2^{17}}{17!}I_{peak} * \frac{r^{34}}{\omega_0^{34}} * \exp\left(-2\frac{r^2}{\omega_0^2}\right)$	$17^{17}I_0/17!\,e^{17}$
18	$\sqrt{18}\omega_0/\sqrt{2}$	$\frac{2^{18}}{18!}I_{peak} * \frac{r^{36}}{\omega_0^{36}} * \exp\left(-2\frac{r^2}{\omega_0^2}\right)$	$18^{18}I_0/18!\,e^{18}$
19	$\sqrt{19}\omega_0/\sqrt{2}$	$\frac{2^{19}}{19!}I_{peak} * \frac{r^{38}}{\omega_0^{38}} * \exp\left(-2\frac{r^2}{\omega_0^2}\right)$	$19^{19}I_0/19!\,e^{19}$
20	$\sqrt{20}\omega_0/\sqrt{2}$	$\frac{2^{20}}{20!}I_{peak} * \frac{r^{40}}{\omega_0^{40}} * \exp\left(-2\frac{r^2}{\omega_0^2}\right)$	$20^{20}I_0/20!\,e^{20}$
m	$\sqrt{m}\omega_0/\sqrt{2}$	$\frac{2^m}{m!}I_{peak} * \frac{r^{2m}}{\omega_0^{2m}} * \exp\left(-2\frac{r^2}{\omega_0^2}\right)$	$m^mI_0/m!\,e^m$

Appendix 3

The setup for cylindrical vector (CV) polarization confirmation in ZEMAX

The Jones Matrix function was applied for polarization confirmation, details can be seen in Figure A3.1.

	Surf:Type	Comment	Radius	Thickness	Material	Coating	Semi-Diameter	Conic	TCE x 1E-6	A real	A imag	B real	B imag	C real	C imag	D real	D imag
0	OBJECT Standard		Infini...	1.000			0.000	0.0...	0.000								
1	STOP Jones Matrix	fast axis		1.000			1.000 U		0.000	0.707	0.000	0.707	0.000	-0.700	0.000	0.707	0.000
2	IMAGE Standard		Infini...	-			1.000	0.0...	0.000								

Figure A3.1 Screenshot of CV polarization confirmation setup in ZEMAX.

Steps for setup:

1. Choosing the polarization method to Z Axis Reference.

2. Selecting a surface type to "Jones matrix", then 8 values will be displayed : A real, A imag, B real, B imag, C real, C imag, D real , D imag. "real" means real part and "imag" means imaginary part in math;

3. Giving a value (Value ≥ 1) to the thickness of the "OBJECT" surface.

4. Defining a value in each real part of "Jones matrix" surface depend on the rotating angle (θ) of the fast axis of the S-waveplate.

5. Checking results in Polarization Pupil Map. In the settings of the Polarization Pupil Map, the input polarization can be defined with Jx, Jy , X-Phase, Y-Phase in X, Y directions for initial polarization state generation.

Appendix 4

A block diagram for the dynamic control Labview program

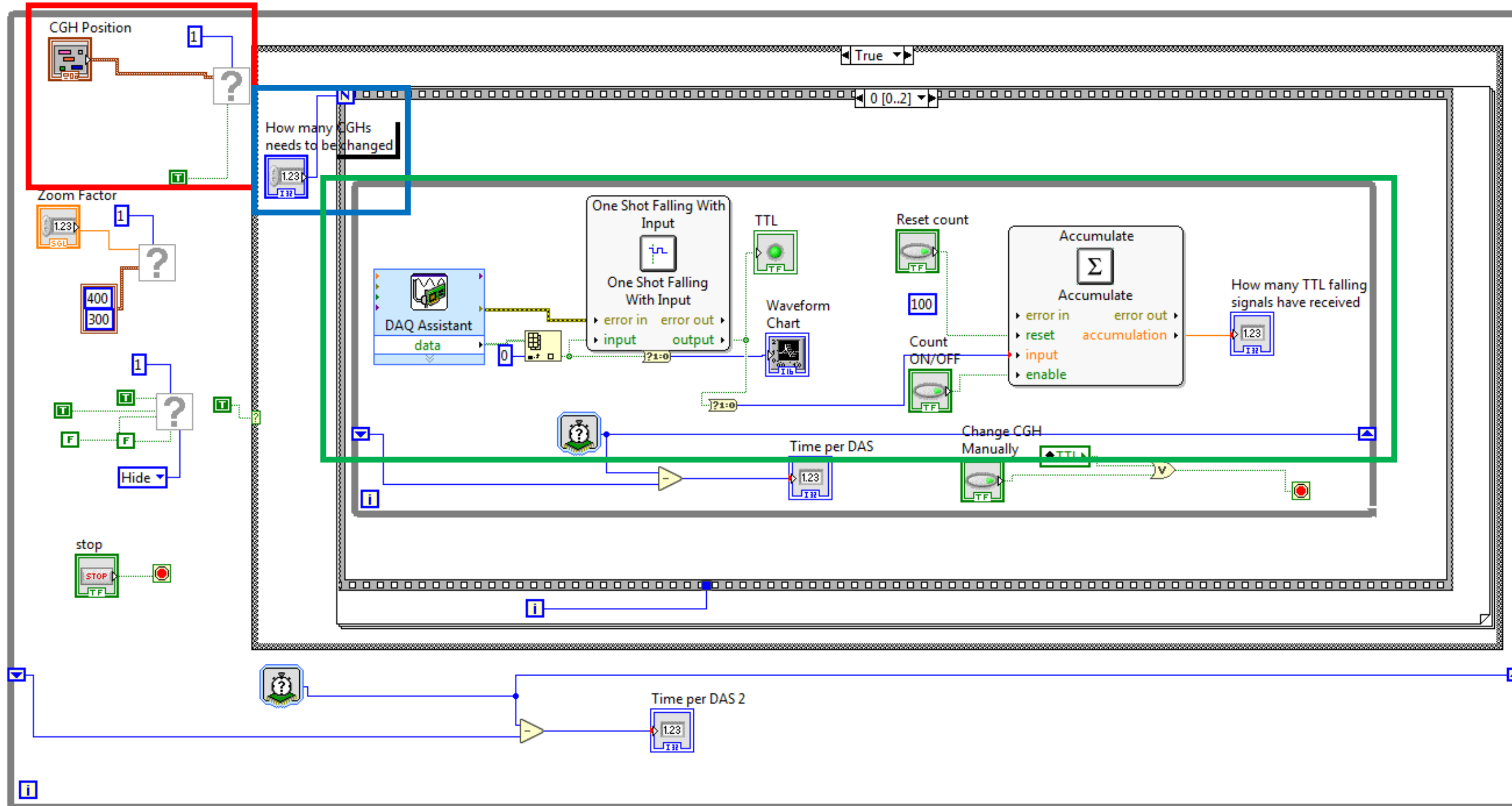

Red box: Displayed CGH position.

Blue box: Defining the numbers of CGH which are going to change.

Green box: Connecting the Labview software with the Aerotech controller (for sending signals) via a data acquisition device (DAQ assisstant). The signals can be received by the data acquisition device and will be countered.